

VELOCITY GRADIENT DYNAMICS IN INCOMPRESSIBLE TURBULENT FLOWS:
DATA-DRIVEN ANALYSIS & MODELING

A Dissertation

by

RISHITA DAS

Submitted to the Graduate and Professional School of
Texas A&M University
in partial fulfillment of the requirements for the degree of
DOCTOR OF PHILOSOPHY

Chair of Committee, Sharath S. Girimaji
Committee Members, Diego Donzis
Adonios Karpetis
Alan Palazzolo
Head of Department, Ivett Leyva

December 2021

Major Subject: Aerospace Engineering

Copyright 2021 Rishita Das

ABSTRACT

Velocity gradients embody the small-scale behavior of turbulence and hold the key to understanding important phenomena such as small-scale intermittency, local-streamline geometry, scalar-mixing, and material-element-deformation. The goal of this dissertation is to investigate velocity-gradient dynamics using direct numerical simulation (DNS) data of turbulent flows to (i) develop deeper understanding of the small-scale dynamics and turbulence processes and (ii) derive a model for the Lagrangian velocity-gradient dynamics in incompressible turbulent flows.

We begin with the proposal that improved insight can be obtained by investigating the internal-structure and the magnitude of the velocity-gradient tensor, individually. This is done by factorizing the velocity-gradient tensor into a bounded normalized velocity-gradient tensor, that represents local-streamline geometry and an intermittent magnitude, that represents the scale of the streamlines. Analysis of the DNS datasets of isotropic turbulence and turbulent channel flow demonstrates that the normalized velocity-gradient geometry exhibits a distinct universality across different Reynolds numbers, while the magnitude grows with Reynolds number.

The dynamics of the velocity-gradient geometry and magnitude in turbulence are investigated within the state-space of the normalized velocity-gradient tensor. The effects of different turbulence processes – inertial, pressure, viscous, and large-scale forcing – on velocity-gradient dynamics are clearly identified and explicated. The key findings are that pressure along with inertia drive all flow geometries toward pure-shear, while viscosity not only reduces the velocity-gradient magnitudes but also drives the local-flow towards strain-dominated geometries.

The turbulence small-scale dynamics is revisited using a novel velocity-gradient triple decomposition. In this decomposition, the effects of normal-strain and pure-rotation are clearly demarcated from that of shear. The analysis of DNS data reveals that shear constitutes the most dominating contribution toward velocity gradients in a turbulent flow field and may be the most responsible for its intermittent nature.

A new Lagrangian velocity-gradient model is derived by modeling the bounded dynamics of

the normalized velocity-gradient tensor and the dynamics of intermittent magnitude separately. The nonlocal flow-physics are captured by a data-driven closure in the bounded four-dimensional state-space of normalized velocity gradients, while the magnitude is modeled as a near-lognormal diffusion process. The resulting velocity-gradient model shows improved agreement with the small-scale statistics of DNS.

DEDICATION

*To my mother, father and big brother who have always supported me no matter what
& to Nayrhit for always believing in me and encouraging me to take the leap.*

ACKNOWLEDGMENTS

First, I would like to extend my sincere gratitude to my advisor, Professor Sharath Girimaji, for giving me this wonderful opportunity to work with him and learn so much under his guidance. I thank him for being a patient mentor and for motivating me when I needed it the most during my PhD. His support and advice has helped me grow as a researcher in a number of ways. He has inspired me to strive to be a thinker, not just a researcher. Everything I have learned from him is a prized possession I am taking forward with me as I finish my PhD.

I would also like to thank my committee members – Professors Diego Donzis, Adonios Karpets and Alan Palazzolo, for their time and guidance. Their insightful comments and questions have helped improve the quality of my thesis work. I would particularly like to express my gratitude to Dr. Donzis for providing most of the datasets used for analysis in this work and for patiently helping me out in the initial stages of processing the datasets.

I am really thankful to Professor Ignacio Rodriguez-Iturbe for being a wonderful teacher, for lending me the most insightful books to read and for the enlightening discussion sessions that I always looked forward to. His distinguished and humble self has been an inspiration for me.

I would like to thank all my labmates - Divya, Ankita, Chetna, Bajrang, Massey, Filipe, Pedram, Steven, Mona, Salar and Swapnil for making this PhD a fun experience. A special thanks to my first office mates Divya and Ankita for helping me learn how to cope with a PhD life and make the most out of it, and to Bajrang and Chetna for being my support system that I could always rely on. I would like to thank my roommate Neha for always being there and helping me get through the tough times. A big thank you to Sualeh, Jyot, Dammati, Roshan, Komal, Pawan and all my friends here at College Station for making this a memorable journey.

Finally, I dedicate this PhD to my parents for their unconditional support and love for me in whatever I chose to do throughout my life, to my big brother who inspired me to be a researcher like him, and to my husband Nayrhit for his love and affection and for being my constant source of motivation even from thousands of miles away.

CONTRIBUTORS AND FUNDING SOURCES

Contributors

This work was supported by a dissertation committee consisting of Professor Sharath S. Girimaji of the Department of Ocean Engineering, Professors Diego Donzis and Adonios Karpetis of the Department of Aerospace Engineering and Professor Alan Palazzolo of the Department of Mechanical Engineering.

Part of the data analyzed in this work was provided by Professor Diego Donzis and part of it was obtained from the Johns Hopkins Turbulence Database. All work conducted for the dissertation was completed by the student independently.

Funding Sources

Graduate study was supported by Teaching assistantships and AERO Graduate Excellence Fellowships from the Department of Aerospace Engineering at Texas A&M University, Research assistantship with funding from the Wofford Cain Chair II endowment, and the Amelia Earhart Fellowship from Zonta International.

The numerical analysis performed in this dissertation were conducted with the advanced computing resources provided by Texas A&M High Performance Research Computing.

NOMENCLATURE

DNS	Direct Numerical Simulation
VG	Velocity Gradient
PDF	Probability Density Function
RE	Restricted Euler
RFD	Recent Fluid Deformation
RDGF	Recent Deformation of Gaussian Fields
RMS	Root-Mean-Square
SFS	Stable Focus Stretching
UFC	Unstable Focus Compression
SN/S/S	Stable-Node/Saddle/Saddle
UN/S/S	Unstable-Node/Saddle/Saddle
CMT	Conditional Mean Trajectory
FIT	Forced Isotropic Turbulence
RHS	Right-Hand-Side
OU	Ornstein-Uhlenbeck
SDE	Stochastic Differential Equation

TABLE OF CONTENTS

	Page
ABSTRACT	ii
DEDICATION	iv
ACKNOWLEDGMENTS	v
CONTRIBUTORS AND FUNDING SOURCES	vi
NOMENCLATURE	vii
TABLE OF CONTENTS	viii
LIST OF FIGURES	xii
LIST OF TABLES.....	xviii
1. INTRODUCTION	1
1.1 Motivation	1
1.2 Background and literature review	3
1.2.1 Velocity gradient tensor	3
1.2.2 Turbulence small-scale behavior.....	5
1.2.3 Geometry of local flow streamlines	6
1.2.4 Velocity gradient dynamics	9
1.2.5 Modeling turbulence small-scale behavior	10
1.3 Dissertation objectives and research tasks	12
2. NORMALIZED VELOCITY GRADIENT TENSOR	16
2.1 Introduction	16
2.2 Governing equations	17
2.2.1 Mathematical bounds of normalized VG tensor	18
2.2.2 Evolution equations of VG magnitude and normalized VG tensor	20
2.2.3 Evolution equations of normalized VG invariants	21
2.3 Numerical simulation data	22
2.4 Results and discussion	23
2.4.1 Unnormalized velocity gradient statistics	23
2.4.2 Normalized velocity gradient statistics	25
2.4.3 Invariants of normalized VG tensor	26
2.4.4 Evolution of normalized VG invariants and VG magnitude	29

2.4.5	Lagrangian velocity gradient modeling	35
2.5	Summary and conclusions	35
3.	GEOMETRY OF LOCAL FLOW STREAMLINES	37
3.1	Introduction	37
3.2	Complete characterization of local streamline geometry	38
3.2.1	Geometry and topology	38
3.2.2	Local flow streamlines	39
3.2.3	Topological classification of streamlines	40
3.2.4	Geometric description of streamlines	43
3.2.5	Kinematic bounds of shape-parameters	49
3.2.6	Characterization of geometric shape in q - r plane	51
3.3	Numerical simulation data	56
3.4	Statistical characterization of local streamline geometry	57
3.4.1	Probability distribution of geometric shape parameters	58
3.4.2	Scale-factor in shape-parameter space	62
3.4.3	Projection of geometric-shape on q - r plane	63
3.4.4	Universality of geometric shape	67
3.5	Summary and conclusions	67
4.	TRIPLE DECOMPOSITION OF VELOCITY GRADIENT TENSOR INTO SHEAR, ROTATION, AND NORMAL STRAIN	69
4.1	Introduction	69
4.2	Triple decomposition of VG tensor	72
4.2.1	Decomposition procedure	73
4.2.1.1	Rotational case	73
4.2.1.2	Non-rotational case	75
4.2.2	Properties of VG tensor constituents	77
4.2.2.1	Composition of velocity gradient magnitude	77
4.2.2.2	Invariants and local streamline geometry	80
4.3	Numerical simulation data	84
4.4	Velocity gradients and pressure field characterization	85
4.4.1	Composition of VG magnitude	85
4.4.2	Dependence of pressure field on VG constituents	89
4.4.3	Alignment properties	92
4.5	Conclusions	95
5.	VELOCITY GRADIENT DYNAMICS: EFFECT OF TURBULENCE PROCESSES ON EVOLUTION OF LOCAL STREAMLINE GEOMETRY	97
5.1	Introduction	97
5.2	Evolution equations of local streamline shape	98
5.3	Conditional mean trajectories (CMTs)	100
5.4	Numerical simulation data	101

5.5	Conditional mean evolution of geometry	101
5.5.1	Conditional mean trajectories in Q - R plane	101
5.5.2	Conditional mean trajectories in q - r plane	102
5.5.3	Cycle time period of CMT	104
5.5.4	Residence time of CMTs in topologies	106
5.6	Effect of different physical processes	107
5.6.1	Inertial effects	107
5.6.2	Pressure effects	108
5.6.3	Pressure and inertial effects	109
5.6.4	Viscous effects	112
5.7	Conclusion	112
6.	EFFECT OF LARGE-SCALE FORCING ON SMALL-SCALE VELOCITY GRADIENT DYNAMICS	114
6.1	Introduction.....	114
6.2	Forcing in velocity-gradient evolution equations	116
6.2.1	Evolution equations of normalized VG tensor	118
6.2.2	Evolution equations of VG magnitude.....	121
6.3	Numerical simulation data	122
6.4	Normalized VG tensor dynamics	123
6.4.1	Non-linear, pressure and viscous effects	125
6.4.2	Forcing effects	129
6.4.3	Helmholtz-Hodge decomposition of the probability currents	133
6.4.3.1	Dilatational and solenoidal current from DNS data	134
6.5	VG magnitude dynamics.....	137
6.5.1	VG magnitude dynamics conditioned on q - r	138
6.5.2	VG magnitude dynamics conditioned on θ^*	140
6.6	Conclusions.....	142
7.	DATA-DRIVEN MODEL FOR LAGRANGIAN VELOCITY GRADIENT DYNAMICS IN TURBULENCE	144
7.1	Introduction.....	144
7.2	Properties and governing equations	147
7.2.1	Normalized VG tensor	148
7.2.2	VG magnitude	149
7.3	Model Formulation	150
7.3.1	Modeling strategy	151
7.3.2	Generalizability	151
7.3.3	Stochastic model for normalized VG tensor	154
7.3.3.1	Drift coefficients	156
7.3.3.2	Diffusion coefficients	159
7.3.4	Stochastic model for VG magnitude	161
7.3.4.1	Model 1 - original OU process	162
7.3.4.2	Model 2 - modified OU process	163

7.3.4.3	Model 3 - consistent modified OU process	165
7.3.5	Model summary	165
7.4	Numerical procedure	168
7.5	Results and comparison with DNS data	169
7.5.1	VG magnitude	170
7.5.2	Normalized VG tensor	172
7.5.3	VG tensor	179
7.6	Conclusion	182
8.	SUMMARY AND CONCLUSIONS	185
8.1	Velocity gradient framework of geometry and magnitude	185
8.2	Velocity gradient decomposition into shear, rotation and normal-strain	186
8.3	Velocity gradient dynamics	186
8.4	Velocity gradient modeling	187
8.5	Future directions	188
	REFERENCES	190
	APPENDIX A. DIRECT NUMERICAL SIMULATION DATASETS	204
	APPENDIX B. UPPER BOUND OF NORMALIZED SHEAR-ROTATION CORRELA- TION TERM	207
	APPENDIX C. FOUR-VARIABLE REPRESENTATION OF NORMALIZED VG TEN- SOR	209
	APPENDIX D. VELOCITY GRADIENT MODEL: DERIVATIONS AND NUMERICAL METHODS	211
D.1	Relevant properties of Itô process	211
D.2	Derivation of b_{ij} SDE from A_{ij} SDE	212
D.3	Incompressibility constraint	213
D.4	Normalization constraint	214
D.5	Galilean invariance	215
D.6	Numerical schemes for stochastic differential equations	217

LIST OF FIGURES

FIGURE	Page
2.1 Even order moments (M_{2n} for $n = 2, 3, 4, 5, 6$) of A_{11} as a function of Re_λ . Dashed lines represent Gaussian moments, i.e. $M_{2n}^G = (2n - 1)!!$, for reference. Reprinted with permission from Das and Girimaji (2019).	24
2.2 PDF of velocity gradient component (a) $A_{11}/\sqrt{\langle A^2 \rangle}$ (b) $A_{12}/\sqrt{\langle A^2 \rangle}$ for different Re_λ . Reprinted with permission from Das and Girimaji (2019).	25
2.3 Even order moments (M_{2n} for $n = 2, 3, 4, 5, 6$) of b_{11} as a function of Re_λ . Dashed lines represent Gaussian moments, i.e. $M_{2n}^G = (2n - 1)!!$ for reference. Reprinted with permission from Das and Girimaji (2019).	26
2.4 PDF of (a-b) normalized longitudinal velocity gradient b_{11} (c-d) normalized transverse velocity gradient b_{12} for $Re_\lambda = 1-35$ and $35-588$. Reprinted with permission from Das and Girimaji (2019).	27
2.5 q -PDF for (a) $Re_\lambda = 1, 6, 9, 14, 18$ and 25 (b) $Re_\lambda = 25, 35, 86, 225, 385, 414$ and 588 . Reprinted with permission from Das and Girimaji (2019).	28
2.6 r -PDF for (a) $Re_\lambda = 1, 6, 9, 14, 18$ and 25 (b) $Re_\lambda = 25, 35, 86, 225, 385, 414$ and 588 . Reprinted with permission from Das and Girimaji (2019).	29
2.7 q - r joint PDF filled contour plots for $Re_\lambda =$ (a) 1 (b) 6 (c) 9 (d) 14 (e) 18 (f) 25. q - r joint PDF line contour plots for $Re_\lambda =$ (g) 25 to 225 (h) 225 to 588. The contour levels are identical for all plots: color scheme for (a-f) is as shown in (a). Reprinted with permission from Das and Girimaji (2019).	30
2.8 Conditional averages of nonlinear (circles), anisotropic pressure (triangles) and viscous (squares) contributions in (a) $\langle \frac{dq}{dt} q \rangle$ (b) $\langle \frac{dq}{dt} r \rangle$ (c) $\langle \frac{dr}{dt} q \rangle$ (d) $\langle \frac{dr}{dt} r \rangle$ for different Re_λ (Refer to equations (2.24) and (2.27); Color scheme: as given in (b)). Reprinted with permission from Das and Girimaji (2019).	31
2.9 Conditional averages of inertial (circles), pressure (triangles) and viscous (squares) contributions in θ -evolution equation conditioned on (a) q (b) r for different Re_λ (Refer to equation 2.18; Color scheme: as given in (a)). Reprinted with permission from Das and Girimaji (2019).	32

2.10	Conditional variance of anisotropic pressure and viscous terms in q -, r - and θ -equations conditioned on q and r : (a) $Var(P_q q)$ vs q (b) $Var(V_q q)$ vs q (c) $Var(P_q r)$ vs r (d) $Var(V_q r)$ vs r (e) $Var(P_r q)$ vs q (f) $Var(V_r q)$ vs q (g) $Var(P_r r)$ vs r (h) $Var(V_r r)$ vs r (i) $Var(P_\theta q)$ vs q (j) $Var(V_\theta q)$ vs q (k) $Var(P_\theta r)$ vs r (l) $Var(V_\theta r)$ vs r for different Re_λ (Color scheme: as given in (a)). Reprinted with permission from Das and Girimaji (2019).....	34
3.1	Classification of local three-dimensional streamlines into non-degenerate topologies in Q - R plane (Chong et al., 1990) for incompressible turbulence. The curved solid lines are discriminant $D = 0$ lines. Reprinted with permission from Das and Girimaji (2020a).....	40
3.2	Summary of the key points of different frameworks for studying local flow streamline structure. Reprinted with permission from Das and Girimaji (2020a).....	49
3.3	Streamline shapes represented by different points, lines and regions of the q - r plane. Reprinted with permission from Das and Girimaji (2020a).....	52
3.4	Joint PDF of (a) q - r (b) q - $ \cos\beta $ (c) q - a_2 (d) a_2 - r (e) a_2 - $ \cos\beta $ (f) $ \cos\beta $ - r for $Re_\lambda = 225$. Dashed line marks the boundary of the realizable region of the phase plane. Thick red line marks the contour level that includes 90% of the field. Reprinted with permission from Das and Girimaji (2020a).....	59
3.5	Conditional mean $\langle A^2 x, y \rangle / \langle A^2 \rangle$ in (a) q - r ($x = r, y = q$) (b) q - $ \cos\beta $ (c) q - a_2 (d) a_2 - r (e) a_2 - $ \cos\beta $ (f) $ \cos\beta $ - r planes for $Re_\lambda = 225$. Reprinted with permission from Das and Girimaji (2020a).....	61
3.6	Conditional average of shape-parameters (a) q , (b) r , (c) a_2 and (d) $ \cos\beta $ conditioned on VG magnitude ($A^2/\langle A^2 \rangle$) for $Re_\lambda = 225$ case. The x-axes are in log-scale and the y-axes are limited by the kinematic bounds of the corresponding shape parameter. Reprinted with permission from Das and Girimaji (2020a).....	64
3.7	Conditional average of (a) intermediate strain-rate: $\langle a_2 q, r \rangle$ and (b) angle of alignment between vorticity and intermediate strain-rate eigenvector: $\langle \cos\beta q, r \rangle$. Reprinted with permission from Das and Girimaji (2020a).....	65
3.8	Isocontour lines of q - r joint PDF of (a) forced isotropic turbulent (FIT) flow at $Re_\lambda = 225, 385, 427, 588$, (b) turbulent channel flow at $Re_\lambda = 81, 110, 132, 183$, and (c) FIT at $Re_\lambda = 225$ and turbulent channel flow at $Re_\lambda = 183$	66
4.1	Two-dimensional example of fluid element deformation due to (a) normal-strain-rate tensor, (b) shear tensor, and (c) rigid-body-rotation tensor. Reprinted with permission from Das and Girimaji (2020b).....	72
4.2	Local streamline shapes and composition of VG tensor in different points/regions of the q - r plane: (a) degenerate cases (b) non-degenerate cases. Reprinted with permission from Das and Girimaji (2020b).....	82

4.3	Volume average of H^2 , N^2 , $2RH$ and R^2 normalized by the volume average of A^2 in the three Re_λ ranges (marked by different background colors). The dashed line marks the volume average of S^2 and W^2 , normalized by $\langle A^2 \rangle$. Reprinted with permission from Das and Girimaji (2020b).	86
4.4	Probability density function (PDF) of A^2 , H^2 , N^2 , R^2 and $2RH$ normalized by volume-averaged VG magnitude $\langle A^2 \rangle$ in log-linear scale for $Re_\lambda = 225$. Reprinted with permission from Das and Girimaji (2020b).	87
4.5	Conditional average of h^2 , n^2 , r^2 and $2rh$ as a function of $A^2/\langle A^2 \rangle$ in the high Re_λ range. Reprinted with permission from Das and Girimaji (2020b).	88
4.6	Conditional average of pressure fluctuation (normalized by turbulent kinetic energy) as a function of s^2 and w^2 for $Re_\lambda = 225$. Reprinted with permission from Das and Girimaji (2020b).	90
4.7	Conditional average of pressure fluctuation (normalized by turbulent kinetic energy) as a function of h^2 , n^2 , r^2 and $2rh$ for $Re_\lambda = 225$. Reprinted with permission from Das and Girimaji (2020b).	91
4.8	PDFs of absolute values of the cosines of angles between the vorticity vector ($\vec{\omega}$) and the N -eigenvectors ($\vec{n}_1, \vec{n}_2, \vec{n}_3$) for locally (a) rotational, and (b) non-rotational points in $Re_\lambda = 225$ case. Black dashed line represents the alignment of $\vec{\omega}$ with the intermediate strain-rate eigenvector \vec{s}_2 . Reprinted with permission from Das and Girimaji (2020b).	93
4.9	PDFs of absolute values of the cosines of the angles between rotation axis (\vec{r}) and the eigenvectors of pressure Hessian ($\vec{\pi}_1, \vec{\pi}_2, \vec{\pi}_3$) for $Re_\lambda = 225$. Reprinted with permission from Das and Girimaji (2020b).	94
5.1	Conditional mean trajectories (CMTs) in (a) Q - R plane for $Re_\lambda = 225$ (b) q - r plane for $Re_\lambda = 225$ (c) q - r plane for $Re_\lambda = 385$ (d) q - r plane for $Re_\lambda = 588$. Background contours indicate the speed of the trajectory at each point, normalized by Kolmogorov time scale. White dashed lines represent the corresponding separatrices. Reprinted with permission from Das and Girimaji (2020a).	103
5.2	(a) A representative inner CMT (point of origin marked by circle) and corresponding (b) q evolution with time (c) r evolution with time. (d) Two representative outer CMTs (points of origin marked by circles) and corresponding (e) q evolution with time (f) r evolution with time. Dashed lines in (a,d) represent the separatrix loop and boundary of realizable region of q - r plane. Reprinted with permission from Das and Girimaji (2020a).	105
5.3	Inertial CMTs in (a) Q - R plane and (b) q - r plane for $Re_\lambda = 225$. Background contours indicate the speed of the trajectory at each point, normalized by Kolmogorov time scale. Reprinted with permission from Das and Girimaji (2020a).	107

5.4	Pressure CMTs in (a) Q - R plane and (b) q - r plane for $Re_\lambda = 225$. Background contours indicate the speed of the trajectory at that point, normalized by Kolmogorov time scale. The dashed lines separate the three types of pressure CMTs in q - r space. Reprinted with permission from Das and Girimaji (2020a).	108
5.5	Pressure-inertial CMTs in (a) Q - R and (b) q - r plane for $Re_\lambda = 225$. Background contours indicate the speed of the trajectory at that point, normalized by Kolmogorov time scale. Reprinted with permission from Das and Girimaji (2020a)..	110
5.6	Viscous CMTs in (a) Q - R plane for $Re_\lambda = 225$ (b) q - r plane for $Re_\lambda = 225$ (c) q - r plane for $Re_\lambda = 385$ (d) q - r plane for $Re_\lambda = 588$. Background contours indicate the speed of the trajectory at that point, normalized by Kolmogorov time scale. Reprinted with permission from Das and Girimaji (2020a).	111
6.1	Isocontours of q - r joint PDF, $\mathcal{F}(q, r)$, for (a) forced isotropic turbulence (FIT), (b) turbulent channel flow, at different Re_λ . The highest PDF level contour is along the right discriminant line and the PDF level drops with distance from the line. Solid black lines in the 3 rd and 4 th quadrants represent the zero-discriminant lines (Cantwell, 1992).	124
6.2	Isocontours of q - r joint PDF, $\mathcal{F}(q, r)$, of FIT at $Re_\lambda = 225$ (blue solid line) and turbulent channel flow at $Re_\lambda = 183$ (red dashed line).	125
6.3	q - r probability current due to non-linear terms (\mathbf{W}_N) for (a) FIT $Re_\lambda = 225$ and (b) turbulent channel flow $Re_\lambda = 183$. The background contours represent the magnitude of the vector \mathbf{W}_N	126
6.4	q - r probability current due to anisotropic pressure (\mathbf{W}_P) for (a) FIT $Re_\lambda = 225$ and (b) turbulent channel flow $Re_\lambda = 183$. The background contours represent the magnitude of the vector \mathbf{W}_P	127
6.5	q - r probability current due to viscous effects (\mathbf{W}_V) for FIT $Re_\lambda = 225$. The background contours represent the magnitude of the vector \mathbf{W}_V	128
6.6	q - r probability currents due to non-linear, pressure and viscous effects, \mathbf{W}_{NPV} , for (a) FIT at $Re_\lambda = 427$, and (b) turbulent channel flow at $Re_\lambda = 132$. The background contours represent the magnitude of the vector \mathbf{W}_{NPV} . The white dash-dotted lines represent the separatrices.	128
6.7	Total q - r probability current (\mathbf{W}) for FIT at $Re_\lambda = 427$. The red squares represent the starting points of the trajectories. The background contours represent the magnitude of the vector \mathbf{W}	130
6.8	q - r probability current due to forcing (\mathbf{W}_F), with background contours representing the magnitude $ \mathbf{W}_F $ for FIT $Re_\lambda = 427$	131

6.9	Relative contribution of forcing probability current with respect to the aggregate of nonlinear-pressure-viscous processes, i.e. $ \mathbf{W}_F /(\mathbf{W}_F + \mathbf{W}_{NPV}) \times 100$, for FIT $Re_\lambda = 427$. Contour levels are in an approximate log-scale.	132
6.10	Dilatational parts of (a) forcing probability current $\mathbf{W}_F^{(dil)}$, and (b) nonlinear-pressure-viscous probability current $\mathbf{W}_{NPV}^{(dil)}$, for FIT $Re_\lambda = 427$. The background contours represent the magnitude of the vector.	135
6.11	Solenoidal parts of: (a) forcing probability current $\mathbf{W}_F^{(sol)}$, and (b) nonlinear-pressure-viscous probability current $\mathbf{W}_{NPV}^{(sol)}$, for FIT $Re_\lambda = 427$. The background contours represent the magnitude of the vector.	136
6.12	PDF of θ^* (dashed line) for FIT $Re_\lambda = 225, 385 \text{ \& } 427$ and standard normal distribution (solid line).	138
6.13	Conditional mean rate-of-change of θ ($\equiv \ln A$) in q - r phase plane due to: (a) non-linear, (b) pressure, (c) viscous, (d) nonlinear-pressure-viscous, (e) forcing, and (f) all processes for FIT $Re_\lambda = 427$	139
6.14	Conditional mean rate-of-change of θ ($\equiv \ln A$) conditioned on θ^* due to different processes, for FIT $Re_\lambda = 427$	141
7.1	Flowchart to explain the behavior of velocity gradient tensor and its constituents in turbulence.	152
7.2	Statistics of θ from DNS datasets of forced isotropic turbulent flows at different Re_λ : (a) global mean $\langle \theta \rangle$ as a function of Re_λ (in natural log scale); dashed line represents a linear least-squares fit of the data ($\langle \theta \rangle = -0.2 + 0.6 \ln Re_\lambda$); and (b) variance $\sigma_\theta^2 = \langle \theta^2 - \langle \theta \rangle^2 \rangle$ as a function of Re_λ (in natural log scale); dashed line represents a linear least-squares fit of the data ($\sigma_\theta^2 = -0.074 + 0.07 \ln Re_\lambda$).	153
7.3	Conditional variance of θ^* conditioned on q - r , i.e. $\langle (\theta^* - \langle \theta^* q, r \rangle)^2 q, r \rangle$, for isotropic turbulent flows of Taylor Reynolds numbers: (a) $Re_\lambda = 225$, (b) $Re_\lambda = 385$, (c) $Re_\lambda = 427$, (d) $Re_\lambda = 588$	164
7.4	Evolution of θ^* statistics: (a) mean, $\langle \theta^* \rangle$ and (b) standard deviation, σ_{θ^*} , for the three models with different θ^* equations. The DNS statistics are marked by the dashed lines. The time axis is in logscale.	170
7.5	PDF of standardized VG magnitude θ^* in: (a) linear-linear scale and (b) linear-log scale, for the three models. The black solid line with symbols represent the θ^* -PDF from DNS data.	171
7.6	PDF of VG magnitude $A/\langle A \rangle$	172

- 7.7 Conditional mean trajectories in the q - r plane due to the inertial, pressure and viscous effects obtained using (a) DNS data and (b) b_{ij} data-driven model. Background contours represent the speed of the trajectory at each point, given by the magnitude of the conditional mean velocity vector, $|\tilde{\mathbf{v}}|$ 173
- 7.8 Evolution of q and r statistics in global normalized time t^* . Means: (a) $\langle q \rangle$ and (b) $\langle r \rangle$; second order moments: (c) $\langle q^2 \rangle$ and (d) $\langle r^2 \rangle$; third order moments: (e) $\langle q^3 \rangle$ and (f) $\langle r^3 \rangle$; fourth order moments: (g) $\langle q^4 \rangle$ and (h) $\langle r^4 \rangle$ for the three models with different θ^* equations. The dashed lines represent the DNS statistics. The time axis is in log-scale. 174
- 7.9 Evolution of the q and r moments: (a) $\langle qr \rangle$, and (b) $\langle q^2 r^2 \rangle$, in global normalized time t^* . The dashed lines represent the DNS statistics. The time axis is in log-scale.. 175
- 7.10 The evolution of the q - r joint PDF during numerical propagation of model 3 at different global normalized time: (a) $t^* = 0.0$, (b) $t^* = 0.1$, (c) $t^* = 0.3$, (d) $t^* = 1.0$, (e) $t^* = 2.0$, (f) $t^* = 5.0$, (g) $t^* = 10.0$, (h) $t^* = 50.0$, (i) $t^* = 500.0$. The dashed lines represent the lines of zero-discriminant ($d = q^3 + (27/4)r^2 = 0$). . 176
- 7.11 Joint PDFs of q - r obtained from the: solutions of (a) model 1, (b) model 2, and (c) model 3, and (d) DNS data. The dashed lines represent the zero-discriminant lines. . 177
- 7.12 PDFs of absolute values of cosine of angles between vorticity vector and strain-rate eigenvectors (1 - most expansive, 2 - intermediate, 3 - most compressive). The solid lines are the PDFs obtained from DNS data. 178
- 7.13 PDFs of: (a) longitudinal component of velocity gradient tensor, $A_{11}/\sqrt{\langle A_{11}^2 \rangle}$, and (b) transverse component of velocity gradient tensor, $A_{12}/\sqrt{\langle A_{12}^2 \rangle}$, in log-linear scale obtained from the solutions of the three models. The solid line marked with symbols represent the PDFs obtained from DNS data. The dashed and dash-dotted lines represent the PDFs obtained from previous models - RDGF (Johnson and Meneveau, 2016a) and PIML (Tian et al., 2021), respectively. 180
- 7.14 PDFs of: (a) dissipation rate, $S_{ij}S_{ij}/\sqrt{\langle S_{ij}S_{ij} \rangle}$, (b) enstrophy, $W_{ij}W_{ij}/\sqrt{\langle W_{ij}W_{ij} \rangle}$, and (c) pseudodissipation rate, $A_{ij}A_{ij}/\sqrt{\langle A_{ij}A_{ij} \rangle}$, in log-linear scale obtained from the solutions of the three models. The black solid line marked with symbols represent the PDFs obtained from DNS data; black dash-dotted line marks the PDFs for the initial field used in the model's simulations; dashed line represent the PDFs from the RDGF model of Johnson and Meneveau (2016a). 183

LIST OF TABLES

TABLE	Page
3.1 Description of streamline shapes at points/lines marked in $q-r$ plane in figure 3.3. Reprinted with permission from Das and Girimaji (2020a).	53
5.1 Percentage composition of topologies in inner and outer regions and residence time (%) of representative CMTs (figure 5.2) in each topology. Reprinted with permission from Das and Girimaji (2020a).	106
7.1 Components of model based on DNS data.	167
7.2 Third, fourth and sixth order moments of VG magnitude ($A = \sqrt{A_{ij}A_{ij}}$), longitudinal VG component (A_{11}), transverse VG component (A_{12}) from DNS data, model 1, model 2, model 3 and RDGF model of Johnson and Meneveau (2016a). For each moment, the DNS value and the model's value closest to DNS are written in bold type font.	181
A.1 Details of forced isotropic incompressible turbulence datasets used in this study. Here, JHTDB represents Johns Hopkins Turbulence Data Base, TACL represents Turbulent and Advanced Computations Laboratory, and TAMU represents Texas A&M University.	205

1. INTRODUCTION

1.1 Motivation

The ubiquity and complexity of turbulent flows have long been recognized. The phenomenon of turbulence critically impacts many flows of interest in nature and engineering. At the largest scales, turbulence plays an important role in astrophysical, atmospheric and oceanic flows. At intermediate scales, turbulence is encountered in fluid flows of engineering interest such as air flow past wind turbine blades, flow of water past marine risers or propellers and fuel-air mixing in engines. Even at the small scales, turbulence can be extremely important in biological flows such as turbulent blood streams and swimming organisms in water. In some flows, turbulence can be advantageous due to its tendency to enhance mixing capabilities, while in other flows it can be a hindrance as it increases the drag. However, despite several decades of research, turbulence remains a challenging phenomenon to understand or predict.

Turbulence is a complex, chaotic and multi-scale system, which is highly dissipative in nature. In a turbulent flow, energy is generally injected at the largest scales of motion which cascades down to smaller scales as the system becomes increasingly chaotic, and eventually the smallest scales dissipate due to viscosity. The behavior of the large scales depend on the physical geometry or the driving mechanism of the flow and thus varies from one flow to the other. On the other hand, the small scales of motion tend to be isotropic and "universal" in different types of turbulent flows at sufficiently high Reynolds numbers (Kolmogorov, 1941; Monin and Yaglom, 2013), and even at lower Reynolds numbers if resolved accurately (Schumacher et al., 2014). As a consequence, canonical turbulent flows have been widely used to understand the small-scale characteristics of turbulence. In this dissertation, we examine two such flows – homogeneous isotropic turbulent flow and turbulent channel flow, to study small-scale dynamics. It is expected that the inferences and physical understanding of small-scale behavior developed in this work can be extended to more complex and practical turbulent flows.

Velocity gradients embody the small-scale behavior of turbulence. The notion of small-scale universality has evolved significantly over the years. It began with the theory of Kolmogorov (1941) and was later refined to include the strong variability of velocity gradients (Oboukhov, 1962; Kolmogorov, 1962) and to account for turbulence intermittency (Sreenivasan and Antonia, 1997; Schumacher et al., 2014). The phenomenon of small-scale intermittency in turbulence is characterized by very localized extreme values of velocity gradients in the flow (Yeung et al., 2018; Buaria et al., 2019). Velocity gradients demonstrate intermittency in the form of its increasing deviation from Gaussian behavior at higher Reynolds numbers (Yakhot and Donzis, 2017), its self-similar nature and multifractal properties (Meneveau and Sreenivasan, 1991), and the geometry of its intense clusters in the flow (Moisy and Jiménez, 2004). Velocity gradient dynamics is also important in the study of energy cascades in a Lagrangian framework (Yu and Meneveau, 2010a). It regulates phenomena such as vortex-stretching and strain self-amplification, which in turn determine the direction of energy cascade. Naturally, deeper understanding of velocity gradients will help elucidate a number of unanswered questions in the theory of turbulence.

The geometry of the small-scale flow structures in turbulence is also determined by the local velocity gradient tensor. The local streamline geometry of the flow can be classified into four distinct topologies based on the invariants of the tensor (Chong et al., 1990). Numerous studies in the past few decades have demonstrated a universal form of the probability distribution of these local streamline patterns in different types of turbulent flows (Soria et al., 1994; Chong et al., 1998; Chacin and Cantwell, 2000; Dodd and Jofre, 2019). Further, investigating the evolution of these geometries in turbulent flows has led to important insights into the nature of turbulence processes.

The study of velocity gradient dynamics and turbulence small-scale behavior directly enhances our understanding and control over flows of practical significance. Velocity gradient dynamics govern the deformation and orientation dynamics of small-scale entities immersed in a turbulent flow such as bubbles, droplets, red-blood-cells and polymer molecules. For instance, the deformation of a red blood cell in a turbulent blood stream is determined by the local velocity gradient tensor. Thus, improved modeling of velocity gradient dynamics provides better predictability of the dam-

age of red blood cells (hemolysis), a concerning issue in mechanical heart valves and ventricular assist devices (Arora et al., 2004; De Tullio et al., 2012). Similarly, the deformation dynamics of bubbles and droplets in a turbulent flow (Biferale et al., 2014), the motion of swimming microorganisms in water bodies (Luchsinger et al., 1999; Pujara et al., 2018) and the stretching of polymer molecules in turbulent wall-bounded flows (Balkovsky et al., 2000), strongly depend on the evolution of the velocity gradients along the particle trajectories. Velocity gradient dynamics further governs material element deformation in turbulent flows, such as flamelet propagation in premixed combustion (Girimaji and Pope, 1990b; Dresselhaus and Tabor, 1992; Zheng et al., 2017), and plays an important role in turbulence-mixing of passive scalars (Fischer, 1973; O’Neill and Soria, 2005; Danish et al., 2016; Sreenivasan, 2019).

Overall, a study of velocity gradient dynamics leads toward a better understanding of the complex physics underlying small-scale turbulence and an enhanced control over several flow phenomena of importance. This further leads to improved modeling of velocity gradients in turbulence which can reproduce small-scale dynamics in a number of practical flows.

1.2 Background and literature review

1.2.1 Velocity gradient tensor

The velocity gradient (VG) tensor is defined as,

$$A_{ij} \equiv \frac{\partial u_i}{\partial x_j} \quad (1.1)$$

where u_i represent the fluctuating velocity components and x_j represent the spatial directions in the flow field. The trace of this tensor is the local dilatation of the flow, which is zero by definition in the entire incompressible flow field. The VG tensor is a Galilean invariant quantity (Pope, 2000) which holds a plethora of information about the localized small-scale behavior of turbulence. The small-scale statistics are commonly investigated by decomposing the VG tensor into a symmetric

strain-rate tensor (S_{ij}) and an anti-symmetric rotation-rate tensor (W_{ij}) as follows

$$A_{ij} = S_{ij} + W_{ij} \quad \text{where} \quad S_{ij} = \frac{1}{2}(A_{ij} + A_{ji}), \quad W_{ij} = \frac{1}{2}(A_{ij} - A_{ji}) \quad (1.2)$$

Here, the dual vector or axial vector of W_{ij} is the vorticity vector ($\vec{\omega} \equiv \nabla \times \vec{u}$), given by $\omega_i = -\epsilon_{ijk}W_{jk}$, where ϵ_{ijk} is the Levi-Civita symbol. The three real eigenvalues of the symmetric strain-rate tensor represent expansion/compression depending upon the signs of the eigenvalues and the corresponding eigenvectors constitute the three orthogonal axes of the principal frame of S_{ij} . Note that the divergence-free condition ($S_{ii} = 0$) further implies that there is at least one strongly positive (most expansive) eigenvalue and one strongly negative (most compressive) eigenvalue. While the intermediate strain-rate eigenvalue can be either positive or negative, previous numerical as well as experimental studies have shown that it is more likely to be positive in a turbulent flow field (Kerr, 1987; Ashurst et al., 1987; Tsinober et al., 1992). Thus, an average fluid element in a turbulent flow field is likely to be compressed strongly in one direction and expanded in the other two orthogonal directions. An important quantity of interest is the alignment of the vorticity vector with the strain-rate eigenvectors, particularly due to its relevance to the vortex stretching term ($\omega_i S_{ij} \omega_j$) that generates enstrophy (Taylor, 1938). In a turbulent flow field, vorticity shows a strong preferential alignment with the intermediate strain-rate eigenvector, as has been demonstrated by numerous studies for different types of turbulent flows and a wide range of Reynolds numbers (Ashurst et al., 1987; Tsinober et al., 1992; Lüthi et al., 2005). This preference of vorticity to align with the intermediate strain-rate eigenvector and not with the most expansive one is what limits the growth rate of vorticity, as opposed to much higher growth rates of material elements and passive vectors in turbulence (Ohkitani, 2002; Lüthi et al., 2005).

While the Cauchy-Stokes decomposition of the VG tensor into strain-rate and vorticity has helped us develop a better understanding of turbulence, it consists of a certain ambiguity – vorticity is unable to distinguish between pure rotation and shearing of the fluid element (Kolář, 2007; Gao and Liu, 2019; Nagata et al., 2019). The effect of shear is present in both S_{ij} and W_{ij} tensors,

which often obscures our understanding of some of the fundamental phenomena in turbulence. Investigating the small-scale behavior of turbulence using a decomposition of the local velocity gradient tensor into three distinct elementary transformations – normal-strain, pure shear and pure rotation, will lead to further clarity into several aspects of turbulence.

1.2.2 Turbulence small-scale behavior

The small-scale universality of turbulence has received a lot of attention since it was first postulated by Kolmogorov (1941). It was later refined by Kolmogorov (1962) and Oboukhov (1962) to consider the strong variability of velocity gradients. Eventually, it led researchers to delve deeper into intermittency of velocity gradients and its multifractal nature. Certain statistical properties of small scales continued to show universality, for example the scaling of velocity derivatives are nearly universal across turbulent flows with different large-scale forcing mechanisms and flow geometries at sufficiently high Reynolds numbers. Over the years, several studies (Donzis et al., 2008; Ishihara et al., 2009) have illustrated this universality and further enhanced our understanding of small-scale behavior of turbulence. In fact, a recent study (Schumacher et al., 2014) has presented evidence for universality even in lower Reynolds number flows.

Velocity gradient components as well as velocity gradient magnitude exhibit unique probability distributions in turbulence. Here, the velocity gradient magnitude is the Frobenius norm squared ($A_{ij}A_{ij}$) of the tensor, which is often referred to as "pseudodissipation" in turbulence when multiplied with kinematic viscosity. The probability density functions (PDFs) of velocity gradient components as well as its magnitude in a turbulent flow field are heavy-tailed distributions that grow wider with Reynolds number. Several different heavy-tailed functions such as stretched exponential (Kailasnath et al., 1992; Buaria et al., 2019) and log-normal (Yeung and Pope, 1989; Pope and Chen, 1990) have been used to fit these PDFs. This indicates that extreme velocity gradient values that are orders of magnitude greater than the mean have a finite probability of occurrence in a turbulent flow field, which in turn reflects intermittency of small-scales in turbulence. The longitudinal velocity gradient (e.g. A_{11}) has a negatively skewed PDF, while the transverse gradients (e.g. A_{12}) have symmetric distributions (Meneveau, 2011).

The higher order moments of velocity gradients and its magnitude follow universal scaling laws as a function of Reynolds number, $\langle A_{11}^n \rangle \sim Re^{f(n)}$, where $f(n)$ is the scaling exponent and n is the order of the moment. Such relations have been derived theoretically as well as obtained numerically/experimentally in several studies (Yakhot, 2006; Schumacher et al., 2014; Yakhot and Donzis, 2017). The moments emerge from nearly Gaussian values at low Reynolds numbers to strongly non-Gaussian values as the Reynolds number increases. This so called anomalous scaling of velocity gradient moments is one of the key measures of small-scale intermittency in turbulence. In order to study and model this intermittent behavior of velocity gradients, a multifractal formalism based on the concept of multiplicative processes is often employed (Mandelbrot, 1974; Frisch, 1985; Meneveau and Sreenivasan, 1987b, 1991).

While the intermittent nature of velocity gradients has been studied extensively in different kinds of turbulent flows, there is still a number of unanswered questions towards a complete understanding of the fundamental nature of small-scale turbulence. For instance, it is now well known that velocity gradient magnitude squared or pseudodissipation ($\sim A_{ij}A_{ij}$) along with its constituents – dissipation ($\sim S_{ij}S_{ij}$) and enstrophy ($\sim W_{ij}W_{ij}$) are strongly intermittent. In fact, various studies have shown that enstrophy is more intermittent than dissipation (Yeung et al., 2018; Buaria et al., 2019), but the reason for this continues to be unclear. Surprisingly, the Laplacian of pressure which is a function of these intermittent quantities in incompressible turbulence, i.e. $\Delta p = -A_{ij}A_{ji} = W_{ij}W_{ij} - S_{ij}S_{ij}$, is non-intermittent and follows Kolmogorov scaling for its lower order moments (Iyer et al., 2019). A deeper investigation and perhaps a different perspective are required to understand these puzzling aspects of small-scale turbulence.

1.2.3 Geometry of local flow streamlines

The trajectory of a fluid particle in a velocity field \vec{u} is obtained by solving the equation

$$\frac{dx_i}{dt} = u_i \quad (1.3)$$

Using critical point analysis and first order Taylor series expansion of the velocity field (Perry and Fairlie, 1975; Perry and Chong, 1987, 1994), the particle trajectory is governed by

$$\frac{dx_i}{dt} = A_{ij}x_j \quad (1.4)$$

Assuming a steady flow and a spatially uniform velocity gradient field in the immediate vicinity of the critical point, the solution trajectories from the above equation represent the local instantaneous streamlines of the flow. It is evident that the geometry of the local streamlines depends on the velocity gradient tensor (A_{ij}).

The work of Chong et al. (1990) is one of the earliest attempts at a well-defined classification scheme of the local streamline geometry. The local streamlines are classified into four distinct topologies based on the values of second (Q) and third (R) invariants of the velocity gradient tensor,

$$Q = -\frac{1}{2}A_{ij}A_{ji} \quad \text{and} \quad R = -\frac{1}{3}A_{ij}A_{jk}A_{ki} \quad (1.5)$$

The first invariant $P = -A_{ii} = 0$ in an incompressible turbulent flow. It was discovered by Cantwell (1993) that the joint PDF of Q - R (streamline topology) in a turbulent flow field has a unique teardrop shape with a high probability of occurrence along the right discriminant line ($Q^3 + (27/4)R^2 = 0, R > 0$). It is now well established that this characteristic tear-drop shape of the Q - R joint PDF occurs in different types of turbulent flows including but not limited to isotropic turbulence, wall-bounded flows, mixing layers, droplet-laden turbulent flows, and flow over an airfoil (Soria et al., 1994; Blackburn et al., 1996; Chong et al., 1998; Chacin and Cantwell, 2000; Dodd and Jofre, 2019; Wu et al., 2019).

Several key features of the local streamline geometry have been established in the last few decades. The preferential alignment of vorticity vector with the intermediate strain-rate eigenvector, which has a higher tendency to be positive than negative in a turbulent flow field, has been demonstrated by several studies since that of Ashurst et al. (1987). Chevillard et al. (2008) illustrated that the vorticity alignment with the most expansive and compressive strainrate eigenvectors

varied with the topology type, while that with the intermediate eigenvector remained the same independent of topology. Study of the non-local part of the velocity gradient tensor led Hamlington et al. (2008) to conclude that vorticity is more aligned with the most expansive eigendirection of the non-local strain-rate. A recent study by Keylock (2018) highlights the effects of non-normality/non-locality of velocity gradient tensor on strainrate production in different topology types. Danish and Meneveau (2018) studied the dependence of the topology (Q - R) distribution on the length scale and reported discernible changes when transitioning from inertial scale to small scale.

The topological classification has enabled important advances in identifying key universal features of local streamline structure and characterization of important velocity gradient processes (section 1.2.4) conditioned upon topology. However, there are two major drawbacks of this framework. Firstly, topology only provides information about the connectivity of the geometric shape; it does not completely define the shape. In other words, any point in the Q - R plane cannot be uniquely mapped to a particular geometric shape, for example, the origin in the Q - R plane not only represents zero-velocity-gradient uniform flow but also represents shear layer (Elsinga and Marusic, 2010a). This leads to ambiguity in the characterization of local streamline geometry of turbulence within this plane. Secondly, owing to the intermittent nature of velocity gradients, the Q - R phase space grows unboundedly with Reynolds number, thus making it difficult to characterize geometry uniquely and completely in this phase space. A unified framework is required that combines and includes all the above mentioned shape features to provide a complete description of the streamline geometric shape in a well-defined phase space. With the enormous amount of numerical simulation data that has been generated in the last few decades, our understanding of self-similarity and universality of scaling in small-scale statistics of turbulence has made tremendous progress. On the other hand, the universal features of small-scale geometry continue to require a more quantitative and complete characterization.

1.2.4 Velocity gradient dynamics

The evolution equation of the velocity gradient tensor, derived from the Navier-Stokes equation for the velocity fluctuations, depends on four important processes - inertial, pressure, viscous and large-scale forcing. The inertial and isotropic pressure terms, referred to as the nonlinear or restricted Euler (RE) contribution, are closed since they are functions of the VG tensor itself. If the intention is to model the VG dynamics in a turbulent flow without solving the entire turbulent flow field, only the anisotropic pressure, viscous and large-scale forcing terms require closure modeling.

The dynamics of local streamline geometry is commonly studied by examining the conditional mean trajectories in the phase space of VG invariants Q - R . The nonlinear or RE effect on the evolution of VG invariants (Q, R) has a closed form solution (Vieillefosse, 1982, 1984; Cantwell, 1992) and it takes trajectories from the stable topologies on the left of the plane towards the unstable topologies on the right of the plane following the discriminant line. The nonlocal effects of pressure and viscosity on the evolution of Q - R have been thoroughly investigated using numerical simulation data of different turbulent flows (Martín et al., 1998b; Bikkani and Girimaji, 2007; Chevillard et al., 2008; Lawson and Dawson, 2015; Johnson and Meneveau, 2016a; Bechlers and Sandberg, 2017a; Wu et al., 2019). The studies have shown that the anisotropic pressure tends to oppose the nonlinear action, while the viscous contribution simply directs all trajectories toward the origin. Further, the mean trajectories in the Q - R plane due to the aggregate of nonlinear, pressure and viscous processes constitute a tendency of spiraling inward toward the origin of the plane (Ooi et al., 1999; Atkinson et al., 2012). However, this spiraling toward origin does not agree with the statistically steady nature of most of these turbulent flows (Elsinga and Marusic, 2010a; Lozano-Durán et al., 2015). While there is some understanding of the role played by pressure and viscosity in evolution of small-scale topology, the contribution of large-scale forcing on small-scale VG dynamics has often been overlooked and requires further investigation.

1.2.5 Modeling turbulence small-scale behavior

The earliest attempts at modeling small-scale behavior of turbulence constituted development of models for dissipation or pseudodissipation rate in turbulence. Based on the idea of self-similar cascade with an associated multiplicative process, Kolmogorov (1962) and Oboukhov (1962) hypothesized that the dissipation rate exhibits lognormal distribution. This was further examined by Yeung and Pope (1989) and Pope and Chen (1990) using numerical simulation data of turbulence, to reveal that the PDF of pseudodissipation or VG magnitude remarkably resembles a lognormal distribution, more closely than dissipation. However, some inadequacies were pointed out in the lognormal assumption in prediction of rare events and higher order moments (Novikov, 1971; Sreenivasan et al., 1977; Meneveau and Sreenivasan, 1991). This was followed by a series of more advanced multiplicative intermittency models that led to the widely accepted multifractal formalism (Mandelbrot, 1974; Frisch et al., 1978; Frisch, 1985; Meneveau and Sreenivasan, 1987a).

Modeling the Lagrangian evolution of the entire nine-component velocity gradient tensor involves further intricacies. It is not only important to model the intermittent VG magnitude correctly but also accurately capture all the internal shape features of the local streamline structure (section 1.2.3) contained within the VG tensor. The earliest and most elementary velocity gradient models were formulated as low-dimensional autonomous dynamical systems based on the so-called restricted-Euler or RE assumption (Vieillefosse, 1982; Cantwell, 1992). Such models reproduce the dynamics of inertial and isotropic pressure contributions, neglecting the unclosed non-local anisotropic-pressure and viscous contributions. However, the solutions of these models diverge toward infinite R along the right zero-discriminant line in the Q - R plane, thus exhibiting the so-called finite-time singularity. This is primarily due to the absence of the pressure and viscous effects to counter the growing inertial action. Girimaji and Speziale (1995) showed that the Reynolds averaged RE equation violated the balance in mean momentum equation for most homogeneous turbulent flows and proposed a modified restricted-Euler equation for the fluctuating VG tensor, which captured certain features of the VG geometry but failed to avoid finite-time

singularity.

With the intention of avoiding this singularity, Martín et al. (1998a) included a linear damping term to constitute the missing anisotropic pressure and viscous contributions in the evolution equations of VG invariants. While the model solution reaches quasi-stationary states reproducing some key small-scale statistics of turbulence, it is unable to counteract finite-time singularity completely. Girimaji and Pope (1990a) developed the first stochastic model for Lagrangian VG dynamics that produces a statistically stationary solution. They imposed lognormality of VG magnitude using exponentiated Ornstein-Uhlenbeck process (Pope and Chen, 1990) and included additional mean drift terms to counteract the growth of the nonlinear inertial term and tune the convergence to correct moment values. A tetrad model for the coarse-grained velocity gradient tensor was proposed by Chertkov et al. (1999) based on the Lagrangian dynamics of four points (tetrad). The geometry of the tetrad is used to model the local pressure effects, while the nonlocal pressure contribution and small-scale fluctuations are modeled by a Gaussian white-noise term. The model solution results in excessive accumulation of points along the right discriminant line and a distorted Q - R joint PDF. Several studies that followed (Naso and Pumir, 2005; Naso et al., 2006) have presented variations of the model for improved performance and accuracy. A Lagrangian linear diffusion model with a variable timescale for the viscous term was proposed by Jeong and Girimaji (2003), which successfully avoids finite-time singularity, but produces a distorted Q - R joint PDF with an overestimated probability density along discriminant line, similar to the tetrad model. Combining a simplified form of the tetrad model for the pressure Hessian and a variant of the Lagrangian linear diffusion model for the viscous Laplacian, Chevillard and Meneveau (2006) developed the recent fluid deformation (RFD) approximation model. The stochastic model predicts the velocity gradient PDF, relative scaling of moments and vorticity-strainrate alignment with a reasonable accuracy, but the Q - R joint PDF continues to be distorted (Chevillard et al., 2008). A variant of this model with Gaussian isotropic field statistics as the upstream condition for the RFD closure, referred to as the recent deformation of Gaussian fields (RDGF) closure, was developed by Johnson and Meneveau (2016a). This model shows improvements in the PDFs and moments of velocity

gradient tensor as well as its invariants over previous models. A recent stochastic model (Pereira et al., 2018) uses the RFD closure as the mean drift term along with an additional damping term and constrains the dynamics of the VG magnitude along the lines of Girimaji and Pope (1990a) to follow a causal and stationary multiplicative chaos instead of exponentiated Ornstein-Uhlenbeck process. The model is consistent with the turbulence multifractal formalism and thus it reproduces the Reynolds number scaling of the VG moments reasonably accurately but the geometric features of the VG tensor deteriorate.

There is still a significant scope for improvement in our modeling capabilities of velocity gradient dynamics in turbulence. The goal is to develop a robust velocity gradient model that accurately reproduces both the self-similarity of the small-scale geometry as well as the Reynolds number dependence of the magnitude. The field of small-scale turbulence has witnessed tremendous advancements owing to the increased computational capacity of simulating highly resolved turbulence. These advanced knowledge and data should be utilized to develop enhanced closures for the non-local pressure and viscous processes in turbulence, leading toward a highly accurate and robust velocity gradient model.

1.3 Dissertation objectives and research tasks

There is an abundance of data available from highly resolved direct numerical simulations (DNS) of canonical turbulent flows. The goal of this dissertation is to utilize these extensive DNS datasets to improve our understanding of velocity gradient dynamics in incompressible turbulent flows and enhance our predictive modeling capabilities. The research objectives are as follows:

1. Propose a new framework to study velocity gradient dynamics by segregating the bounded normalized velocity gradients that represent the internal structure from the intermittent magnitude that represents the scale.
2. Present a triple decomposition technique to separate the pure-rotation and the normal-strain from the shear deformation and revisit key small-scale properties of turbulence using this decomposition.

3. Examine and identify the role of different turbulence processes – inertia, pressure, viscosity and large-scale forcing – on velocity gradient dynamics using the normalized velocity gradient state-space.
4. Based on the foundation of the new physical understanding developed, construct a data-driven Lagrangian velocity gradient model for incompressible turbulent flows, that accurately models the bounded dynamics of velocity gradient structure as well as the dynamics of the intermittent magnitude.

The research tasks undertaken to fulfill these objectives are outlined below.

Chapter 2: The intermittent nature of the velocity gradient tensor renders characterization of its dynamics and its modeling quite challenging. In this chapter, we propose an alternative framework to study velocity gradient dynamics. We present a normalized velocity gradient tensor that is mathematically bounded and contains all the geometric information of the VG tensor. We analyze DNS datasets of forced isotropic turbulence to compare and contrast the statistics of normalized VG tensor with that of VG tensor. The Reynolds number dependence of velocity gradient statistics and processes in turbulence is examined within this framework to reveal a distinct universality of the normalized velocity gradients.

Chapter 3: This chapter begins with a description of the fundamental difference between topology and geometry of local flow streamlines. While geometric features such as local streamline topology and vorticity-strainrate alignment have been studied individually, the complete geometric shape has not been characterized. In this chapter, we integrate all these shape features to provide a further refined framework that completely characterizes the local streamline geometry. The complete geometric description is presented as a function of four shape-parameters by extending critical point analysis to the normalized VG tensor. The VG magnitude is shown to represent the scale of the local streamline structure. The probability distribution of the geometric shape as well as the scale of local streamlines is examined in homogeneous isotropic turbulent flow and inhomogeneous anisotropic turbulent channel flow.

Chapter 4: Decomposition of VG tensor into the symmetric strain-rate and the anti-symmetric

rotation-rate tensors is unable to segregate the effect of shear present in both these tensors. In this chapter, we present a procedure to decompose the VG tensor of the entire turbulent flow field into three elementary transformations - pure shear, normal-strain and rigid-body-rotation. Next, we derive the important kinematic properties of these constituent tensors and determine the interrelation between this decomposition and the local streamline shape. DNS data sets of forced isotropic turbulence at different Reynolds numbers are analyzed to understand the role of shear, normal-strain and pure rotation in turbulence intermittency. The study further investigates the pressure field and alignment properties using this triple decomposition.

Chapter 5: This chapter identifies the role of fundamental physical processes in the evolution of the geometry of velocity gradient tensor in turbulence. First, the governing differential equations of normalized VG invariants, representing streamline geometry, are derived in terms of the inertial, pressure and viscous processes. Using DNS data of homogeneous isotropic turbulence, we illustrate the conditional mean trajectories in the phase-space of normalized VG invariants and discuss the key features of this dynamical system. We further examine the individual contributions of the inertial, pressure and viscous processes to reveal novel insights into the nature of these processes and their impact on small-scale flow geometry.

Chapter 6: While the influence of inertia, pressure and viscous mechanisms on the evolution of velocity gradients has been investigated considerably in literature, the role of large-scale forcing is not well understood. In this chapter, we illustrate this subtle but crucial role of forcing in the evolution of both geometry as well as magnitude of the velocity gradient tensor. The study begins with the derivation of the required velocity gradient evolution equations including the forcing term. We investigate the interplay among large-scale forcing, inertia, pressure and viscous effects that leads to the universal small-scale geometric statistics in turbulent flows with isotropic as well as anisotropic forcing. We further explicate the role of these processes in the dynamics of VG magnitude or pseudodissipation.

Chapter 7: Modeling the Lagrangian evolution of velocity gradients in a turbulent flow requires the closure of complex non-local flow physics. Previous attempts at modeling have shown promis-

ing results but continue to require improvement and better accuracy. We propose a generalizable model for the normalized velocity gradient tensor using a data-driven closure of the non-local processes in its bounded state-space, universally applicable to turbulent flows at different Reynolds numbers. A separate diffusion model for the intermittent scalar – velocity gradient magnitude, is presented with parameters depending on Reynolds number. The stochastic model equations are numerically propagated with a much smaller ensemble of particles than a typical DNS and leads to a statistically stationary state closely resembling the small-scale behavior of DNS. The resultant statistics are analyzed in detail and compared with that of DNS and previous models to show improved agreement of small-scale behavior.

Chapter 8: The final conclusions of the dissertation and future research directions are presented in this chapter.

2. NORMALIZED VELOCITY GRADIENT TENSOR

2.1 Introduction

Velocity-gradient (VG) dynamics underlies many critical turbulence phenomena such as intermittency, multi-fractality, streamline topology, material-element deformation and scalar mixing (Soria et al., 1994; Blackburn et al., 1996; Martín et al., 1998b; Suman and Girimaji, 2010; Danish et al., 2016). It is of fundamental interest to understand velocity-gradient dynamics and develop Lagrangian closure models that capture key turbulence features (Girimaji and Pope, 1990a; Martín et al., 1998a; Jeong and Girimaji, 2003; Chevillard et al., 2008; Meneveau, 2011; Pereira et al., 2018). The multi-fractal and intermittent nature of velocity gradients renders characterization of its dynamics quite challenging (Yakhot and Sreenivasan, 2005; Donzis et al., 2008; Yeung et al., 2015). It has been demonstrated in recent literature (Yakhot and Donzis, 2017) that intermittency effects manifest even at Taylor Reynolds number $Re_\lambda \sim \mathcal{O}(10)$ and are significant by $Re_\lambda \sim \mathcal{O}(100)$. To complement the findings of the above studies, the goal of this investigation is to establish the Reynolds number dependence of the internal structure of the velocity gradients and constituent dynamical processes. We demonstrate that such an examination leads to improved insight into important aspects of velocity gradient dynamics, including a clear distinction between internal structure and magnitude effects.

We factorize the velocity gradient tensor (A_{ij}) into the magnitude (A - Frobenius norm of \mathbf{A}) and normalized velocity gradient tensor \mathbf{b} (Girimaji and Speziale, 1995; Bikkani and Girimaji, 2007; Bechlars and Sandberg, 2017b):

$$b_{ij} = \frac{A_{ij}}{A} \quad \text{where} \quad A = \sqrt{A^2} = \sqrt{A_{mn}A_{mn}} \quad (2.1)$$

Reprinted with permission from: Das, R. and Girimaji, S. S. (2019). On the Reynolds number dependence of velocity-gradient structure and dynamics. *Journal of Fluid Mechanics*, 861:163–179, Copyright 2018 Cambridge University Press.

The tensor \mathbf{b} is of intrinsic physical interest as it provides insight into many turbulence structural features such as local streamline topology and the orientation between strain-rate eigendirections and vorticity (Ashurst et al., 1987; Wang et al., 2014). The b_{ij} -tensor is mathematically bounded and thus expected to be more amenable to analysis and closure modeling. Furthermore, it is demonstrated that the processes requiring closure in the b_{ij} and A^2 equations are identical. Thus, the evolution of unbounded- A^2 can be cast in terms of bounded- b_{ij} dynamics.

The goal of the present study is to exploit the bounded nature of the b_{ij} tensor to examine the velocity-gradient structure and non-local processes. We seek to:

1. Develop appropriately scaled b_{ij} and A^2 evolution equations and exhibit that the processes requiring closure in the two cases are similar.
2. Examine the Reynolds number dependence of the velocity gradient structure: b_{ij} - moments, probability density functions (PDFs) and invariants (q and r). Although q and r are bounded, the normalization does not guarantee self-similarity at different Reynolds numbers.
3. Establish the Reynolds number dependence of the unclosed non-local pressure and viscous processes in the b_{ij} and A^2 evolution equations conditioned upon q and r .

The work employs forced isotropic turbulence simulation data in the Taylor-scale Reynolds number range $Re_\lambda = 1$ to 588. The remainder of the paper is arranged as follows. Section 2.2 contains the evolution equations of A^2 , b_{ij} and its invariants. A brief description of the data sets used in the study is given in Section 2.3. The Re_λ -dependence of various velocity gradient features are presented in Section 2.4. The paper concludes in Section 2.5 with a brief summary.

2.2 Governing equations

Differentiating the incompressible Navier Stokes equation with respect to spatial coordinates (x_j) yields the evolution equation of the velocity gradient tensor (Cantwell, 1992),

$$\frac{d}{dt}(A_{ij}) + A_{ik}A_{kj} = -\frac{\partial^2 p}{\partial x_i \partial x_j} + \nu \frac{\partial^2 A_{ij}}{\partial x_k \partial x_k}; \quad i, j = 1, 2, 3 \quad (2.2)$$

Using the incompressibility condition $A_{ii} = 0$, the isotropic pressure Hessian term can be written as

$$A_{ik}A_{ki} = -\frac{\partial^2 p}{\partial x_i \partial x_i} \quad (2.3)$$

The non-local anisotropic pressure Hessian and the viscous diffusion term are:

$$H_{ij} = -\frac{\partial^2 p}{\partial x_i \partial x_j} + \frac{\partial^2 p}{\partial x_k \partial x_k} \frac{\delta_{ij}}{3} ; \quad T_{ij} = \nu \frac{\partial^2 A_{ij}}{\partial x_k \partial x_k} \quad (2.4)$$

Thus, the velocity gradient equation may be written as,

$$\frac{dA_{ij}}{dt} + A_{ik}A_{kj} - \frac{1}{3}A_{mk}A_{km}\delta_{ij} = H_{ij} + T_{ij} \quad (2.5)$$

In a Lagrangian reference frame, the A_{ij} -dynamics depends upon the non-local pressure and viscous terms. One of the earliest attempts at developing closure models for velocity gradient dynamics was made by Vieillefosse (1982) by neglecting the non-local terms. There have since been several Lagrangian velocity-gradient models that develop closure for H_{ij} and T_{ij} to replicate turbulence behavior. However, the intermittent nature of the velocity-gradient magnitude renders the modeling rather challenging. Recently, Pereira et al. (2018) have used multifractal considerations, to first model A^2 and then determine the closure for A_{ij} -evolution.

We seek an alternative approach by segregating the evolution of the magnitude (A) from that of normalized velocity gradient tensor b_{ij} as defined in equation (2.1). We propose that modeling b_{ij} first has advantages due to the boundedness of the tensor components. Further, b_{ij} is of intrinsic interest as it characterizes the orientation of velocity gradients and local flow structures.

2.2.1 Mathematical bounds of normalized VG tensor

Longitudinal b_{ij} -components satisfy the incompressibility condition,

$$b_{ii} = b_{11} + b_{22} + b_{33} = 0 \quad (2.6)$$

$$\Rightarrow b_{33} = -(b_{11} + b_{22}) \quad (2.7)$$

By virtue of normalization, the following inequality holds true:

$$b_{11}^2 + b_{22}^2 + b_{33}^2 \leq 1 \quad (2.8)$$

Applying equation (2.7) in the above inequality we obtain the following constraint:

$$b_{11}^2 + b_{22}^2 + b_{11}b_{22} \leq \frac{1}{2} \quad (2.9)$$

The bounds of b_{11} subject to the above constraint can be obtained as

$$\frac{1}{2} \left(-\sqrt{2 - 3b_{22}^2} - b_{22} \right) \leq b_{11} \leq \frac{1}{2} \left(\sqrt{2 - 3b_{22}^2} - b_{22} \right) \quad (2.10)$$

Now let us examine the minimum possible value of the lower bound. Minimizing the lower bound yields a b_{22} value of

$$b_{22} = \frac{1}{\sqrt{6}} \quad (2.11)$$

Similarly, the upper bound attains the maximum value when

$$b_{22} = -\frac{1}{\sqrt{6}} \quad (2.12)$$

Therefore, b_{11} or any other longitudinal velocity gradient is bounded as:

$$-\sqrt{\frac{2}{3}} \leq b_{ij} \leq \sqrt{\frac{2}{3}} \quad \forall i = j \quad (2.13)$$

Transverse components can be the sole non-zero element in the velocity gradient tensor. These components are only constrained by normalization and are therefore only limited by unity,

$$-1 \leq b_{ij} \leq 1 \quad \forall i \neq j \quad (2.14)$$

2.2.2 Evolution equations of VG magnitude and normalized VG tensor

Multiplying the velocity-gradient equation (2.5) through by A_{ij}/A^3 yields

$$\frac{A_{ij}}{A^3} \frac{d}{dt}(A_{ij}) = -\frac{A_{ij}A_{ik}A_{kj}}{A^3} + \frac{1}{3A^3}A_{km}A_{mk}\delta_{ij}A_{ij} + \frac{A_{ij}H_{ij}}{A^3} + \frac{A_{ij}T_{ij}}{A^3} \quad (2.15)$$

Using the incompressibility condition, we obtain the following equation:

$$\frac{1}{A^3} \frac{dA^2}{dt} = \frac{1}{A^3} \frac{d}{dt}(A_{ij}A_{ij}) = -2b_{ij}b_{ik}b_{kj} + 2b_{ij}h_{ij} + 2b_{ij}\tau_{ij} \quad (2.16)$$

where the non-local physics is incumbent in the normalized anisotropic pressure Hessian and viscous diffusion terms:

$$h_{ij} = \frac{H_{ij}}{A^2} \quad \text{and} \quad \tau_{ij} = \frac{T_{ij}}{A^2} \quad (2.17)$$

It is convenient to describe magnitude evolution in terms of $\theta \equiv \ln A \equiv \frac{1}{2} \ln A^2$:

$$\frac{d\theta}{dt'} = \frac{1}{2} \left(N_\theta + P_\theta + V_\theta \right), \quad (2.18)$$

where the normalized time increment and nonlinear (inertial), pressure and viscous contributions are:

$$dt' \equiv A dt, \quad N_\theta = -2b_{ij}b_{ik}b_{kj}, \quad P_\theta = 2b_{ij}h_{ij}, \quad V_\theta = 2b_{ij}\tau_{ij} \quad (2.19)$$

Next we turn our attention to the evolution of the normalized tensor b_{ij} :

$$\frac{db_{ij}}{dt} = \frac{d}{dt} \left(\frac{A_{ij}}{A} \right) = \frac{1}{A} \frac{dA_{ij}}{dt} - \frac{A_{ij}}{2} \left(\frac{1}{A^3} \frac{dA^2}{dt} \right) \quad (2.20)$$

Using equations (2.5), (2.16) and (2.20), the governing equation for b_{ij} is obtained in normalized time t' :

$$\frac{db_{ij}}{dt'} = -b_{ik}b_{kj} + h_{ij} + \tau_{ij} + \frac{1}{3}b_{mk}b_{km}\delta_{ij} + b_{ij}(b_{mk}b_{kn} - h_{mn} - \tau_{mn})b_{mn} \quad (2.21)$$

The processes that require closure in the b_{ij} -equation – the non-local pressure term h_{ij} and viscous term τ_{ij} – are same as those in the A^2 -equation. Although the boundedness of h_{ij} and τ_{ij} are not guaranteed, the requirement that b_{ij} be bounded renders the modeling of pressure and viscous terms more tractable. Once the b_{ij} -evolution closure model equation is developed, the magnitude equation requires no further closure modeling.

2.2.3 Evolution equations of normalized VG invariants

Let p, q and r represent the invariants of \mathbf{b} :

$$p = -b_{ii} = 0, \quad q = -\frac{1}{2}b_{im}b_{mi}, \quad r = -\frac{1}{3}b_{im}b_{mk}b_{ki} \quad (2.22)$$

These invariants are of interest as the local streamline structure can be classified into four distinct topologies based on q and r (Chong et al., 1990). Now, we seek equations for q and r . Using (2.21), the following equation for inner product of \mathbf{b} is obtained

$$\begin{aligned} \frac{d}{dt'}(b_{in}b_{nj}) = & -2b_{ik}b_{kn}b_{nj} + \frac{2}{3}b_{mk}b_{km}b_{ij} + 2b_{in}b_{nj}b_{mq}b_{mk}b_{kq} + h_{in}b_{nj} + b_{in}h_{nj} \\ & -2h_{mq}b_{mq}b_{in}b_{nj} + \tau_{in}b_{nj} + b_{in}\tau_{nj} - 2\tau_{mq}b_{mq}b_{in}b_{nj} \end{aligned} \quad (2.23)$$

Taking the trace of equation (2.23), the evolution equation of q is determined as

$$\frac{dq}{dt'} = -3r + 2qb_{ij}b_{ik}b_{kj} - h_{in}(b_{ni} + 2qb_{in}) - \tau_{in}(b_{ni} + 2qb_{in}) = N_q + P_q + V_q \quad (2.24)$$

where N_q, P_q and V_q represent nonlinear inertial, pressure and viscous contributions toward the evolution of q :

$$N_q = -3r + 2qb_{ij}b_{ik}b_{kj}, \quad P_q = -h_{in}(b_{ni} + 2qb_{in}), \quad V_q = -\tau_{in}(b_{ni} + 2qb_{in})$$

To obtain the equation of r , we first derive the equation for triple inner product of \mathbf{b} using

equations (2.21) and (2.23),

$$\begin{aligned}
\frac{d}{dt'}(b_{il}b_{ln}b_{nj}) &= -3b_{il}b_{lk}b_{kn}b_{nj} + b_{il}b_{lj}b_{mk}b_{km} + 3b_{il}b_{ln}b_{nj}b_{mq}b_{mk}b_{kq} + (b_{il}h_{ln}b_{nj} \\
&+ b_{il}b_{ln}h_{nj} + h_{il}b_{ln}b_{nj} - 3h_{mq}b_{mq}b_{il}b_{ln}b_{nj}) + (b_{il}\tau_{ln}b_{nj} + b_{il}b_{ln}\tau_{nj} \\
&+ \tau_{il}b_{ln}b_{nj} - 3\tau_{mq}b_{mq}b_{il}b_{ln}b_{nj})
\end{aligned} \tag{2.25}$$

Applying the Cayley-Hamilton Theorem,

$$b_{il}b_{lk}b_{kj} + pb_{ik}b_{kj} + qb_{ij} + r\delta_{ij} = 0 \tag{2.26}$$

in the trace of equation (2.25), the evolution equation of r is obtained as follows,

$$\frac{dr}{dt'} = \frac{2}{3}q^2 + 3rb_{ij}b_{ik}b_{kj} - h_{mn}(b_{im}b_{ni} + 3rb_{mn}) - \tau_{mn}(b_{im}b_{ni} + 3rb_{mn}) = N_r + P_r + V_r \tag{2.27}$$

where the local nonlinear (inertial and isotropic pressure), anisotropic pressure and viscous contributions in the evolution of r are

$$N_r = \frac{2}{3}q^2 + 3rb_{ij}b_{ik}b_{kj}, \quad P_r = -h_{mn}(b_{im}b_{ni} + 3rb_{mn}), \quad V_r = -\tau_{mn}(b_{im}b_{ni} + 3rb_{mn})$$

The goal of the remainder of this paper is to use DNS data sets to establish the Reynolds number dependence of the statistics of b_{ij} , q and r . Then we will also characterize the effect of changing Reynolds number on unclosed pressure (h_{ij}) and viscous (τ_{ij}) processes by examining the evolution of q , r and θ . The investigation of the unclosed invariants will yield further insight into velocity-gradient dynamics and provide guidance for developing closure models.

2.3 Numerical simulation data

DNS datasets of homogeneous isotropic turbulent flow with stochastic forcing are used in this study. The details of these simulations are presented in appendix A. Twelve forced isotropic in-

compressible turbulence datasets with Taylor Reynolds numbers,

$$Re_\lambda \equiv \frac{u'\lambda}{\nu} = 1, 6, 9, 14, 18, 25, 35, 86, 225, 385, 414 \text{ and } 588$$

are used in this work. All the datasets have been used previously to study intermittency, anomalous exponents, Reynolds number scaling and non-linear depletion (Donzis et al., 2008; Donzis and Sreenivasan, 2010; Donzis et al., 2012; Gibbon et al., 2014). Here, u' is the root-mean-square (RMS) velocity and ν is the kinematic viscosity. λ (Taylor microscale) and ϵ (dissipation rate) are given by

$$\lambda = \left(\frac{15\nu(u')^2}{\epsilon} \right)^{1/2}, \quad \text{where } \epsilon = 2\nu \langle S_{ij}S_{ij} \rangle \quad (2.28)$$

and $S_{ij} = (A_{ij} + A_{ji})/2$ is the strain-rate tensor. All the derivatives used in this study are calculated using spectral method.

2.4 Results and discussion

We start by exhibiting the known features of velocity gradients as a function of Reynolds number - anomalous scaling of the normalized higher-order moments and increasingly stretched exponential tails of the probability density functions (PDFs). We then contrast the known A_{ij} behavior against the b_{ij} moments and PDF. Then the Re_λ -dependence of various velocity-gradient dynamics processes conditioned on q and r is established.

2.4.1 Unnormalized velocity gradient statistics

Even-order moments (M_{2n}^A for $n = 2, 3, 4, 5, 6$) of the longitudinal velocity gradient ($A_{11} = \frac{\partial u}{\partial x}$) given by,

$$M_{2n}^A = \frac{\overline{A_{11}^{2n}}}{\overline{A_{11}}^{2n}} \quad (2.29)$$

are plotted as a function of Re_λ in figure 2.1. Here, $\overline{(\quad)}$ implies volume averaging. It is observed that for $Re_\lambda \leq 9$, the moments are nearly Gaussian. For $Re_\lambda > 9$, the values of all the moments steadily increase with Re_λ in agreement with the anomalous scaling observed by Yakhot and Donzis (2017). Note that the Re_λ -range considered in this study is much wider than that

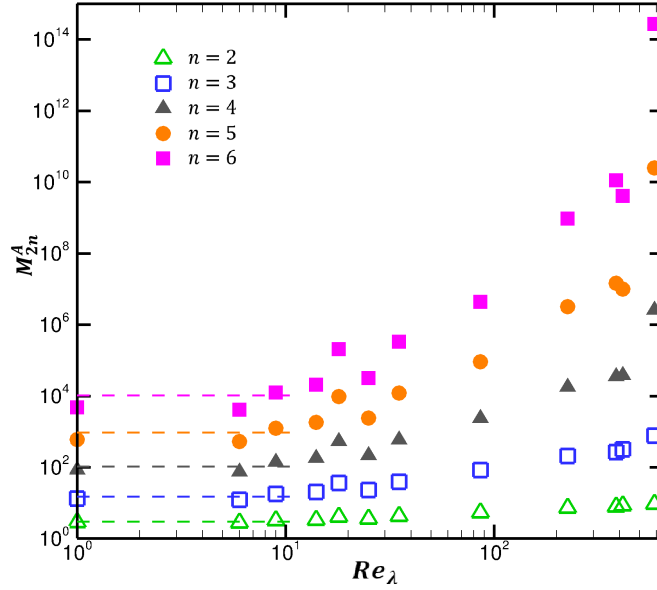


Figure 2.1: Even order moments (M_{2n} for $n = 2, 3, 4, 5, 6$) of A_{11} as a function of Re_λ . Dashed lines represent Gaussian moments, i.e. $M_{2n}^G = (2n-1)!!$, for reference. Reprinted with permission from Das and Girimaji (2019).

of Yakhot and Donzis (2017). Anomalous scaling of the moments is a clear indication of the intermittent behavior of A_{ij} . This observation is further reinforced in the PDF plots of velocity gradients.

The PDFs of A_{11} and A_{12} are shown in figure 2.2. As expected, at sufficiently high Re_λ , the longitudinal and transverse PDFs exhibit stretched exponential tails that grow with increasing Re_λ (Kailasnath et al., 1992; Chevillard and Meneveau, 2006; Schumacher et al., 2014).

Another feature of turbulent flows relevant to this study is dissipative anomaly (Donzis et al., 2005). In the asymptotic limit of high Re_λ , the normalized energy dissipation rate ($\epsilon L/u'^3$) asymptotes to a constant value of approximately 0.4 – 0.45. Here, L is the integral length scale and u' is the RMS velocity. In other words, the normalized mean energy dissipation rate is independent of viscosity provided the value of Re_λ is sufficiently high. The onset of this dissipative anomaly in forced isotropic turbulence is observed at $Re_\lambda \sim 200$ (Sreenivasan, 1998; Kaneda et al., 2003; Donzis et al., 2005). We will invoke this result later in the study.

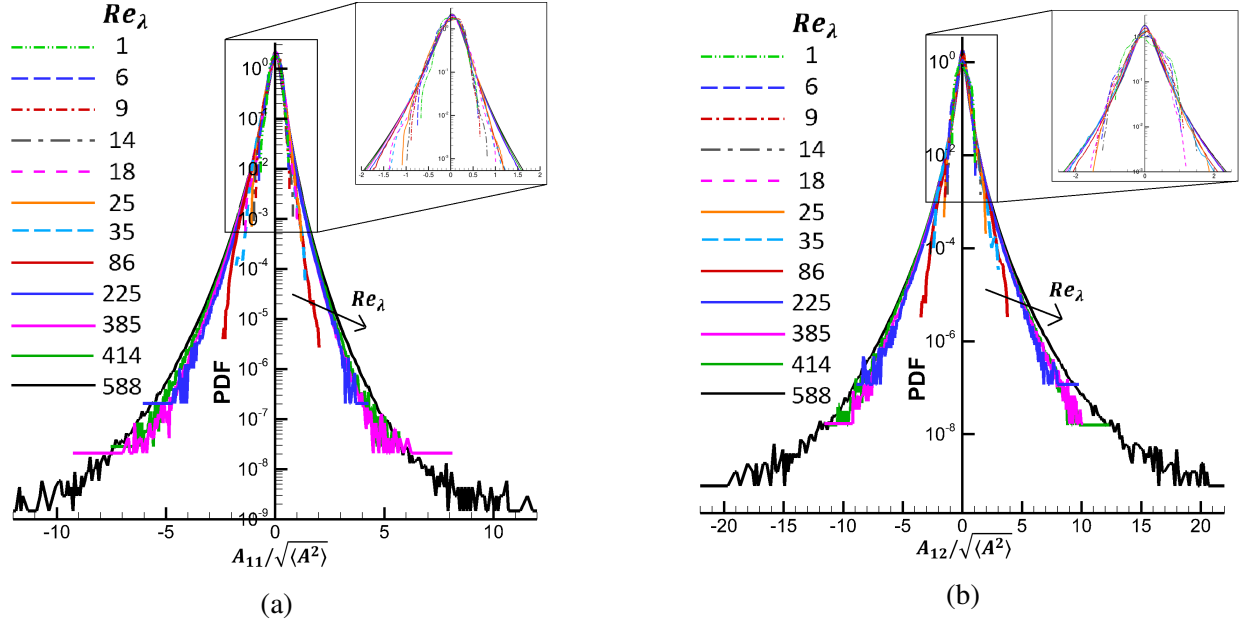


Figure 2.2: PDF of velocity gradient component (a) $A_{11}/\sqrt{\langle A^2 \rangle}$ (b) $A_{12}/\sqrt{\langle A^2 \rangle}$ for different Re_λ . Reprinted with permission from Das and Girimaji (2019).

2.4.2 Normalized velocity gradient statistics

In this subsection, we investigate the statistical characteristics of the tensor \mathbf{b} . The even-order moments of b_{11} are given by

$$M_{2n}^b = \frac{\overline{b_{11}^{2n}}}{b_{11}^{2n}} \quad (2.30)$$

Even-order moments (M_{2n}^b for $n = 2, 3, 4, 5, 6$) of b_{11} at different Re_λ are plotted in figure 2.3. b_{11} -moments are sub-Gaussian and nearly invariant across the entire Re_λ -range. This behavior is to be expected as b_{ij} is bounded by unity. This also clearly demonstrates the contrast between the Reynolds number scaling of b_{ij} and A_{ij} .

We will next examine the PDFs of b_{ij} at different Re_λ . In figure 2.4 (a) and (c) we present b_{11} - and b_{12} - PDFs respectively over the lower range of Reynolds numbers ($Re_\lambda \leq 35$). In this range, the PDF undergoes slight changes in shape with changing Re_λ . Figure 2.4 (b) and (d) show that for $Re_\lambda \geq 35$, both b_{11} - and b_{12} - PDFs converge to a characteristic shape, which remains unchanged at higher Re_λ . This statistical self-similarity is anticipated from the collapse of higher-order

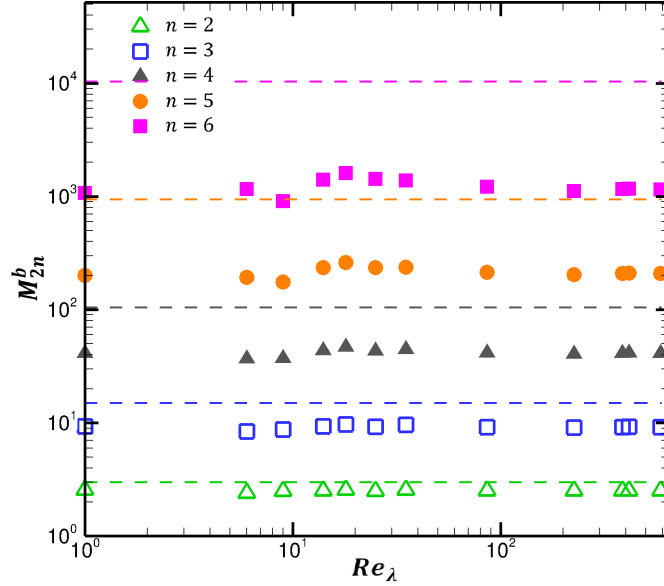
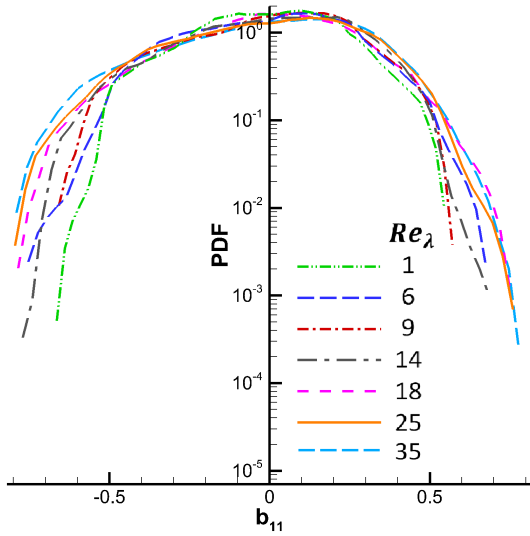


Figure 2.3: Even order moments (M_{2n} for $n = 2, 3, 4, 5, 6$) of b_{11} as a function of Re_λ . Dashed lines represent Gaussian moments, i.e. $M_{2n}^G = (2n - 1)!!$ for reference. Reprinted with permission from Das and Girimaji (2019).

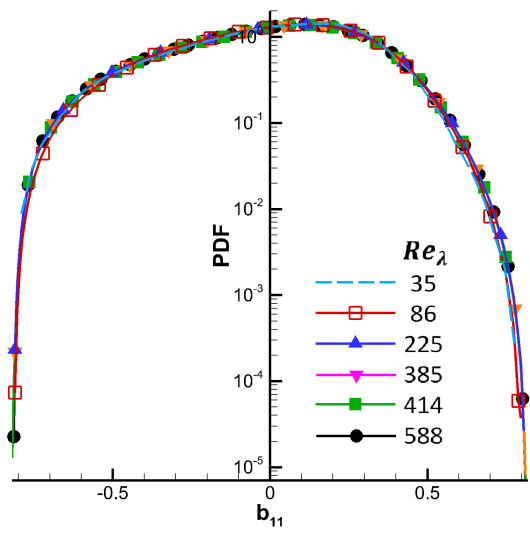
moments of b_{11} to constant values. Note that the minimum and maximum longitudinal (b_{11}) and transverse (b_{12}) velocity gradient values are in accordance with the bounds obtained analytically in equations (2.13) and (2.14).

2.4.3 Invariants of normalized VG tensor

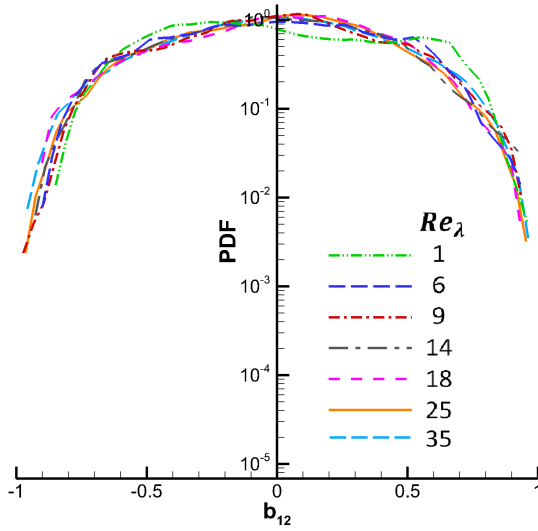
Delving further, we examine the marginal PDFs of q and r in figures 2.5 and 2.6. Figure 2.5(a) shows that in the range where $Re_\lambda \leq 25$, the q -PDF appears to have a characteristic shape but shows discernible statistical variation about this shape. For $25 \leq Re_\lambda \leq 225$ (figure 2.5 b), the distribution shifts towards more negative values of q with increasing Re_λ . In this range the probability of strain dominated topology ($q < 0$) increases, while that of rotation dominated topology ($q > 0$) decreases. This is due to the fact that viscosity affects the strain-dominated topologies more than rotation-dominated topologies and lower viscous influence at higher Reynolds numbers causes a higher percentage of strain-dominated topologies to be generated. Finally, q -PDF attains a self-similar shape for flows above $Re_\lambda \sim 200$. In the middle range of $Re_\lambda \in (25, 200)$ the PDF



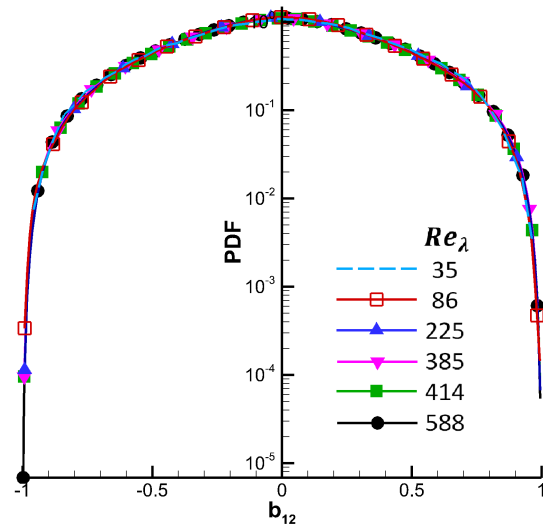
(a)



(b)



(c)



(d)

Figure 2.4: PDF of (a-b) normalized longitudinal velocity gradient b_{11} (c-d) normalized transverse velocity gradient b_{12} for $Re_{\lambda} = 1-35$ and $35-588$. Reprinted with permission from Das and Girimaji (2019).

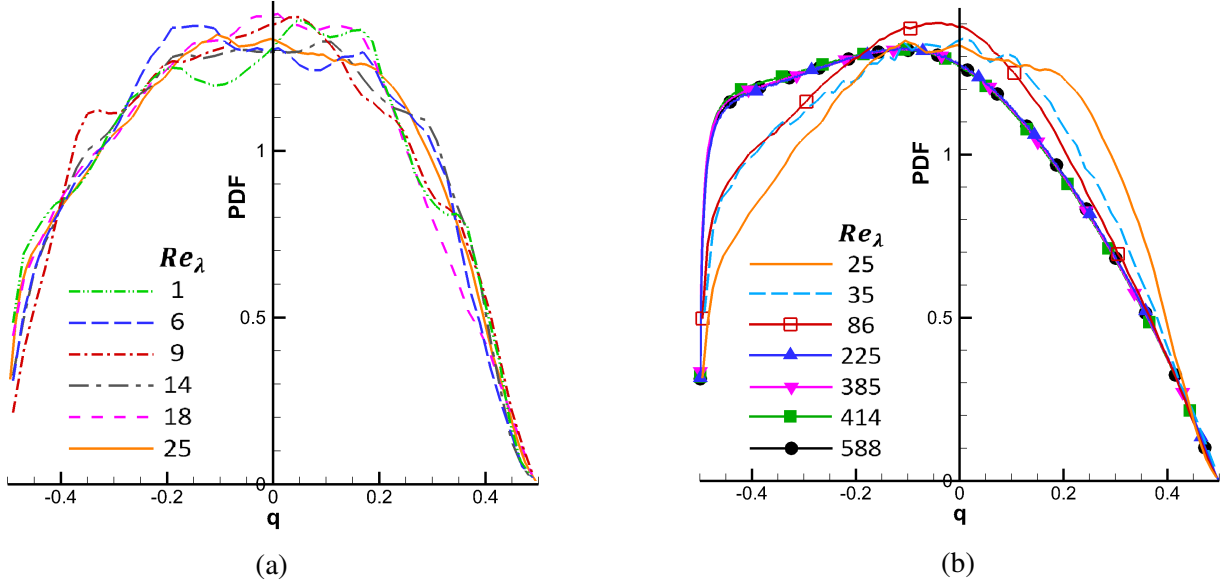


Figure 2.5: q -PDF for (a) $Re_\lambda = 1, 6, 9, 14, 18$ and 25 (b) $Re_\lambda = 25, 35, 86, 225, 385, 414$ and 588 . Reprinted with permission from Das and Girimaji (2019).

transitions from one characteristic shape to another.

Unlike q -PDF, the r -PDF shows only a subtle Re_λ -dependence. It may be noted from figure 2.6 that irrespective of the Re_λ value, r -PDF peaks at $r = 0$. The shape of r -PDF remains fairly unchanged while its peak increases with Re_λ in the range $Re_\lambda \in (1, 200)$. It appears to be invariant above $Re_\lambda \sim 200$. Note that the variation in r -PDF with Re_λ is minimal compared to q -PDF.

The q - r joint PDFs are plotted in figure 2.7 for different Re_λ . Figure 2.7(a-f) shows the variation in shape of the q - r joint PDF in the low Re_λ range. At $Re_\lambda = 1$, the joint PDF is fairly symmetric about the q -axis and does not have a preferential distribution along the zero-discriminant (restricted Euler) line in the fourth quadrant. In fact, at this Re_λ the distribution resembles that of invariants of a Gaussian field (Pereira et al. (2016)). As Re_λ increases in the range $(1, 9)$, the q - r joint PDF changes shape significantly and begins to develop a high-density region along the zero-discriminant line. It acquires a teardrop-like shape around $Re_\lambda = 9$. This value is in the same range as the transition Re_λ for onset of anomalous scaling of A_{ij} moments (Yakhot and Donzis (2017)). For $9 < Re_\lambda \leq 225$, the contours undergo refinements in the teardrop shape. Figure 2.7(g) clearly

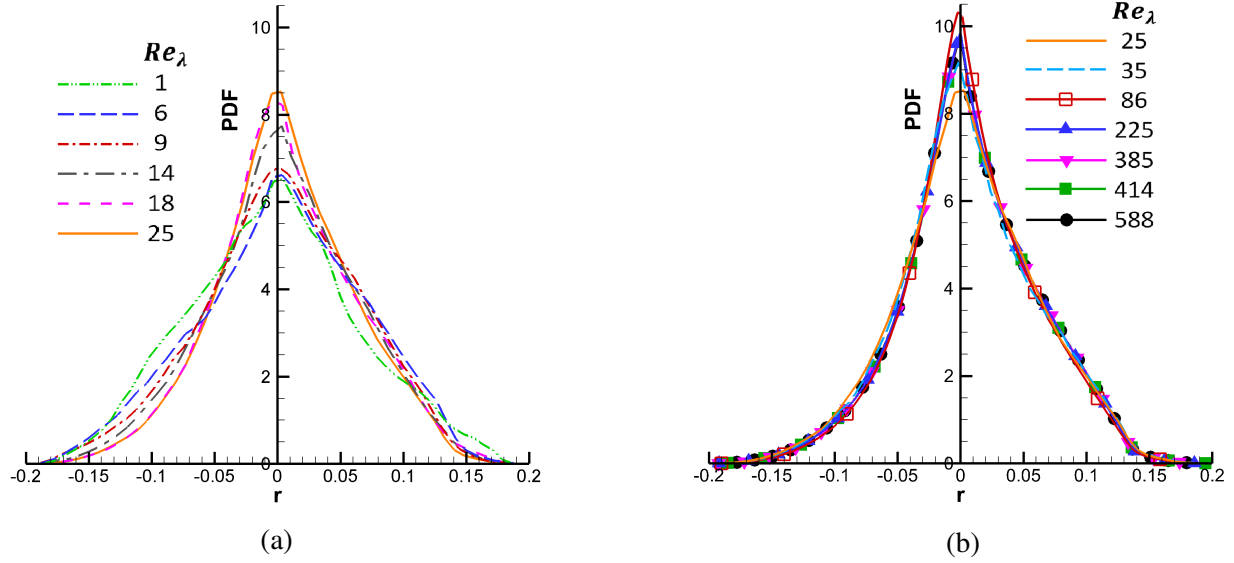


Figure 2.6: r -PDF for (a) $Re_\lambda = 1, 6, 9, 14, 18$ and 25 (b) $Re_\lambda = 25, 35, 86, 225, 385, 414$ and 588 . Reprinted with permission from Das and Girimaji (2019).

depicts these changes amounting to an increase in probability of strain dominated topologies with respect to rotation dominated topologies with increasing Re_λ . This reiterates the observation from marginal PDF of q (figure 2.5). Finally, the joint PDF contours become invariant for $Re_\lambda > 200$ as shown in figure 2.7(h).

The joint q - r PDF exhibits three distinct ranges of variation with Re_λ . In the range $Re_\lambda \in (1, 10)$, it shows significant qualitative variation from near-Gaussian behavior to a teardrop-like shape. Small quantitative changes are evident in the contours for $10 \leq Re_\lambda \leq 200$. Finally, an invariant joint distribution in the characteristic teardrop shape is attained for $Re_\lambda \geq 200$.

2.4.4 Evolution of normalized VG invariants and VG magnitude

In this subsection we study the dynamics of q - and r -evolution which lays the foundation for modeling both b_{ij} and A^2 . We also characterize the Reynolds number dependence of θ -dynamics conditioned on q and r . We consider the Reynolds number range: $Re_\lambda \in 86, 588$, in this subsection to understand the role of different turbulent processes in q, r -phase space.

The averages of nonlinear inertial, pressure and viscous terms of $\frac{dq}{dt'}$ (equation 2.24) conditioned

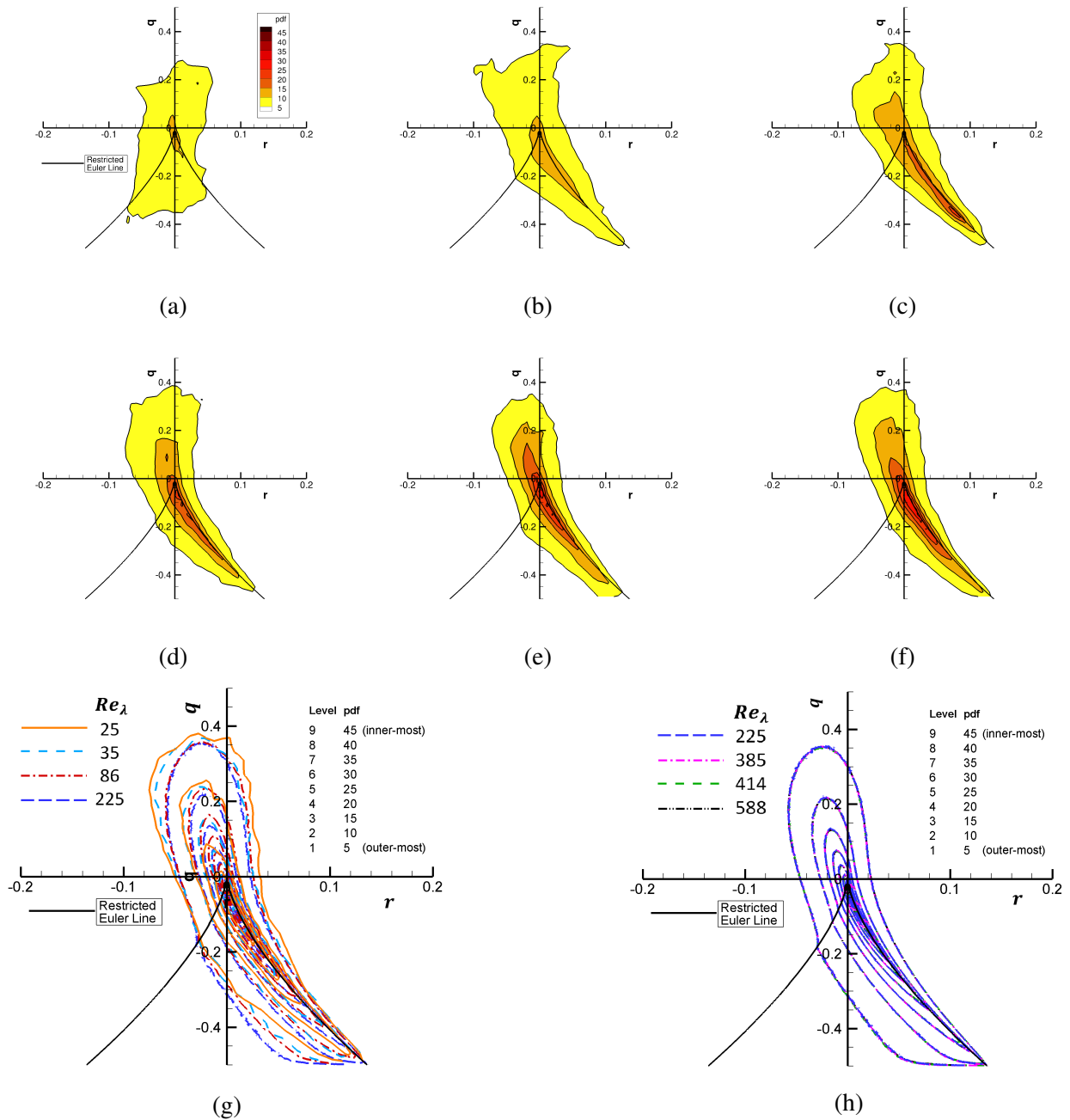


Figure 2.7: q - r joint PDF filled contour plots for $Re_\lambda = (a) 1 (b) 6 (c) 9 (d) 14 (e) 18 (f) 25$. q - r joint PDF line contour plots for $Re_\lambda = (g) 25$ to 225 $(h) 225$ to 588. The contour levels are identical for all plots: color scheme for (a-f) is as shown in (a). Reprinted with permission from Das and Girimaji (2019).

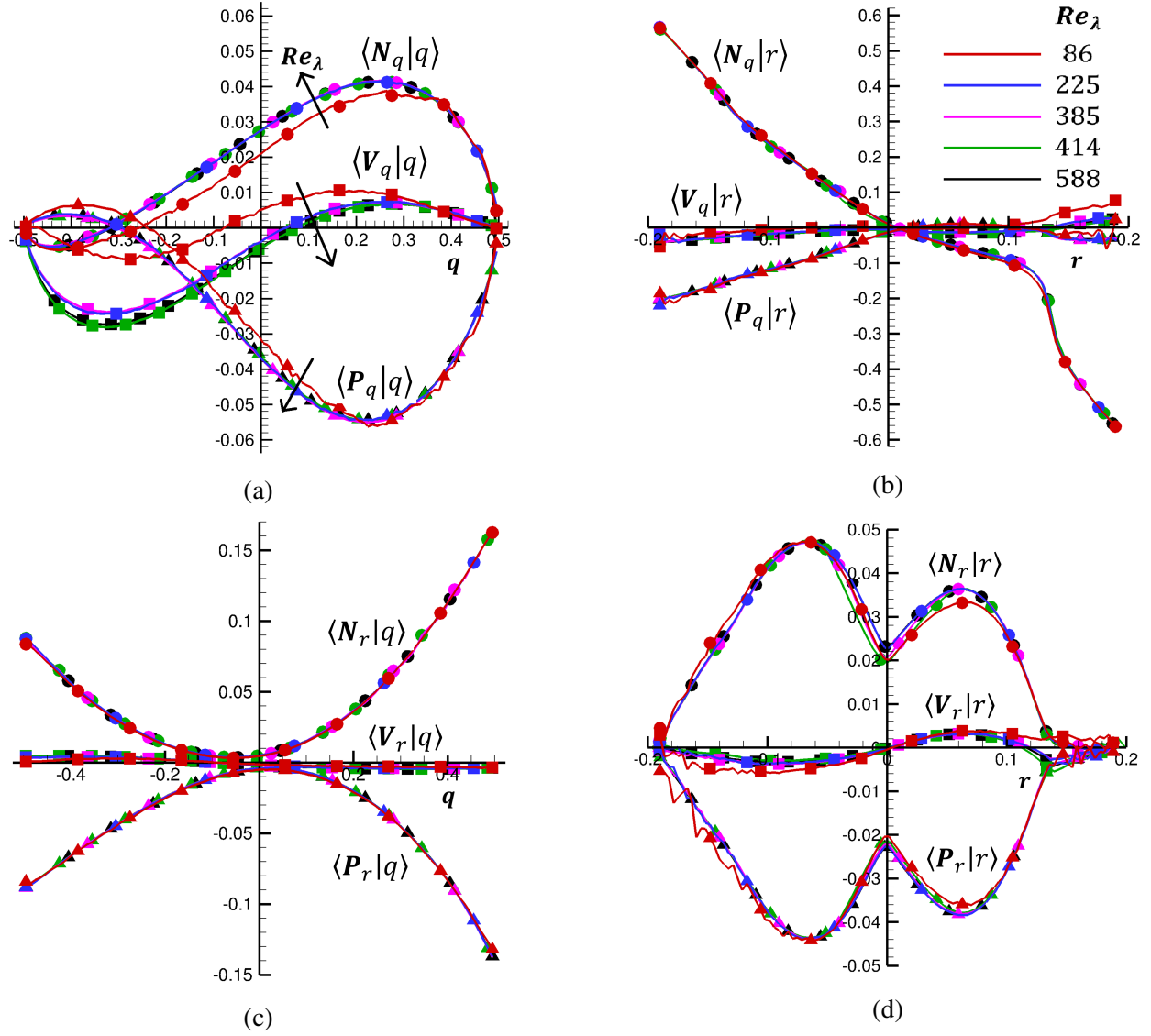


Figure 2.8: Conditional averages of nonlinear (circles), anisotropic pressure (triangles) and viscous (squares) contributions in (a) $\langle \frac{dq}{dt} | q \rangle$ (b) $\langle \frac{dq}{dt} | r \rangle$ (c) $\langle \frac{dr}{dt} | q \rangle$ (d) $\langle \frac{dr}{dt} | r \rangle$ for different Re_λ (Refer to equations (2.24) and (2.27); Color scheme: as given in (b)). Reprinted with permission from Das and Girimaji (2019).

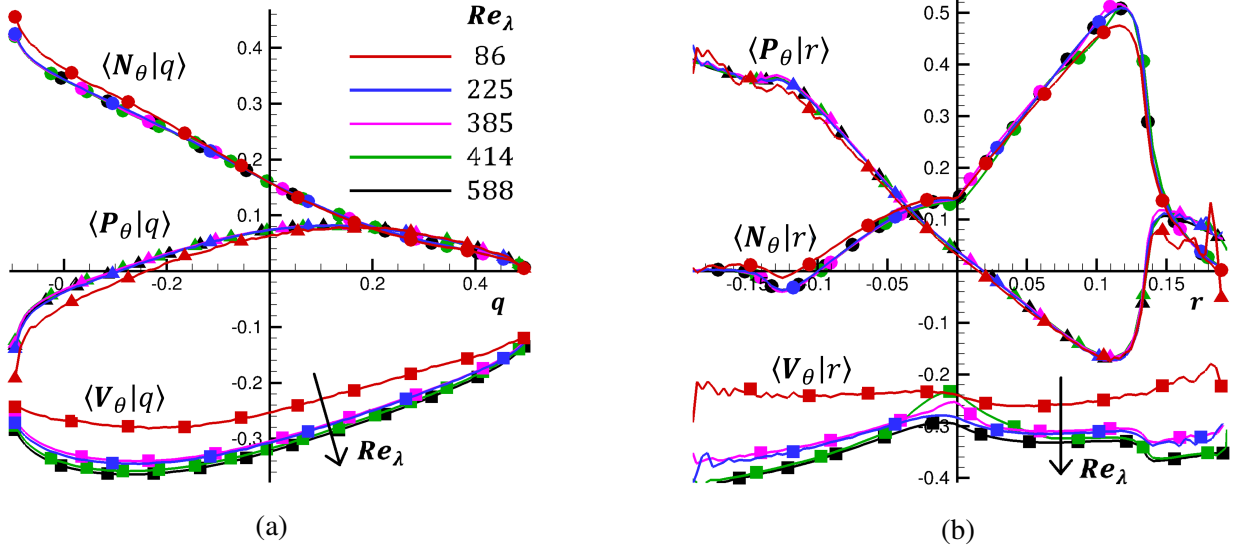


Figure 2.9: Conditional averages of inertial (circles), pressure (triangles) and viscous (squares) contributions in θ -evolution equation conditioned on (a) q (b) r for different Re_λ (Refer to equation 2.18; Color scheme: as given in (a)). Reprinted with permission from Das and Girimaji (2019).

on q and r have been plotted in figure 2.8 (a) and (b). The inertial and pressure terms conditioned on q show Re_λ dependence at low Re_λ 's and attain nearly invariant forms for $Re_\lambda \geq 225$. The viscous term conditioned on q shows a significant Reynolds number dependence at low Re_λ values, but is nearly invariant in the higher range. All q -evolution terms conditioned on r appear to be completely insensitive to Re_λ .

The conditional averages of local nonlinear (inertial and isotropic pressure), anisotropic pressure and viscous contributions in $\frac{dr}{dt}$ (as shown in equation 2.27) are reasonably insensitive to Re_λ , as shown in figure 2.8 (c) and (d). The average viscous contribution (V_r) conditioned on both q and r is negligible in comparison to the other terms. This suggests that r -evolution is relatively impervious to viscosity and dominated by inertial and pressure terms. The fact that the probability distribution of r is nearly insensitive to Re_λ (figure 2.6 b) is consistent with this inference.

The different processes in the θ -evolution (as given in equation 2.18) conditioned on q and r are plotted in figure 2.9 (a) and (b). The average nonlinear inertial term (N_θ) is positive for almost all q and r values – implying that inertia is a source of A^2 . The sign of the anisotropic

pressure contribution (P_θ) depends on the q and r values. Expectedly, the viscous term (V_θ) is negative across all values of q and r indicating that it is always a sink of A^2 . Viscous effects are stronger in strain-dominated topologies ($q < 0$) and weaker in rotation-dominated topologies ($q > 0$). However, it is nearly independent of r . Overall, the conditionally-averaged inertial and pressure processes in the θ -equation appear to approach asymptotic behavior at high Re_λ (~ 200). The viscous term on the other hand appears to have a discernible Reynolds number dependence throughout the Re_λ range.

Finally, we plot the conditional variance of the unclosed pressure and viscous terms in the q -, r - and θ -evolution equations in figure 2.10. The variance of the pressure term in q -evolution conditioned on both q and r have invariant forms irrespective of Re_λ (figure 2.10 a,c). However, the conditional variance of the viscous contribution to dq/dt' (figure 2.10 b,d) does not converge even in the high- Re_λ limit. In fact, it shows a progressive increase in the variance-magnitude with increasing Re_λ . Similarly, the conditional variance of the anisotropic pressure contribution in the r -evolution is invariant with changing Re_λ (figure 2.10 e,g). On the other hand, the variance of the viscous term increases with increasing Re_λ (figure 2.10 f,h). We also observe that the variance of P_θ conditioned on both q and r exhibits reasonable collapse, while that of V_θ exhibits a distinct Reynolds number dependence with the magnitude increasing with Re_λ (figure 2.10 i-l).

Therefore, we find that conditional statistics (mean and variance) of the pressure contribution to q -, r - and θ -evolution become nearly invariant for $Re_\lambda > 200$. The mean viscous contribution to q - and r -evolution also exhibits self-similarity beyond $Re_\lambda > 200$. On the other hand, the conditional mean of the viscous term in θ -evolution shows a quantitative increase in magnitude with Re_λ . The conditional variance of pressure processes in q -, r - and θ -evolution are independent of Re_λ while that of the viscous contribution shows steady growth in magnitude with increasing Re_λ . This implies that all of the Re_λ -dependence in the velocity gradient dynamics is due to viscous effects, which is to be expected.

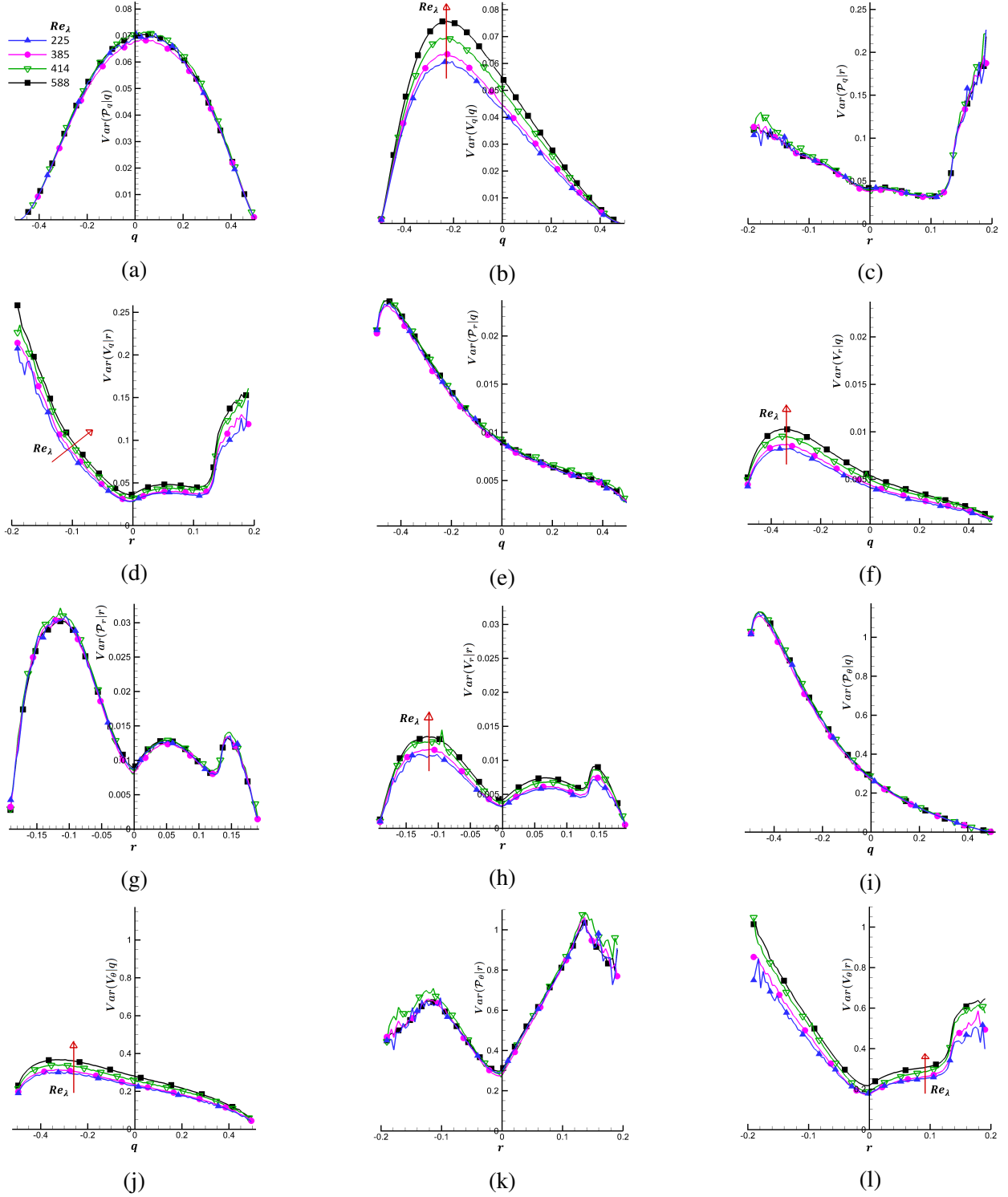


Figure 2.10: Conditional variance of anisotropic pressure and viscous terms in q -, r - and θ -equations conditioned on q and r : (a) $Var(P_q|q)$ vs q (b) $Var(V_q|q)$ vs q (c) $Var(P_q|r)$ vs r (d) $Var(V_q|r)$ vs r (e) $Var(P_r|q)$ vs q (f) $Var(V_r|q)$ vs q (g) $Var(P_r|r)$ vs r (h) $Var(V_r|r)$ vs r (i) $Var(P_\theta|q)$ vs q (j) $Var(V_\theta|q)$ vs q (k) $Var(P_\theta|r)$ vs r (l) $Var(V_\theta|r)$ vs r for different Re_λ (Color scheme: as given in (a)). Reprinted with permission from Das and Girimaji (2019).

2.4.5 Lagrangian velocity gradient modeling

One of the long-term goals of this work is to develop a Lagrangian stochastic model for velocity gradients along the lines of Girimaji and Pope (1990a). The main distinction is that we plan to develop a model for b_{ij} -evolution rather than A_{ij} -evolution as was the case in Girimaji and Pope (1990a).

It is anticipated that h_{ij} and τ_{ij} will be more tractable than their A_{ij} -counterparts. The proposal is to decompose each term into a conditional mean and a stochastic (white noise) term:

$$h_{ij}(\mathbf{b}) = \langle h_{ij}|q, r, \mathbf{b} \rangle + h'_{ij}(q, r, \mathbf{b}) \quad (2.31)$$

$$\tau_{ij}(\mathbf{b}) = \langle \tau_{ij}|q, r, \mathbf{b} \rangle + \tau'_{ij}(q, r, \mathbf{b}) \quad (2.32)$$

The conditional statistics (means and variances) established in this paper (figures 2.8, 2.9 and 2.10) will provide guidance for this model development. Once h_{ij} and τ_{ij} models are established, Lagrangian evolution equations for A^2 and A_{ij} can be developed without need for any further closures (equations 2.5 and 2.16).

2.5 Summary and conclusions

The main objective of the work is to clearly characterize the Reynolds number dependence of the different aspects of velocity-gradient structure and dynamics. In the analysis, we segregate the velocity-gradient magnitude ($A \equiv \sqrt{A_{ij}A_{ij}}$) from the normalized-gradient tensor b_{ij} . The b_{ij} -tensor and the evolution of its invariants are the subject of this study. Some of the key findings of this study are summarized below:

1. Higher-order moments (M_{2n}^b) of b_{ij} do not show any statistically significant variation across the entire range of Re_λ investigated in this study. This is in contrast with A_{ij} , which exhibits a significant increase of normalized moment values with increasing Re_λ . Moreover, A_{ij} -PDFs exhibit clear stretch in tails as Re_λ increases, while b_{ij} -PDFs achieve self-similarity for $Re_\lambda > 35$.

2. PDFs and joint PDFs of b_{ij} -invariants (q, r) are more sensitive to changing Re_λ than individual b_{ij} -components:

- (a) The q - r joint PDF changes qualitatively for $Re_\lambda \in (1, 10)$ from Gaussian to a teardrop shape.
- (b) For $Re_\lambda \in (10, 200)$, the q - r joint PDF and marginal PDFs undergo minor quantitative changes with increasing Re_λ to accommodate an increasing proportion of strain-dominated topologies.
- (c) The q and r individual PDFs as well as the q - r joint PDF converge to the characteristic teardrop shape for $Re_\lambda > 200$. Note that this asymptotic behavior is observed in similar range of Re_λ as the onset of dissipative anomaly (Donzis et al., 2005).

3. Physical processes contributing to the evolution of b_{ij} -invariants and A^2 are also examined:

- (a) For $Re_\lambda \geq 200$, the conditional mean and variance of the unclosed pressure term in the evolution of q , r and θ are independent of Re_λ .
- (b) The mean-viscous contribution to q - and r - evolution shows asymptotic convergence for $Re_\lambda > 200$. The mean viscous contribution to θ -evolution does not vary qualitatively but shows a continued quantitative dependence on Re_λ . The conditional variance of viscous term in all three evolution equations continue to exhibit Re_λ -dependence.
- (c) It is surmised that viscous processes are the primary source of the Reynolds number dependence of A^2 .

In future works, we plan to develop closure models for h_{ij} and τ_{ij} as a function of q and r . This will lead to a Lagrangian closure model for b_{ij} -evolution, and ultimately to A^2 -evolution.

3. GEOMETRY OF LOCAL FLOW STREAMLINES

3.1 Introduction

The last few decades have witnessed many important advances toward understanding the internal structure of A_{ij} (Ashurst et al., 1987; Kerr, 1987) and describing local streamline topology in terms of A_{ij} invariants (Chong et al., 1990). The topological classification of local streamline structure has enabled further advances in (i) identifying key universal features of local streamline structure (Soria et al., 1994; Blackburn et al., 1996; Chacín et al., 1996; Chacin and Cantwell, 2000; Elsinga and Marusic, 2010b) and (ii) characterization of important velocity gradient processes conditioned upon topology (Martín et al., 1998b; Ooi et al., 1999; Elsinga and Marusic, 2010a; Atkinson et al., 2012; Bechlars and Sandberg, 2017a). Other studies on the structure of A_{ij} have led to improved understanding of internal alignment properties, characteristic length scales and non-normality in different topologies (Hamlington et al., 2008; Chevillard et al., 2008; Danish and Meneveau, 2018; Keylock, 2018).

The goal of this study is to develop a more complete description of local streamline geometry that can be used for enhanced characterization of velocity gradient dynamics. An important feature of the approach is that it combines internal structural features of A_{ij} (Ashurst et al., 1987) with topological classification (Chong et al., 1990) to render a more complete geometric basis for conditioning non-local velocity gradient processes. At the very outset, it is important to formally distinguish between topology and geometry. The geometry of an object is constituted by its shape and size (Yale, 1968; Smart, 1998). Shape and size are quantified in terms of shape-parameters and scale-factor, respectively. Geometric shape is defined as the structural characteristics of the object, that is invariant to translation, rotation and reflection independent of size. Topology, on the other

Part of this chapter is reprinted with permission from: Das, R. and Girimaji, S. S. (2020). Characterization of velocity-gradient dynamics in incompressible turbulence using local streamline geometry, *Journal of Fluid Mechanics*, 895. Copyright The Author(s), 2020. Published by Cambridge University Press.

hand, is a class of geometric shapes that have similar connectivity and can be transformed from one to the other by continuous deformation (Kinsey, 1993; Blackett, 2014). Clearly, a description of streamline geometry requires additional details to those derived from a topological classification.

The primary objectives of the present study are (i) to derive a description of local streamline shape-parameters by extending critical point analysis (Perry and Fairlie, 1975; Perry and Chong, 1987); (ii) to employ DNS data sets of different turbulent flows to determine the statistical distribution of local shape-parameters and scale-factor of streamlines in turbulent flow fields. Toward this end, we utilize the framework developed in the previous chapter. As shown in chapter 2, the VG tensor can be factorized into the mathematically bounded normalized VG tensor and intermittent VG magnitude. In this study, we analytically demonstrate that all the geometric features of local streamlines are contained within the normalized VG tensor and that the scale of the streamline depends upon the VG magnitude.

The remaining sections of this study are arranged as follows. Section 3.2 develops the framework for the description of local streamline shape. Section 3.3 provides a brief description of the DNS data used for analysis. The probability distributions of streamline shape parameters and the mean scale-factor for different geometric-shapes are presented in section 3.4. Finally, the key findings of the study are summarized in section 3.5.

3.2 Complete characterization of local streamline geometry

We first reiterate the fundamental distinction between topological and geometric descriptions of an object in the context of the present work. These concepts are then used to establish that the A_{ij} -invariants cannot uniquely describe the local streamline geometry or shape. Then, we develop a complete description of local streamline geometry in terms of shape parameters and scale factor.

3.2.1 Geometry and topology

The *geometry* of any object can be described with two principal attributes - shape and size. *Geometric shape* is the structural characterization of an object that is independent of size and invariant under translation, rotation, reflection and any other similarity transformation (Yale, 1968;

Smart, 1998). Shape describes the internal structural arrangement and is parameterized by the unique combination of angles between edges and ratios of lengths of edges. *Scale-factor* is a measure of the size of such a geometric shape, which can be scaled through simple enlargement or shrinking without altering the angles and ratios of distances. It is also known as stretching factor (Yale, 1968) or ratio of similarity (Smart, 1998). In general the number of shape-parameters required to describe an object depends upon the complexity of its geometry and its dimensionality. In the present context, the shrinking and enlargement are the same in all directions (isotropic) and therefore only one scale-factor is required to specify the size. The geometries of two objects are *similar* if all the shape parameters are identical. If two objects have identical shape parameters and scale factors, they are called *congruent*.

Topology describes a set of geometric shapes that exhibit the following attributes (Kinsey, 1993; Smart, 1998; Blackett, 2014): (i) different shapes of the set can be transformed from one to the other by continuous deformations or homeomorphisms, such as stretching, compression, torsion and shearing; and (ii) all shapes of the set have the same connectivity (e.g. singly or doubly connected). Thus, topology does not completely define the specific geometric shape of an object, but identifies a set of shapes with certain common features. We will next examine the topology and geometry of local streamline structures.

3.2.2 Local flow streamlines

The fluid particle evolution equation forms the basis of the streamline structure analysis. The position of a fluid particle in a velocity field evolves according to

$$\frac{dx_i}{dt} = u_i \quad (3.1)$$

The deformation of infinitesimal material line and area elements (Orszag, 1970a; Monin and Yaglom, 2013; Girimaji and Pope, 1990b) can be inferred from this equation. This Lagrangian description can also be used to describe the shape of streaklines and streamlines in a flow. Using critical point analysis and first-order Taylor series expansion of the velocity field (Perry and Fair-

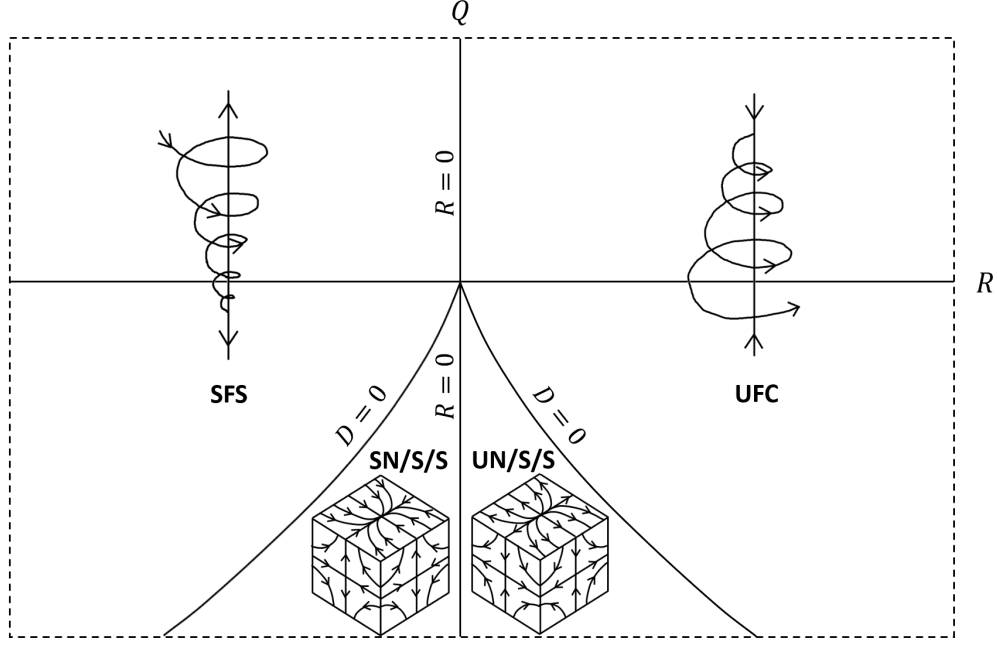


Figure 3.1: Classification of local three-dimensional streamlines into non-degenerate topologies in Q - R plane (Chong et al., 1990) for incompressible turbulence. The curved solid lines are discriminant $D = 0$ lines. Reprinted with permission from Das and Girimaji (2020a).

lie, 1975; Perry and Chong, 1987, 1994), the particle trajectory is governed by

$$\frac{dx_i}{dt} = A_{ij}x_j \quad (3.2)$$

Subject to simplification of a steady flow and spatially uniform velocity gradient field in the immediate vicinity of the free-slip critical point, the solution trajectories from the above equation represent the local instantaneous streamlines. The streamline structure can be described in different levels of details such as (i) topological classification, or (ii) full geometry description.

3.2.3 Topological classification of streamlines

The topological classification of local streamline structure in incompressible flows can be achieved with only the VG tensor invariants (Chong et al., 1990),

$$Q = -\frac{1}{2}A_{ij}A_{ji} \quad \text{and} \quad R = -\frac{1}{3}A_{ij}A_{jk}A_{ki} \quad (3.3)$$

The $R = 0$ and the discriminant $D = Q^3 + (27/4)R^2 = 0$ lines divide the Q - R plane into four regions, each representing a topology, as depicted in figure 3.1. These four non-degenerate three-dimensional topologies are stable focus stretching (SFS), unstable focus compression (UFC), unstable-node/saddle/saddle (UN/S/S) and stable-node/saddle/saddle (SN/S/S). This classification groups together streamline shapes that are “topologically equivalent” or geometrically homeomorphic. In other words, different shapes related to each other by affine transformations are categorized as the same topology. A representative streamline shape of each topology, based on a canonical form of VG tensor, is shown in figure 3.1.

The topological description in the Q - R plane does not uniquely describe the geometric shape of streamlines. This is best illustrated by the following example of an elliptic (closed) two-dimensional streamline flow. A VG tensor of the form (Blaisdell and Shari, 1996),

$$\mathbf{A} = \begin{bmatrix} 0 & -\gamma - e \\ \gamma - e & 0 \end{bmatrix} \quad \text{where } 0 < |e| < |\gamma| \quad (3.4)$$

describes local elliptic streamlines in the x_1 - x_2 plane with major axis along the x_1 direction. It is easy to recognize that in terms of VG magnitude ($A \equiv \sqrt{A_{ij}A_{ij}}$) and invariants, the parameters γ and e are:

$$\gamma = \sqrt{\frac{1}{2} + \frac{Q}{A^2}} \quad , \quad e = \sqrt{\frac{1}{2} - \frac{Q}{A^2}} \quad (3.5)$$

It may be recalled here that $R = 0$ for all two-dimensional streamlines. The shape of an ellipse is defined by the aspect ratio E , which is the ratio of major to minor axes of the ellipse. It can be shown that the aspect ratio of the elliptic streamlines is (Blaisdell and Shari, 1996):

$$E = \sqrt{\frac{\gamma + e}{\gamma - e}} = \sqrt{\frac{\sqrt{\frac{1}{2} + \frac{Q}{A^2}} + \sqrt{\frac{1}{2} - \frac{Q}{A^2}}}{\sqrt{\frac{1}{2} + \frac{Q}{A^2}} - \sqrt{\frac{1}{2} - \frac{Q}{A^2}}}} \quad (3.6)$$

It is evident from equation (3.6) that for the same value of Q , different values of VG magnitude A results in different aspect ratios (E), i.e. different shapes, of the local streamlines. For example,

for the same value of Q , $A^2 = 2Q$ represents circular streamlines while $A^2 \gg Q$ represents an infinitely elongated ellipse. Clearly, Q does not uniquely describe the aspect ratio. On the other hand the variable

$$q \equiv \frac{Q}{A^2} \quad (3.7)$$

uniquely determines the aspect ratio of the ellipse, i.e.

$$E(q) = \sqrt{\frac{\sqrt{\frac{1}{2} + q} + \sqrt{\frac{1}{2} - q}}{\sqrt{\frac{1}{2} + q} - \sqrt{\frac{1}{2} - q}}} \quad (3.8)$$

Therefore, in this two-dimensional case, q is the only shape-parameter and it uniquely characterizes the streamline shape.

The velocity components at any location (x_1, x_2) on a streamline can be obtained using equations (3.2) and (3.4) as follows,

$$\begin{aligned} u_1 = A_{1k}x_k &= -\frac{A}{\sqrt{2}} \left(\sqrt{\frac{1}{2} + q} + \sqrt{\frac{1}{2} - q} \right) x_2 \\ u_2 = A_{2k}x_k &= \frac{A}{\sqrt{2}} \left(\sqrt{\frac{1}{2} + q} - \sqrt{\frac{1}{2} - q} \right) x_1 \end{aligned} \quad (3.9)$$

Clearly, each of the velocity components scale by a factor of A . Therefore, A only influences the speed along the streamline, the shape of which is defined by q . From equation (3.9), the major and minor axis lengths of any given streamline are

$$\begin{aligned} L_{maj}(A, q) &\propto \frac{1}{A} \times \left(\sqrt{\frac{1}{2} + q} - \sqrt{\frac{1}{2} - q} \right)^{-1} \\ L_{min}(A, q) &\propto \frac{1}{A} \times \left(\sqrt{\frac{1}{2} + q} + \sqrt{\frac{1}{2} - q} \right)^{-1} \end{aligned} \quad (3.10)$$

If there are two geometrically similar ellipses of same aspect ratio $E(q)$ and different VG magni-

tudes - A_1 and A_2 , then one can be scaled to the other by the ratio,

$$\frac{L_{maj1}(A_1, q)}{L_{maj2}(A_2, q)} = \frac{L_{min1}(A_1, q)}{L_{min2}(A_2, q)} = \frac{A_2}{A_1} \quad (3.11)$$

Therefore, the scale-factor of an elliptic streamline is inversely proportional to the VG magnitude A .

This example illustrates that the shape of the ellipse is not uniquely defined by Q as it combines the streamline shape and scale information. Similarly in three-dimensional flow, the invariants Q and R can not uniquely define the streamline shape or scale. Any point in the Q - R plane can represent multiple streamline shapes, which are homeomorphic but not necessarily *similar*.

3.2.4 Geometric description of streamlines

From equation (3.2), it is evident that all elements of A_{ij} must be known to fully describe local streamline geometry. The locally linearized velocity vector field is given by,

$$u_i = A_{ij}x_j \quad (3.12)$$

Since a streamline is always tangential to the velocity, the equation of a streamline can be obtained as follows:

$$d\vec{s} \times \vec{u} = 0 \quad \text{where} \quad d\vec{s} = dx_1\hat{i} + dx_2\hat{j} + dx_3\hat{k} \quad (3.13)$$

Here, $d\vec{s}$ is the infinitesimal arc-length vector along the streamline. Therefore,

$$(u_3dx_2 - u_2dx_3)\hat{i} + (u_1dx_3 - u_3dx_1)\hat{j} + (u_2dx_1 - u_1dx_2)\hat{k} = 0 \quad (3.14)$$

Now, setting each vector component to zero, we obtain the following differential equations:

$$\frac{dx_2}{dx_3} = \frac{u_2}{u_3} = \frac{A_{2j}x_j}{A_{3k}x_k}, \quad \frac{dx_3}{dx_1} = \frac{u_3}{u_1} = \frac{A_{3j}x_j}{A_{1k}x_k}, \quad \frac{dx_1}{dx_2} = \frac{u_1}{u_2} = \frac{A_{1j}x_j}{A_{2k}x_k} \quad (3.15)$$

The above differential equations can be integrated to obtain the equations describing streamlines.

Our goal is to derive a geometric description that separates shape and size features. We start by factorizing the VG tensor \mathbf{A} into its magnitude A and normalized VG tensor or VG structure tensor \mathbf{b} (Das and Girimaji, 2019) such that

$$A_{ij} = Ab_{ij} \quad (3.16)$$

We now seek the streamline structure corresponding to the b_{ij} -field. We define a local velocity field given by

$$u_i^* \equiv b_{ij}x_j \quad (3.17)$$

The corresponding b_{ij} -streamlines are given by,

$$d\vec{s}^* \times \vec{u}^* = 0 \quad \text{where} \quad d\vec{s}^* = dx_1^*\hat{i} + dx_2^*\hat{j} + dx_3^*\hat{k} \quad (3.18)$$

where $d\vec{s}^*$ is the infinitesimal arc-length vector along the b_{ij} -streamline. Using equations (3.15), (3.16) and (3.18), we can write the following identities involving A_{ij} - and b_{ij} - streamlines.

$$\frac{dx_\alpha^*}{dx_\beta^*} = \frac{u_\alpha^*}{u_\beta^*} = \frac{b_{\alpha i}x_i}{b_{\beta j}x_j} \equiv \frac{A_{\alpha k}x_k}{A_{\beta l}x_l} = \frac{dx_\alpha}{dx_\beta} \quad \forall \quad \alpha, \beta = 1, 2, 3 \quad \text{and} \quad \alpha \neq \beta \quad (3.19)$$

Thus, all the internal structure features, including ratios of distances and alignments, of A_{ij} - and b_{ij} - streamlines are identical. Therefore, the shape-parameters of the two sets of streamlines must be the same. It is now clear from equation (3.19) that all the b_{ij} -elements are required in order to determine the streamline shape.

From equations (3.12) and (3.17), at any location ($\vec{x} = \vec{x}_0$) of a streamline, it can be shown that

$$\vec{u} = \mathbf{A}\vec{x}_0 = A \mathbf{b}\vec{x}_0 = Au^* \implies \vec{u} = Au^* \quad (3.20)$$

Therefore, it is clear that the velocities of A_{ij} - and b_{ij} - streamlines only differ in magnitude by a factor of A . As shown for the case of two-dimensional elliptic streamlines, this implies that the

streamline scale-factor is inversely proportional to A . From the analysis so far, we conclude the following:

1. The shape features of the streamline geometry are entirely contained in b_{ij} .
2. All independent elements of b_{ij} are required to completely describe the streamline geometric shape.
3. The VG magnitude A determines the streamline scale-factor and is inversely proportional to the scale-factor.

Now we examine the properties of normalized VG tensor (\mathbf{b}) in order to understand the shape characteristics of local streamline geometry. The second and third invariants of \mathbf{b} ,

$$q = -\frac{1}{2}b_{ij}b_{ji} = \frac{Q}{A^2} \quad \text{and} \quad r = -\frac{1}{3}b_{ij}b_{jk}b_{ki} = \frac{R}{A^3} \quad (3.21)$$

classify streamline topology as before, and have the added advantage of separating shape from scale. The other advantage is that b_{ij} -elements are bounded as follows:

$$-\sqrt{\frac{2}{3}} \leq b_{ij} \leq \sqrt{\frac{2}{3}} \quad \forall \quad i = j \quad \text{and} \quad -1 \leq b_{ij} \leq 1 \quad \forall \quad i \neq j \quad (3.22)$$

We now seek the smallest set of independent b_{ij} -elements or parameters required to characterize the normalized VG tensor and hence the local streamline shape. The tensor \mathbf{b} can be decomposed into its symmetric and anti-symmetric counterparts as follows

$$\mathbf{b} = \mathbf{s} + \mathbf{w} \quad , \quad \text{where} \quad s_{ij} = (b_{ij} + b_{ji})/2 \quad \text{and} \quad w_{ij} = (b_{ij} - b_{ji})/2 \quad (3.23)$$

Here, s_{ij} is the normalized strain-rate tensor and w_{ij} is the normalized rotation-rate tensor. Since the orientation of streamlines with respect to the laboratory frame of reference is immaterial for shape description, the tensor components can be considered in any coordinate system of choice to simplify geometric shape description. Therefore, for present purposes, \mathbf{b} can be expressed in the

principal frame of \mathbf{s} without any loss of generality as

$$\mathbf{b} = \begin{bmatrix} a_1 & 0 & 0 \\ 0 & a_2 & 0 \\ 0 & 0 & a_3 \end{bmatrix} + \begin{bmatrix} 0 & -\omega_3 & \omega_2 \\ \omega_3 & 0 & -\omega_1 \\ -\omega_2 & \omega_1 & 0 \end{bmatrix} \quad \text{where } a_1 \geq a_2 \geq a_3 \quad (3.24)$$

Here, a_i are the normalized strain-rates, i.e. eigenvalues of tensor \mathbf{s} . For incompressible flow, $a_1 (> 0)$ is the most expansive strain-rate, $a_3 (< 0)$ is the most compressive strain-rate and a_2 can be positive, negative or zero. The corresponding eigenvectors - \vec{E}_{a_1} , \vec{E}_{a_2} and \vec{E}_{a_3} - are mutually orthogonal and constitute the principal directions of the symmetric tensor \mathbf{s} . Further, ω_i are the components of normalized vorticity vector ($\vec{\omega}$) along the strain-rate eigendirections (Note that the unnormalized vorticity vector is given by $2A\vec{\omega}$). Therefore, these six parameters - $a_1, a_2, a_3, \omega_1, \omega_2$ and ω_3 - completely define the normalized VG tensor and thence the geometric-shape of the local streamlines.

In a previous study, Chakraborty et al. (2005) describe the VG tensor in terms of a scale-factor and four parameters. In that study, the scale-factor is the largest strain-rate eigenvalue and the four shape-parameters are relative vorticity magnitude (a), strain-field parameter (ξ) and orientation angles of vorticity vector with respect to strain-rate eigendirections (θ and ϕ). Then, they proceed to reduce the system to three parameters - $\|\Omega\|/\|S\|$, ξ and ψ - that completely determines the VG tensor eigenvalues, but not the entire geometric shape. Different local streamline geometries are characterized in the phase space of $\|\Omega\|/\|S\|-\psi$ at specific values of ξ . It must be noted that one of the parameters describing the streamline shapes is unbounded: $\|\Omega\|/\|S\| \in (0, \infty)$. In the present study, we seek an alternate framework where all the shape-parameters are mathematically bounded, thus providing a compact space for characterizing streamline-shapes. The Frobenius norm of VG tensor (A) is selected as the scale-factor due to its inherent advantage of directly representing pseudo-dissipation. As described in Das and Girimaji (2019), using A as the scale-factor also leads to ease of VG tensor modeling.

We begin by reducing the six parameters defining VG tensor in equation (3.24) into the smallest

independent set. First, we apply the incompressibility condition,

$$a_1 + a_2 + a_3 = 0 \implies a_3 = -(a_1 + a_2) \quad (3.25)$$

Then, due to normalization of VG tensor, we have,

$$b_{ij}b_{ij} = s_{ij}s_{ij} + w_{ij}w_{ij} = a_1^2 + a_2^2 + a_3^2 + 2(\omega_1^2 + \omega_2^2 + \omega_3^2) = 1 \quad (3.26)$$

These constraints reduce the system to a total of four functionally independent parameters, which completely specify \mathbf{b} in the principal frame of \mathbf{s} and therefore determine the exact local streamline shape. It is expeditious to choose the frame-independent invariants, q and r , as two of the four parameters.

Following the work of Ashurst et al. (1987), which demonstrates a preferential alignment of vorticity vector with the intermediate strain-rate eigenvector in a turbulent flow field, we choose the other two parameters to be the intermediate strain-rate eigenvalue a_2 and the vorticity component along the intermediate strain-rate eigendirection $|\omega_2|$. From equation (3.21), we have

$$-\frac{1}{2}b_{ij}b_{ji} = \frac{1}{2}(w_{ij}w_{ij} - s_{ij}s_{ij}) = q \quad (3.27)$$

Note that a positive q represents rotation-dominated flow while a negative q represents strain-dominated flow. Using equations (3.26) and (3.27),

$$s_{ij}s_{ij} = a_1^2 + a_2^2 + a_3^2 = \frac{1}{2} - q \quad (3.28)$$

Equations (3.25) and (3.28) can be used to show that:

$$a_1 = \frac{1}{2}(-a_2 + \sqrt{1 - 3a_2^2 - 2q}) \quad \text{and} \quad a_3 = \frac{1}{2}(-a_2 - \sqrt{1 - 3a_2^2 - 2q}) \quad (3.29)$$

Therefore, a_1 and a_3 may be calculated from the four parameter set. Next, the third invariant in

equation (3.21) can be expanded as follows

$$\begin{aligned} r &= -\frac{1}{3}b_{ij}b_{jk}b_{ki} = -\frac{1}{3}(s_{ij}s_{jk}s_{ki} + 3s_{ij}w_{jk}w_{ki}) \\ \implies r &= -a_1a_2a_3 - a_1\omega_1^2 - a_2\omega_2^2 - a_3\omega_3^2 \end{aligned} \quad (3.30)$$

From equations (3.26) and (3.27), we also obtain,

$$w_{ij}w_{ij} = 2(\omega_1^2 + \omega_2^2 + \omega_3^2) = \frac{1}{2} + q \quad (3.31)$$

Solving equations (3.30) and (3.31) leads to:

$$\omega_1 = \pm \frac{1}{2\sqrt{2}} \sqrt{(1 + 2q - 4\omega_2^2) - \frac{8a_2^3 + 8r - a_2(3 - 2q - 12\omega_2^2)}{\sqrt{1 - 3a_2^2 - 2q}}} = f(q, r, a_2, \omega_2) \quad (3.32)$$

$$\omega_3 = \pm \frac{1}{2\sqrt{2}} \sqrt{(1 + 2q - 4\omega_2^2) + \frac{8a_2^3 + 8r - a_2(3 - 2q - 12\omega_2^2)}{\sqrt{1 - 3a_2^2 - 2q}}} = g(q, r, a_2, \omega_2) \quad (3.33)$$

Equations (3.29), (3.32) and (3.33) exhibit that a_1 , a_3 , $|\omega_1|$ and $|\omega_3|$ can be completely and uniquely determined in terms of q , r , a_2 and $|\omega_2|$, thus completely specifying the tensor \mathbf{b} . Therefore, each combination of q , r , a_2 and $|\omega_2|$ represents a unique geometric shape. These four quantities are now designated as the shape-parameters.

This four-parameter system is consistent with that of Chakraborty et al. (2005), as previously mentioned. Each of their four parameters can be expressed in terms of the shape-parameters as follows:

$$\begin{aligned} a &\equiv \frac{|\omega|}{2a_1} = \frac{\sqrt{1+2q}}{2a_1} = \frac{\sqrt{1+2q}}{-a_2 + \sqrt{1-3a_2^2-2q}}, \\ \xi &\equiv -\frac{2a_2}{a_1} = -\frac{2a_2}{a_1} = -\frac{4a_2}{-a_2 + \sqrt{1-3a_2^2-2q}}, \\ \theta &= \cos^{-1}\left(\frac{2\omega_1}{\sqrt{1+2q}}\right) = \cos^{-1}\left(\frac{2f(q, r, a_2, \omega_2)}{\sqrt{1+2q}}\right) \text{ and} \\ \phi &= \tan^{-1}\left(\frac{\omega_3}{\omega_2}\right) = \tan^{-1}\left(\frac{g(q, r, a_2, \omega_2)}{\omega_2}\right) \end{aligned} \quad (3.34)$$

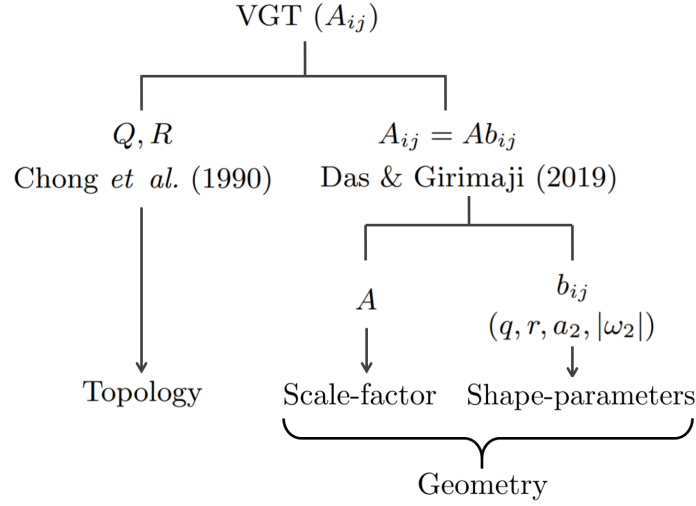


Figure 3.2: Summary of the key points of different frameworks for studying local flow streamline structure. Reprinted with permission from Das and Girimaji (2020a).

As mentioned earlier, the advantage of the current approach is that the shape is completely defined in a compact parameter space.

The streamline-shape and its scale-factor together constitute the complete geometry of the local streamlines. Figure 3.2 summarizes the important distinctions between topological and geometric descriptions of streamlines.

3.2.5 Kinematic bounds of shape-parameters

We now seek to establish the bounds of the shape-parameters. Let us first determine the bounds of the invariant parameter q . From equations (3.28) and (3.31), we can write

$$s_{ij}s_{ij} = \frac{1}{2} - q \geq 0 \quad \text{and} \quad w_{ij}w_{ij} = \frac{1}{2} + q \geq 0 \quad (3.35)$$

leading to

$$-\frac{1}{2} \leq q \leq \frac{1}{2} \quad (3.36)$$

Applying the conditions $a_1 \geq a_2 \geq a_3$ in equation (3.29) and solving for a_2 in the resulting inequality equations, we obtain

$$-\sqrt{\frac{1-2q}{12}} \leq a_2 \leq \sqrt{\frac{1-2q}{12}} \quad (3.37)$$

The most expansive strain-rate (a_1) is non-negative by definition and attains its maximum value when a_2 is minimum, thus,

$$0 \leq a_1 \leq \sqrt{\frac{1-2q}{3}} \quad (3.38)$$

Similarly, the most compressive strain-rate (a_3) has the following bounds,

$$-\sqrt{\frac{1-2q}{3}} \leq a_3 \leq 0 \quad (3.39)$$

From equation (3.31) it is seen that all vorticity components have identical bounds:

$$|\omega_i|^2 \leq \frac{q}{2} + \frac{1}{4} \quad \implies \quad -\sqrt{\frac{q}{2} + \frac{1}{4}} \leq \omega_i \leq \sqrt{\frac{q}{2} + \frac{1}{4}} \quad \forall \quad i = 1, 2, 3 \quad (3.40)$$

Determining the bounds of the third invariant r is quite involved and the steps are not displayed here. Substituting the upper bounds of ω_1 and ω_3 (equation 3.40) into equations (3.32) and (3.33) and applying the bounds of a_2 and $|\omega_2|$ (equations 3.37 and 3.40) leads to the following inequality:

$$-\frac{1+q}{3} \left(\frac{1-2q}{3} \right)^{1/2} \leq r \leq \frac{1+q}{3} \left(\frac{1-2q}{3} \right)^{1/2} \quad (3.41)$$

This represents the kinematic bounds of r for a given value of q and therefore the boundary of the realizable region of q - r plane. The extreme values of r occur at $q = 0$. Therefore, the absolute bounds of r (also derived by Wang et al. (2014) in a different context) are

$$-\frac{\sqrt{3}}{9} \leq r \leq \frac{\sqrt{3}}{9} \quad (3.42)$$

Equations (3.36), (3.37), (3.40) and (3.41) define the kinematic bounds of the shape-parameters - q , a_2 , $|\omega_2|$ and r . Further constraints may be possible and will be investigated in future work.

3.2.6 Characterization of geometric shape in q - r plane

First, we classify the topologies in q - r space in a manner similar to that in Q - R space (Chong et al., 1990), as shown in figure 3.3. The $r = 0$ and discriminant $d = q^3 + (27/4)r^2 = 0$ lines divide the plane into four non-degenerate topology types. A schematic representation of the general streamline shapes belonging to these topologies are depicted in figure 3.3. The difference here is that q - r provides a mathematically bounded phase plane and each (q, r) combination represents a unique streamline shape. For the sake of completeness, we reiterate this classification in the context of the present framework.

In focal streamlines ($d > 0$), \mathbf{b} has one real (λ_2) and two complex conjugate ($\lambda_{1,3}$) eigenvalues:

1. Stable focus stretching or SFS streamlines ($r < 0$ or $\lambda_2 > 0$) spiral towards a stable focus while stretching out of the focal plane.
2. Unstable focus compression or UFC streamlines ($r > 0$ or $\lambda_2 < 0$) spiral away from the center while being compressed into the focal plane.

In nodal streamlines ($d < 0$), \mathbf{b} has three distinct real eigenvalues ($\lambda_1 > \lambda_2 > \lambda_3$) and three solution planes (not necessarily orthogonal):

3. Stable node/saddle/saddle (SN/S/S) streamlines consist of a stable node ($\lambda_2 < 0$ or $r < 0$) in one plane and saddle nodes in two planes.
4. Unstable node/saddle/saddle (UN/S/S) streamlines consist of an unstable node ($\lambda_2 > 0$ or $r > 0$) in one plane and saddle nodes in two planes.

The focus is now on the complete description of various streamline shapes associated with different locations in the q - r plane. We examine the streamline shapes at several lines and points of geometric significance in the q - r plane as marked in figure 3.3. The corresponding streamline

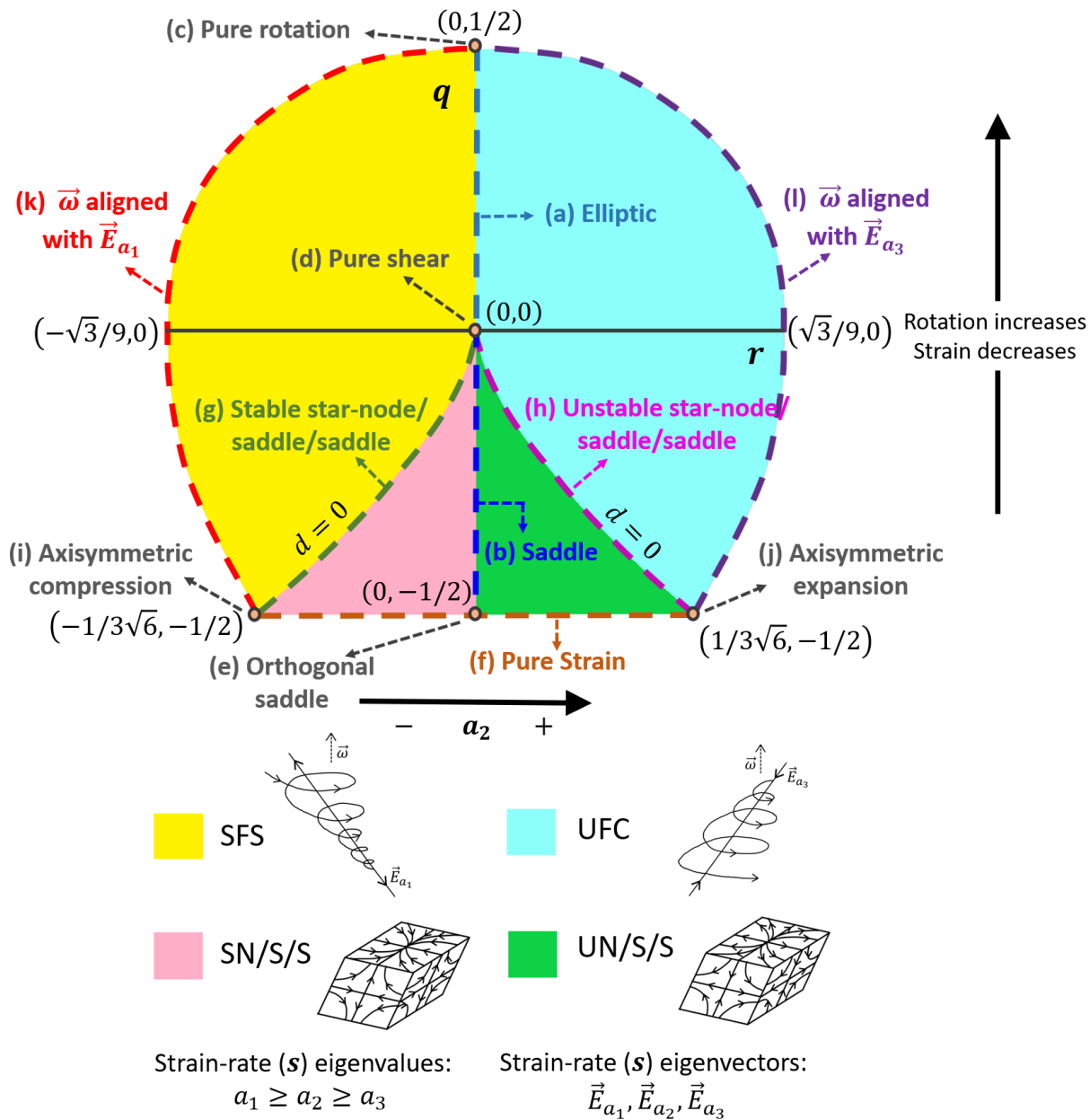


Figure 3.3: Streamline shapes represented by different points, lines and regions of the q - r plane. Reprinted with permission from Das and Girimaji (2020a).


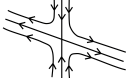
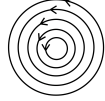
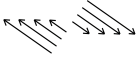
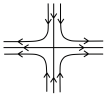
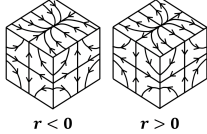






Streamline shape	Location in (q,r) plane	Description	Schematic diagram
(a) Elliptic:	$q > 0, r = 0$	$\lambda_{1,3} = \pm i\lambda, \lambda_2 = 0$	
(b) Saddle:	$q < 0, r = 0$	$\lambda_{1,3} = \pm\lambda, \lambda_2 = 0$	
(c) Pure rotation:	$q = \frac{1}{2}, r = 0$	$\lambda_{1,3} = \pm i\lambda, \lambda_2 = 0, a_i = 0$	
(d) Pure shear:	$q = 0, r = 0$	All $\lambda_i = 0$	
(e) Orthogonal saddle:	$q = -\frac{1}{2}, r = 0$	$\lambda_{1,3} = a_{1,3}, \vec{\omega} = 0$	
(f) Pure strain:	$q = -\frac{1}{2}$	$\lambda_i = a_i, \vec{\omega} = 0$	
(g) Stable star-node/ saddle/saddle:	left $d = 0$ line	$\lambda_2 = \lambda_3 = -\frac{\lambda_1}{2}$	
(h) Unstable star-node/ saddle/saddle:	right $d = 0$ line	$\lambda_1 = \lambda_2 = -\frac{\lambda_3}{2}$	
(i) Axisymmetric compression:	$q = -\frac{1}{2}, r = -\frac{1}{3\sqrt{6}}$	$\lambda_2 = \lambda_3 = -\frac{\lambda_1}{2},$ $\vec{\omega} = 0$	
(j) Axisymmetric expansion:	$q = -\frac{1}{2}, r = \frac{1}{3\sqrt{6}}$	$\lambda_1 = \lambda_2 = -\frac{\lambda_3}{2},$ $\vec{\omega} = 0$	
(k) Orthogonal stretching of stable spiral:	$r = -\frac{1+q}{3} \left(\frac{1-2q}{3} \right)^{\frac{1}{2}}$	$\vec{\omega}$ aligned with \vec{E}_{a_1} if $a_2 = a_3 = -\frac{a_1}{2}$	
(l) Orthogonal compression of unstable spiral:	$r = \frac{1+q}{3} \left(\frac{1-2q}{3} \right)^{\frac{1}{2}}$	$\vec{\omega}$ aligned with \vec{E}_{a_3} if $a_1 = a_2 = -\frac{a_3}{2}$	

Table 3.1: Description of streamline shapes at points/lines marked in $q-r$ plane in figure 3.3. Reprinted with permission from Das and Girimaji (2020a).

shape descriptions are listed in table 3.1, along with a schematic representation of each shape. The details of the various shapes are further discussed below:

Two-dimensional streamlines: The $r = 0$ line represents two-dimensional planar flow streamlines. At every point along this line the intermediate eigenvalue of \mathbf{b} is zero ($\lambda_2 = 0$) but the intermediate strain-rate eigenvalue (a_2) is not necessarily zero. In the event that the vorticity vector ($\vec{\omega}$) is perfectly aligned with the intermediate strain-rate eigenvector (\vec{E}_{a_2}), a_2 is zero. The specific shapes at different q values along this line are as follows:

1. *Elliptic:* Upper half of the $r = 0$ line represents closed elliptic streamlines or centers (Kaplan (1958) figure 11-10) with the aspect ratio of the ellipse dependent on the q -value as given in equation (3.8). Here, \mathbf{b} has one real and two purely imaginary eigenvalues ($\lambda_2, \lambda_{1,3} = \pm i\lambda_i$).
2. *Pure-rotation:* The top-most point in the plane, (i.e. $q = 1/2, r = 0$), represents circular streamlines undergoing pure or solid-body rotation. A pure rotation flow is elliptic flow with aspect ratio 1. Here, the strain-rate eigenvalues are zero, i.e. $a_1 = a_2 = a_3 = 0$, and the normalized VG tensor, \mathbf{b} , is only composed of vorticity/rotation rate tensor (\mathbf{w}).
3. *Pure-shear:* The entire $q = 0$ line represents streamlines with equal contributions of strain and rotation ($s_{ij}s_{ij} = w_{ij}w_{ij}$). The $r = 0$ point on this line is of particular significance since at this point all the eigenvalues of \mathbf{b} are zero and therefore it represents only shear deformation of the local fluid element. The eigenvalues of \mathbf{s} and \mathbf{w} are individually non-zero due to the contribution of shear to each of these tensors. Thus, the origin of the q - r plane represents pure-shear parallel streamlines (Kaplan (1958) figure 11-11).
4. *Saddle:* Any point on the lower half ($q < 0$) of the $r = 0$ line has two real equal and opposite eigenvalues ($\lambda_{1,3} = \pm\lambda$) of \mathbf{b} . These points represent open hyperbolic streamlines, constituted by a saddle point with compression in one eigendirection and expansion in the other (Kaplan (1958) figure 11-4). These eigenvectors of \mathbf{b} are in general oblique and become progressively orthogonal as q approaches its lower limit.

5. *Orthogonal saddle*: At the bottom-most point ($q = -1/2, r = 0$) on this line, there is no vorticity and the two real eigenvectors of \mathbf{b} are perpendicular to each other. This results in a two-dimensional orthogonal saddle with the compressing streamlines perpendicular to the expanding streamlines.

Pure-strain: The entire bottom-most line ($q = -1/2$) represents three-dimensional nodal streamlines with three orthogonal solution planes (\mathbf{b} -eigenvectors) of compression and expansion. This is due to the fact that along this line streamlines have zero vorticity ($\vec{\omega} = 0$ and $w_{ij} = 0$) and thus, \mathbf{b} ($= \mathbf{s}$) is a symmetric tensor. The $q = -1/2$ line, therefore, represents pure-strain streamlines.

Star-node/saddle/saddle: The zero discriminant lines demarcating the focal streamlines from nodal streamlines also have a specific streamline shape. At any point on the left $d = 0$ line, the tensor \mathbf{b} has one positive real eigenvalue, λ_1 , and two equal negative real eigenvalues, $\lambda_2 = \lambda_3 = -\lambda_1/2$. This results in a stable symmetrical node or star-node, i.e. straight streamlines directed towards the critical point (see Kaplan (1958) figure 11-9a), in one of the three eigenvector planes and saddles in the other two eigenvector planes. Similarly, on the right $d = 0$ line, \mathbf{b} has two equal positive eigenvalues, $\lambda_1 = \lambda_2 = -\lambda_3/2$, thus representing an unstable symmetrical node or star-node (straight streamlines directed away from the critical point) in one of the solution planes and saddles in the other two.

Axisymmetric compression/expansion: A special case of the above mentioned shape occurs at the points of intersection of the $d = 0$ lines with the pure-strain line, i.e. at the corner points ($q = -1/2, r = \pm 1/3\sqrt{6}$) of the q - r plane. Due to the orthogonality of the eigenvector planes, the bottom-left corner of the plane represents axisymmetric compression accompanied by twice as strong expansion perpendicular to it, forming an elongated tube-like streamline structure. And the bottom-right corner represents axisymmetric expansion with twice as strong compression perpendicular to it, forming a flatter disk-like streamline geometry.

Orthogonal focal stretching/compression: Next we emphasize on the significance of the left and right boundaries of the q - r plane as given by equation (3.41). When r is at its lower bound

for a given q (left boundary), $\vec{\omega}$ is perfectly aligned with the most expansive strain-rate eigenvector (\vec{E}_{a_1}) provided a_1 is equal to its upper kinematic limit for that q value (or a_2 is equal to its lower kinematic limit, implying $a_2 = a_3 = -a_1/2$). In other words, when:

$$\omega_1 = \omega = \sqrt{\frac{1}{4} + \frac{q}{2}}, \quad \omega_2 = \omega_3 = 0 \quad \text{and} \quad a_2 = -\sqrt{\frac{1-2q}{12}} \quad (3.43)$$

solving equation (3.32) yields,

$$r = -\frac{1+q}{3} \left(\frac{1-2q}{3} \right)^{1/2}, \quad (3.44)$$

which is the left boundary of the q - r plane. This result is important as it will be shown in section 3.4.3 that in a turbulent flow field, a_1 achieves its maximum value along the left boundary and therefore $\vec{\omega}$ is indeed most likely aligned with \vec{E}_{a_1} along the left boundary of the plane. This line therefore represents SFS streamlines stretching in a direction perpendicular to the plane of rotation/spiraling. Similarly, the right boundary of the q - r plane represents perfect alignment of $\vec{\omega}$ with the most compressive strain-rate eigenvector (\vec{E}_{a_3}) provided a_3 is at its most negative limit for a given q value (i.e. $a_1 = a_2 = -a_3/2$). This line represents UFC streamlines with compression perpendicular to the focal plane. Again, the DNS data substantiates this result.

It is evident that shape-defining geometric properties, such as strain-rate eigenvalues and alignment of vorticity with strain-rate eigendirections, vary in a specific manner across the q - r plane. There is scope for further characterization of this variation within the non-degenerate topologies of the q - r plane, which will be pursued in future work.

3.3 Numerical simulation data

Direct numerical simulation (DNS) datasets of incompressible forced homogeneous isotropic turbulence (FIT) have been used in this study to investigate streamline geometry and scale. Three different flow cases of Taylor Reynolds numbers, $Re_\lambda = 225, 385$ and 588 are used for the present analysis. Further details of the DNS data sets are included in appendix A. All these datasets are well-resolved and have been used previously to study intermittency, anomalous exponents, Reynolds number scaling and non-linear depletion (Donzis et al., 2008; Donzis and Sreenivasan,

2010; Donzis et al., 2012; Gibbon et al., 2014). The spatial derivatives are computed using Fourier transforms.

DNS data of turbulent channel flow from the Johns Hopkins Turbulence Database (Li et al., 2008; Lee and Moser, 2015) is also used in this study to examine the universality of small-scale geometry across different types of turbulent flows. The friction velocity Reynolds number of the channel flow is

$$Re_\tau \equiv \frac{u_\tau h}{\nu} = 5186 \quad (3.45)$$

where u_τ is the friction velocity and h is the channel half-height. Other details about the data set are presented in appendix A. The velocity field is homogeneous in the stream-wise (x) and span-wise (z) directions and inhomogeneous in the wall-normal (y) direction. In order to circumvent averaging over statistically inhomogeneous wall-normal (y) direction, we use data at specific y^+ planes, each corresponding to a particular Taylor Reynolds number: $y^+ = 100$ ($Re_\lambda = 81$), $y^+ = 203$ ($Re_\lambda = 110$), $y^+ = 302$ ($Re_\lambda = 132$), and $y^+ = 852$ ($Re_\lambda = 182$). Data from multiple time instants are considered to achieve adequate sampling.

3.4 Statistical characterization of local streamline geometry

Four independent shape-parameters - q , r , a_2 and $|\omega_2|$ - determine the local streamline shape as shown in the previous section. Since the magnitude of vorticity (ω) is a function of q (equation 3.31), we propose a new independent parameter in place of ω_2 :

$$\cos\beta = \frac{\omega_2}{\omega} = \frac{\omega_2}{\sqrt{\frac{1}{4} + \frac{q}{2}}} \quad (3.46)$$

Here, β is the angle between vorticity and intermediate eigenvector of strain-rate.

Due to the complexity of illustrating the probability distribution of a four-dimensional state space (q , r , a_2 , $|\cos\beta|$), joint PDFs of these parameters are presented in two-dimensional phase planes to exhibit the shape characteristics. Then, we examine the conditional mean scale-factor as a function of geometric-shape. Finally, the conditional averaged a_2 and $|\cos\beta|$ are investigated in

the frame-invariant q - r plane.

3.4.1 Probability distribution of geometric shape parameters

The various shape-parameter joint PDFs are plotted in figure 3.4 for the turbulence flow field of $Re_\lambda = 225$. We now examine each joint PDF in detail. In what follows, we refer to the region within kinematic bounds of the phase space as the realizable space.

1. **q, r PDF** (figure 3.4a): The q - r joint PDF resembles the teardrop shape of Q - R but with a thicker tail, as previously shown by Das and Girimaji (2019). The distribution exhibits high density along the right $d = 0$ or Vieillefosse line (Vieillefosse, 1984; Bikkani and Girimaji, 2007). Such behavior is also observed in the Q - R plane (Soria et al., 1994; Blackburn et al., 1996; Chong et al., 1998). Joint PDF values as high as 40 occur along the right discriminant line and decreases monotonically on either side. Nearly 90% of the total distribution occupies less than half of the total realizable area of the q - r plane.
2. **$q, |\cos\beta|$ PDF** (figure 3.4b): The realizable region of q - $|\cos\beta|$ phase plane is given by the kinematic bounds: $|\cos\beta| \in [0, 1]$ and $q \in [-1/2, 1/2]$. The upper and lower boundaries represent pure rotation and pure strain respectively. The right boundary ($|\cos\beta| = 1$) represents perfect alignment of vorticity with the intermediate strain-rate eigenvector while $|\cos\beta| = 0$ represents orthogonality between the two. The joint PDF demonstrates that the highest probability of occurrence is when the vorticity vector is perfectly aligned with the intermediate strain-rate eigenvector, consistent with the findings of Ashurst et al. (1987) and other alignment studies in the literature. The joint PDF further shows that in rotation-dominated streamlines, vorticity is likely to better align with the intermediate strain-rate eigenvector.
3. **q, a_2 PDF** (figure 3.4c): The q - a_2 plane is bounded within a parabolic realizable domain (equation 3.37). If $a_2 < 0$, then expansion (a_1) is the strongest strain-rate while $a_2 > 0$ implies the strongest strain-rate is compression (a_3). The q - a_2 probability distribution is more dispersed than other phase spaces, covering a large part of the total realizable area.

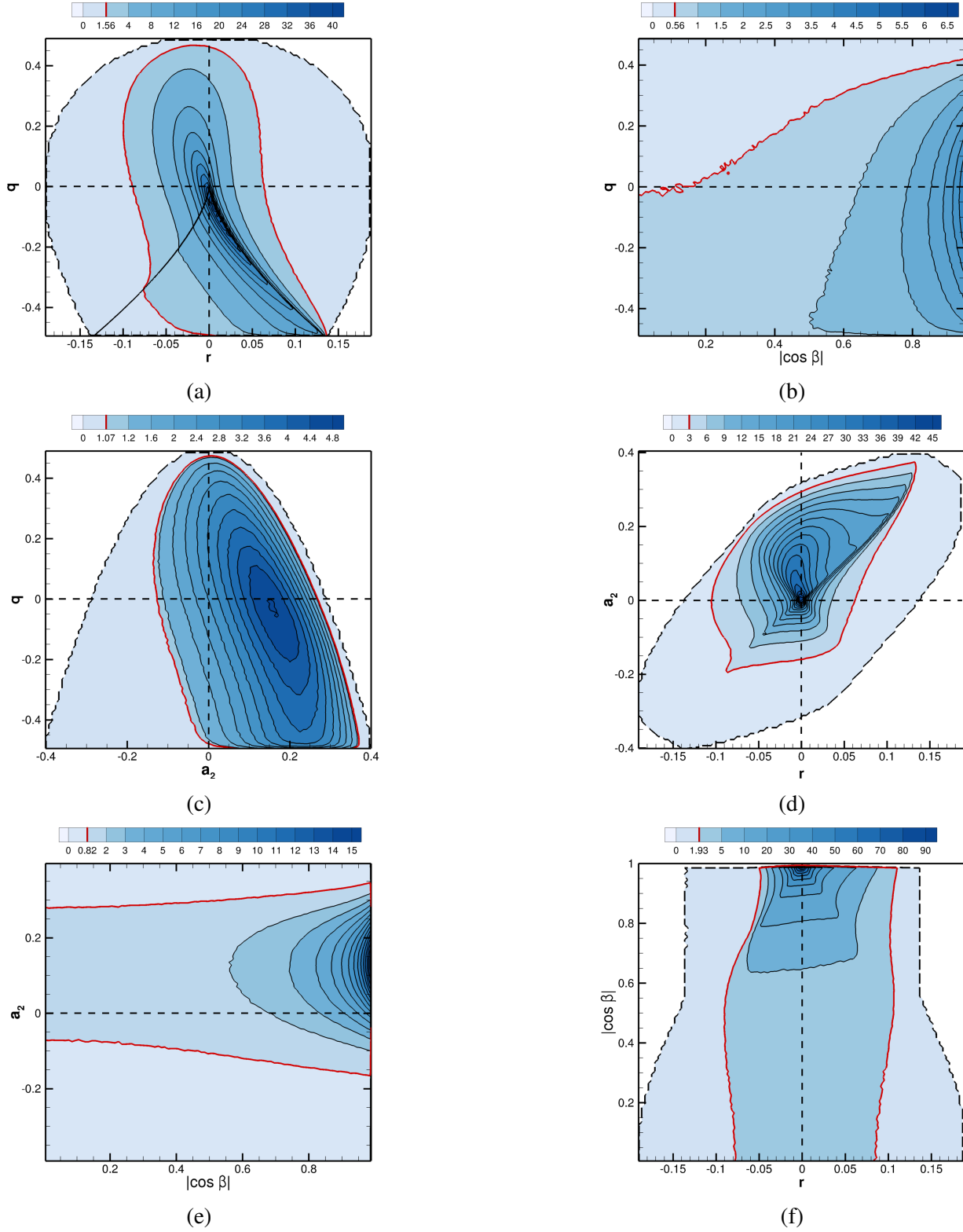


Figure 3.4: Joint PDF of (a) $q-r$ (b) $q-|\cos\beta|$ (c) $q-a_2$ (d) a_2-r (e) $a_2-|\cos\beta|$ (f) $|\cos\beta|-r$ for $Re_\lambda = 225$. Dashed line marks the boundary of the realizable region of the phase plane. Thick red line marks the contour level that includes 90% of the field. Reprinted with permission from Das and Girimaji (2020a).

It is clear that the intermediate strain-rate eigenvalue (a_2) is highly likely to be positive, in agreement with the results of Kerr (1987) and Ashurst et al. (1987). The highest probability is around $a_2 \approx 0.15$ and $q \approx 0$. Furthermore, the intermediate strain-rate is likely to be more expansive in the strain-dominated streamlines than in the rotation-dominated streamlines.

4. a_2, r PDF (figure 3.4d): This figure suggests that a turbulent flow field is highly likely to have unstable topologies, i.e. diverging streamlines directed away from the critical point ($r > 0$), with expansive intermediate strain-rate ($a_2 > 0$). The peak value of the PDF occurs at $a_2 = 0$ and $r = 0$, which further indicates that nearly planar or two-dimensional local geometries are highly probable. The PDF contour value is high along the $a_2 = 2.17r$ line.
5. $a_2, |\cos\beta|$ PDF (figure 3.4e): The $a_2-|\cos\beta|$ plane has a rectangular realizable region with the kinematic bounds of $-1/\sqrt{6} \leq a_2 \leq 1/\sqrt{6}$ (from equation 3.37) and $0 \leq |\cos\beta| \leq 1$. This joint PDF reinforces the previous observations that the local streamlines in turbulence are most likely to have positive intermediate strain-rate while vorticity is most aligned with the intermediate strain-rate eigendirection.
6. $|\cos\beta|, r$ PDF (figure 3.4f): The top and bottom boundaries of this phase plane represent alignment and orthogonality of vorticity with intermediate strain-rate eigen vector. The left and right boundaries are obtained numerically from the DNS data set. The probability distribution is highly concentrated around $|\cos\beta| = 1, r = 0$ with a very high PDF value of 90 - maximum among all the phase spaces. This reaffirms that vorticity is most aligned with intermediate strain-rate eigen direction in nearly planar streamlines. The PDF value reduces nearly symmetrically with increase in r magnitude on either side of the $r = 0$ line.

The joint distributions of shape-parameters at $Re_\lambda = 385,588$ (not presented separately) are nearly identical to that of $Re_\lambda = 225$. Therefore, not only $q-r$, but all the other shape-parameters exhibit “universal” distributions in high Reynolds number turbulence.

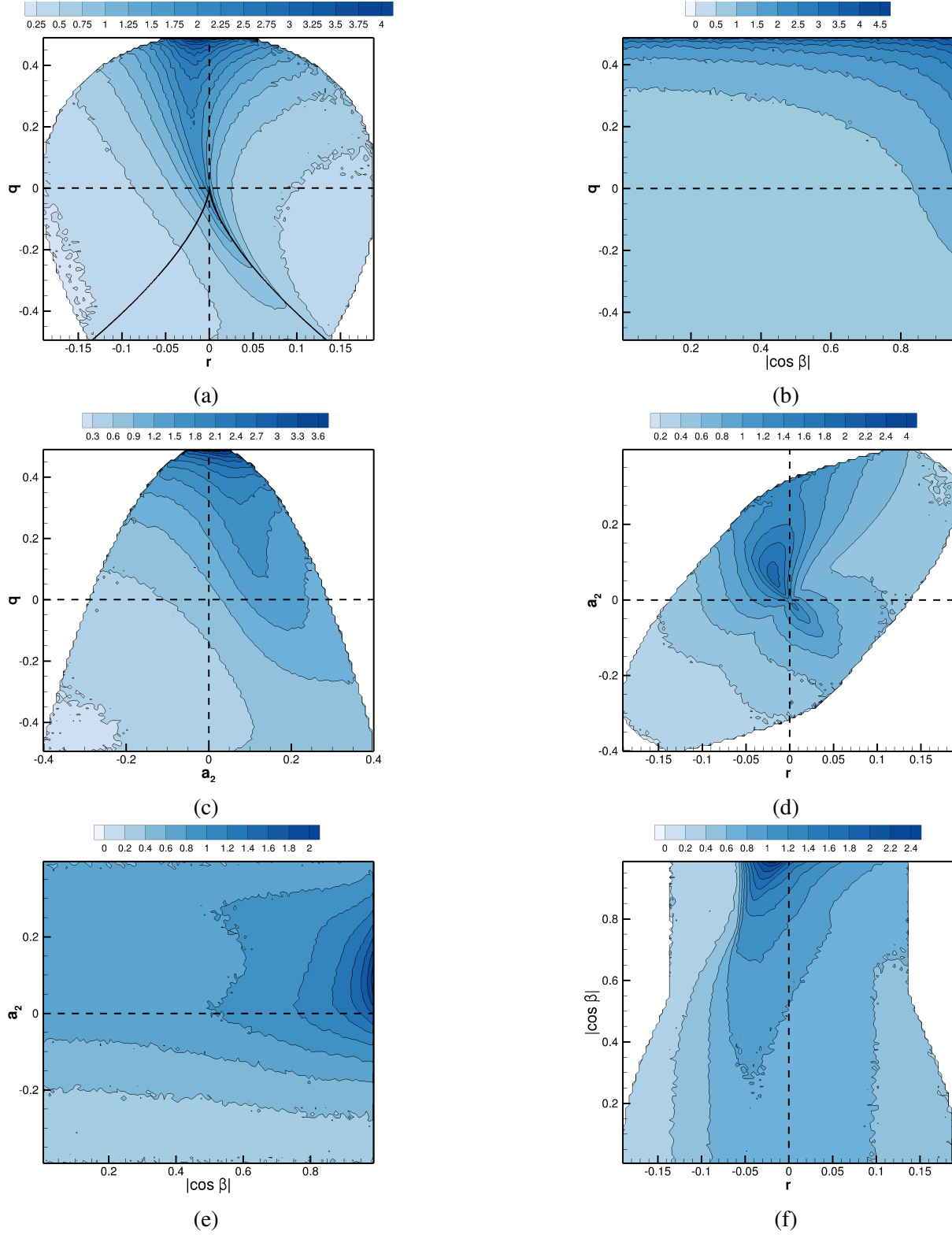


Figure 3.5: Conditional mean $\langle A^2|x, y \rangle / \langle A^2 \rangle$ in (a) $q-r$ ($x = r, y = q$) (b) $q-|\cos \beta|$ (c) $q-a_2$ (d) a_2-r (e) $a_2-|\cos \beta|$ (f) $|\cos \beta|-r$ planes for $Re_\lambda = 225$. Reprinted with permission from Das and Girimaji (2020a).

3.4.2 Scale-factor in shape-parameter space

The scale-factor of a given streamline shape is defined by the Frobenius norm of VG tensor, $A = \sqrt{A_{ij}A_{ij}}$, as shown in section 3.2.4. Higher magnitude A implies a smaller length-scale of the streamlines. Average VG magnitude squared $\langle A^2 \rangle$ increases monotonically with Reynolds number (Yeung et al., 2018; Buaria et al., 2019). Thus, scale-factor strongly depends on Reynolds number. The distribution of streamline geometric shape, on the other hand, is nearly invariant with Reynolds number (section 3.4.1). We now examine the dependence of scale-factor on shape. Figure 3.5 shows the conditional mean distribution of A^2 , normalized by global mean $\langle A^2 \rangle$, in the phase planes of shape-parameters. The primary observations from these figures are summarized below.

1. Figure 3.5 (a-c) indicates that the highest conditional mean VG magnitude or smallest scale-factor values occur when $q \approx 1/2$ (pure-rotation streamlines) and decreases progressively as q decreases.
2. Figure 3.5 (c-e) suggests that A^2 tends to be high when intermediate strain-rate eigenvalue is positive and in the range, $a_2 \in (0, 0.2)$.
3. VG magnitude is the highest when r is in the slightly negative range as shown in figure 3.5 (a,d,f). This represents stable converging streamlines directed towards the critical point.
4. Figure 3.5 (b,e,f) illustrates that conditional mean A^2 is the highest when $|\cos\beta| \approx 1$, i.e. vorticity is aligned with the intermediate strain-rate eigen direction. Furthermore, the VG magnitude tends to decrease monotonically with $|\cos\beta|$ provided $q > 0$, $a_2 > 0$ and r is slightly negative.
5. The conditional average in q - r plane (figure 3.5 a) further shows that in rotation-dominated streamlines ($q > 0$), A^2 is high along a curved line slightly to the left of the $r = 0$ line, representing nearly planar SFS streamlines. While in the strain-dominated streamline shapes

($q < 0$), A^2 is high along the right discriminant line, with a slight preference towards the sheet-like UN/S/S streamline shapes.

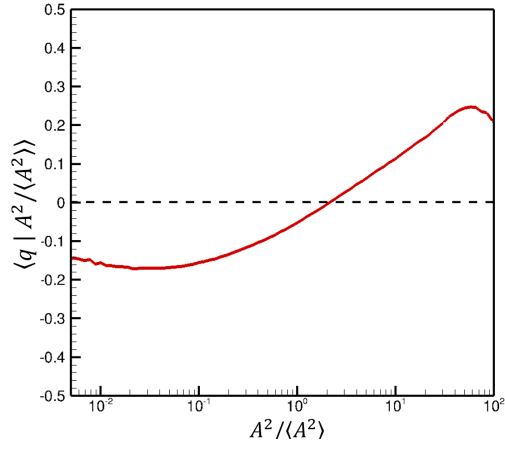
6. If $a_2 < 0$, then the VG magnitude increases monotonically with a_2 irrespective of vorticity-strainrate alignment (see figure 3.5 e).

For the sake of completeness, the conditional averages of the shape-parameters (q , r , a_2 and $|\cos\beta|$) are plotted as a function of scale-factor ($A^2/\langle A^2 \rangle$) in figure 3.6. These results succinctly summarize the above-mentioned findings: (a) $q > 0$ at high A^2 , (b) r has negligible variation with respect to magnitude, except for a slight tendency to be negative at high A^2 , (c) a_2 exhibits a small positive conditional average at nearly all magnitudes, and (d) $\vec{\omega}$ is most aligned with intermediate strain-rate eigenvector at high A^2 .

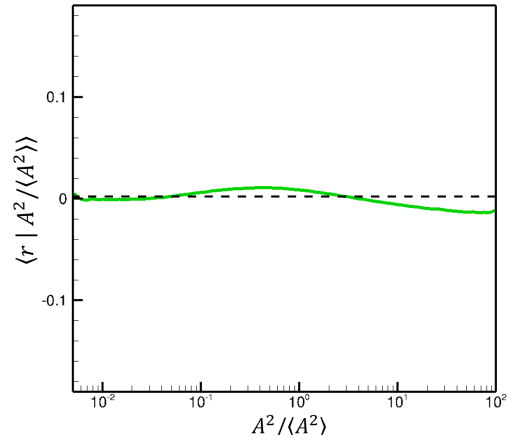
3.4.3 Projection of geometric-shape on q - r plane

It is of interest to examine the internal alignment properties as a function of the invariants. The conditional mean intermediate strain-rate eigenvalue (a_2) in the q - r plane (figure 3.7 a) shows that a_2 is strongly positive along the densely populated right discriminant line, resulting in a positive global average of a_2 (Ashurst et al., 1987). In the nodal streamline region of the q - r plane, a_2 shows negligible dependence on q and a monotonic increase with r . At any q value, a_2 is minimum (most negative) along the left boundary and maximum (most positive) along the right boundary of the plane. As mentioned before, minimum a_2 for a given q implies that a_1 is maximum for that q . Thus, the left boundary represents SFS streamlines with the maximum possible expansive strain-rate a_1 . Similarly, the right boundary of the q - r plane represents UFC streamlines with the maximum possible compressive strain-rate a_3 .

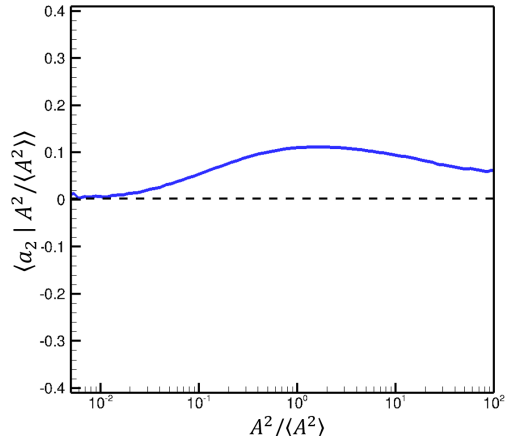
As shown in section 3.2.6, the vorticity vector ($\vec{\omega}$) is aligned with the most expansive strain-rate eigenvector at the left boundary and with the most compressive strain-rate eigenvector at the right boundary (figure 3.7 b). The conditional mean $|\omega_1|$ and $|\omega_3|$ in the q - r plane (not presented) for the DNS datasets further reaffirms this result. Thus, *the left boundary of the q - r plane represents orthogonal stretching of stable spiral and the right boundary represents orthogonal compression*



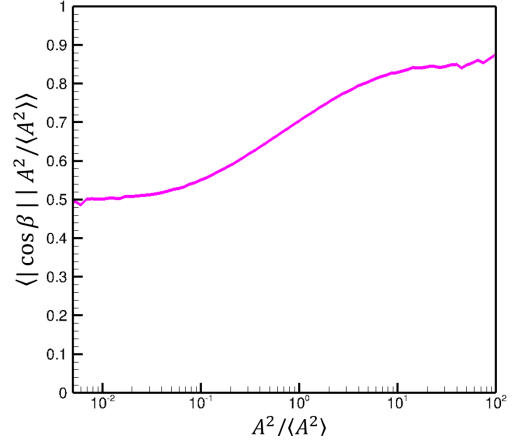
(a)



(b)



(c)



(d)

Figure 3.6: Conditional average of shape-parameters (a) q , (b) r , (c) a_2 and (d) $|\cos\beta|$ conditioned on VG magnitude ($A^2/\langle A^2 \rangle$) for $Re_\lambda = 225$ case. The x-axes are in log-scale and the y-axes are limited by the kinematic bounds of the corresponding shape parameter. Reprinted with permission from Das and Girimaji (2020a).

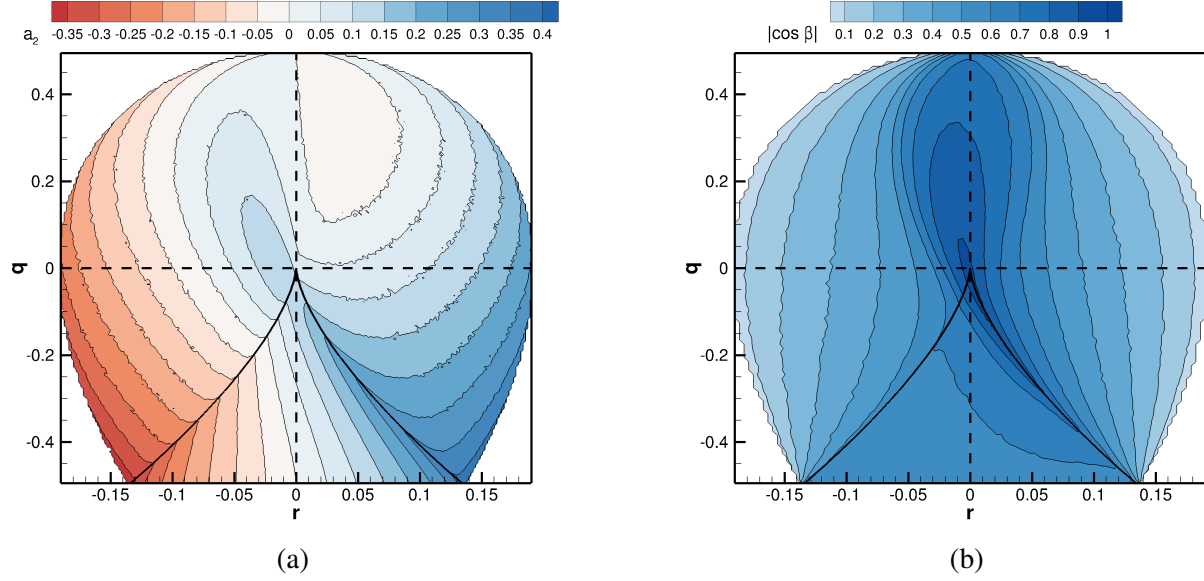


Figure 3.7: Conditional average of (a) intermediate strain-rate: $\langle a_2 | q, r \rangle$ and (b) angle of alignment between vorticity and intermediate strain-rate eigenvector: $\langle |\cos \beta| | q, r \rangle$. Reprinted with permission from Das and Girimaji (2020a).

of unstable spiral.

Figure 3.7 (b) further shows that $\vec{\omega}$ is most likely to be aligned with the intermediate strain-rate direction in the region around $r = 0$ line for $q > 0$ and along the densely populated right discriminant line for $q < 0$. Assuming perfect alignment along the right $d = 0$ line, i.e.

$$\omega_2 \approx \sqrt{\frac{1}{4} + \frac{q}{2}} \quad \text{when} \quad r^2 + \frac{4}{27}q^3 = 0, \quad q \leq 0 \quad (3.47)$$

and solving equations (3.29) and (3.30), we obtain the following solution for a_2 along the right $d = 0$ line,

$$a_2 \approx \sqrt{-q/3} \quad (3.48)$$

This analytical expression of a_2 agrees reasonably well with the conditional mean a_2 values along the right $d = 0$ line in figure 3.7 (a).

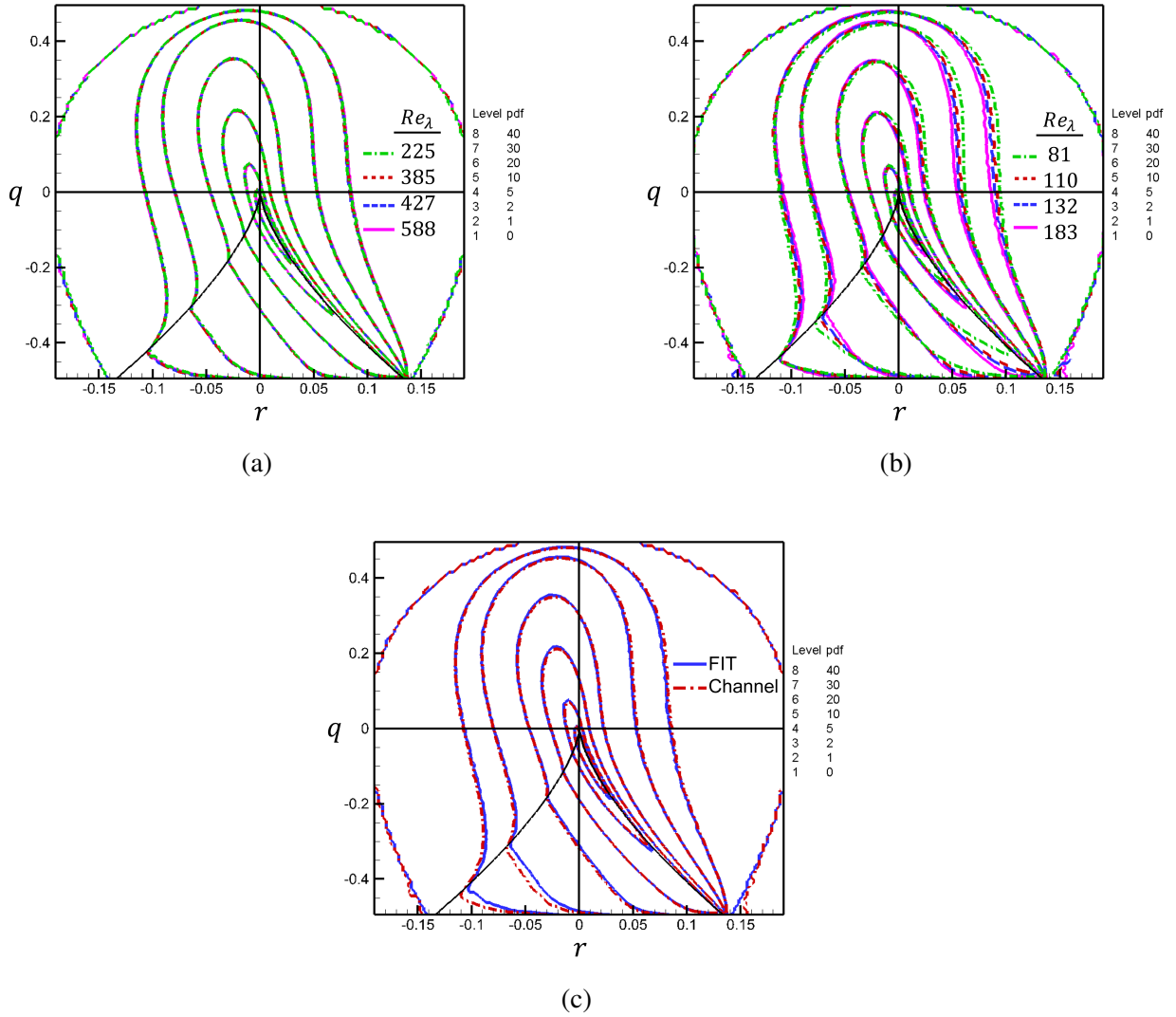


Figure 3.8: Isocontour lines of q - r joint PDF of (a) forced isotropic turbulent (FIT) flow at $Re_\lambda = 225, 385, 427, 588$, (b) turbulent channel flow at $Re_\lambda = 81, 110, 132, 183$, and (c) FIT at $Re_\lambda = 225$ and turbulent channel flow at $Re_\lambda = 183$.

3.4.4 Universality of geometric shape

It is evident from the previous subsection that both a_2 and ω_2 have a unique trend in the q - r plane, which is similar in a broad range of Reynolds number. Therefore, we expect to be able to express a_2 and ω_2 as approximate functions of (q, r) . In doing so, we reduce the overall shape-parameter space to only two dimensions, i.e. q, r phase plane. We now test the universality of geometric shape in different types of turbulent flows - forced isotropic turbulence and turbulent channel flow - at different Reynolds numbers. The q - r joint PDFs of forced isotropic turbulence at $Re_\lambda = 225, 385, 427$ and 588 are plotted in figure 3.8(a). These joint PDFs are nearly invariant with Re_λ . The q - r joint PDFs for turbulent channel flow at different y^+ locations, corresponding to $Re_\lambda = 81, 110, 132$ and 183 , are shown in figure 3.8(b). In this case, the PDF has a slight dependence on Reynolds number. However, the variation is very negligibly small. The q - r joint PDFs of forced isotropic turbulence and turbulent channel flow at the closest available Reynolds numbers ($Re_\lambda = 225$ & 183 , respectively) are compared in figure 3.8(c). Clearly, the q - r joint PDFs of the two different types of turbulent flows are nearly identical, particularly in the densely populated regions of the plane. This result is a strong evidence of universality of small-scale geometry in turbulent flows at sufficiently high Reynolds numbers.

3.5 Summary and conclusions

The study provides a description of the local streamline geometry by separating geometric-shape and scale-factor of the streamlines and characterizes their statistics in turbulent flows. This work is composed of two parts. In the first part, a complete description of the local streamline geometry is developed in terms of geometric-shape and scale-factor. It is established that the normalized VG tensor b_{ij} completely determines the streamline shape while the scale of the streamline structure depends on VG magnitude A (inversely). Geometric-shape is characterized by only four shape-parameters - q, r, a_2 and $|\omega_2|$. The study further demonstrates that the frame-invariant shape-parameters q and r constitute a bounded phase-space with unique specification of streamline shape and therefore, provide a useful platform to study VG dynamics.

In the second part of this work, DNS data of forced isotropic turbulence is employed to investigate the statistical distribution of streamline shape and scale features in turbulence. It is demonstrated that the probability distribution of local streamline shape in this four-dimensional shape-parameter space is invariant with Reynolds number for $Re_\lambda > 200$. The PDFs reaffirm that the streamlines are most likely to have positive intermediate strain-rate and vorticity aligned with the intermediate strain-rate eigen direction. Furthermore, DNS data reveals that the VG magnitude is highest (streamline scale-factor is smallest) in stable streamlines undergoing nearly pure rotation with vorticity vector along positive intermediate strain-rate. Finally, the comparison between the q - r joint PDFs of isotropic turbulence as well as turbulent channel flow, reveals the universality of small-scale geometry across different types of turbulent flows at sufficiently high Reynolds numbers.

4. TRIPLE DECOMPOSITION OF VELOCITY GRADIENT TENSOR INTO SHEAR, ROTATION, AND NORMAL STRAIN

4.1 Introduction

The velocity gradient (VG) dynamics and small-scale behavior of turbulence have largely been investigated in literature by decomposing the velocity gradient tensor ($A_{ij} = \partial u_i / \partial x_j$) into symmetric (strain-rate tensor, S_{ij}) and anti-symmetric (rotation-rate or vorticity tensor, W_{ij}) parts:

$$A_{ij} = S_{ij} + W_{ij} \quad \text{where} \quad S_{ij} = \frac{1}{2}(A_{ij} + A_{ji}), \quad W_{ij} = \frac{1}{2}(A_{ij} - A_{ji}) \quad (4.1)$$

This decomposition has led to important insight into small-scale intermittency (Sreenivasan and Antonia, 1997; Yeung et al., 2018; Buaria et al., 2019), intense structures in turbulence (Sanada et al., 1991; Hosokawa et al., 1997; Jimenez and Wray, 1998; Moisy and Jiménez, 2004) and local streamline geometry (Ashurst et al., 1987; Kerr, 1987; Lüthi et al., 2009). However, recent studies (Kolář, 2007; Gao and Liu, 2019; Nagata et al., 2019) have shown that strain-rate and vorticity do not clearly identify the presence of normal-straining and rigid-body-rotation of the fluid. The presence of shear in both strain-rate and vorticity often obscures our understanding of some of the fundamental phenomena in turbulence. The purpose of this work is to revisit some of the prominent results of small-scale turbulence by segregating the role of normal-strain, shear and pure rotation in fluid motions. Reinterpretation of the classical results leads to further clarity and deeper insight into velocity gradient behavior in turbulence.

The triple decomposition in this study partitions the local velocity gradients into three elementary constituent transformations - normal strain, rigid-body-rotation and pure shear (figure 4.1). The normal strain-rate tensor N_{ij} is a diagonal tensor that represents the compression and extension

Reprinted with permission from: Das, R., and Girimaji, S. S. (2020). Revisiting turbulence small-scale behavior using velocity gradient triple decomposition. *New Journal of Physics*, 22(6), 063015. Copyright 2021 IOP Publishing. (Das and Girimaji, 2020b)

of the fluid element in different directions in a volume-preserving manner. The rigid-body-rotation tensor R_{ij} is an anti-symmetric tensor that represents pure-rotation of the fluid element by a certain angular velocity. The shear tensor H_{ij} is a lower triangular tensor containing the transverse gradients of velocity components that represent shearing of the fluid element.

Kolář (2007) presented a procedure for triple decomposition of the VG tensor by extracting the pure-shearing motion from the swirling action of vorticity. The method comprises of determination of a so-called basic reference frame among all possible frame rotations, which is computationally very expensive for a three-dimensional flow field. This technique has been used for vortex-structure identification and investigation of internal shear layers in wall-bounded flows (Eisma et al., 2015; Šístek et al., 2012; Maciel et al., 2012). It has recently been used for investigating regions of strong shearing or rotation and detecting internal shear layer in homogeneous isotropic turbulence at Taylor Reynolds numbers, $Re_\lambda = 27$ and 140 (Nagata et al., 2019). Aside from Kolář’s method, Gao and Liu (2019) formulated a “Rortex”-based VG tensor decomposition for locally fluid-rotational points (VG tensor has complex eigenvalues) in a turbulent flow field. This method (Tian et al., 2018) of separating the rigid-body-rotation (Rortex) from shear in vorticity is computationally more viable and has been employed in some studies (Dong et al., 2019; Li et al., 2019; Gui et al., 2019; Arun et al., 2019) for investigation of coherent vortex structures in turbulent flows. In another recent study, Keylock (2017) presented a decomposition of the VG tensor into normal and non-normal tensors such that the non-normal counterpart represents the local effects of shear.

The goal of this study is to examine velocity gradient statistics in turbulence using the decomposition of VG tensor into normal-strain-rate, rigid-body-rotation and pure-shear tensors. We revisit certain important velocity gradient behavior and characterize them in terms of N_{ij} , R_{ij} and H_{ij} . The specific objectives of this study are as follows:

1. Develop a triple decomposition strategy valid for the entire flow field by combining the above-mentioned proposals of Gao and Liu (2019) and Keylock (2017) and derive important kinematic characteristics of the various constituents.
2. Characterize the local streamline shapes in terms of normal-strain, pure-shear and rigid-

body-rotation tensors in the phase space of VG tensor invariants.

3. Establish the contribution of different velocity gradient constituents in a turbulent flow field as a function of Reynolds number. Recall that the average strain-rate and vorticity contributions are approximately equal in an isotropic flow field.
4. Examine the velocity gradient constituents conditioned on magnitude at high Reynolds numbers to gain insight into intermittency. It is generally believed that vorticity magnitude or enstrophy is more intermittent than strain-rate magnitude or dissipation (Yeung et al., 2018; Buaria et al., 2019).
5. Analyze the behavior of the pressure field as a function of the velocity gradient constituents.
6. Examine the alignment properties of the local rigid-body-rotation axis.

The triple decomposition presented in the study can further our understanding of several aspects of velocity gradient dynamics in turbulent flows: (i) the local-structure of flow field in regions of intermittency; (ii) clear distinction between solid-body rotation and vorticity; and (iii) relation between pressure and velocity gradient fluctuations. Such understanding is of intrinsic scientific value and can also lead to improved modeling of sub-grid constitutive relations, material element deformation (Orszag, 1970a; Girimaji and Pope, 1990b) and mixing enhancement (Ottino et al., 1989; Ottino, 1990; Girimaji, 1994; Danish et al., 2016).

The next section of this work outlines the procedure for triple decomposition of VG tensor, followed by a comprehensive description of the properties of its constituents and its implication in local streamline geometry. In the third section, details about the DNS datasets of forced isotropic turbulence are briefly discussed. The results are illustrated in the fourth section – velocity gradient composition of a turbulent flow field is examined in detail along with its Reynolds number dependence, followed by investigation of the pressure field conditioned on velocity gradient constituents and examination of the alignment properties of the rotation axis in high Reynolds number turbulence. Finally, the important findings of this study are summarized in the conclusions section.

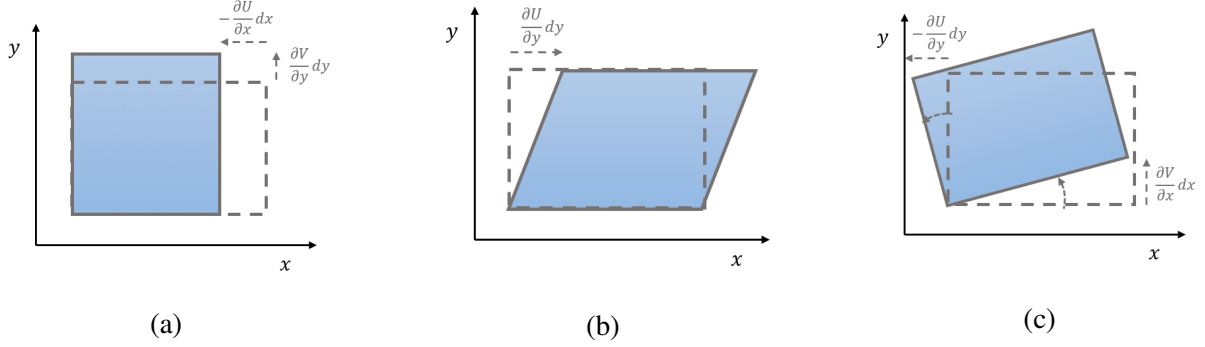


Figure 4.1: Two-dimensional example of fluid element deformation due to (a) normal-strain-rate tensor, (b) shear tensor, and (c) rigid-body-rotation tensor. Reprinted with permission from Das and Girimaji (2020b).

4.2 Triple decomposition of VG tensor

The additive decomposition of the VG tensor (\mathbf{A}) into normal-strain-rate tensor (\mathbf{N}), pure-shear tensor (\mathbf{H}) and rigid-body-rotation-rate tensor (\mathbf{R}) is given by

$$A_{ij} = N_{ij} + H_{ij} + R_{ij} \quad (4.2)$$

The N_{ij} , H_{ij} and R_{ij} tensors represent normal-straining, pure-shearing and rigid-body-rotation of a fluid element, respectively. These transformations are illustrated with some elementary examples in figure 4.1 for reference. The decomposition entails considerable level of effort and the technique is different for a fluid element undergoing rigid-body-rotation ($\mathbf{R} \neq 0$) and one that has no rotation component ($\mathbf{R} = 0$). The former is called local fluid rotational while the latter is referred to as local fluid non-rotational (Tian et al., 2018) in the rest of this work. In this section, we first outline the decomposition procedure for the two cases. Then we proceed to establish the kinematic properties of the constituent tensors, including the streamline shapes of local fluid motion corresponding to each tensor.

4.2.1 Decomposition procedure

If \mathbf{A} has two complex conjugate eigenvalues ($\lambda_{cr} \pm i\lambda_{ci}$) and one real eigenvalue (λ_r), then it represents locally rotational flow. On the other hand, if \mathbf{A} has only real eigenvalues ($\lambda_1, \lambda_2, \lambda_3$), it implies that the flow is locally non-rotational. Our procedure combines two different proposals in literature for rotational and non-rotational parts of the flow field. The procedure of VG tensor decomposition for both the cases are now discussed in detail.

4.2.1.1 Rotational case

For the rotational case, we follow the VG tensor decomposition procedure outlined by Gao and Liu (2019). This method involves two coordinate-frame rotations to obtain the VG tensor in the desired lower block triangular form for decomposition. The steps are listed below:

1. First we identify the rotation axis (\vec{r}), which is the eigenvector of the real eigenvalue of \mathbf{A} . Then the coordinate frame is rotated such that the Z-axis of the new frame is aligned with \vec{r} . The VG tensor in this new coordinate frame is given by

$$\mathbf{A}' = \mathbf{Q}\mathbf{A}\mathbf{Q}^T \quad (4.3)$$

where, \mathbf{Q} is a proper rotation matrix obtained from real Schur decomposition of \mathbf{A} as shown by Liu et al. (2018).

2. Next, the coordinate frame is further rotated about the Z-axis, i.e. in the XY-plane, by an azimuthal angle θ . This angle θ is chosen such that the angular velocity of the fluid is minimum. The VG tensor in this new coordinate frame (\mathbf{A}^*) is then given by

$$\mathbf{A}^* = \mathbf{P}\mathbf{A}'\mathbf{P}^T \quad \text{where} \quad \mathbf{P} = \begin{bmatrix} \cos \theta & \sin \theta & 0 \\ -\sin \theta & \cos \theta & 0 \\ 0 & 0 & 1 \end{bmatrix} \quad (4.4)$$

is also a proper rotation matrix.

These steps result in the VG tensor in a rotated coordinate frame such that it is of the form

$$\mathbf{A}^* = \begin{bmatrix} \lambda_{cr} & -\phi & 0 \\ \phi + s_3 & \lambda_{cr} & 0 \\ s_2 & s_1 & \lambda_r \end{bmatrix} \quad (4.5)$$

The VG tensor is then decomposed into the following constituent tensors,

$$\mathbf{A}^* = \mathbf{N} + \mathbf{H} + \mathbf{R} \quad \text{where}$$

$$\mathbf{N} = \begin{bmatrix} \lambda_{cr} & 0 & 0 \\ 0 & \lambda_{cr} & 0 \\ 0 & 0 & \lambda_r \end{bmatrix}, \quad \mathbf{H} = \begin{bmatrix} 0 & 0 & 0 \\ s_3 & 0 & 0 \\ s_2 & s_1 & 0 \end{bmatrix}, \quad \mathbf{R} = \begin{bmatrix} 0 & -\phi & 0 \\ \phi & 0 & 0 \\ 0 & 0 & 0 \end{bmatrix} \quad (4.6)$$

We define \mathbf{N} as the normal-strain-rate tensor, which is a diagonal tensor containing the real parts of eigenvalues of VG tensor. Here, λ_{cr} is the real part of the complex conjugate eigenvalues of \mathbf{A} and λ_r is the only real eigenvalue of \mathbf{A} . The tensor \mathbf{N} represents the normal compression and expansion of the fluid element along different directions. It must be noted that the volume of the fluid element is preserved. Incompressibility imposes the following condition:

$$\lambda_r = -2\lambda_{cr} \quad (4.7)$$

The tensor \mathbf{H} represents the pure shearing deformation of the fluid element. The shear tensor is a lower triangular tensor with three elements - s_1 , s_2 and s_3 - that constitute the transverse gradients of velocity components. The s_3 component represents shearing within the plane of rigid-body-rotation and is non-negative by definition (Gao and Liu, 2019). Moreover, the eigenvalues of such a tensor are zero. Finally, the rigid-body-rotation tensor \mathbf{R} is an anti-symmetric tensor depending on only one unknown, ϕ . The tensor represents pure-rotation of the fluid element with an angular

velocity given by ϕ . The rotational strength is defined as twice the value of this angular velocity of the fluid element ($\tilde{R} \equiv 2\phi$). The rotation axis, \vec{r} , lies along the axial vector of the rigid-body-rotation tensor. Thus, the Rortex vector is given by (Gao and Liu, 2019),

$$\vec{R} = \tilde{R}\vec{r} = 2\phi\vec{r} \quad (4.8)$$

The rigid-body-rotation tensor has one zero and two purely imaginary eigenvalues ($\pm i\phi$). Note that this additive triple decomposition of the VG tensor is in the principal frame of the normal-strain-rate tensor.

4.2.1.2 Non-rotational case

In this case, we use Schur decomposition to segregate the normal-strain-rate tensor from the shear tensor, as the rigid-body-rotation is identically zero. In a previous study, Keylock (2017) segregated the effect of shear from the VG tensor by performing complex Schur decomposition, which however results in complex component tensors. In this study, we use real Schur decomposition for locally non-rotational points in the flow. Since \mathbf{A} contains only real eigenvalues in this case, it can be transformed into an upper triangular tensor by real Schur decomposition:

$$\mathbf{A}^\dagger = \mathbf{Q}^{*T} \mathbf{A} \mathbf{Q}^* \quad (4.9)$$

such that \mathbf{A}^\dagger is a real upper triangular tensor which can now be decomposed into a diagonal (normal) tensor and a strictly upper-triangular (non-normal) tensor. Here, \mathbf{Q}^* is an orthogonal matrix responsible for coordinate transformation of the VG tensor from \mathbf{A} to \mathbf{A}^\dagger . In order to be consistent with the lower triangular form of the shear tensor obtained in the triple decomposition method for the rotational case, we perform real Schur decomposition of the VG tensor transpose (\mathbf{A}^T)

$$\mathbf{A}^{**} = \mathbf{Q}^T \mathbf{A}^T \mathbf{Q} \quad (4.10)$$

Then, the transpose of the resulting tensor yields

$$\mathbf{A}^* = \mathbf{A}^{**T} = \mathbf{Q}^T \mathbf{A} \mathbf{Q} \quad (4.11)$$

where \mathbf{A}^* is the Schur decomposition of \mathbf{A} in lower triangular form. Now, the VG tensor can be decomposed into the following normal and non-normal tensors

$$\mathbf{A}^* = \mathbf{N} + \mathbf{H} \quad \text{where}$$

$$\mathbf{N} = \begin{bmatrix} \lambda_1 & 0 & 0 \\ 0 & \lambda_2 & 0 \\ 0 & 0 & \lambda_3 \end{bmatrix}, \quad \mathbf{H} = \begin{bmatrix} 0 & 0 & 0 \\ s_3 & 0 & 0 \\ s_2 & s_1 & 0 \end{bmatrix} \quad (4.12)$$

Here, \mathbf{N} is the normal tensor, i.e. a diagonal tensor containing the eigenvalues of \mathbf{A} . It is therefore referred to as the normal-strain-rate tensor and reflects the compression and expansion that the fluid element undergoes along different directions. In order to ensure that the VG tensor decomposition is unique, the ordering of diagonal elements of the normal-strain-rate tensor is fixed to $\lambda_1 \geq \lambda_2 \geq \lambda_3$. This tensor consists of only two unknowns due to the incompressibility condition,

$$\lambda_1 + \lambda_2 + \lambda_3 = 0 \quad (4.13)$$

The lower triangular tensor \mathbf{H} is the non-normal tensor containing information about the eigenvectors of \mathbf{A} . This tensor consists of three independent elements representing shearing of the fluid element in three orthogonal planes and is therefore, referred to as the shear tensor.

The VG tensor decomposition in both rotational and non-rotational cases are considered in the principal frame of \mathbf{N} . In the remaining sections of this work, the VG tensor will be used in this coordinate frame for convenience and will be represented by \mathbf{A} . The results presented in this study are frame invariant and do not depend on the coordinate frame of reference.

4.2.2 Properties of VG tensor constituents

The shear tensor can be further divided into symmetric (\mathbf{H}_S) and anti-symmetric (\mathbf{H}_W) counterparts:

$$\mathbf{H}_S = \frac{1}{2}(\mathbf{H} + \mathbf{H}^T) \quad \text{and} \quad \mathbf{H}_W = \frac{1}{2}(\mathbf{H} - \mathbf{H}^T) \quad (4.14)$$

The symmetric-shear tensor along with the normal-strain-rate tensor recovers the strain-rate tensor while the anti-symmetric-shear tensor along with the rigid-body-rotation tensor constitutes the rotation-rate or vorticity tensor, i.e.

$$\mathbf{S} = \mathbf{N} + \mathbf{H}_S \quad \text{and} \quad \mathbf{W} = \mathbf{H}_W + \mathbf{R} \quad (4.15)$$

It is evident that shear contributes to vorticity as well as strain-rate. In this subsection, we first describe the composition of velocity gradient magnitude based on the VG tensor decomposition. Next, we characterize the local streamline shape associated with each of these velocity gradient constituents in the phase plane of VG tensor invariants.

4.2.2.1 Composition of velocity gradient magnitude

In terms of strain-rate and rotation-rate, velocity gradient magnitude (Frobenius norm squared: $A^2 = A_{ij}A_{ij}$) can be written as:

$$A^2 = S^2 + W^2 \quad (4.16)$$

where $S^2 = S_{ij}S_{ij}$ is strain-rate magnitude related to dissipation (νS^2) and $W^2 = W_{ij}W_{ij}$ is vorticity magnitude or enstrophy. The triple decomposition of VG tensor results in the following expression for magnitude:

$$A_{ij}A_{ij} = N_{ij}N_{ij} + H_{ij}H_{ij} + R_{ij}R_{ij} + 2R_{ij}H_{ij} \quad (4.17)$$

which can be restated as

$$A^2 = N^2 + H^2 + R^2 + 2RH \quad (4.18)$$

where $N^2 = N_{ij}N_{ij}$, $H^2 = H_{ij}H_{ij}$ and $R^2 = R_{ij}R_{ij}$ are defined as the magnitudes (Frobenius norm squared) of normal-strain-rate, shear and rigid-body-rotation tensors, respectively. For locally fluid rotational case (equations 4.6 and 4.7), these are of the form

$$N^2 = 6\lambda_{cr}^2 \quad , \quad H^2 = s_1^2 + s_2^2 + s_3^2 \quad , \quad R^2 = 2\phi^2 \quad (4.19)$$

and for the fluid non-rotational case (equations 4.12 and 4.13), these constituent magnitudes are of the form

$$N^2 = 2(\lambda_1^2 + \lambda_2^2 + \lambda_1\lambda_2) \quad , \quad H^2 = s_1^2 + s_2^2 + s_3^2 \quad , \quad R^2 = 0 \quad (4.20)$$

The term $RH = R_{ij}H_{ij}$ is defined as the correlation term between the \mathbf{R} and \mathbf{H} tensors. The other possible correlation terms such as $N_{ij}H_{ij}$ and $N_{ij}R_{ij}$ are identically zero since \mathbf{N} is a diagonal matrix while both \mathbf{H} and \mathbf{R} are hollow matrices (all diagonal elements are zero). Using equation (4.6) it can be shown that the shear-rotation correlation term, which exists only if the flow is locally rotational, is given by,

$$2RH = 2R_{ij}H_{ij} = 2\phi s_3 \quad (4.21)$$

Therefore, the shear-rotation correlation term contributing to velocity gradient (VG) magnitude depends only on the rigid-body-rotation strength (2ϕ) and the component of shear that is in the plane of rigid-body-rotation (s_3). Since both ϕ and s_3 are non-negative (Gao and Liu, 2019) by definition, $2RH \geq 0$.

In order to measure the contribution of each component toward VG magnitude, we normalize these magnitudes by the local VG magnitude

$$n^2 \equiv \frac{N^2}{A^2} \quad , \quad h^2 \equiv \frac{H^2}{A^2} \quad , \quad r^2 \equiv \frac{R^2}{A^2} \quad , \quad 2rh \equiv \frac{2RH}{A^2} \quad (4.22)$$

Then, the normalized normal-strain, shear and rigid-body-rotation magnitudes have the following bounds,

$$0 \leq n^2 \leq 1 \quad , \quad 0 \leq h^2 \leq 1 \quad , \quad 0 \leq r^2 \leq 1 \quad (4.23)$$

It can be shown using equation (4.6) that the normalized correlation term $2rh$ have more restricted bounds, i.e.

$$0 \leq 2rh \leq \frac{1}{\sqrt{2}+1} \approx 0.41 \quad (4.24)$$

A detailed proof of the above result is included in Appendix B.

As shown previously in equation (4.15), the shear tensor contributes to both \mathbf{S} as well as \mathbf{W} in the form of its symmetric (\mathbf{H}_S) and anti-symmetric (\mathbf{H}_W) counterparts, respectively. Since the shear tensor is a lower triangular tensor, the symmetric-shear and anti-symmetric-shear tensors are of the form

$$\mathbf{H}_S = \begin{bmatrix} 0 & s_3/2 & s_2/2 \\ s_3/2 & 0 & s_1/2 \\ s_2/2 & s_1/2 & 0 \end{bmatrix} \quad \text{and} \quad \mathbf{H}_W = \begin{bmatrix} 0 & -s_3/2 & -s_2/2 \\ s_3/2 & 0 & -s_1/2 \\ s_2/2 & s_1/2 & 0 \end{bmatrix} \quad (4.25)$$

The magnitudes of \mathbf{H}_S and \mathbf{H}_W are equal since,

$$H_S^2 = H_W^2 = \frac{1}{2}(s_1^2 + s_2^2 + s_3^2) = \frac{H^2}{2} \quad (4.26)$$

Therefore, the shear-magnitude H^2 is divided equally between strain-rate and vorticity magnitudes.

From equation (4.15) and equation (4.26), we then obtain

$$S^2 = N^2 + \frac{H^2}{2} \quad , \quad W^2 = R^2 + 2RH + \frac{H^2}{2} \quad (4.27)$$

It may be noted that vorticity has an additional dependence on shear via the shear-rotation correlation term.

The occurrence of extreme values of A^2 is critical in the investigation of turbulence intermittency. The primary goal of this study is to examine the contribution of normal-strain-rate, shear and rigid-body-rotation towards the overall VG magnitude and its relation with the pressure field.

4.2.2.2 Invariants and local streamline geometry

In this subsection, we revisit local streamline topology and geometry using triple decomposition of VG tensor. The topology of local streamlines in incompressible turbulent flows is defined by the second and third invariants of VG tensor as proposed by Chong et al. (1990),

$$Q_A = -\frac{1}{2}A_{ij}A_{ji}, \quad R_A = -\frac{1}{3}A_{ij}A_{jk}A_{ki} \quad (4.28)$$

In the fluid rotational case, the invariants can be expressed in terms of VG tensor constituents (applying equations 4.6 and 4.7) as follows,

$$\begin{aligned} Q_A &= -3\lambda_{cr}^2 + \phi^2 + \phi s_3 = \frac{1}{2}(R^2 + 2RH - N^2) \\ R_A &= 2\lambda_{cr}(\lambda_{cr}^2 + \phi^2 + \phi s_3) = \lambda_{cr}\left(\frac{N^2}{3} + R^2 + 2RH\right) \end{aligned} \quad (4.29)$$

It is important to note here that the invariants do not depend on the components of shear outside the plane of rigid body rotation, i.e. s_1 and s_2 . Therefore, the topology of locally rotational streamlines can be expressed as a function of normal-strain-rate eigenvalues, rigid-body-rotation strength and the component of shear within the plane of rigid-body-rotation. The invariants of each of the constituent tensor (\mathbf{N} , \mathbf{R} and \mathbf{H}) are given by,

$$\begin{aligned} Q_N &= -3\lambda_{cr}^2, \quad Q_R = \phi^2, \quad Q_H = 0 \\ R_N &= -2\lambda_{cr}^3, \quad R_R = 0, \quad R_H = 0 \end{aligned} \quad (4.30)$$

In the fluid non-rotational case (applying equations 4.12 and 4.13), the VG tensor invariants are given by

$$\begin{aligned} Q_A &= -(\lambda_1^2 + \lambda_2^2 + \lambda_1\lambda_2) = -\frac{N^2}{2} \\ R_A &= \lambda_1\lambda_2(\lambda_1 + \lambda_2) = -\lambda_1\left(\frac{N^2}{2} - \lambda_1^2\right) \end{aligned} \quad (4.31)$$

In this case, both Q_A and R_A are functions of only the normal-strain-rate tensor and do not depend on the shear tensor at all. In fact, invariants of the constituent tensors \mathbf{N} and \mathbf{H} are given by

$$\begin{aligned} Q_N &= Q_A, & Q_H &= 0 \\ R_N &= R_A, & R_H &= 0 \end{aligned} \tag{4.32}$$

Therefore, the topology of locally non-rotational streamlines depends only on the normal strain-rate tensor.

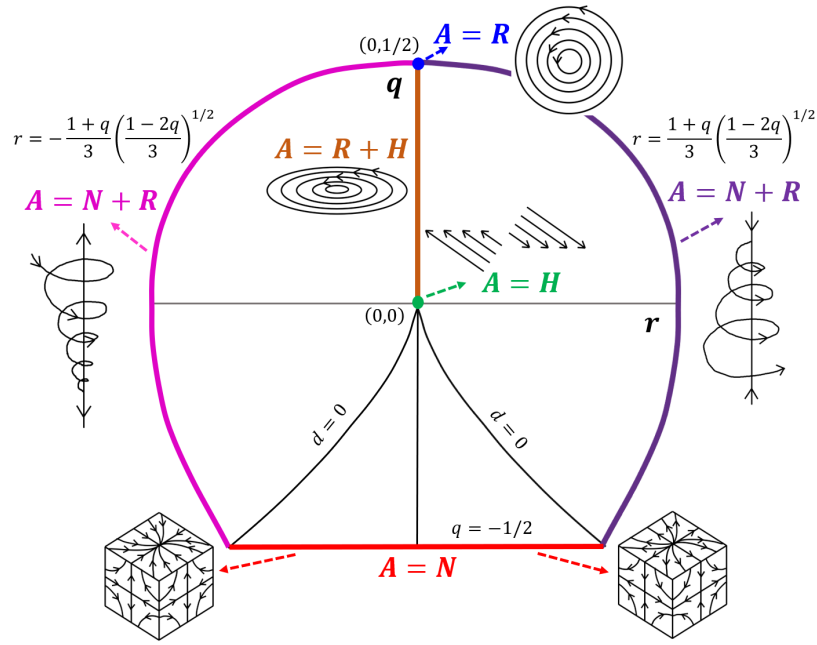
Topology, however, only provides information about the connectivity of a geometric shape. The complete geometric shape, as shown by Das and Girimaji (2019, 2020a), is better represented in the bounded phase space of normalized VG tensor invariants given by,

$$q = \frac{Q_A}{A^2}, \quad r = \frac{R_A}{(A^2)^{\frac{3}{2}}} \tag{4.33}$$

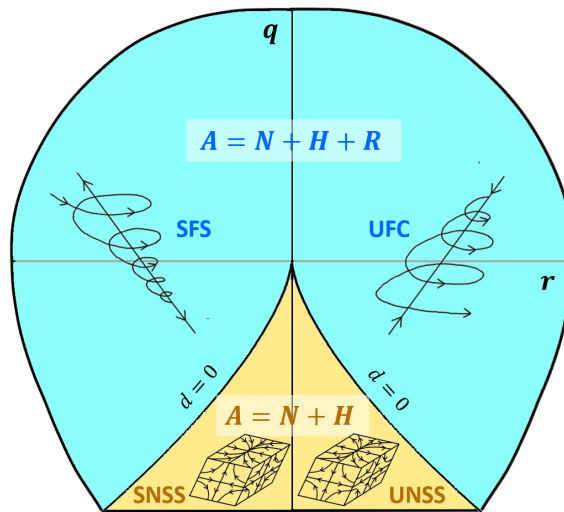
Note that these normalized invariants depend on all the shear components due to the normalization. Thus, shear might not be as critical in determining the topology of the local flow but it is important in determining its complete geometric shape. We now examine the shape of the local streamline geometry associated with the different velocity gradient tensor components \mathbf{N} , \mathbf{H} and \mathbf{R} in the q - r plane.

Degenerate geometries: These are the limiting cases, illustrated in figure 4.2 (a), that represent a point or a line in the q - r plane. These degenerate shapes are discussed below:

1. Pure-rotation ($\mathbf{A} = \mathbf{R}; \mathbf{N} = \mathbf{H} = 0$): The top-most point in the plane ($r = 0, q = 1/2$) represents an anti-symmetric VG tensor with one zero and two purely imaginary eigenvalues. This results in pure rigid-body-rotation of the fluid element or locally planar circular streamlines.
2. Pure-shear ($\mathbf{A} = \mathbf{H}; \mathbf{N} = \mathbf{R} = 0$): The lower triangular tensor \mathbf{H} has zero second and third invariants by its definition. Therefore, the origin of the q - r plane represents pure shearing of the fluid element.



(a)



(b)

Figure 4.2: Local streamline shapes and composition of VG tensor in different points/regions of the q - r plane: (a) degenerate cases (b) non-degenerate cases. Reprinted with permission from Das and Girimaji (2020b).

3. Normal-straining ($\mathbf{A} = \mathbf{N}$; $\mathbf{R} = \mathbf{H} = 0$): The $q = -1/2$ line or bottom-most boundary of the plane constitutes the case when the VG tensor itself is a normal matrix. This represents pure stretching/compression of the fluid element in three orthogonal directions.
4. Rotation and shear ($\mathbf{A} = \mathbf{R} + \mathbf{H}$; $\mathbf{N} = 0$): The upper half ($q > 0$) of the $r = 0$ line represents VG tensor with zero normal-strain-rate tensor. The VG tensor here has one zero and two purely imaginary eigenvalues, resulting in planar closed circulating streamlines that are elliptic in shape due to the presence of shear. In the absence of shear, the streamlines are purely circular (at $q = 1/2$).
5. Normal-strain and rotation ($\mathbf{A} = \mathbf{N} + \mathbf{R}$; $\mathbf{H} = 0$): The shear tensor is zero at the left and right boundaries of the plane given by (Das and Girimaji, 2020a)

$$r = \pm \left(\frac{1+q}{3} \right) \left(\frac{1-2q}{3} \right)^{1/2} \quad (4.34)$$

The left boundary of the plane represents rigid-body-rotation about the expansive normal-strain-rate eigenvector while the right boundary represents rigid-body-rotation about the compressive normal-strain-rate eigenvector, both in the absence of any shear. This implies locally stable/unstable spiraling streamlines stretching/compressing perpendicular to its focal plane.

Non-degenerate geometries: figure 4.2 (b) illustrates the four non-degenerate geometries covering the area of the q - r plane and the corresponding VG tensor decomposition. These are discussed below:

1. Rotational geometries ($\mathbf{A} = \mathbf{N} + \mathbf{R} + \mathbf{H}$): Above the zero discriminant ($d = q^3 + (27/4)r^2 = 0$) lines the VG tensor has complex eigenvalues and the flow is locally rotational. All three constituent tensors are in general non-zero. In the stable-focus-stretching (SFS) topology, the unique eigenvalue of \mathbf{N} (λ_r : real eigenvalue of \mathbf{A}) is positive, i.e. $\lambda_r > 0$, representing stretching of the fluid element. The other two equal eigenvalues of \mathbf{N} are negative, i.e.

$\lambda_{cr} < 0$, representing convergence of the local streamlines towards a stable focus. Similarly in unstable-focus-compression (UFC) topology, $\lambda_r < 0$ represents compression of the fluid element and $\lambda_{cr} > 0$ represents diverging streamlines from an unstable focus. The non-zero eigenvalues of tensor \mathbf{R} ($\pm i\phi$) denote the angular velocity of rigid-body-rotation of the fluid element. The tensor \mathbf{H} controls the shearing of the fluid element, resulting in varied orientations of the spiraling with respect to the direction of stretching/compression. The angle of alignment between the vorticity vector ($\vec{\omega} \equiv$ dual vector of \mathbf{W}) and the eigenvectors of \mathbf{S} can take any value. On the contrary, in this decomposition the rotation vector ($\vec{r} \equiv$ dual vector of \mathbf{R}) is always aligned along the unique eigenvector of \mathbf{N} .

2. Non-rotational geometries ($\mathbf{A} = \mathbf{N} + \mathbf{H}$; $\mathbf{R} = 0$): Below the zero discriminant line, VG tensor has only real eigenvalues. Stable-node-saddle-saddle (SN/S/S) topology region represents compression in two directions and expansion in one, i.e. $\lambda_1 > 0, \lambda_{2,3} < 0$, while unstable-node-saddle-saddle (UN/S/S) topology implies $\lambda_{1,2} > 0, \lambda_3 < 0$. However, these directions are in general oblique with respect to each other. The information about the magnitude of stretching/compression is contained in \mathbf{N} but the orientation of these directions, designated by the λ_i -eigenvectors, are contained in \mathbf{H} .

In summary, pure shear occurs at the origin of the q - r plane while normal-straining and rigid-body-rotation occur at the boundaries of the plane. The entire area inside the plane is populated in a turbulent flow field as a result of the combination of all three constituents. The distribution asymptotes to a nearly universal teardrop-like shape around the origin following the right discriminant line in fully-developed turbulent flows (Das and Girimaji, 2019).

4.3 Numerical simulation data

Direct numerical simulation (DNS) data sets of incompressible forced isotropic turbulence at Taylor Reynolds numbers,

$$Re_\lambda = 1, 6, 9, 14, 18, 25, 35, 86, 225, 385 \text{ and } 588$$

are used in this study to further characterize VG behavior in terms of the new constituent tensors. The details of the DNS data sets are presented in appendix A. These data sets have been used in past studies for investigating intermittency, anomalous exponents and Reynolds number scaling (Donzis et al., 2008; Donzis and Sreenivasan, 2010; Gibbon et al., 2014; Yakhot and Donzis, 2017, 2018).

The work of Yakhot and Donzis (2017) demonstrated the existence of a transition Reynolds number at $Re_\lambda \sim 9$ for isotropic turbulence forced with random Gaussian forcing. The normalized even-order moments of velocity gradients are Gaussian below this Reynolds number and exhibit the so-called anomalous scaling above this Reynolds number. In addition, a recent study by Das and Girimaji (2019) shows that certain VG statistics and dynamical characteristics asymptote towards a universal nature above $Re_\lambda \approx 200$. For example, the q - r joint probability density function (PDF) is nearly invariant for $Re_\lambda > 200$. To better understand turbulence velocity gradient behavior as a function of Re_λ we investigate VG composition in three ranges:

1. Low Reynolds number (Gaussian regime) - $Re_\lambda \in (1, 9)$
2. Intermediate Reynolds number - $Re_\lambda \in (9, 200)$
3. High Reynolds number (Asymptotic regime) - $Re_\lambda \in (200, 600)$

4.4 Velocity gradients and pressure field characterization

4.4.1 Composition of VG magnitude

Subject to triple decomposition, the VG magnitude is composed of the following four constituents – normal-strainrate magnitude (N^2), rigid-body-rotation magnitude (R^2), shear magnitude (H^2) and shear-rotation correlation term ($2RH$), as given in equation (4.17). The volume-averages of these constituents normalized by the volume-average of total VG magnitude (A^2) is plotted in figure 4.3 as a function of Reynolds number. It is evident from the figure that shear is the most dominant component at all Reynolds numbers, followed by normal-strain-rate and then rigid-body-rotation. In the low Reynolds number range, mean shear increases with increasing Re_λ while

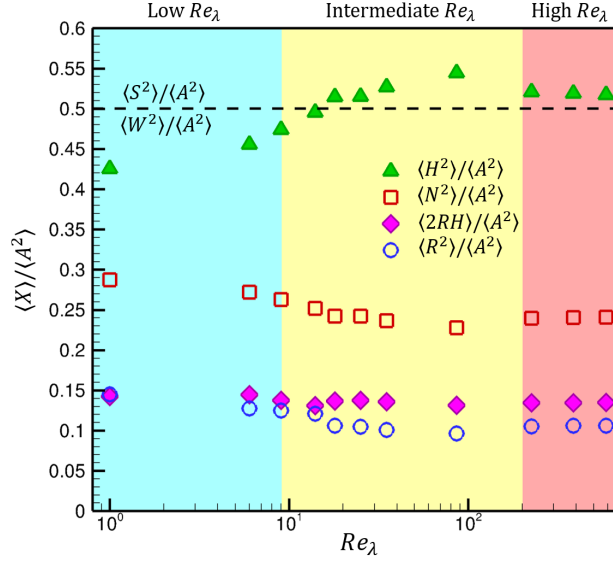


Figure 4.3: Volume average of H^2 , N^2 , $2RH$ and R^2 normalized by the volume average of A^2 in the three Re_λ ranges (marked by different background colors). The dashed line marks the volume average of S^2 and W^2 , normalized by $\langle A^2 \rangle$. Reprinted with permission from Das and Girimaji (2020b).

mean normal-strain decreases. Similar trend continues in the intermediate range of Reynolds number, where shear increases with Re_λ to values higher than 50% of the mean VG magnitude. The mean rigid-body-rotation decreases with Re_λ in the low and intermediate ranges of Reynolds numbers. The correlation term $2RH$ is fairly independent of Re_λ and maintains a constant value of $\langle 2RH \rangle \approx 13\%$ of $\langle A^2 \rangle$. Finally, the volume averages of all the constituents asymptote to distinct values in the high Reynolds number range. In this asymptotic regime of Re_λ , $\langle H^2 \rangle \approx 52\%$, $\langle N^2 \rangle \approx 24\%$ and $\langle R^2 \rangle \approx 11\%$ of $\langle A^2 \rangle$.

For reference, we have also plotted the VG magnitude composition in terms of S_{ij} and W_{ij} . In an isotropic flow field it is well-known that $\langle S^2 \rangle / \langle A^2 \rangle = \langle W^2 \rangle / \langle A^2 \rangle = 0.5$. Thus, of the 50% constituted by average enstrophy or $\langle W^2 \rangle$, only about 11% is directly from rigid-body-rotation. The remainder of enstrophy is constituted of contributions from shear: $\langle H^2_W \rangle = 26\%$, $\langle 2RH \rangle = 13\%$. Similarly, only half of the average strain-rate magnitude or $\langle S^2 \rangle$ is constituted by normal-strain-rate; the other half is from shear.

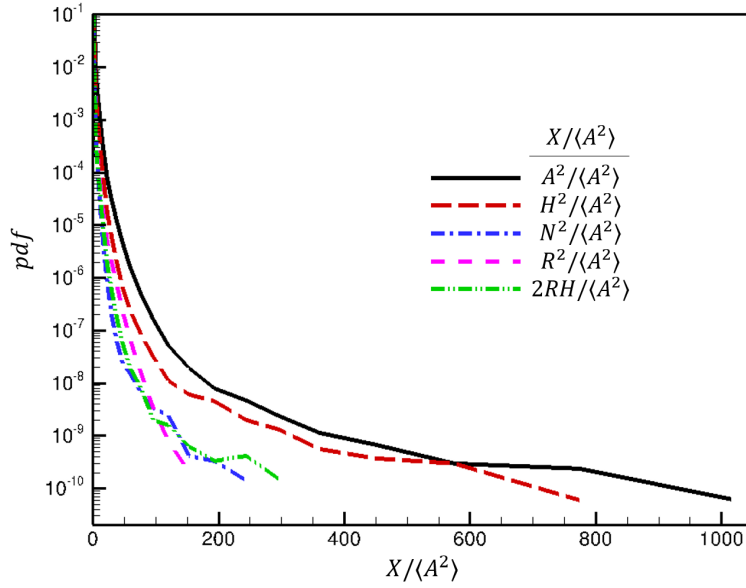


Figure 4.4: Probability density function (PDF) of A^2 , H^2 , N^2 , R^2 and $2RH$ normalized by volume-averaged VG magnitude $\langle A^2 \rangle$ in log-linear scale for $Re_\lambda = 225$. Reprinted with permission from Das and Girimaji (2020b).

The PDF of A^2 and its composition are of much interest in the discussion of turbulence intermittency. It has been shown in several previous studies that A^2 exhibits a heavy-tailed PDF, characteristic of intermittency (Yeung and Pope, 1989; Yeung et al., 2006). It has further been shown that in the conventionally used decomposition, enstrophy exhibits a PDF with a wider tail and is more intermittent than dissipation (Yeung et al., 2018; Buaria et al., 2019). The PDFs of VG magnitude and its triple decomposition constituents are plotted in figure 4.4 for a high Reynolds number case ($Re_\lambda = 225$). Interestingly, the figure illustrates that shear-magnitude (H^2) exhibits a wider tail than all the other components. The PDF-tails of N^2 , R^2 and $2RH$ span across smaller ranges of values than that of H^2 . This is observed at all the investigated Reynolds numbers (plots not displayed) and is particularly apparent in the high Re_λ cases. Clearly, in this decomposition the shear-magnitude contributes most toward the heavy-tailed PDF of A^2 . It is further evident that it is the contribution of shear rather than rigid-body-rotation, that renders enstrophy so strongly intermittent.

Now we further investigate the contributions of different velocity gradient constituents at dif-

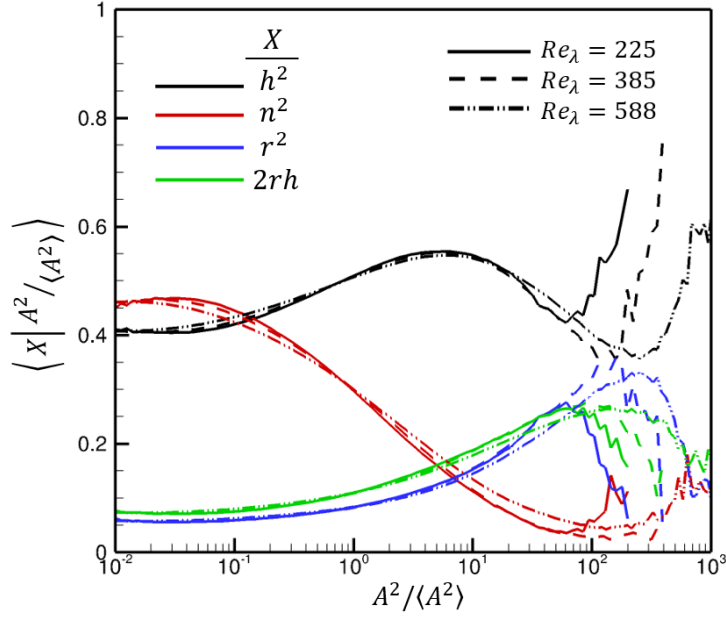


Figure 4.5: Conditional average of h^2 , n^2 , r^2 and $2rh$ as a function of $A^2/\langle A^2 \rangle$ in the high Re_λ range. Reprinted with permission from Das and Girimaji (2020b).

ferent values of A^2 . The conditional mean of the normalized constituents – n^2 , r^2 , h^2 and $2rh$ (see equation 4.22) are plotted as a function of VG magnitude in figure 4.5 for the high Reynolds number cases. Normal-strain-rate dominates at very low VG magnitudes ($A^2/\langle A^2 \rangle < \mathcal{O}(0.1)$) but it declines steadily with increasing A^2 . For a major portion of the VG magnitude range, shear is the most dominating component. The rigid-body-rotation magnitude and shear-rotation correlation term have very similar variation of conditional average with respect to A^2 . Both r^2 and $2rh$ increase steadily with A^2 , except at the extreme A^2 values. There appears to be a critical value of $A^2/\langle A^2 \rangle$ in the extreme range ($\sim \mathcal{O}(10^2 - 10^3)$), above which r^2 and $2rh$ exhibit a sharp decline with A^2 while h^2 displays a steep increase. The contribution of n^2 is small in this range of $A^2/\langle A^2 \rangle$. The critical $A^2/\langle A^2 \rangle$ value ≈ 60 ($Re_\lambda = 225$), ≈ 166 ($Re_\lambda = 385$) and ≈ 260 ($Re_\lambda = 588$), clearly increases with Re_λ . The conditional average plots of all the components of VG magnitude below this critical value are nearly invariant with Re_λ .

This subsection demonstrates that on average shear is the dominant contributor to VG magnitude in a turbulent flow field while rigid-body-rotation magnitude contributes the least. It is further

shown that shear-magnitude is most responsible for the heavy-tailed PDF of VG magnitude. Moreover, shear-magnitude increases steeply while rigid-body-rotation magnitude decreases at extreme A^2 values. It is, therefore, reasonable to infer that shear dominates in regions of high intermittency.

4.4.2 Dependence of pressure field on VG constituents

Pressure field in an incompressible turbulent flow is governed by the pressure Poisson equation wherein the source term depends on the local velocity gradients:

$$\nabla^2 p' = -A_{ij}A_{ji} \quad (4.35)$$

Here p' is the pressure fluctuation normalized by density. In terms of strain-rate and vorticity tensors this equation is of the form,

$$\nabla^2 p' = W_{ij}W_{ij} - S_{ij}S_{ij} = W^2 - S^2 = A^2(w^2 - s^2) \quad (4.36)$$

where, $s^2 = S^2/A^2$ and $w^2 = W^2/A^2$ represent the fractions of contribution of strain-rate and vorticity towards A^2 (equation 4.16). As shown by Yeung et al. (2012), p' and $\nabla^2 p'$ are negatively correlated in a homogeneous field. Therefore, we expect from equation (4.36) that high s^2 is likely associated with positive p' and high w^2 is associated with negative p' . The mean pressure fluctuation (normalized by turbulent kinetic energy $0.5\langle u'^2 \rangle$) conditioned on s^2 and w^2 are plotted in figure 4.6 for a high Re_λ case. The figure displays that when s^2 dominates in the flow, mean $p' > 0$ implying a high pressure region, which is expected in a strain-dominated flow. On the other hand, when vorticity magnitude dominates, the local flow consists of a low pressure center. However, note that when $w^2 < 1/2$ even if the flow has a significant amount of vorticity, the pressure fluctuation is likely to be positive. This reiterates the fact that vorticity does not necessarily indicate the presence of a rotating flow with a low pressure center.

Even though $\nabla^2 p'$ depends on two intermittent quantities (S^2 and W^2), it has been shown to follow Kolmogorov scaling and is essentially non-intermittent in nature (Iyer et al., 2019). We now

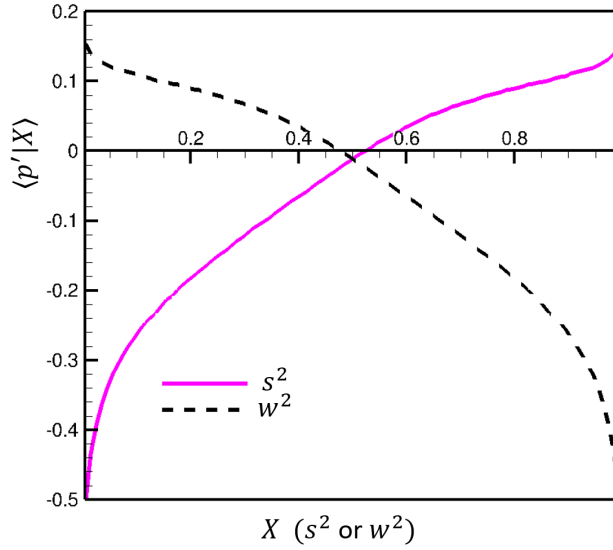


Figure 4.6: Conditional average of pressure fluctuation (normalized by turbulent kinetic energy) as a function of s^2 and w^2 for $Re_\lambda = 225$. Reprinted with permission from Das and Girimaji (2020b).

use triple decomposition of VG tensor to provide a plausible explanation for this. Using equation (4.2) in the governing equation of pressure (equation 4.35) we obtain

$$\begin{aligned} \nabla^2 p' = & -(R_{ij}R_{ji} + N_{ij}R_{ji} + H_{ij}R_{ji} + R_{ij}N_{ji} + N_{ij}N_{ji} \\ & + H_{ij}N_{ji} + R_{ij}H_{ji} + N_{ij}H_{ji} + H_{ij}H_{ji}) \end{aligned} \quad (4.37)$$

Applying the properties of the tensors from equation (4.6), we can substitute the following in above equation

$$R_{ij}H_{ji} = H_{ij}R_{ji} = -2RH \quad \text{and} \quad N_{ij}R_{ji} = R_{ij}N_{ji} = N_{ij}H_{ji} = H_{ij}N_{ji} = H_{ij}H_{ji} = 0 \quad (4.38)$$

to obtain an alternate expression for source term in Laplace equation for pressure,

$$\nabla^2 p' = R^2 + 2RH - N^2 = A^2(r^2 + 2rh - n^2) \quad (4.39)$$

Thus, the Laplacian of pressure does not depend on the shear-magnitude (H^2). The contribution

of H^2 to the magnitudes of strain-rate and vorticity are equal, as shown in equation (4.26), and they nullify each other in the Laplacian of pressure expression. As shown in Section 4.4.1, shear magnitude is the predominant contributor in attaining extreme VG magnitudes. The absence of this most intermittent VG tensor constituent H^2 renders the Laplacian of pressure significantly less intermittent than A^2 .

It is evident in equation (4.39) that the sole effect of shear on pressure is through the shear-rotation correlation term that depends only on shearing in the rigid-body-rotation plane (s_3). Now, if the local flow has no rigid-body-rotation at all (non-rotational), the pressure Poisson equation is given by,

$$\nabla^2 p' = -N^2 = -A^2 n^2 \quad (4.40)$$

In this case, the Laplacian of pressure solely depends on the magnitude of normal-strain-rate tensor.

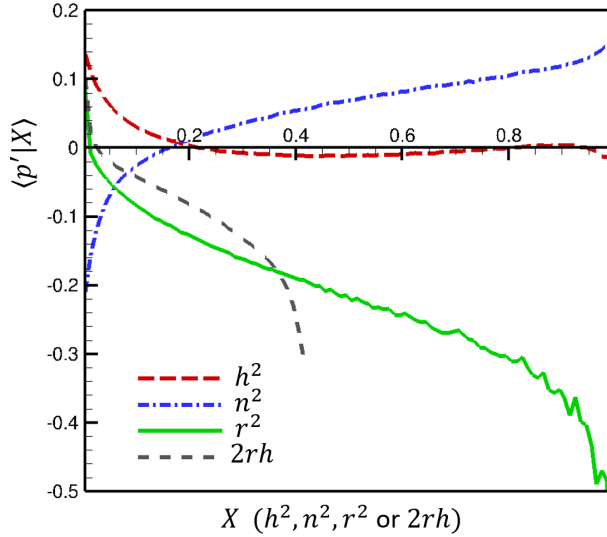


Figure 4.7: Conditional average of pressure fluctuation (normalized by turbulent kinetic energy) as a function of h^2 , n^2 , r^2 and $2rh$ for $Re_\lambda = 225$. Reprinted with permission from Das and Girimaji (2020b).

Now, we examine the mean normalized p' conditioned on each of the normalized VG constituents, i.e. n^2 , h^2 , r^2 and $2rh$, in figure 4.7. It is evident that the mean pressure fluctuation is

negative whenever rigid-body-rotation is present in the flow. Clearly, rigid-body-rotation is much more strongly correlated with low pressure regions than vorticity (w^2 in figure 4.6). Similarly, normal-strain-rate magnitude is more strongly associated with positive p' or high pressure regions than s^2 . As r^2 increases, $\langle p'|r^2 \rangle$ becomes more negative and as n^2 increases, $\langle p'|n^2 \rangle$ increases. Shear-magnitude is mostly associated with nearly zero conditional mean pressure fluctuations. This is due to the fact that purely shearing motion does not require any pressure gradient to drive the flow and the incompressibility condition is inherently satisfied. The shear-rotation correlation term lies within its bounds $2rh \in (0, 0.41)$ as given in equation (4.24) and the pressure fluctuations conditioned on $2rh$ becomes more negative as $2rh$ increases, similar to r^2 . The figures in this subsection illustrate the results for $Re_\lambda = 225$; the other Re_λ cases also display similar behavior and have not been presented separately.

4.4.3 Alignment properties

An important feature of velocity gradients in a turbulent flow field is the preferential alignment of vorticity along the intermediate eigenvector of strain-rate and pressure Hessian tensors (Ashurst et al., 1987; Tsinober et al., 1995; Lüthi et al., 2005; Kalelkar, 2006; Chevillard et al., 2008). In this subsection, we first examine the alignment of vorticity vector ($\vec{\omega}$) and rotation axis (\vec{r} defined in equation 4.8) with the eigenvectors of normal strain-rate tensor, \mathbf{N} . Then, the alignment of \vec{r} with the eigenvectors of pressure Hessian tensor is investigated.

The eigenvectors of \mathbf{N} for its three real eigenvalues are given by \vec{n}_1 , \vec{n}_2 and \vec{n}_3 . If the flow is locally rotational, \vec{n}_1 and \vec{n}_2 are eigenvectors corresponding to the two equal eigenvalues (λ_{cr}) and \vec{n}_3 corresponds to the unique eigenvalue λ_r . By construction, the rotation axis, \vec{r} , is aligned with the unique eigenvector \vec{n}_3 . If the flow is locally non-rotational, eigenvectors - \vec{n}_1 , \vec{n}_2 , \vec{n}_3 - correspond to the \mathbf{N} -eigenvalues arranged in descending order: $\lambda_1 \geq \lambda_2 \geq \lambda_3$. The PDFs of absolute values of cosines of angles between vorticity vector and \mathbf{N} -eigenvectors are plotted for locally rotational and non-rotational cases in a high Re_λ flow in figure 4.8. For reference, the PDF of angle cosine between $\vec{\omega}$ and intermediate strain-rate eigenvector (\vec{s}_2) is also plotted. There is a discernible difference in the alignment of $\vec{\omega}$ and \vec{s}_2 in rotational and non-rotational cases. The

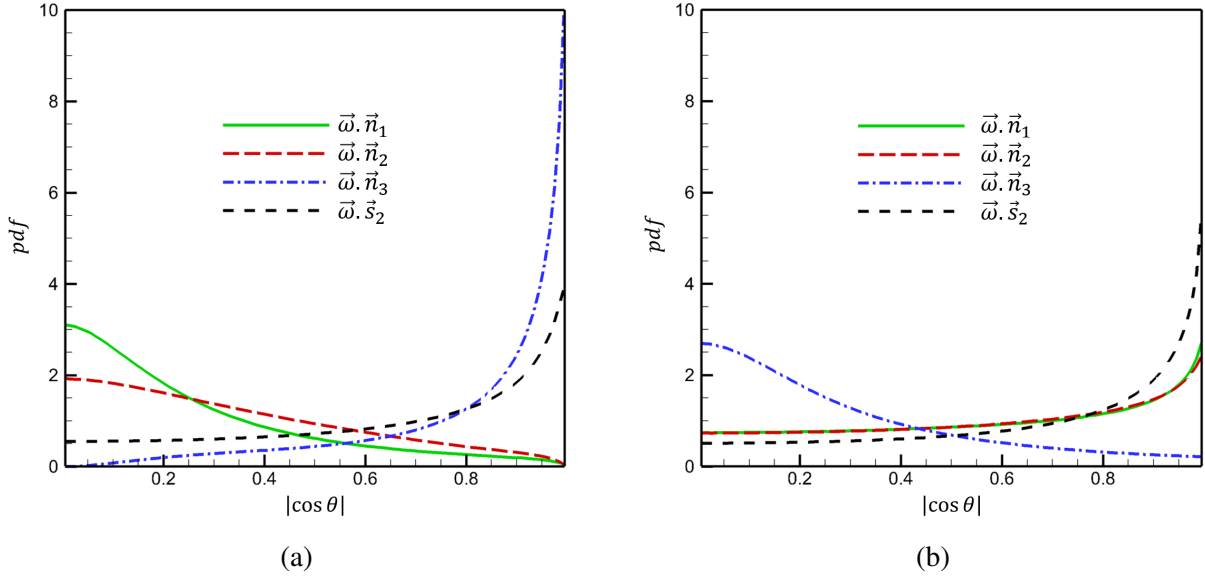


Figure 4.8: PDFs of absolute values of the cosines of angles between the vorticity vector ($\vec{\omega}$) and the \mathbf{N} -eigenvectors ($\vec{n}_1, \vec{n}_2, \vec{n}_3$) for locally (a) rotational, and (b) non-rotational points in $Re_\lambda = 225$ case. Black dashed line represents the alignment of $\vec{\omega}$ with the intermediate strain-rate eigenvector \vec{s}_2 . Reprinted with permission from Das and Girimaji (2020b).

probability of $\vec{\omega}$ - \vec{s}_2 alignment is higher in locally non-rotational flow than in locally rotational flow.

In the rotational case (figure 4.8a), vorticity displays a strong preferential alignment with \vec{n}_3 and therefore with the rotation axis \vec{r} . Thus, in a turbulent flow field when the flow is locally rotational, vorticity is most likely aligned with the rotation axis. Note that the perfect alignment of vorticity with rotation axis occurs when shear is zero. It is evident from the figure that this alignment of vorticity with the unique eigenvector of \mathbf{N} has a significantly higher probability of occurrence than the alignment of vorticity with intermediate eigenvector of \mathbf{S} .

In the non-rotational case (figure 4.8b), vorticity is equally well aligned with both most expansive and intermediate eigenvectors of \mathbf{N} . In fact, the PDFs indicate nearly identical distribution of $\vec{\omega}$ -alignment with \vec{n}_1 and \vec{n}_2 . It may be noted that the probability of each of these two alignments is weaker than the $\vec{\omega}$ -alignment with \vec{s}_2 . Vorticity is most likely to be on the plane perpendicular to \vec{n}_3 – the most compressive eigenvector of \mathbf{N} . This behavior is similar to vorticity being on a plane normal to the most compressive eigenvector of \mathbf{S} (Ashurst et al., 1987).

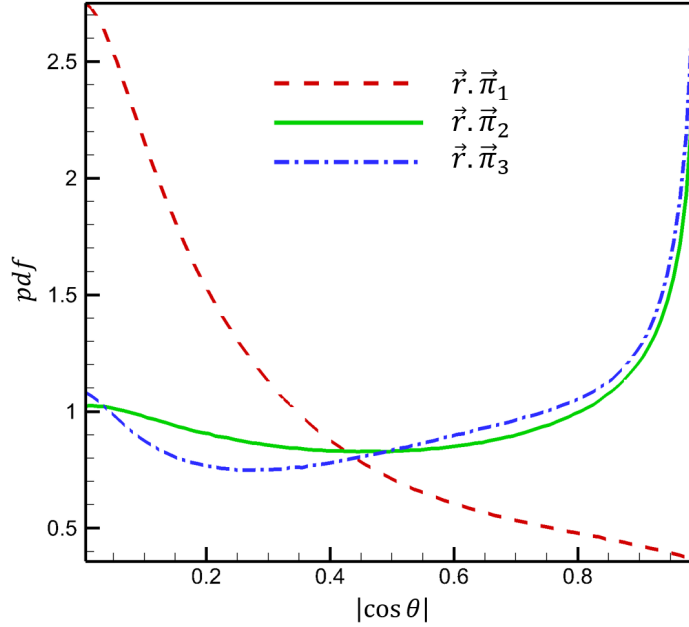


Figure 4.9: PDFs of absolute values of the cosines of the angles between rotation axis (\vec{r}) and the eigenvectors of pressure Hessian ($\vec{\pi}_1, \vec{\pi}_2, \vec{\pi}_3$) for $Re_\lambda = 225$. Reprinted with permission from Das and Girimaji (2020b).

The pressure Hessian tensor is important as it represents the contribution of non-local effects towards the evolution of velocity gradients. It is given by

$$P_{ij} = \frac{\partial^2 p'}{\partial x_i \partial x_j} \quad (4.41)$$

Note that the pressure Laplacian is the trace of this tensor, i.e. $\nabla^2 p' = P_{ii}$. In this work, $\vec{\pi}_1, \vec{\pi}_2$ and $\vec{\pi}_3$ denote the eigenvectors of \mathbf{P} corresponding to eigenvalues in a decreasing order: $\rho_1 \geq \rho_2 \geq \rho_3$. The PDFs of alignment of the rotation axis (\vec{r}) with the pressure Hessian eigenvectors in a high Re_λ case is illustrated in figure 4.9. It is evident that the rotation axis shows nearly equal likelihood of alignment with $\vec{\pi}_2$ and $\vec{\pi}_3$ eigenvectors. Further, \vec{r} has a high probability of being in a plane perpendicular to the $\vec{\pi}_1$ eigenvector of the pressure Hessian tensor. In contrast, vorticity shows strong alignment with $\vec{\pi}_2$ and only a slight tendency of alignment with $\vec{\pi}_3$ (Tsinober et al., 1995; Kalelkar, 2006; Chevillard et al., 2008).

4.5 Conclusions

The study proposes using a novel triple decomposition of velocity-gradient (VG) tensor to revisit key small-scale features of turbulence. The VG tensor is partitioned into normal-strain-rate, pure-shear and rigid-body-rotation-rate tensors. Each of these tensors signifies an elementary form of deformation of a fluid element and has a specific role to play in the turbulence phenomenon. Specifically, the decomposition permits isolating the effect of rigid-body rotation from vorticity (W_{ij}) and normal-strain-rate from strain-rate (S_{ij}). The key results and findings from this study are:

1. The various local streamline topologies and geometries can be more intuitively understood in terms of normal-strain, rigid-body-rotation and pure-shear tensors.
2. On average, shear is the most dominating constituent in turbulent flow fields at all Reynolds numbers while rigid-body-rotation contributes the least.
3. The average contribution of shear increases while that of normal-strain-rate and rigid-body-rotation-rate decreases with Reynolds number at low and intermediate Re_λ (< 200). Shear-rotation correlation term does not show any Re_λ - dependence. At high Re_λ (> 200), all the average contributions are fairly invariant with Reynolds number.
4. Shear contribution (H^2) is most responsible for the heavy-tailed probability distribution of A^2 . Shear-magnitude shows a steep increase in contribution at extreme A^2 values while rotation-magnitude declines.
5. Further, it is shown that shear, rather than rigid-body-rotation is the main cause of the strong intermittency exhibited by enstrophy.
6. The shear-magnitude, which contributes the most in regions of high intermittency of velocity gradients, is absent in the expression for Laplacian of pressure. Thus, the pressure Laplacian does not exhibit discernible intermittency.

7. Low-pressure regions are strongly associated with rigid-body-rotation and high-pressure regions are prevalent when normal-strain-rate dominates. Shear is associated with nearly zero pressure fluctuations.
8. Vorticity demonstrates a strong preferential alignment with the unique eigenvector of normal strain-rate tensor or the rotation axis in locally rotational flow. This alignment is significantly higher in probability than its alignment with the intermediate strain-rate eigenvector. In the locally non-rotational regions, vorticity shows high probability of alignment with both most expansive and intermediate normal strain-rate eigenvectors.
9. The axis of rigid-body-rotation shows a high probability of alignment with the pressure Hessian eigenvectors of both the intermediate and the smallest eigenvalues.

Overall, the study presents some novel insight into velocity-gradients and, hence, small scales of turbulence. This work specifically highlights the key role of shear in turbulence small-scale dynamics previously attributed to strain-rate and vorticity. The new intuition developed from this triple decomposition of the VG tensor not only leads to deeper understanding of critical turbulence phenomena, but also paves the way for improved modeling of velocity-gradients in turbulence.

5. VELOCITY GRADIENT DYNAMICS: EFFECT OF TURBULENCE PROCESSES ON EVOLUTION OF LOCAL STREAMLINE GEOMETRY

5.1 Introduction

The structure of velocity-gradient tensor (A_{ij}) and its evolution in a turbulent flow provide valuable insight into key turbulence processes including non-local pressure and viscous effects. The nonlinear – inertial and isotropic pressure – terms in the velocity gradient evolution equations are explicit functions of A_{ij} and are referred to as the restricted Euler (RE) effect. The nonlinear or RE effect constitute a closed autonomous dynamical system for the evolution of A_{ij} and has been studied by many (Vieillefosse, 1982, 1984; Cantwell, 1992; Martín et al., 1998a) to understand its effect on VG invariants. Studying the nonlocal pressure and viscous effects, on the other hand, is more involved and requires analysis of large datasets obtained from numerical simulation or experimentation.

The evolution of local streamline topology is generally examined by illustrating conditional trajectories in the phase space of Q - R (Martín et al., 1998b). Several studies have investigated such trajectories using numerical simulation data of different turbulent flows (Martín et al., 1998b; Ooi et al., 1999; Bikkani and Girimaji, 2007; Chevillard et al., 2008; Elsinga and Marusic, 2010a; Atkinson et al., 2012; Lawson and Dawson, 2015; Bechlers and Sandberg, 2017a; Wu et al., 2019). This has led to a better understanding of the nonlocal effects of pressure and viscosity on the evolution of Q - R . The improved comprehension of turbulence velocity gradient dynamics derived from these studies has been employed to develop Lagrangian VG tensor evolution models (Cantwell, 1992; Girimaji and Pope, 1990a; Girimaji and Speziale, 1995; Martín et al., 1998a; Chertkov et al., 1999; Jeong and Girimaji, 2003; Chevillard and Meneveau, 2006; Chevillard et al., 2008; Johnson

Part of this chapter is reprinted with permission from: Das, R. and Girimaji, S. S. (2020). Characterization of velocity-gradient dynamics in incompressible turbulence using local streamline geometry, *Journal of Fluid Mechanics*, 895. Copyright The Author(s), 2020. Published by Cambridge University Press.

and Meneveau, 2016a). While much progress has been made, our comprehension of VG dynamics, specifically the non-local pressure and viscous processes, remains incomplete and the closure models need further improvement.

The unbounded nature of Q and R makes it difficult to study the VG dynamics in this plane in a standardized manner. Further, the Q - R phase plane is unable to uniquely represent local streamline geometry, as demonstrated in section 3.2. Therefore, in this chapter we study the dynamics of streamline geometry in the bounded phase space of the key shape-parameters – normalized VG invariants (q,r) . First, we derive the governing equations of q and r and define the conditional mean trajectories to be investigated. Then, we use DNS data sets of homogeneous isotropic turbulent flow to develop a well-defined dynamical system characterization of (i) the overall mean evolution of geometry in turbulence and (ii) the non-local pressure and viscous processes, conditioned on q - r .

5.2 Evolution equations of local streamline shape

As derived in section 3.2, the local streamline geometric shape is completely defined by only four shape-parameters - q, r, a_2 and ω_2 . Here, q and r are the second and third invariants of the normalized VG tensor (b_{ij}) ,

$$\begin{aligned} b_{ij} &= \frac{A_{ij}}{A} \quad \text{where } A = \sqrt{A_{ij}A_{ij}} \\ q &= -\frac{1}{2}b_{ij}b_{ji} \quad , \quad r = -\frac{1}{3}b_{ij}b_{jk}b_{ki}, \end{aligned} \tag{5.1}$$

while, a_2 is the intermediate eigenvalue of the normalized strain-rate tensor, $s_{ij} = (b_{ij} + b_{ji})/2$, and ω_2 is the vorticity component along the intermediate strain-rate eigenvector.

We now present the governing equations of the shape parameters in a turbulent flow field. From the Navier-Stokes equation, one can derive the following governing equations for the elements of normalized VG tensor components (equation 2.21),

$$\frac{db_{ij}}{dt'} = -b_{ik}b_{kj} + h_{ij} + \tau_{ij} + \frac{1}{3}b_{mk}b_{km}\delta_{ij} + b_{ij}(b_{mk}b_{kn} - h_{mn} - \tau_{mn})b_{mn} \tag{5.2}$$

where $dt' \equiv A dt$ is the normalized time increment. Here, the normalized anisotropic pressure Hessian and viscous diffusion terms, given by,

$$h_{ij} = \frac{H_{ij}}{A^2} = \frac{1}{A^2} \left(-\frac{\partial^2 p}{\partial x_i \partial x_j} + \frac{\partial^2 p}{\partial x_k \partial x_k} \frac{\delta_{ij}}{3} \right) \quad \text{and} \quad \tau_{ij} = \frac{T_{ij}}{A^2} = \frac{\nu}{A^2} \frac{\partial^2 A_{ij}}{\partial x_k \partial x_k} \quad (5.3)$$

represent the non-local physics. Further manipulations of equation (5.2) lead to the following evolution equations for the invariant parameters, q and r ,

$$\frac{dq}{dt'} = \underbrace{-3r + 2qb_{ij}b_{ik}b_{kj}}_I - \underbrace{h_{ij}(b_{ji} + 2qb_{ij})}_{\mathcal{P}} - \underbrace{\tau_{ij}(b_{ji} + 2qb_{ij})}_V \quad (5.4)$$

$$\frac{dr}{dt'} = \underbrace{2q^2 + 3rb_{ij}b_{ik}b_{kj}}_I - \underbrace{\frac{4}{3}q^2 - h_{ij}(b_{jk}b_{ki} + 3rb_{ij})}_{\mathcal{P}} - \underbrace{\tau_{ij}(b_{jk}b_{ki} + 3rb_{ij})}_V \quad (5.5)$$

as derived in section 2.2.3. Terms representing the role of different physical processes, namely inertial (I), pressure (\mathcal{P}) and viscous (V) contributions, toward the evolution of q and r , are marked in the equation above. Note that the pressure term in the r -equation consists of an isotropic part ($= -\frac{4}{3}q^2$) and an anisotropic part ($= -h_{mn}(b_{im}b_{ni} + 3rb_{mn})$). However, the pressure contribution in the q -equation does not involve an isotropic component. The inertial and isotropic pressure terms constitute the local contribution to the evolution of streamline shape, while the anisotropic pressure and viscous terms represent the non-local effects. The local terms form a closed dynamical system of equations called restricted Euler equations (Vieillefosse, 1984). The non-local terms are unclosed in the system of equations and need to be modeled. Characterization of these terms is one of the principal objectives of this study.

The evolution equations for frame-dependent parameters, a_2 and ω_2 , are more complicated since they depend on the evolution of eigenvectors of the strain-rate tensor. Readers are referred to the works of Dresselhaus and Tabor (1992) and Nomura and Post (1998) for these governing equations. It is important to note that the large-scale forcing term has not been included in the above governing equations. The effect of large-scale forcing is not considered in this chapter, in

line with the assumption of most of the previous studies in this field that the small-scale gradient of large-scale forcing term in the Navier-Stokes equation is negligible with respect to the other terms (Chevillard et al., 2008). However, this role of large-scale forcing is evaluated in the next chapter leading to some important revelations against this argument.

5.3 Conditional mean trajectories (CMTs)

The dynamics of the velocity gradient invariants, Q and R , is commonly investigated by examining the conditional mean trajectories (CMTs) (Martín et al., 1998b; Ooi et al., 1999). The CMTs are obtained by time integration of the conditional mean velocity vector field (\mathbf{V}) in the Q - R plane:

$$\mathbf{V} = \begin{pmatrix} V_Q \\ V_R \end{pmatrix} = \left\langle \begin{pmatrix} dQ/dt \\ dR/dt \end{pmatrix} \middle| Q, R \right\rangle. \quad (5.6)$$

Similarly, the q - r CMTs are obtained by integrating the vector field of conditional mean velocity (\mathbf{v}) in the q - r plane:

$$\mathbf{v} = \begin{pmatrix} v_q \\ v_r \end{pmatrix} = \left\langle \begin{pmatrix} dq/dt \\ dr/dt \end{pmatrix} \middle| q, r \right\rangle. \quad (5.7)$$

Using equations (5.4) and (5.5), the q - r CMTs due to inertial (I), pressure (\mathcal{P}), and viscous (V) processes can be individually defined as:

$$\begin{aligned} \mathbf{v}_I &= \left\langle \begin{pmatrix} A(-3r + 2qb_{ij}b_{ik}b_{kj}) \\ A(2q^2 + 3rb_{ij}b_{ik}b_{kj}) \end{pmatrix} \middle| q, r \right\rangle; \\ \mathbf{v}_{\mathcal{P}} &= \left\langle \begin{pmatrix} -A(h_{ij}(b_{ji} + 2qb_{ij})) \\ -A(\frac{4}{3}q^2 + h_{ij}(b_{jk}b_{ki} + 3rb_{ij})) \end{pmatrix} \middle| q, r \right\rangle; \\ \mathbf{v}_V &= \left\langle \begin{pmatrix} -A(\tau_{ij}(b_{ji} + 2qb_{ij})) \\ -A(\tau_{ij}(b_{jk}b_{ki} + 3rb_{ij})) \end{pmatrix} \middle| q, r \right\rangle. \end{aligned} \quad (5.8)$$

5.4 Numerical simulation data

Direct numerical simulation (DNS) datasets of incompressible forced isotropic turbulence have been used in this study to investigate the dynamics of streamline geometry due to the different turbulence processes. Three different flow cases of Taylor Reynolds numbers, $Re_\lambda = 225, 385$ and 588 are used for the present analysis. Further details of the DNS data sets are included in appendix A. All these datasets are well-resolved and have been used previously to study intermittency, anomalous exponents, Reynolds number scaling and non-linear depletion (Donzis et al., 2008; Donzis and Sreenivasan, 2010; Donzis et al., 2012; Gibbon et al., 2014). The spatial derivatives are computed using spectral methods.

5.5 Conditional mean evolution of geometry

The objective is to characterize turbulence velocity gradient dynamics conditioned upon shape-parameters. The evolution of streamline geometric shape is investigated in the phase plane of frame-invariant shape-parameters - q and r . Evolution in other shape parameter spaces will be considered in future work. In addition to providing improved insight into turbulence physics, the study is also expected to serve as a foundation for developing Lagrangian velocity-gradient models.

5.5.1 Conditional mean trajectories in Q - R plane

For reference we first present the conditional mean trajectories (CMTs) in the Q - R plane for the $Re_\lambda = 225$ case in figure 5.1 (a). Following the works of Martín et al. (1998b) and Ooi et al. (1999), the CMTs in Q - R space are obtained by time-integration of the conditional mean velocity vector field given in equation (5.6). The contours in the background represent the normalized conditional mean velocity magnitude,

$$|\overline{\mathbf{V}}| = \frac{\sqrt{V_Q^2 + V_R^2}}{1/\tau_\eta} \quad \text{where} \quad \tau_\eta \sim \frac{1}{\langle A \rangle} \quad (5.9)$$

to indicate the speed of the trajectories in different parts of the plane normalized by the global Kolmogorov time scale (τ_η). Consistent with the findings of Martín et al. (1998b), Ooi et al.

(1999) and Chevillard et al. (2008), Q - R CMTs tend to spiral in a clockwise manner around the origin, which is a stable focus of the phase-space. Large values of Q and R , away from the origin, imply a high VG magnitude. The figure shows that the velocity of the trajectories is higher in regions of large Q and R . The evolution rate slows down significantly near the origin and along the right discriminant line. It is difficult to infer many other details from Q - R CMTs, especially in the regions of large Q and R . We now demonstrate that the CMTs in q - r space provide further information about various turbulent processes, not evident in Q - R space.

5.5.2 Conditional mean trajectories in q - r plane

The CMTs in the normalized invariant q - r plane are displayed for different Reynolds number cases in figure 5.1 (b-d). The speed of the trajectories or the normalized conditional mean velocity magnitude,

$$|\overline{\mathbf{v}}| = \frac{\sqrt{v_q^2 + v_r^2}}{1/\tau_\eta} \quad \text{where} \quad \tau_\eta \sim \frac{1}{\langle A \rangle} \quad (5.10)$$

is indicated by the background contours.

It is evident from figures 5.1 (b-d) that the compact q - r CMTs are well behaved throughout the domain and highlight many more features than the Q - R CMTs. The q - r CMTs can be divided into two distinct types - inner and outer trajectories, separated by the white dashed loop (separatrix) marked in the figure. Inner CMTs spiral clockwise towards the origin while outer CMTs asymptote to the lower boundary of the plane in a clockwise manner.

The q - r equations can be considered a dynamical system in a compact phase space. The description of the behavior of this dynamical system is of much value for understanding and modeling VG dynamics. The system consists of two attractors - the attracting focus ($q \approx 0, r \approx 0$) represents pure-shear geometry and the attracting manifold ($q = -1/2$ line) represents pure strain shape, as shown in section 3.2.6. The dashed loop is the separatrix - an invariant manifold that separates the domain of attraction of the two attractors. Trajectories originating on the separatrix loop continue to circle along the loop until a small deviation causes it to gradually leave the loop.

The evolution is generally faster in the focal streamline region of the q - r plane, particularly

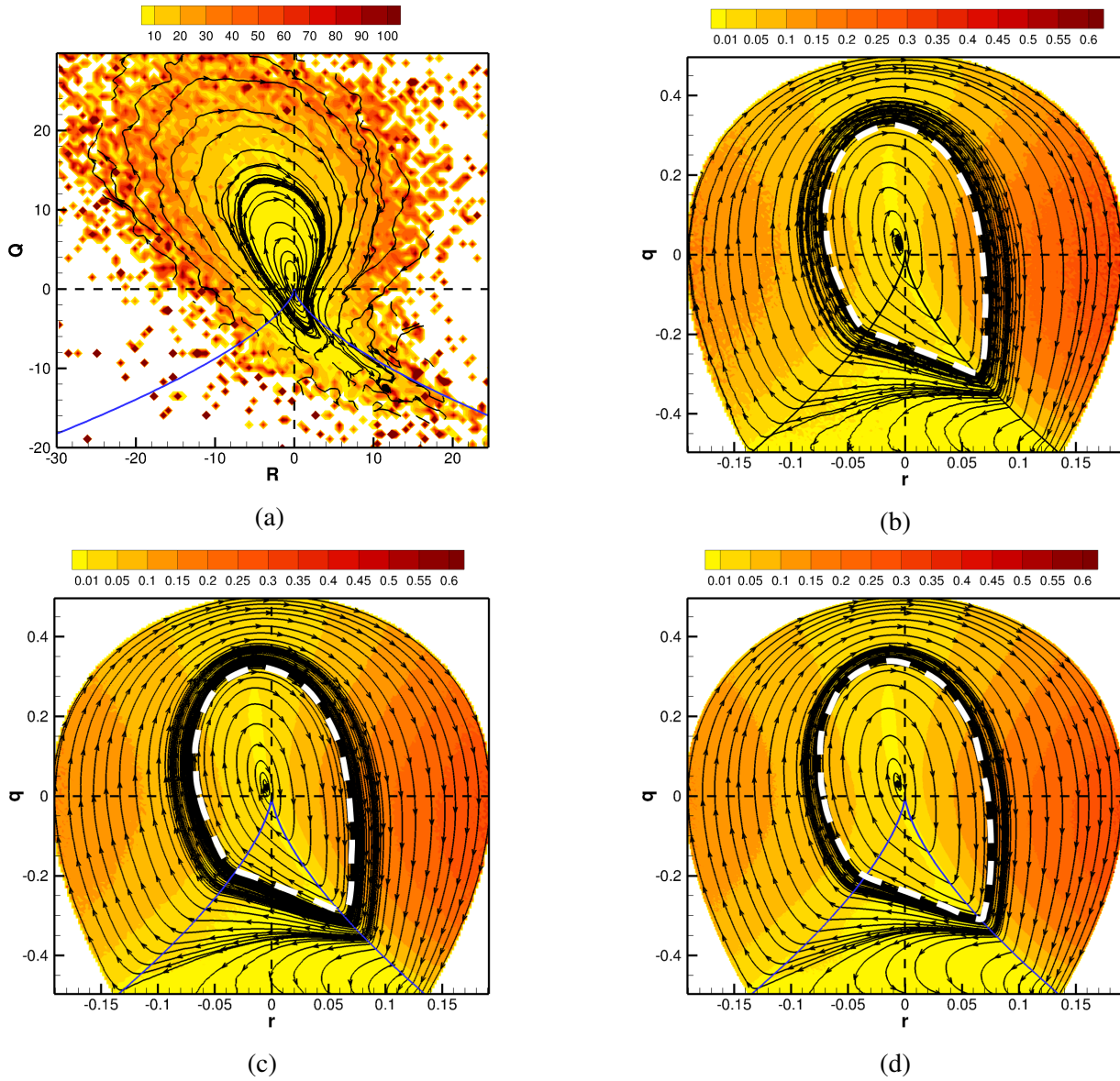


Figure 5.1: Conditional mean trajectories (CMTs) in (a) $Q-R$ plane for $Re_\lambda = 225$ (b) $q-r$ plane for $Re_\lambda = 225$ (c) $q-r$ plane for $Re_\lambda = 385$ (d) $q-r$ plane for $Re_\lambda = 588$. Background contours indicate the speed of the trajectory at each point, normalized by Kolmogorov time scale. White dashed lines represent the corresponding separatrices. Reprinted with permission from Das and Girimaji (2020a).

when vorticity is more aligned with the most expansive or most compressive strain-rates. CMTs become considerably slower after crossing the right discriminant line. The nodal streamline shapes with extremely low rate of evolution, therefore, constitute the long-lived structures in turbulent flow. The extremely low velocities near the discriminant line in the Q - R plane prompted many to believe that the discriminant line is an attractor (Martín et al., 1998b). However, the q - r plane clearly indicates that even though the trajectories slow down near the discriminant line, it is not an attractor of the system.

The q - r CMTs for all the investigated Reynolds numbers, $Re_\lambda = 225, 385$ and 588 , are very similar: (i) The two attractors of the system are identically located. (ii) However, the location of the separatrix appears to vary slightly with Reynolds number. These discrepancies could be due to the differences in resolutions ($k_{max}\eta$) of the DNS data sets.

5.5.3 Cycle time period of CMT

Figure 5.2 (a-c) illustrates the time evolution of q and r for a representative CMT in inner q - r plane. The inner trajectories spiral towards the attractor in nearly periodic cycles. Both q and r oscillate in time with decreasing amplitude and asymptote to the close neighborhood of the attractor ($q \approx 0, r \approx 0$). The time period of cycle decreases monotonically as the trajectory goes from the separatrix to the attractor: $T_{sep} \sim 35\tau_\eta$ at the separatrix and $T_{in} \sim 25\tau_\eta$ at the innermost oscillations about the attractor. Similar behavior is observed at other Reynolds numbers ($Re_\lambda = 385, 588$). This range, $T \in (25\tau_\eta, 35\tau_\eta)$, includes the characteristic cycle time of $30\tau_\eta$ reported by Martín et al. (1998b) for spiraling trajectories in Q - R plane in a lower Re_λ forced homogeneous isotropic turbulence.

The outer trajectories exhibit aperiodic behavior and tend toward the pure strain attracting manifold. This is illustrated by two CMTs in figure 5.2 (d-f) at the two extreme ends of the outer region - one remains close to the separatrix (solid magenta line) and the other travels towards the boundary of the realizable region (dash-dot blue line). A CMT originating on the separatrix continues to move along the separatrix for a number of cycles with a time period $\sim T_{sep}$ until it slightly drifts out of this loop on either one of the sides and evolves toward the corresponding

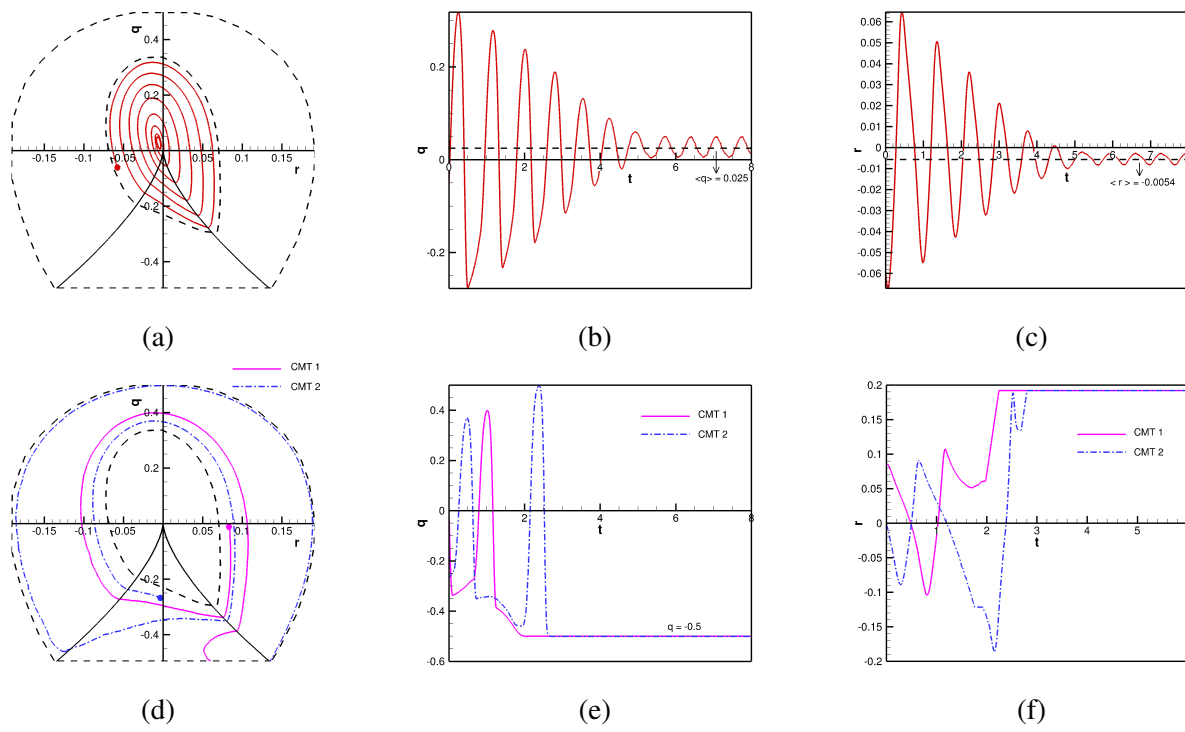


Figure 5.2: (a) A representative inner CMT (point of origin marked by circle) and corresponding (b) q evolution with time (c) r evolution with time. (d) Two representative outer CMTs (points of origin marked by circles) and corresponding (e) q evolution with time (f) r evolution with time. Dashed lines in (a,d) represent the separatrix loop and boundary of realizable region of q - r plane. Reprinted with permission from Das and Girimaji (2020a).

	SFS	UFC	UN/S/S	SN/S/S
Inner region % composition	44.7	27.6	21.5	6.2
Inner CMT residence time (%)	44.0	26.8	22.4	6.7
Outer region % composition	26.0	20.9	40.7	12.3
Outer CMT1 residence time (%)	31.9	19.3	34.0	14.8
Outer CMT2 residence time (%)	22.7	13.8	29.6	33.9

Table 5.1: Percentage composition of topologies in inner and outer regions and residence time (%) of representative CMTs (figure 5.2) in each topology. Reprinted with permission from Das and Girimaji (2020a).

attractor.

5.5.4 Residence time of CMTs in topologies

The percentage of total time spent by a q - r CMT in each topology type is the residence time (referred to as mean lifetime by Parashar et al. (2019)) for that topology. The residence time is a measure of the average lifetime of that topology in turbulence. Therefore, it is compared with the percentage composition of each topology in a turbulent flow field. The residence time of the representative CMTs shown in figure 5.2, are listed in table 5.1 along with the percentage composition of each topology in inner and outer regions for comparison. The residence time percentages of the inner CMTs are very close to the population percentages of the corresponding topologies in the inner region. In the outer region, CMT-1 (closer to the separatrix) has residence times fairly close to the population percentages while the residence times of CMT-2 show significant deviation from the population fractions. The high-density inner region constitutes majority of the population and the residence time here conforms well with the population percentages. The results agree well with the work of Parashar et al. (2019), who showed that the residence time of Lagrangian trajectories (obtained from particle tracking) in each topology is in the same proportion as the percentage composition of the topology. In contrast, the residence times based on Q - R CMTs investigated by Martín et al. (1998b) and Elsinga and Marusic (2010a) do not compare well with the Lagrangian results. This demonstrates yet another advantage of examining the CMTs in the q - r space.

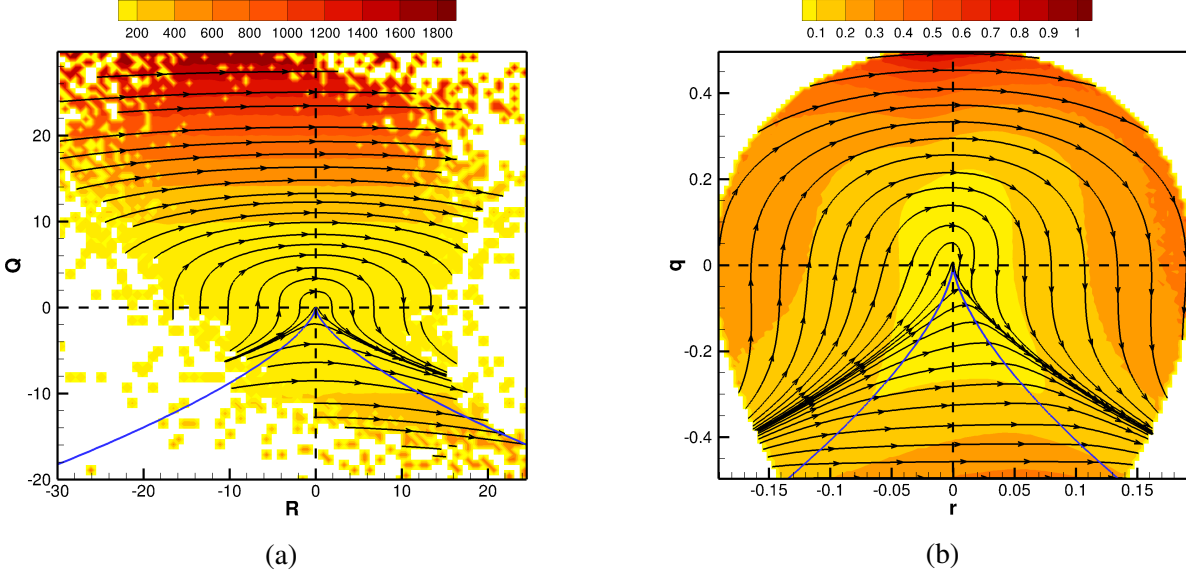


Figure 5.3: Inertial CMTs in (a) Q - R plane and (b) q - r plane for $Re_\lambda = 225$. Background contours indicate the speed of the trajectory at each point, normalized by Kolmogorov time scale. Reprinted with permission from Das and Girimaji (2020a).

5.6 Effect of different physical processes

The evolution of the invariants, q and r , depends on three distinct physical processes - inertial, pressure and viscous. The effect of each of these processes is examined in isolation in the following sub-sections.

5.6.1 Inertial effects

Q-R plane: The inertial CMTs in Q - R plane, as depicted in figure 5.3 (a), move from left to right in the plane, rendering stable topologies unstable. This is in line with the CMTs obtained from the restricted Euler solution (Cantwell, 1992) shown by Martín et al. (1998a), Ooi et al. (1999) and Chevillard et al. (2008). Some of the trajectories tend to asymptote to a line above the right $D = 0$ line (invariant line of restricted Euler solution) due to the absence of the isotropic pressure term. This line is also different from the invariant line of Burger's equation, shown in Bikkani and Girimaji (2007), since the incompressibility condition is not enforced in that case.

q-r plane: The q,r -evolution due to inertial effects, as given in equation (5.8), is plotted in

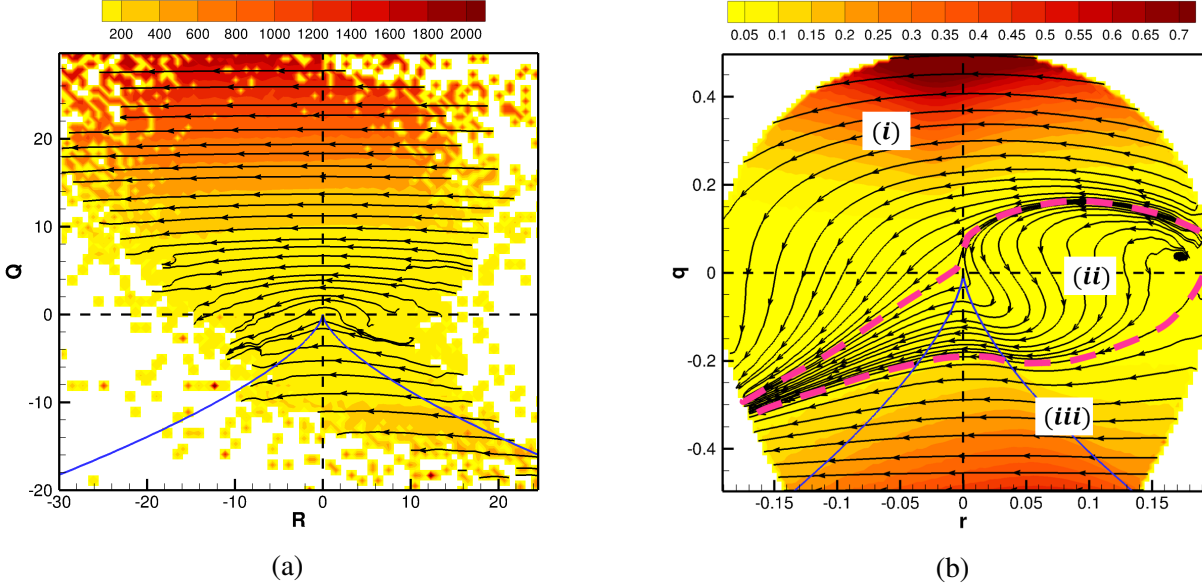


Figure 5.4: Pressure CMTs in (a) Q - R plane and (b) q - r plane for $Re_\lambda = 225$. Background contours indicate the speed of the trajectory at that point, normalized by Kolmogorov time scale. The dashed lines separate the three types of pressure CMTs in q - r space. Reprinted with permission from Das and Girimaji (2020a).

figure 5.3 (b) for $Re_\lambda = 225$. Since the inertial terms only depend on \mathbf{b} , the CMTs for other Re_λ cases are exactly identical and are not displayed separately. As observed for the Q - R plane (Martín et al., 1998a), the origin of the q - r plane also appears to be a degenerate saddle point. Clearly, in this compact and bounded phase space, the left boundary acts as a repeller and the right boundary acts as an attractor of the system. Referring back to figure 3.3, it is evident that inertia, whilst acting in isolation, causes the intermediate strain-rate to become more positive and the vorticity vector to be more aligned with the most compressive strain-rate eigendirection.

5.6.2 Pressure effects

Q-R plane: Figure 5.4 (a) shows the Q - R CMTs due to pressure action. As opposed to the anisotropic pressure Hessian contribution to Q - R evolution illustrated in previous studies (Chevillard et al., 2008; Johnson and Meneveau, 2016a), the complete pressure Hessian term has been plotted here. It shows that pressure action opposes the inertial action.

q-r plane: The q - r CMTs based on the pressure terms considered in isolation from the other

terms, as given in equation (5.8), are plotted in Figure 5.4 (b) for the $Re_\lambda = 225$ case. It is clear that there are three types of pressure CMTs - (i) CMTs of rotation-dominated focal streamlines near the top of the plane travel directly from the right boundary to the left boundary with very high speeds. (ii) CMTs in the middle region of the plane are repelled from a small region close to the right boundary and are attracted towards a small region in the left boundary. These relatively slow-moving CMTs tend to traverse along a line in the upper UFC region, get deflected by what appears to be a degenerate saddle point at origin and converges to the attractor in the lower SFS region. (iii) The strain-dominated streamlines near the bottom of the plane evolve reasonably fast, straight from the right to left boundary. Overall, pressure action causes UFC streamlines with vorticity along most compressive strain-rate (right boundary of the plane) to change towards SFS streamlines with vorticity aligned along the most expansive strain-rate (left boundary of the plane). In general the pressure trajectories oppose the inertial trajectories except the type-ii CMTs in the middle region of UFC topology, where pressure contribution aligns with the inertial contribution. The isotropic pressure term ($dq/dt = 0, dr/dt = -4Aq^2/3$) simply drives the streamline shapes from right to left in straight horizontal lines. All the additional features of the pressure CMTs stem from the anisotropic pressure term. Pressure q,r -CMTs at other Reynolds numbers (not displayed) are nearly identical to the present case and therefore effect of pressure on local streamline shape can be deemed nearly independent of Reynolds number at high enough Re_λ .

5.6.3 Pressure and inertial effects

In incompressible flows, the role of pressure is to counter inertial action in a manner that the velocity field is divergence free. As the action of pressure is a response to inertial effect on the velocity field, it may be useful to examine the combined outcome of the two processes.

Q-R plane: The $Q-R$ CMTs due to pressure and inertia are plotted in figure 5.5 (a) for $Re_\lambda = 225$. All trajectories appear to be repelled from the origin and moving outwards in clockwise direction. This indicates that pressure and inertia together increases the VG magnitude, evolving the streamline topology outward in the $Q-R$ plane.

q-r plane: The $q-r$ CMTs of pressure and inertial processes are plotted in figure 5.5 (b). The

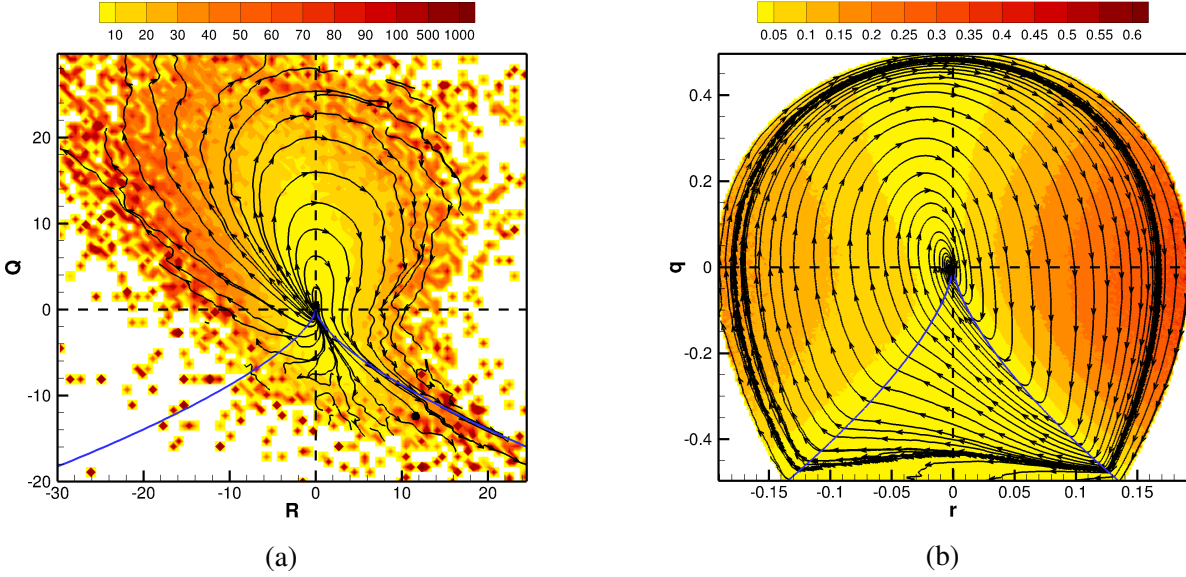


Figure 5.5: Pressure-inertial CMTs in (a) Q - R and (b) q - r plane for $Re_\lambda = 225$. Background contours indicate the speed of the trajectory at that point, normalized by Kolmogorov time scale. Reprinted with permission from Das and Girimaji (2020a).

trajectories suggest a very different picture. The pressure-inertial q - r CMTs are attracted towards the origin, which is in contrast to the pressure-inertial Q - R CMTs. The reason for this difference is that the Q - R trajectories predominantly reflect the growth in magnitude (altering the scale of streamline structure) and are unable to distinguish the effects on streamline shape.

There are two attractors in the q - r phase space - the origin, representing pure-shear, and the $q = -1/2$ line, representing pure strain. The CMTs spiral clockwise towards both the attractors. The basin of attraction of pure-shear attractor spans almost the entire q - r plane, with only a few CMTs in the slender outer region of extremely low population density that asymptote to the pure-strain attractor. The pressure-inertial CMTs are exactly identical in other Reynolds number cases (not displayed). Therefore, we conclude that *pressure responds to inertial action in a manner that most of the geometric shapes of streamlines evolve towards pure-shear geometry irrespective of the Reynolds number of the flow.*

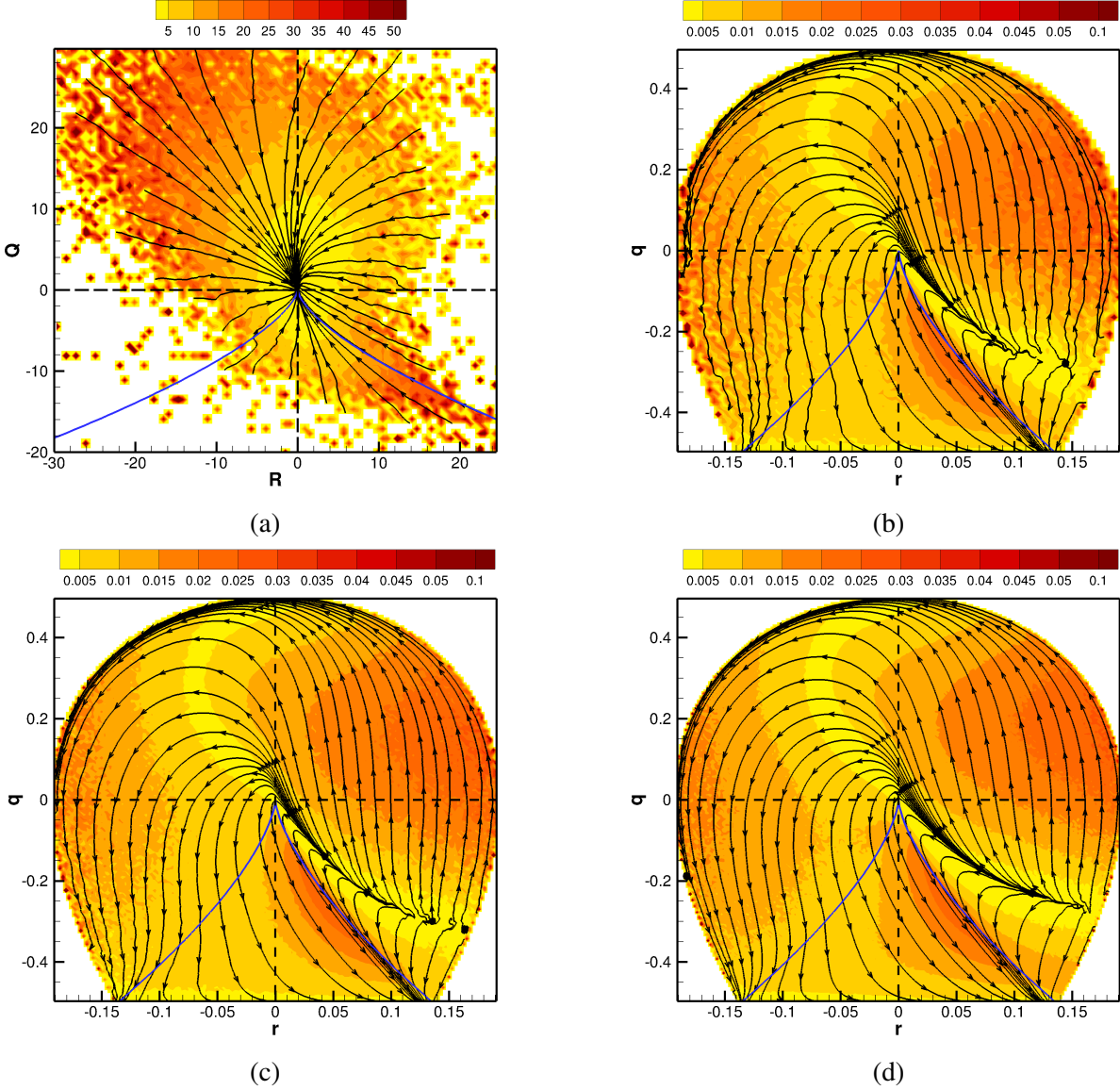


Figure 5.6: Viscous CMTs in (a) $Q-R$ plane for $Re_\lambda = 225$ (b) $q-r$ plane for $Re_\lambda = 225$ (c) $q-r$ plane for $Re_\lambda = 385$ (d) $q-r$ plane for $Re_\lambda = 588$. Background contours indicate the speed of the trajectory at that point, normalized by Kolmogorov time scale. Reprinted with permission from Das and Girimaji (2020a).

5.6.4 Viscous effects

Q-R plane: The viscous contribution to $Q-R$ evolution is plotted in figure 5.6 (a) and is in accordance with the results of Chevillard et al. (2008) and Johnson and Meneveau (2016a). Viscous action directs all trajectories in the $Q-R$ plane towards the origin. The evolution rate diminishes as the trajectories approach the origin. This reflects the damping effect of viscous action, which is to reduce the VG magnitudes of all streamline topologies alike. However, the effect of viscosity on evolution of geometric shape can not be surmised from the $Q-R$ CMTs.

q-r plane: The CMTs due to the viscous contribution to $q-r$ evolution, as given in equation (5.8), are plotted in figure 5.6 (b-d) for $Re_\lambda = 225, 385$ and 588 . Again, important features not apparent in the $Q-R$ CMTs are evident here. The viscous $q-r$ CMTs demonstrate that aside from reducing VG magnitude, the viscous action has a distinct influence on the geometric shape of the local streamlines. There exists a clearly defined repelling manifold in the lower UFC region. The only attracting manifold in this system is the $q = -1/2$ line, representing pure-strain streamlines with mutually orthogonal stretching and compression. Starting at the repelling manifold, viscous CMTs either follow a short path directly towards the attractor through UN/S/S streamline topology or take a longer path through SFS followed by SN/S/S and UN/S/S streamlines. Clearly, the viscous evolution of $q-r$ depends on its precise point of origin. Overall, *viscous action directs streamlines away from strain-dominated vortex compression towards pure-strain*. Even though the magnitude of viscous contribution is much lower than the pressure-inertial contribution, viscous action alters the pressure-inertial $q-r$ evolution by reducing the domain of attraction of pure-shear attractor and expanding that of pure-strain attracting manifold. The viscous action exhibits slight variation with Re_λ resulting in the weak Re_λ -dependence of the CMT separatrix observed in figure 5.1. This will be examined in detail in a future study using higher resolution DNS data.

5.7 Conclusion

This study characterizes the mean Lagrangian evolution of geometric shape using conditional mean trajectories (CMTs) in the phase space of normalized velocity gradient invariants (q,r). The

q - r plane provides a compact phase space to clearly identify the dynamical system behavior of the small-scale geometric shape due to the various turbulence processes. New features of the nonlocal pressure and viscous processes become evident in this plane, which are obscured by the presence of VG magnitude in the Q - R plane. The key findings are summarized below:

1. The q - r phase space can be divided into inner and outer regions. Inner CMTs spiral (clockwise) towards the pure-shear attractor at origin while outer CMTs (also clockwise) asymptote to pure-strain attracting manifold ($q = -1/2$). Inner CMTs are periodic in nature with time period, $T \in (25\tau_\eta, 35\tau_\eta)$, decreasing progressively inwards while outer CMTs are aperiodic in nature.
2. The residence times of CMTs in different topologies are proportional to their percentage compositions particularly in the inner region. Therefore, it is evident that q - r CMTs are fairly accurate approximations of mean Lagrangian evolution of local streamline shape.
3. Pressure-inertial effects dominate in the inner region driving all geometric shapes towards pure-shear attractor while in the outer region, pressure-inertial-viscous effects together direct all streamline shapes towards pure-strain.
4. q - r CMTs are nearly invariant with Re_λ at high enough Reynolds numbers, except for a slight dependence of the separatrix on Re_λ , possibly due to the viscous effects.

The study highlights some of the key features of turbulence processes in evolution of internal structure of streamlines, not evident in previously studied frameworks. The characterization of pressure and viscous processes in the evolution of geometric shape indicate the amenability of their closure modeling in the bounded q - r phase space, thus leading toward a Lagrangian model for VG tensor evolution. In future work, the evolution of the entire four-parameter system - q , r , a_2 and $|\omega_2|$ - will be characterized to determine the complete streamline shape dynamics.

6. EFFECT OF LARGE-SCALE FORCING ON SMALL-SCALE VELOCITY GRADIENT DYNAMICS

6.1 Introduction

While the principal role of large-scale forcing is to sustain turbulence, it also has a profound effect on the small-scale dynamics. In most flows occurring in nature, large-scale forcing takes the form of production which extracts kinetic energy from the mean flow and injects it into the turbulent field (Tennekes and Lumley, 2018; Pope, 2000). Production, which is a function of the mean velocity gradients and Reynolds stresses, is strongly flow dependent and can be anisotropic and inhomogeneous. Numerically generated turbulence is sustained by randomized forcing at large scales (Eswaran and Pope, 1988). In most cases, the kinetic energy is introduced in the large scales and it subsequently cascades to smaller scales, due to the non-linear inertial action, before being dissipated at the viscous small scales. Even though the forcing mechanism is prominent at the larger scales, it is responsible for sustaining turbulence at all scales of motion.

Kolmogorov (1941) proposes that at high enough Reynolds numbers, the small-scale behavior is insensitive to the manner of large-scale forcing. In recent years some studies (Yeung and Brasseur, 1991; Biferale and Vergassola, 2001; Danaila et al., 2002) have shown that anisotropic features of large-scale forcing do carry over to the small scales to some degree. Nonetheless, the small-scale universality is observed in a variety of flows with different types of forcing. As a consequence, numerical simulations of forced isotropic turbulence have been widely used to understand small-scale characteristics such as velocity-gradient (VG) structure functions and scaling exponents. Much attention has been given to the probability distribution and dynamical behavior of second and third invariants (Q , R) of the VG tensor due to their importance in classifying the local streamline topology (Chong et al., 1990). It is now well established that the Q - R joint probability density function (PDF) has a characteristic tear-drop shape in various turbulent flows subject to different types of forcing (Soria et al., 1994; Blackburn et al., 1996; Chong et al., 1998;

Dodd and Jofre, 2019). In addition, it has also been shown that the Q - R conditional mean trajectories due to inertia, pressure and viscous mechanisms are very similar in different types of flows such as forced isotropic turbulence, turbulent boundary layers, mixing layers, etc. (Martín et al., 1998b; Ooi et al., 1999; Chevillard et al., 2008; Atkinson et al., 2012; Lawson and Dawson, 2015; Bechlars and Sandberg, 2017a; Wu et al., 2019). To date, the role of large-scale production (or random forcing) in small-scale dynamics has not been established. Lacking such understanding, our knowledge of turbulence small scales must be considered incomplete.

The objective of this study is to examine the role of large-scale forcing in velocity-gradient dynamics. Specifically, we seek to establish the interplay between forcing, inertial, pressure and viscous mechanisms that leads to the “universal” features of velocity-gradients, such as the tear-drop shape of the Q - R joint PDF and near log-normal distribution of the pseudo-dissipation (Oboukhov, 1962; Yeung and Pope, 1989). While the Q - R phase plane accurately classifies the local streamlines into four distinct topologies, it cannot uniquely determine the streamline geometry (Elsinga and Marusic, 2010a; Das and Girimaji, 2020a). Further, Q, R values can grow without bounds with increasing Reynolds numbers. It is pointed out by Girimaji and Speziale (1995) that VG tensor normalized by its magnitude (Frobenius norm) is better suited for examining many aspects of small-scale dynamics. Specifically, the normalized invariants (q, r) provide a bounded phase-space that uniquely characterizes the complete shape of the local flow streamlines (Das and Girimaji, 2019, 2020a). In this study, we first demonstrate that the q - r PDF exhibits a greater degree of self-similarity over different flows than Q - R PDF. The inertial, pressure and viscous action in the compact q - r plane constitutes a well-defined but incomplete dynamical system and yet yields important insight into the nature of these turbulence processes (Das and Girimaji, 2020a). To complete the description of VG dynamics, the effect of forcing is examined in the normalized q - r framework. In the next part, we present a thorough investigation into the effect of inertia, pressure, viscosity and large-scale forcing on the evolution of the VG magnitude.

Toward this end, we first derive the governing equations for the normalized VG tensor and the VG magnitude highlighting the contribution of the forcing term. We develop the PDF evolution

equations for the normalized invariants, q and r , as well as the VG magnitude, A , in Section 6.2. Analysis of the DNS data and a discussion of the findings are given in Sections 6.3 - 6.5. The final conclusions are presented in Section 6.6.

6.2 Forcing in velocity-gradient evolution equations

The governing Navier-Stokes equations for velocity fluctuations, u_i , as obtained from the mass and momentum conservation of an incompressible flow are given by

$$\frac{\partial u_i}{\partial t} + u_k \frac{\partial u_i}{\partial x_k} = -\frac{\partial p}{\partial x_i} + \nu \nabla^2 u_i + f_i \quad (6.1a)$$

$$\frac{\partial u_i}{\partial x_i} = 0 \quad (6.1b)$$

where, p is the pressure fluctuation, ν is the kinematic viscosity, and f_i represents forcing. The pressure and viscous terms represent important non-local effects on the evolution of the velocity field. The forcing term is responsible for the production of energy at the large scales, which compensates for the viscous dissipation of energy at the smaller scales. The general form of forcing encountered in most turbulent flows is

$$f_i = -\langle U_k \rangle \frac{\partial u_i}{\partial x_k} - u_k \frac{\partial \langle U_i \rangle}{\partial x_k} + \frac{\partial}{\partial x_k} \langle u_i u_k \rangle \quad (6.2)$$

where, $U_i = \langle U_i \rangle + u_i$ is the total velocity. Here $\langle . \rangle$ indicates ensemble averaging or spatial averaging in the homogeneous directions. The forcing depends on the mean flow field and inhomogeneity of turbulent fluctuations (Rogallo, 1981; Rogers and Moin, 1987; Lee and Moser, 2015; Quadrio et al., 2016). Forcing in a numerical simulation of homogeneous isotropic turbulence with no mean flow ($\langle U_i \rangle = 0$) entails injecting energy into the lowest wave number shells. This forcing is a function of time and space and can be of different types (Eswaran and Pope, 1988; Machiels, 1997; Overholt and Pope, 1998; Donzis and Yeung, 2010).

We examine the effect of forcing on the evolution of the velocity gradient tensor,

$$A_{ij} = \frac{\partial u_i}{\partial x_j} \quad \text{where } A_{ii} = 0. \quad (6.3)$$

From equation (6.1a), the evolution equation for VG tensor A_{ij} can be derived:

$$\frac{\partial A_{ij}}{\partial t} + u_k \frac{\partial A_{ij}}{\partial x_k} = -A_{ik}A_{kj} - \frac{\partial^2 p}{\partial x_i \partial x_j} + \nu \nabla^2 A_{ij} + \frac{\partial f_i}{\partial x_j}. \quad (6.4)$$

Here, $(-A_{ik}A_{kj})$ is referred to as the inertial term, which includes vortex stretching and strain self-amplification. Using the incompressibility condition ($A_{ii} = 0$) in equation (6.4), it can be shown that

$$-\frac{\partial^2 p}{\partial x_i \partial x_i} + \frac{\partial f_i}{\partial x_i} = A_{ik}A_{ki}. \quad (6.5)$$

Note that the second term is zero in forced isotropic turbulence since f_i is a solenoidal field by construction. Applying equation (6.5), the VG tensor evolution equation (6.4) can be written as

$$\frac{dA_{ij}}{dt} = -A_{ik}A_{kj} + \frac{1}{3}A_{mk}A_{km}\delta_{ij} + H_{ij} + T_{ij} + G_{ij} \quad (6.6)$$

where $d/dt = \partial/\partial t + u_k \partial/\partial x_k$ is material or substantial derivative. Here, \mathbf{H} is the anisotropic pressure Hessian tensor, \mathbf{T} is the viscous Laplacian tensor, and \mathbf{G} is the anisotropic forcing tensor, defined as follows:

$$H_{ij} = -\frac{\partial^2 p}{\partial x_i \partial x_j} + \frac{\partial^2 p}{\partial x_k \partial x_k} \frac{\delta_{ij}}{3}; \quad T_{ij} = \nu \nabla^2 A_{ij}; \quad G_{ij} = \frac{\partial f_i}{\partial x_j} - \frac{\partial f_k}{\partial x_k} \frac{\delta_{ij}}{3}. \quad (6.7)$$

The anisotropic forcing tensor G_{ij} represents the influence of the mean flow and inhomogeneity on the fluctuating velocity gradient evolution. In case of forced isotropic turbulence, G_{ij} represents the effect of artificial large scale forcing on the fluctuating field.

Following Girimaji and Speziale (1995) and Das and Girimaji (2019), A_{ij} is factorized into

velocity-gradient magnitude A and a normalized velocity gradient tensor (b_{ij}):

$$b_{ij} \equiv \frac{A_{ij}}{A} \quad \text{where } A \equiv \|\mathbf{A}\|_F = \sqrt{A_{ij}A_{ij}}. \quad (6.8)$$

Here, $\|\cdot\|_F$ is the Frobenius norm of the tensor. All of the information about the geometry of the local streamline structure of the flow is contained within the mathematically bounded tensor b_{ij} (Das and Girimaji, 2020a). Furthermore, the topological classification of the local flow streamlines (Chong et al., 1990) can also be described in the bounded phase-plane of b_{ij} invariants, q and r :

$$q = -\frac{1}{2}b_{ij}b_{ji} \quad ; \quad r = -\frac{1}{3}b_{ij}b_{jk}b_{ki}. \quad (6.9)$$

The VG magnitude A , on the other hand, determines the scale-factor of the local flow streamlines. In this work we examine the effect of forcing on A and b_{ij} individually.

6.2.1 Evolution equations of normalized VG tensor

Using equations (6.6) and (6.8), we can derive the following evolution equation for b_{ij} ,

$$\begin{aligned} \frac{db_{ij}}{dt'} = & - b_{ik}b_{kj} + \frac{1}{3}b_{km}b_{mk}\delta_{ij} + b_{ij}b_{mk}b_{kn}b_{mn} + (h_{ij} - b_{ij}b_{kl}h_{kl}) \\ & + (\tau_{ij} - b_{ij}b_{kl}\tau_{kl}) + (g_{ij} - b_{ij}b_{kl}g_{kl}) \end{aligned} \quad (6.10)$$

where $dt' = A dt$ represents a normalized time increment and

$$h_{ij} = \frac{H_{ij}}{A^2} \quad ; \quad \tau_{ij} = \frac{T_{ij}}{A^2} \quad ; \quad g_{ij} = \frac{G_{ij}}{A^2} \quad (6.11)$$

are the normalized anisotropic pressure Hessian, viscous Laplacian and anisotropic forcing tensors, respectively. Similarly, the following governing equations for q and r can be derived (Das and Girimaji, 2019) from equation (6.10):

$$\frac{dq}{dt'} = -3r + 2qb_{ij}b_{ik}b_{kj} - h_{ij}(b_{ji} + 2qb_{ij}) - \tau_{ij}(b_{ji} + 2qb_{ij}) - g_{ij}(b_{ji} + 2qb_{ij}), \quad (6.12)$$

$$\begin{aligned} \frac{dr}{dt'} = & \frac{2}{3} q^2 + 3rb_{ij}b_{ik}b_{kj} - h_{ij}(b_{jk}b_{ki} + 3rb_{ij}) - \tau_{ij}(b_{jk}b_{ki} + 3rb_{ij}) \\ & - g_{ij}(b_{jk}b_{ki} + 3rb_{ij}). \end{aligned} \quad (6.13)$$

The first two terms on the right-hand-side (RHS) of equations (6.12-6.13) are referred to as the non-linear (N) terms that constitute the inertial and isotropic pressure effects in a turbulent flow. The third RHS term represents anisotropic pressure effect (P) while the fourth term embodies viscous action (V) on the q - r dynamics. Finally, the last term in both the equations represent the effect of forcing (F) on the evolution of q and r .

b_{ij} -PDF evolution equation: Following the methodology of Girimaji and Pope (1990a), the governing differential equation for the joint PDF of b_{ij} , $\mathbb{F}(\mathbf{b})$, is given by

$$\frac{d\mathbb{F}}{dt'} = -\frac{d}{db_{ij}} \left(\mathbb{F} \left\langle \frac{db_{ij}}{dt'} \middle| \mathbf{b} \right\rangle \right). \quad (6.14)$$

Here, the $\frac{db_{ij}}{dt'}$ is given by equation (6.10). In this work, we restrict our analysis to the \mathbf{b} invariants - q and r . The evolution equation for the q - r joint PDF, $\mathcal{F}(q, r)$, is given by,

$$\frac{d\mathcal{F}}{dt'} = -\frac{d}{dq} \left(\mathcal{F} \left\langle \frac{dq}{dt'} \middle| q, r \right\rangle \right) - \frac{d}{dr} \left(\mathcal{F} \left\langle \frac{dr}{dt'} \middle| q, r \right\rangle \right). \quad (6.15)$$

The above conditional average terms are comprised of the effects of non-linear, pressure, viscous and forcing processes from equations (6.12-6.13).

Conditional Mean Velocity: The dynamics of the velocity gradient invariants, q and r , is commonly investigated by examining the conditional mean trajectories (CMTs) (Martín et al., 1998b). The CMTs are obtained by integrating a vector field of conditional mean velocity ($\tilde{\mathbf{v}}$) in the q - r plane, given by

$$\tilde{\mathbf{v}} = \left\langle \left(\begin{array}{c} dq/dt' \\ dr/dt' \end{array} \right) \middle| q, r \right\rangle. \quad (6.16)$$

Probability Current: Probability current, \mathbf{W} , is the PDF-weighted conditional mean velocity

(van der Bos et al., 2002; Chevillard et al., 2008):

$$\mathbf{W} = \mathcal{F}\tilde{\mathbf{v}} = \mathcal{F}(q, r) \times \left\langle \left(\begin{array}{c} dq/dt' \\ dr/dt' \end{array} \right) \middle| q, r \right\rangle. \quad (6.17)$$

The evolution equation of q - r joint PDF (equation 6.15) can therefore be written as,

$$\frac{d\mathcal{F}}{dt'} + \nabla \cdot \mathbf{W} = 0. \quad (6.18)$$

The divergence of \mathbf{W} determines the evolution rate of the PDF, $\mathcal{F}(q, r)$, at a given point in the q - r space. Probability current has identical trajectories as the CMTs, since \mathbf{W} is obtained by multiplying $\tilde{\mathbf{v}}$ with a non-negative function $\mathcal{F}(q, r)$. The difference between the two is only in the speed of these trajectories. Probability current is used to examine the mean q - r evolution in this study owing to its inherent physical relevance. The q - r probability currents due to non-linear (N), anisotropic pressure (P), viscous (V) and forcing (F) effects can be defined individually as follows, from equations (6.12-6.13) and (6.17):

$$\begin{aligned} \mathbf{W}_N &= \mathcal{F} \left\langle \left(\begin{array}{c} -3r + 2qb_{ij}b_{ik}b_{kj} \\ \frac{2}{3}q^2 + 3rb_{ij}b_{ik}b_{kj} \end{array} \right) \middle| q, r \right\rangle; \\ \mathbf{W}_P &= \mathcal{F} \left\langle \left(\begin{array}{c} -h_{ij}(b_{ji} + 2qb_{ij}) \\ -h_{ij}(b_{jk}b_{ki} + 3rb_{ij}) \end{array} \right) \middle| q, r \right\rangle; \\ \mathbf{W}_V &= \mathcal{F} \left\langle \left(\begin{array}{c} -\tau_{ij}(b_{ji} + 2qb_{ij}) \\ -\tau_{ij}(b_{jk}b_{ki} + 3rb_{ij}) \end{array} \right) \middle| q, r \right\rangle; \\ \mathbf{W}_F &= \mathcal{F} \left\langle \left(\begin{array}{c} -g_{ij}(b_{ji} + 2qb_{ij}) \\ -g_{ij}(b_{jk}b_{ki} + 3rb_{ij}) \end{array} \right) \middle| q, r \right\rangle. \end{aligned} \quad (6.19)$$

Statistically Stationary Homogeneous Flow: The q - r PDF equation (6.18) for a statistically

steady and homogeneous turbulent flow leads to

$$\frac{d\mathcal{F}}{dt'} = \frac{\partial\mathcal{F}}{\partial t'} = -\nabla \cdot \mathbf{W} = -\nabla \cdot (\mathbf{W}_N + \mathbf{W}_P + \mathbf{W}_V + \mathbf{W}_F) = 0. \quad (6.20)$$

Most studies in the past (Martín et al., 1998b; Ooi et al., 1999; Chevillard et al., 2008; Atkinson et al., 2012) have examined only the non-linear, pressure and viscous effects. From DNS data presented in these studies, $\nabla \cdot (\mathbf{W}_N + \mathbf{W}_P + \mathbf{W}_V) \neq 0$ and correspondingly the CMTs or probability currents given by $(\mathbf{W}_N + \mathbf{W}_P + \mathbf{W}_V)$ do not form closed loop orbits. Clearly, in order for $\nabla \cdot \mathbf{W} = 0$, the contribution of the forcing terms is critically important. This must also render the CMTs to form closed loops.

6.2.2 Evolution equations of VG magnitude

The dynamics of VG magnitude (A) is examined in terms of

$$\theta \equiv \ln A. \quad (6.21)$$

The evolution equation for θ , as derived from equation (6.6), is

$$\frac{d\theta}{dt^*} = \frac{1}{\langle A \rangle} (-b_{ik}b_{kj}A_{ij} + h_{ij}A_{ij} + \tau_{ij}A_{ij} + g_{ij}A_{ij}) \quad (6.22)$$

where $t^* = \langle A \rangle t$ represents time normalized by mean VG magnitude. It is found that this normalization is more appropriate for examining VG magnitude. Here, the four terms on the RHS of the above equation represent the nonlinear (N), pressure (P), viscous (V), and forcing (F) effects on VG magnitude evolution.

θ -PDF evolution equation: The governing differential equation for the PDF of θ , $\tilde{f}(\theta)$, is given by (Pope, 1985)

$$\frac{d\tilde{f}}{dt^*} = -\frac{d}{d\theta} \left(\tilde{f} \left\langle \frac{d\theta}{dt^*} \middle| \theta \right\rangle \right). \quad (6.23)$$

Conditional mean rate of change: The VG magnitude dynamics is examined in terms of the

mean rate of change of θ conditioned on θ ,

$$\tilde{u} = \left\langle \frac{d\theta}{dt^*} \middle| \theta \right\rangle = \tilde{u}_N + \tilde{u}_P + \tilde{u}_V + \tilde{u}_F \quad (6.24)$$

where,

$$\begin{aligned} \tilde{u}_N &= \frac{1}{\langle A \rangle} \langle -b_{ik}b_{kj}A_{ij} | \theta \rangle ; & \tilde{u}_P &= \frac{1}{\langle A \rangle} \langle -h_{ij}A_{ij} | \theta \rangle ; \\ \tilde{u}_V &= \frac{1}{\langle A \rangle} \langle -\tau_{ij}A_{ij} | \theta \rangle ; & \tilde{u}_F &= \frac{1}{\langle A \rangle} \langle -g_{ij}A_{ij} | \theta \rangle \end{aligned} \quad (6.25)$$

represent the mean non-linear, pressure, viscous and forcing effects. For a statistically stationary homogeneous turbulent flow, the equation (6.23) can now be written as

$$\frac{d\tilde{f}}{dt^*} = \frac{\partial \tilde{f}}{\partial t^*} = -\frac{\partial}{\partial \theta} [\tilde{f}(\tilde{u}_N + \tilde{u}_P + \tilde{u}_V + \tilde{u}_F)] = 0. \quad (6.26)$$

Therefore, for the PDF $\tilde{f}(\theta)$ to be stationary, the sum of the PDF-weighted conditional mean contributions of all the processes should not be a function of θ .

6.3 Numerical simulation data

Established DNS data sets of forced isotropic turbulence and turbulent channel flow at high Reynolds numbers are used for analysis in this study. Additional detail of these datasets are included in the appendix A.

The forced isotropic turbulence (FIT) data from the Johns Hopkins Turbulence Database (Perlman et al., 2007; Li et al., 2008) is used in the present study. The Taylor Reynolds number of the field data used is,

$$Re_\lambda \equiv \frac{u'\lambda}{\nu} = 427, \quad \text{where } \lambda = \sqrt{\frac{15\nu u'^2}{\epsilon}}. \quad (6.27)$$

Here λ is the Taylor microscale, u' is the root-mean-square velocity, and $\epsilon = 2\nu \langle S_{ij}S_{ij} \rangle$ is the mean dissipation rate. The simulation is well resolved and has been widely used for investigating velocity gradient statistics (Johnson and Meneveau, 2016b; Elsinga et al., 2017; Danish and Meneveau,

2018) as well as its Lagrangian dynamics (Yu and Meneveau, 2010a,b) in turbulence. Field velocity data at multiple consecutive time steps, separated by $\Delta t = 0.0002$, is used to compute the temporal derivatives.

Three forced isotropic turbulence data sets from the Turbulence and Advanced Computations Laboratory (Donzis et al., 2008; Yakhot and Donzis, 2017) at Texas A&M University are also used. The Taylor Reynolds numbers of these simulations are $Re_\lambda = 225, 385$ and 588 . These data sets have been used in past studies to examine higher-order statistics, intermittency, and Reynolds number scaling of velocity gradients (Donzis et al., 2008; Donzis and Sreenivasan, 2010; Yakhot and Donzis, 2017; Das and Girimaji, 2019).

Turbulent channel flow data is also obtained from the Johns Hopkins Turbulence Database (Li et al., 2008; Lee and Moser, 2015). The data set used in the computations here is obtained after statistical stationarity is achieved. The friction velocity Reynolds number of the channel flow is

$$Re_\tau \equiv \frac{u_\tau h}{\nu} = 5186 \quad (6.28)$$

where u_τ is the friction velocity and h is the channel half-height. The velocity field is homogeneous in the stream-wise (x) and span-wise (z) directions and inhomogeneous in the wall-normal (y) direction. As suggested in the work of Lozano-Durán et al. (2015), integrating over a statistically inhomogeneous region can considerably bias the Lagrangian statistics. Therefore, to circumvent averaging over statistically inhomogeneous wall-normal (y) direction, we use data at specific y^+ planes: $y^+ = 100$ ($Re_\lambda = 81$), $y^+ = 203$ ($Re_\lambda = 110$), $y^+ = 302$ ($Re_\lambda = 132$), and $y^+ = 852$ ($Re_\lambda = 183$). Data from multiple time instants are considered to achieve adequate sampling.

6.4 Normalized VG tensor dynamics

The large-scale forcing mechanisms are very different in homogeneous isotropic turbulence and inhomogeneous anisotropic turbulent channel flow, as outlined in section 6.2. In this section, we first investigate the effect of the different types of forcing on the probability distribution of the invariants of the normalized velocity gradient tensor. Then, we proceed to examine the nonlinear,

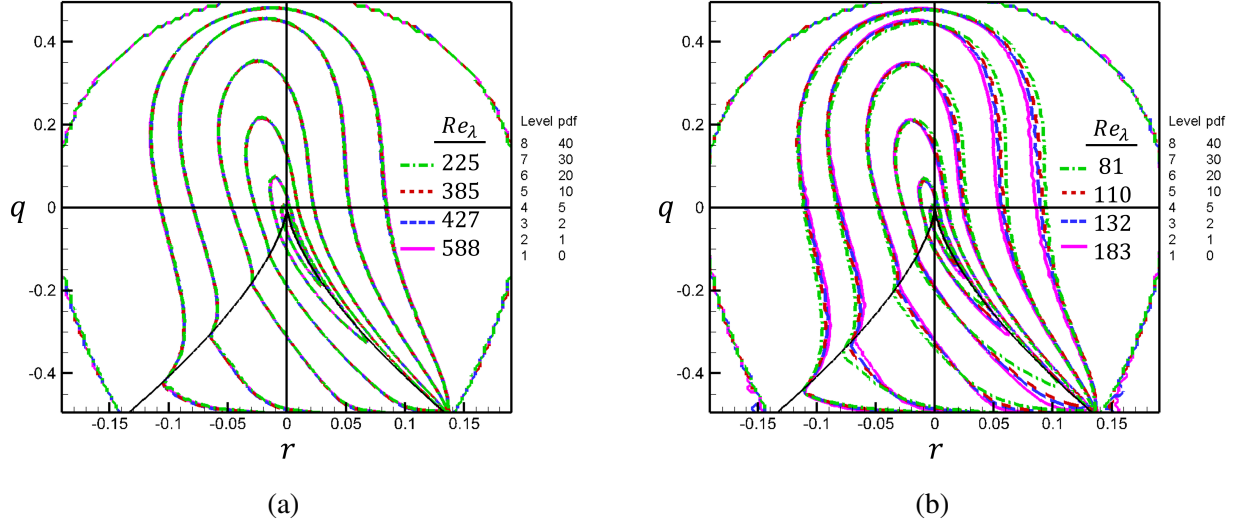


Figure 6.1: Isocontours of q - r joint PDF, $\mathcal{F}(q, r)$, for (a) forced isotropic turbulence (FIT), (b) turbulent channel flow, at different Re_λ . The highest PDF level contour is along the right discriminant line and the PDF level drops with distance from the line. Solid black lines in the 3rd and 4th quadrants represent the zero-discriminant lines (Cantwell, 1992).

pressure, and viscous contributions to the evolution of the invariants in these flows.

The isocontour lines of the q - r joint PDF in forced isotropic turbulent flows at different Re_λ and turbulent channel flow at different y^+ planes, are plotted in figure 6.1. The solid black lines in the third and fourth quadrants of the q - r plane mark the lines of zero discriminant: $d = q^3 + (27/4)r^2 = 0$. The q - r plane above the discriminant lines represents focal/spiraling topologies of local flow streamlines - stable focus stretching (SFS) and unstable focus compression (UFC). The q - r plane below the discriminant lines mark nodal/hyperbolic streamlines with node-saddle combinations - stable-node/saddle/saddle (SN/S/S) and unstable-node/saddle/saddle (UN/S/S) (Chong et al., 1990; Das and Girimaji, 2020a). Topologies to the left of $r = 0$ axis are stable or converging, while those to the right are unstable or diverging. The q - r joint PDFs for isotropic turbulent flow at $Re_\lambda = 225, 385, 427$ and 588 have the characteristic teardrop shape with a high probability of occurrence along the right discriminant line or Vieillefosse tail (Vieillefosse, 1984). It is evident that the PDF is nearly invariant at high enough Re_λ . The q - r joint PDFs for turbulent channel

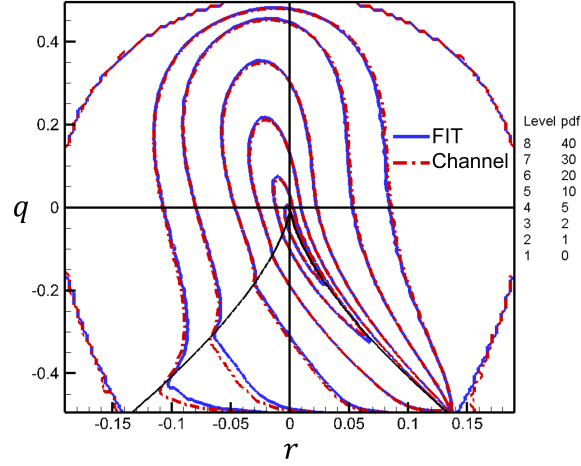


Figure 6.2: Isocontours of q - r joint PDF, $\mathcal{F}(q, r)$, of FIT at $Re_\lambda = 225$ (blue solid line) and turbulent channel flow at $Re_\lambda = 183$ (red dashed line).

flow at different y^+ locations, corresponding to $Re_\lambda = 81, 110, 132$ and 183 , are shown in figure 6.1(b). In this case, the PDF shows slight dependence on Reynolds number. As Re_λ increases, the isocontour lines in the focal topologies shrink closer towards the q -axis and the isocontour lines near the tail of the teardrop widen.

The q - r PDFs of forced isotropic turbulence at $Re_\lambda = 225$ and turbulent channel flow at $Re_\lambda = 183$, are compared in figure 6.2. It is evident that in the densely populated regions of the plane, the PDF values are nearly identical. There is a small difference between the PDF isocontours only in the low probability regions of the SN/S/S topology. Thus, despite having different forms of large-scale forcing, the joint probability distribution of normalized velocity gradient invariants are nearly identical in both the flows, even at moderately high Reynolds numbers. It is reasonable then to expect the overall VG dynamics to be statistically similar in both cases. To examine this further, we now investigate probability currents.

6.4.1 Non-linear, pressure and viscous effects

The q - r probability currents given in equation (6.19) represent the dynamical effects of the constituent mechanisms. The probability current of the inertial and isotropic pressure (\mathbf{W}_N) is

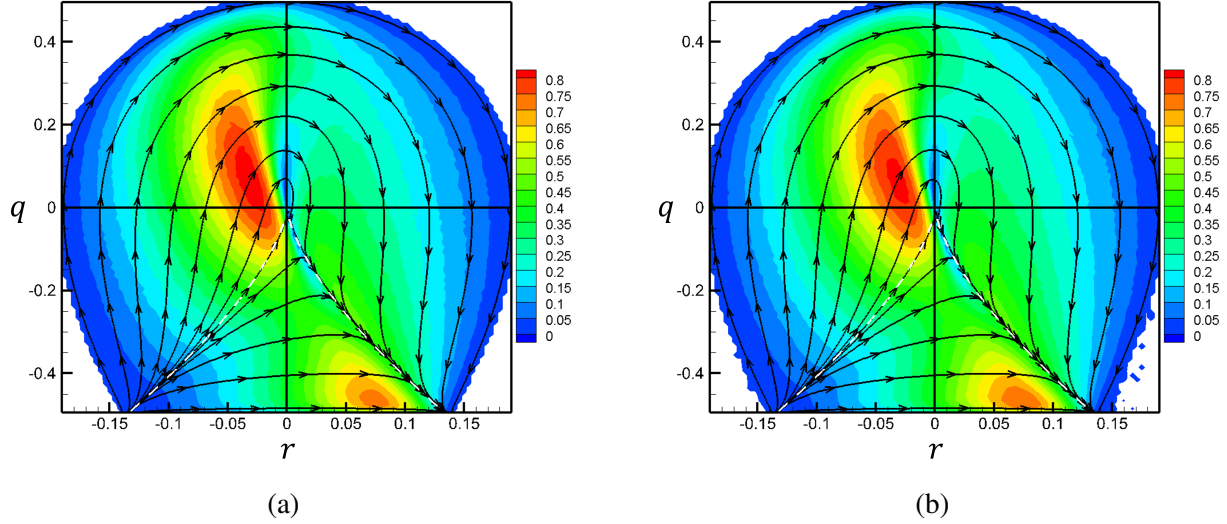


Figure 6.3: q - r probability current due to non-linear terms (\mathbf{W}_N) for (a) FIT $Re_\lambda = 225$ and (b) turbulent channel flow $Re_\lambda = 183$. The background contours represent the magnitude of the vector \mathbf{W}_N .

plotted in figure 6.3 for isotropic turbulent flow and turbulent channel flow. The background color contours represent the magnitude of \mathbf{W}_N , i.e. the speed of the trajectories. The non-linear effect (Cantwell, 1992; Bikkani and Girimaji, 2007) take trajectories from the left toward the right bottom corner along the zero-discriminant line. These probability currents are invariant with Re_λ and identical in different types of flows, due to the fact that \mathbf{W}_N (6.19) is fully determined by b_{ij} .

Next, the probability current due to the anisotropic pressure (\mathbf{W}_P), is illustrated in figure 6.4. The currents exhibit slight variations at low Re_λ and are nearly invariant at higher Re_λ . Only high Re_λ cases for both isotropic turbulence and channel flow are plotted. The principal action of the anisotropic pressure is to oppose the non-linear current (\mathbf{W}_N) in majority of the q - r plane, except in the middle UFC region where \mathbf{W}_P is nearly aligned with \mathbf{W}_N . The pressure probability currents repel trajectories away from the top right UFC region and attract them toward the bottom left corner of the plane, which is the repeller of the \mathbf{W}_N field. The effect of non-local pressure is stronger in the UN/S/S topology region below the right discriminant line and in the rotation-dominated SFS region. \mathbf{W}_P contribution is nearly identical in FIT and channel flow. The results clearly suggest

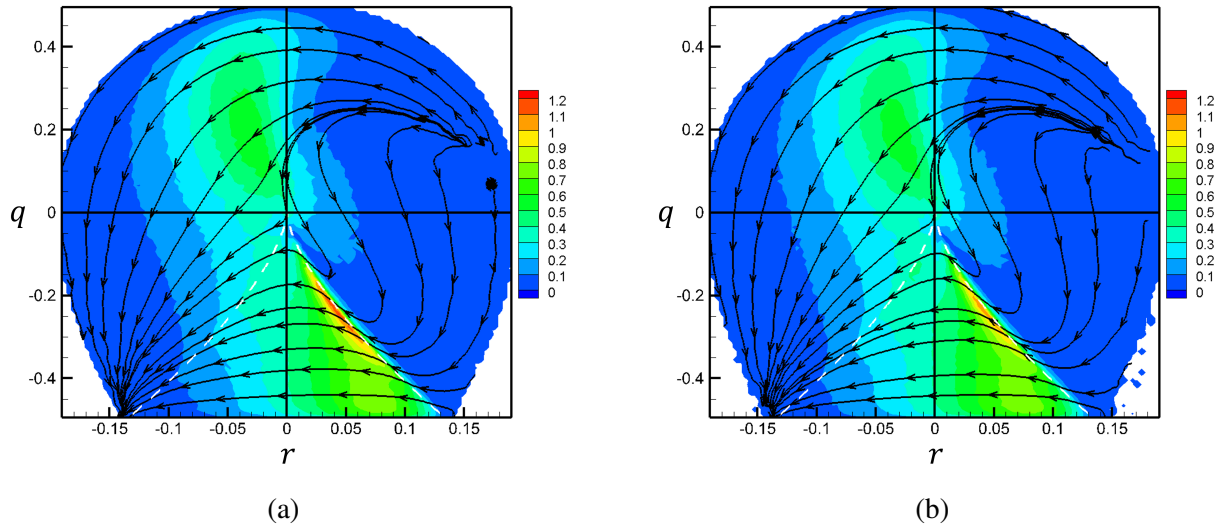


Figure 6.4: $q-r$ probability current due to anisotropic pressure (\mathbf{W}_P) for (a) FIT $Re_\lambda = 225$ and (b) turbulent channel flow $Re_\lambda = 183$. The background contours represent the magnitude of the vector \mathbf{W}_P .

that the effect of pressure on $q-r$ dynamics is reasonably independent of large-scale forcing.

Expectedly, the $q-r$ probability currents due to the viscous effects (\mathbf{W}_V) show some dependence on Re_λ in both isotropic turbulence as well as turbulent channel flow. The viscous probability current of $Re_\lambda = 225$ of forced isotropic turbulence is plotted in figure 6.5 to illustrate the general behavior. The viscous probability current has a repeller in the lower middle UFC region and takes all trajectories toward pure-strain geometry ($q = -1/2$ line), with a slight tendency to bend toward the right corner of the plane. The viscous effects are strongest in the unstable nodal topologies near the right discriminant line.

Although the viscous probability current has a slight dependence on Re_λ , it is significantly smaller in magnitude than the inertial and pressure contributions. As a result, the aggregate of the non-linear (N), anisotropic pressure (P), and viscous (V) contributions, represented by the subscript “ NPV ” is nearly self-similar at high enough Re_λ in both flows as shown in figure 6.6. Thus, two different types of large-scale forcing lead to similar VG statistical evolution due to inertia, pressure and viscosity.

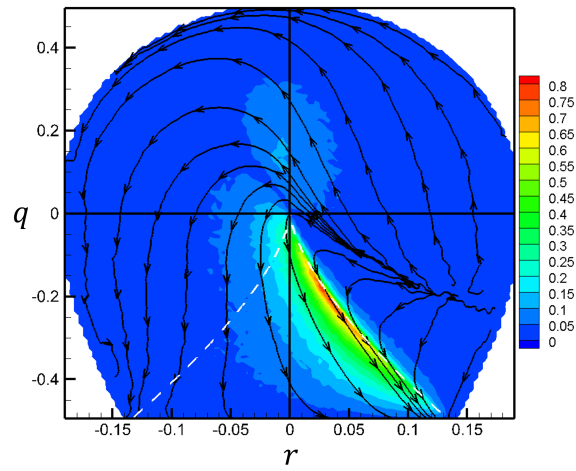


Figure 6.5: q - r probability current due to viscous effects (\mathbf{W}_V) for FIT $Re_\lambda = 225$. The background contours represent the magnitude of the vector \mathbf{W}_V .

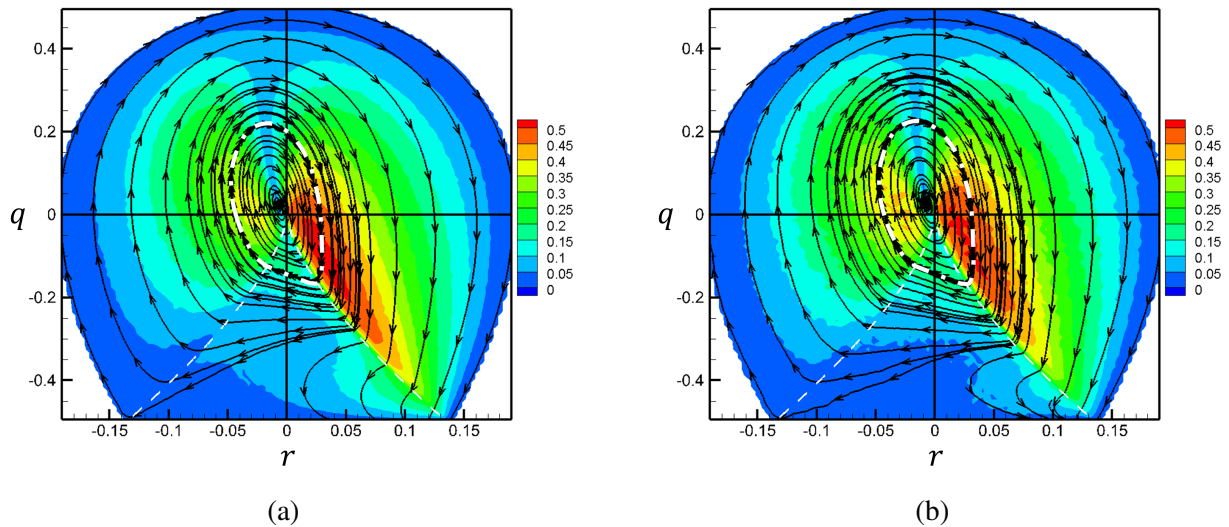


Figure 6.6: q - r probability currents due to non-linear, pressure and viscous effects, \mathbf{W}_{NPV} , for (a) FIT at $Re_\lambda = 427$, and (b) turbulent channel flow at $Re_\lambda = 132$. The background contours represent the magnitude of the vector \mathbf{W}_{NPV} . The white dash-dotted lines represent the separatrices.

In figure 6.6, the non-linear, pressure and viscous contributions cause the q, r values closer to the origin to spiral towards the attractor near the origin, which represents pure shear streamlines (Das and Girimaji, 2020a). This basin of attraction is surrounded by a separatrix loop, marked by the white dash-dotted line in the figure. The q, r values outside the separatrix loop evolve toward the $q = -1/2$ line, which represents pure strain streamlines. The trajectories move the fastest in the unstable focal topologies and slow down significantly near the right discriminant line and at the top of the spirals. Overall, the evolution of q, r due to all the turbulence processes excluding large-scale forcing does not form closed loop trajectories. Unclosed trajectories represent a system where the $q-r$ PDF is not stationary in time (Lozano-Durán et al., 2015).

The findings thus far from forced isotropic turbulence and channel flow can be summarized as follows: (i) both are statistically steady flows with stationary $q-r$ joint PDF, (ii) their $q-r$ joint PDFs are nearly identical, and (iii) the evolution of $q-r$ joint PDF due to nonlinear-pressure-viscous contributions are nearly identical, but do not form closed loop trajectories. It is reasonable to deduce that the missing effect of large-scale forcing is key in establishing closed loop trajectories in statistically stationary turbulence. It can also be inferred that the contribution of forcing is very similar in both the flows. In the remainder of the study we analyze only forced isotropic turbulence to examine and understand the effect of forcing on VG dynamics.

6.4.2 Forcing effects

Direct computation of the forcing term is rendered difficult due to the fact that force field is not archived in most data sets. To identify and isolate the effect of forcing on the evolution of $q-r$ we follow a three-step procedure.

1. Determine the total rate of change (material derivatives) of q and r by calculating the following:

$$\frac{dq}{dt'} = \frac{1}{A} \left(\frac{\partial q}{\partial t} + u_k \frac{\partial q}{\partial x_k} \right); \quad \frac{dr}{dt'} = \frac{1}{A} \left(\frac{\partial r}{\partial t} + u_k \frac{\partial r}{\partial x_k} \right). \quad (6.29)$$

A recent study by Lozano-Durán et al. (2015) has shown that computing the material derivatives of velocity-gradient invariants is highly prone to numerical errors from both spatial and

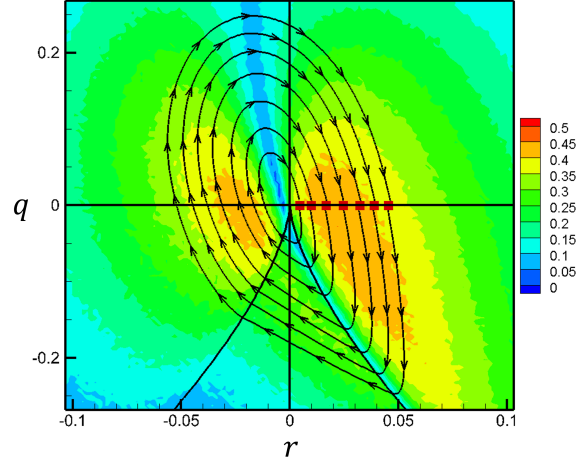


Figure 6.7: Total q - r probability current (\mathbf{W}) for FIT at $Re_\lambda = 427$. The red squares represent the starting points of the trajectories. The background contours represent the magnitude of the vector \mathbf{W} .

temporal differentiation. Inaccurate computations of these derivatives can lead to deformed CMTs. We follow the guidelines suggested in their work for accurate computation of CMTs. The spatial derivatives are computed on a two-times dealiased grid, i.e. expanding the number of modes by a factor of two in all three directions. The temporal derivatives are computed using a 4th-order central difference scheme with a CFL of 0.11.

2. Calculate the rate of change of q, r due to the nonlinear, anisotropic pressure and viscous terms on the RHS of equations (6.12-6.13).
3. Obtain the rate of change due to forcing, by subtracting the nonlinear, anisotropic pressure and viscous contributions (step (ii)) from the overall rate of change of q, r (step (i)).

Detailed analysis is first performed to demonstrate that the total derivative is captured with adequate precision in step (i). The overall probability current due to the total rate of change of q and r , i.e. \mathbf{W} , is plotted in figure 6.7 for forced isotropic turbulent flow ($Re_\lambda = 427$) in the moderate to high density region of the q - r plane. The figure shows seven trajectories in the q - r plane that start at the points marked by the red squares and complete a cycle in the plane. The

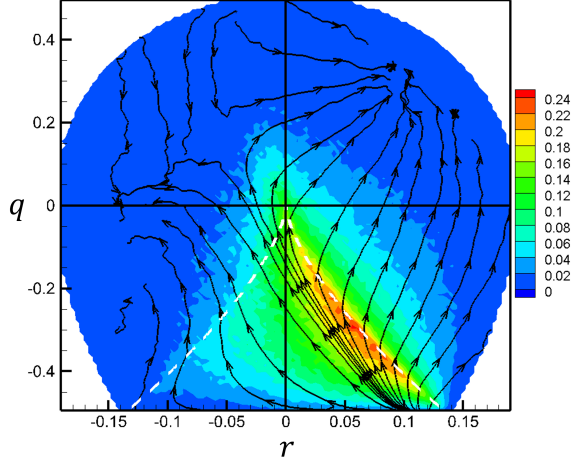


Figure 6.8: q - r probability current due to forcing (\mathbf{W}_F), with background contours representing the magnitude $|\mathbf{W}_F|$ for FIT $Re_\lambda = 427$.

trajectories form closed periodic orbits around a center near the origin, indicating that the PDF $\mathcal{F}(q, r)$ remains stationary in time (Chevillard et al., 2008; Lozano-Durán et al., 2015). It must be pointed out that lower order temporal derivatives and/or aliasing errors in spatial derivatives do not lead to closed loop trajectories.

Next, the q - r probability current due to forcing (\mathbf{W}_F) is obtained by subtracting the \mathbf{W}_{NPV} from the total \mathbf{W} ,

$$\mathbf{W}_F(q, r) = \mathbf{W}(q, r) - \mathbf{W}_{NPV}(q, r). \quad (6.30)$$

The forcing probability current, \mathbf{W}_F , is plotted in figure 6.8, in which the background color contours represent the speed of the trajectories. It is evident that the effect of forcing on q - r evolution strongly depends on the local streamline topology. The forcing action has a repeller at the right bottom corner of the plane, where local streamlines experience axisymmetric expansion. Forcing trajectories exhibit an attractor at the top right corner, i.e. the rotation-dominated UFC topology, while some trajectories bend toward the left boundary of the plane (SFS topology). The effect of forcing is very weak in the rotation-dominated streamlines, while it is the strongest in the UN/S/S streamlines near the right zero-discriminant line. Comparing these trajectories with that of non-

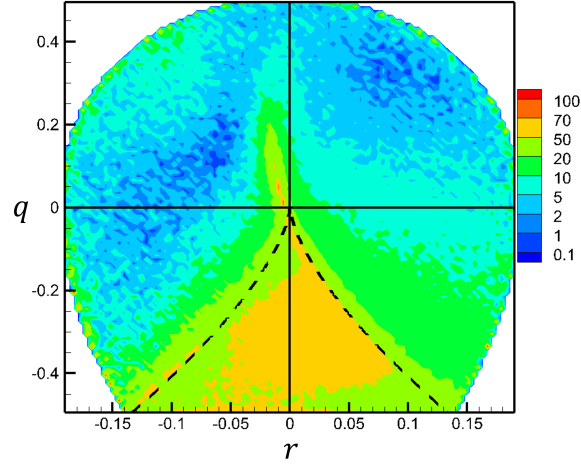


Figure 6.9: Relative contribution of forcing probability current with respect to the aggregate of nonlinear-pressure-viscous processes, i.e. $|\mathbf{W}_F|/(|\mathbf{W}_F| + |\mathbf{W}_{NPV}|) \times 100$, for FIT $Re_\lambda = 427$. Contour levels are in an approximate log-scale.

linear, pressure and viscous action (figures 6.3, 6.4 and 6.5), it is clear that the repeller of forcing action nearly coincides with the attractors of nonlinear and viscous actions. This indicates that the key role of forcing is to counter the restricted Euler effect (Bikkani and Girimaji, 2007) in the region of Vieillefosse tail. Further, the forcing attractor in UFC region is close to the repeller of pressure action. Evidently, large-scale forcing strongly opposes non-linear and viscous action in the strain-dominated streamlines, while it balances anisotropic pressure action in the rotation-dominated unstable focal streamlines.

The relative magnitude of the forcing contribution with respect to the aggregate of non-linear, pressure and viscous action, is plotted as a percentage in figure 6.9. The contribution of forcing is comparable to that of nonlinear-pressure-viscous contribution in the nodal/hyperbolic streamlines, i.e. below the discriminant line. The effect of forcing is weaker ($< 20\%$) in the focal/spiraling streamlines, i.e. above the discriminant lines, except in the extremely high-density region. Overall, large-scale forcing plays a critical role toward sustaining the classical tear drop shape of the q - r joint PDF.

6.4.3 Helmholtz-Hodge decomposition of the probability currents

From equation (6.20), in a homogeneous statistically stationary turbulent flow, the stationarity of the q - r PDF requires that

$$\nabla \cdot \mathbf{W} = 0. \quad (6.31)$$

More insight into the role of various processes on small-scale turbulence dynamics can be obtained by decomposing the probability current vectors in q - r phase-space into dilatational and solenoidal parts:

$$\mathbf{W} = \mathbf{W}^{(dil)} + \mathbf{W}^{(sol)}. \quad (6.32)$$

The curl-free dilatational part and the divergence-free solenoidal part can be obtained by using the Helmholtz-Hodge decomposition of a two-dimensional vector field (Chorin and Marsden, 2012; Petronetto et al., 2009),

$$\mathbf{W}^{(dil)} = \nabla \phi \quad \text{and} \quad \mathbf{W}^{(sol)} = J(\nabla \psi) \quad (6.33)$$

where ϕ and ψ are scalar potential fields, and $J(\cdot)$ represents clockwise rotation of a vector by 90° . Here, the rotation operator applied to the gradient of scalar potential ψ is analogous to the curl of a vector potential for a three-dimensional field. In general, there is also a harmonic term which has both zero divergence and zero curl, but that term is zero in this case due to boundary condition.

Segregating the effect of forcing from the other processes, equation (6.31) becomes

$$\nabla \cdot (\mathbf{W}_{NPV} + \mathbf{W}_F) = 0 \quad \implies \quad \nabla \cdot \mathbf{W}_F = -\nabla \cdot \mathbf{W}_{NPV}. \quad (6.34)$$

Helmholtz-Hodge decomposition of the forcing probability current and the nonlinear-pressure-viscous probability current results in

$$\mathbf{W}_F = \mathbf{W}_F^{(dil)} + \mathbf{W}_F^{(sol)}, \quad \text{where} \quad \mathbf{W}_F^{(dil)} = \nabla \phi_F \quad \text{and} \quad \mathbf{W}_F^{(sol)} = J(\nabla \psi_F); \quad (6.35a)$$

$$\mathbf{W}_{NPV} = \mathbf{W}_{NPV}^{(dil)} + \mathbf{W}_{NPV}^{(sol)}, \quad \text{where} \quad \mathbf{W}_{NPV}^{(dil)} = \nabla \phi_{NPV} \quad \text{and} \quad \mathbf{W}_{NPV}^{(sol)} = J(\nabla \psi_{NPV}). \quad (6.35b)$$

The divergence of the solenoidal vector fields is zero by construction. Therefore, the condition (equation 6.34) for a stationary process is

$$\nabla \cdot \mathbf{W}_F^{(dil)} = -\nabla \cdot \mathbf{W}_{NPV}^{(dil)}. \quad (6.36)$$

We now examine the DNS data to further analyse the role of dilatational and solenoidal components of the probability currents.

6.4.3.1 Dilatational and solenoidal current from DNS data

From equation (6.35a) the following can be obtained (Petronetto et al., 2009):

$$\nabla \cdot \mathbf{W}_F = \nabla \cdot \mathbf{W}_F^{(dil)} = \Delta \phi_F, \quad \nabla \times \mathbf{W}_F = \nabla \times \mathbf{W}_F^{(sol)} = -\Delta \psi_F \quad (6.37)$$

where Δ is the Laplacian operator ($\Delta \equiv \nabla^2$). The system of Poisson equations (6.37) is numerically solved in the bounded q - r domain (Ω) to determine the potential functions $\phi_F(q, r)$ and $\psi_F(q, r)$. The solenoidal vector field is taken to be tangential at the boundary of the domain ($\partial\Omega$). The boundary condition for the dilatational vector field is chosen such that it is compatible with that of the total vector field at the boundary. The resulting system of Poisson equations and boundary conditions is given by:

$$\Delta \phi_F = \nabla \cdot \mathbf{W}_F \quad \text{and} \quad \Delta \psi_F = -\nabla \times \mathbf{W}_F \quad \text{in} \quad \Omega, \quad (6.38a)$$

$$\nabla \phi_F \cdot \hat{\mathbf{n}} = \mathbf{W}_F \cdot \hat{\mathbf{n}} \quad \text{and} \quad J(\nabla \psi_F) \cdot \hat{\mathbf{n}} = 0 \quad \text{in} \quad \partial\Omega. \quad (6.38b)$$

Here $\hat{\mathbf{n}}$ represents the outward normal vector at the boundary of the domain. The rectangular q - r domain is discretized into 100×100 points and second-order accurate central difference scheme is used to solve the above system of equations. A convergence study is performed to ensure that the solution does not change with increasing q - r space resolution. While solving the discrete system of equations with pure Neumann boundary conditions, the issue of non-uniqueness of the solution is encountered. An augmented system of equations (Rosales et al., 2020) is solved with an additional

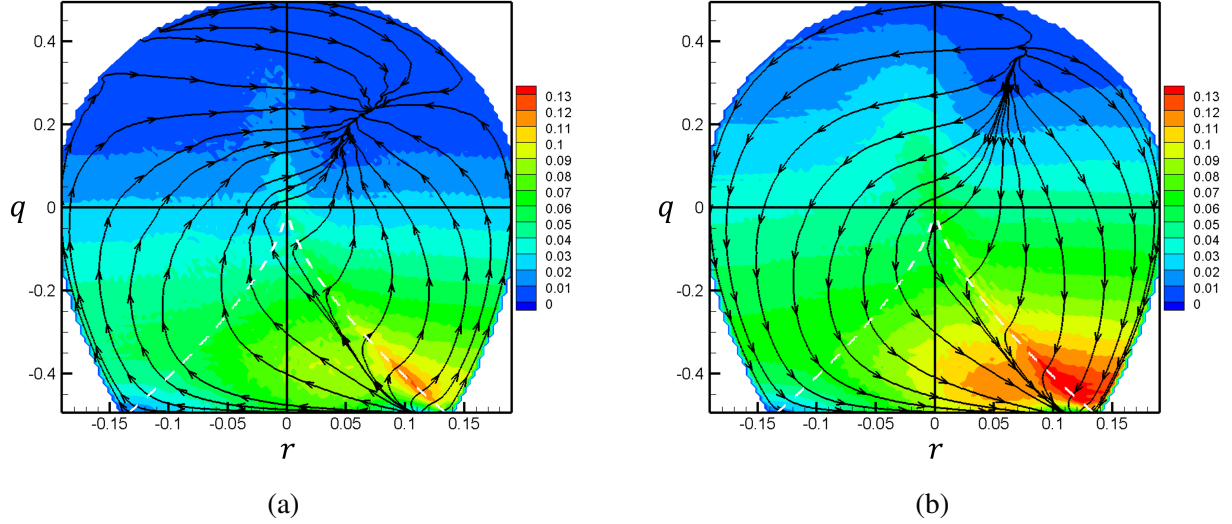


Figure 6.10: Dilatational parts of (a) forcing probability current $\mathbf{W}_F^{(dil)}$, and (b) nonlinear-pressure-viscous probability current $\mathbf{W}_{NPV}^{(dil)}$, for FIT $Re_\lambda = 427$. The background contours represent the magnitude of the vector.

scalar variable (Lagrange multiplier) to impose a restriction on the sum of the scalar potential. This in turn satisfies the discrete compatibility condition and enforces uniqueness of the solution up to an additive constant (Barton and Barton, 1989; Rosales et al., 2020). Once the scalar potentials, $\phi_F(q, r)$ and $\psi_F(q, r)$, are obtained for the entire q - r plane, the dilatational and solenoidal vector components of \mathbf{W}_F are determined from their gradients (see equation 6.35a). A similar procedure is followed to compute the dilatational and solenoidal components of \mathbf{W}_{NPV} , as given in equation (6.35b).

The dilatational parts of \mathbf{W}_F and \mathbf{W}_{NPV} are plotted in figures 6.10 (a) and (b), respectively. The background color contours represent the local speed of the trajectories. The $\mathbf{W}_F^{(dil)}$ probability current has an attractor at the bottom right corner of the plane (axisymmetric expansion) and a repeller in the rotation-dominated unstable focal streamlines. In contrast, the dilatational part of the nonlinear-pressure-viscous contribution ($\mathbf{W}_{NPV}^{(dil)}$), has a repeller in the rotation-dominated UFC topology and an attractor near axisymmetric expansion. Thus, the repeller of one nearly coincides with the attractor of the other and vice-versa. Additionally, the magnitudes of the probability

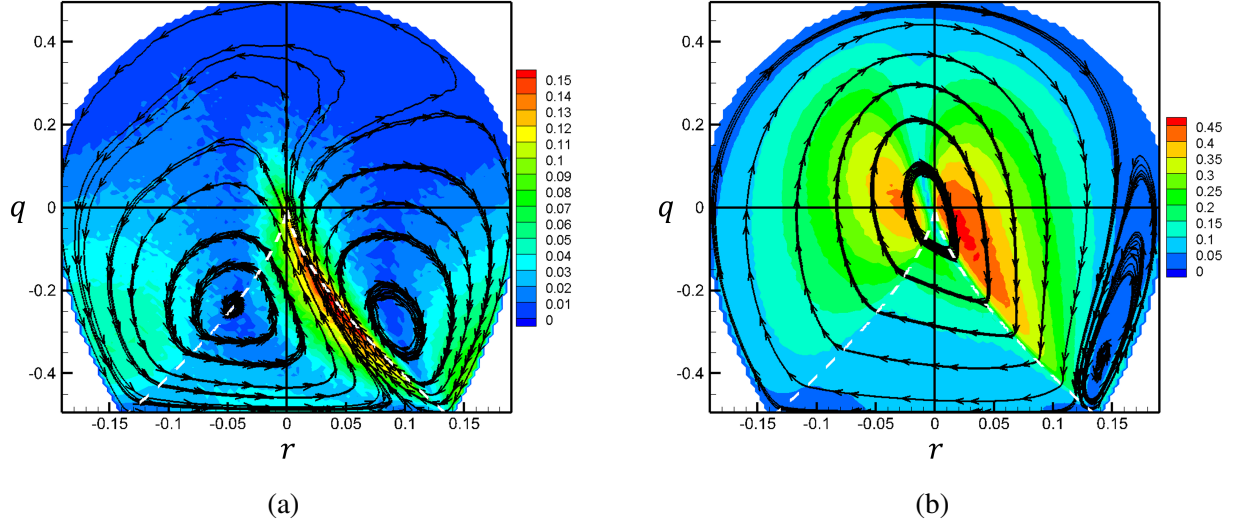


Figure 6.11: Solenoidal parts of: (a) forcing probability current $\mathbf{W}_F^{(sol)}$, and (b) nonlinear-pressure-viscous probability current $\mathbf{W}_{NPV}^{(sol)}$, for FIT $Re_\lambda = 427$. The background contours represent the magnitude of the vector.

currents at different q - r locations are similar in both the cases. The magnitudes reduce in value as q becomes more positive, i.e. rotation-dominated. The dilatational part of the forcing action is approximately negative of the dilatational part of the nonlinear-pressure-viscous action. While there are minor differences between the two fields, the sum of the divergence of $\mathbf{W}_F^{(dil)}$ and $\mathbf{W}_{NPV}^{(dil)}$ is nearly zero throughout the domain, as required for statistical stationarity (equation 6.36).

The solenoidal parts of \mathbf{W}_F and \mathbf{W}_{NPV} are plotted in figures 6.11(a) and (b), respectively. It is first evident that the solenoidal component of forcing is smaller in magnitude than its dilatational counterpart (figure 6.10a), over most of the q - r plane. On the other hand, the magnitude of the solenoidal part of \mathbf{W}_{NPV} is much larger than its dilatational part (figure 6.10b) in most of the q - r plane. Now, the solenoidal components are divergence free by construction and form closed loop trajectories in the q - r plane. The solenoidal forcing, $\mathbf{W}_F^{(sol)}$, exhibits two centers in the domain about which the trajectories orbit. One center lies on the left zero-discriminant line and the other is in the UFC topology slightly above the right zero-discriminant line. The solenoidal part of nonlinear-pressure-viscous effects, $\mathbf{W}_{NPV}^{(sol)}$, is significantly higher in magnitude than $\mathbf{W}_F^{(sol)}$. It

consists of closed periodic orbits around a center located near the origin. The closed loop trajectories appear to slow down substantially in the nodal/hyperbolic topology region in the plane. There exists another center near the right boundary of the q - r plane, in the extremely low-density region. It is important to note that the solenoidal NPV probability current is very similar to the total probability current in figure 6.7, especially in the sufficiently populated regions of the plane.

The key findings from this analysis can be summarized as follows:

1. The most important role of large-scale forcing is to oppose and nullify the dilatational probability current due to inertial, pressure and viscous effects.
2. The solenoidal part of forcing current is considerably smaller in magnitude and hence plays a secondary role in VG dynamics.
3. The solenoidal part of nonlinear-pressure-viscous probability current dominates the overall dynamics of VG tensor invariants. For the most part, $\mathbf{W}_{NPV}^{(sol)}$ dictates the universal features of the small-scale dynamics.

Thus, large-scale forcing enforces statistical stationarity with a smaller or secondary influence on the conditional mean evolution of the velocity gradient invariants.

6.5 VG magnitude dynamics

The PDF of the standardized variable,

$$\theta^* = \frac{\theta - \langle \theta \rangle}{\sigma_\theta} \quad \text{where} \quad \theta \equiv \ln A, \quad \sigma_\theta = \sqrt{\langle (\theta - \langle \theta \rangle)^2 \rangle} \quad (6.39)$$

is displayed in figure 6.12 for FIT at $Re_\lambda = 225, 385$ and 427 . The PDF of standard normal distribution, with zero mean and unit standard deviation, is also plotted in the figure for comparison. Clearly, the PDFs of θ^* at all Re_λ nearly coincide with that of the normal distribution (Oboukhov, 1962; Yeung and Pope, 1989). It must be noted however that due to intermittency, the PDF of pseudo-dissipation can not be precisely log-normal (Orszag, 1970b; Mandelbrot, 1999). We now

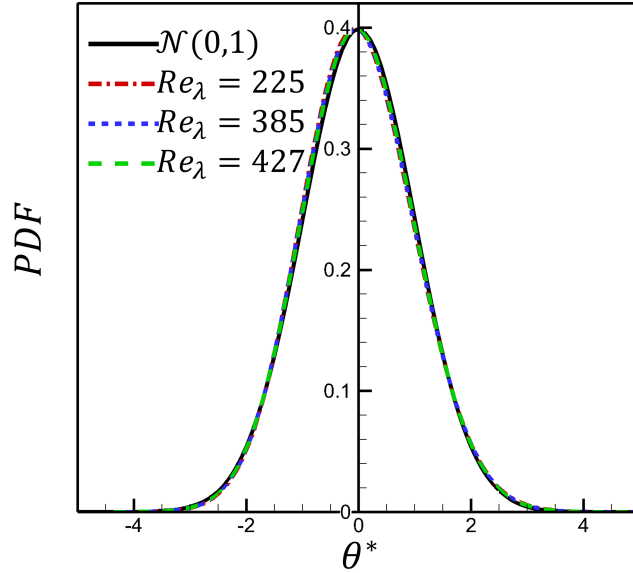


Figure 6.12: PDF of θ^* (dashed line) for FIT $Re_\lambda = 225, 385$ & 427 and standard normal distribution (solid line).

investigate the role of different turbulence processes in VG magnitude dynamics of statistically stationary turbulence.

6.5.1 VG magnitude dynamics conditioned on $q-r$

The total rate of change of θ is calculated by following the same procedure and guidelines used for q and r in subsection 6.4.2. The rate of change of θ due to the different processes (equation 6.22) is conditioned on $q-r$ and plotted in figure 6.13. The nonlinear (N) action is predominantly positive in the high density regions of the $q-r$ plane, particularly along the right discriminant line including the axisymmetric expansion. Thus, nonlinear contribution increases the VG magnitude in most of the turbulent flow field. Nonlinear action diminishes the VG magnitude along the left discriminant line, especially at axisymmetric compression. Pressure (P) opposes the nonlinear effect in the strain-dominated topologies ($q < 0$) with the exception of the UFC region. It, however, augments the nonlinear action in the rotation-dominated topologies ($q > 0$). This behavior is unlike the $q-r$ probability current, where pressure opposes nonlinear action in both strain- and rotation-

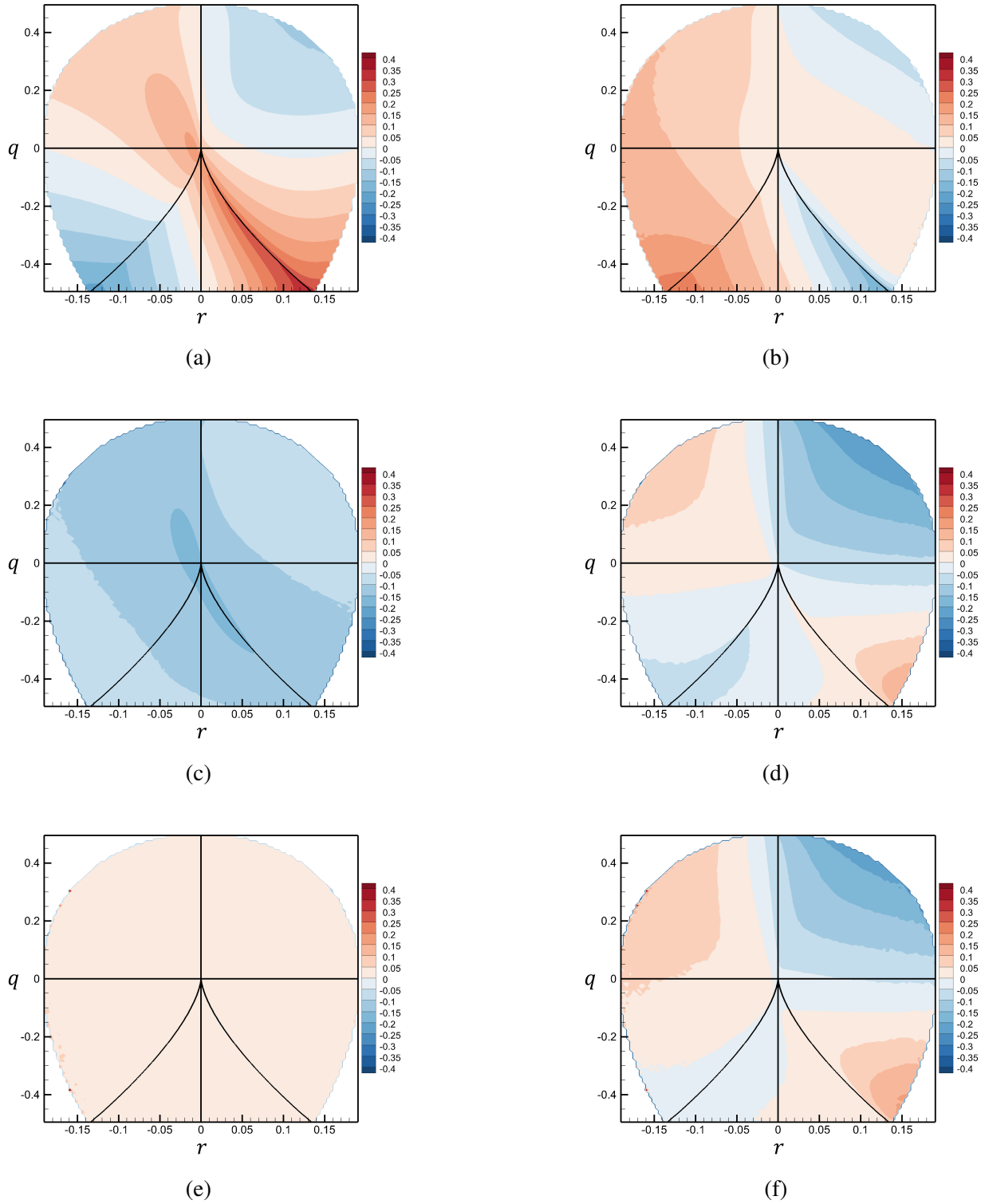


Figure 6.13: Conditional mean rate-of-change of θ ($\equiv \ln A$) in q - r phase plane due to: (a) nonlinear, (b) pressure, (c) viscous, (d) nonlinear-pressure-viscous, (e) forcing, and (f) all processes for FIT $Re_\lambda = 427$.

dominated topologies alike. The viscous (V) action shows a relatively weaker dependence on the local streamline topology and is negative throughout the q - r plane. In other words, viscosity tries to diminish the VG magnitude at all streamline topologies. It is important to note that the viscous action opposes the non-linear action in the densely-populated regions of the plane.

The aggregate of nonlinear, pressure, and viscous (NPV) processes in each of the four quadrants of the q - r plane can be summarized as follows: it increases VG magnitude in rotation-dominated stable and strain-dominated unstable topologies; it decreases VG magnitude in rotation-dominated unstable and strain-dominated stable topologies. It is the strongest in the rotation-dominated unstable (UFC) topology.

Expectedly, the forcing (F) contributes toward increasing VG magnitude nearly uniformly at all q - r values. The conditional mean effect of forcing in the q - r plane is weaker than the other processes. Although the viscous and forcing effects are nearly independent of topology, the nonlinear and pressure effects on the evolution of VG magnitude are strongly dependent on q - r . As a result, the net rate of change of VG magnitude due to the combination of all four processes (figure 6.13f) is a strong function of topology. On average, the VG magnitude increases in the SFS, UN/S/S and strain-dominated UFC topologies, and it decreases in the SN/S/S and rotation-dominated UFC topologies. It is further evident that this resulting total evolution of VG magnitude is primarily driven by the aggregate of nonlinear-pressure-viscous action with a small but distinct influence of large-scale forcing.

6.5.2 VG magnitude dynamics conditioned on θ^*

The conditional mean rate-of-change of θ (equations 6.24-6.25) is plotted as a function of the standardized variable θ^* in figure 6.14. The total conditional mean rate of change (\tilde{u}) is nearly equal to zero at all θ^* . This satisfies the statistical stationarity condition given in equation (6.26). The nonlinear (N) term is positive at all magnitudes, while the viscous (V) effect is always negative. The pressure (P) and forcing (F) action exhibit different behaviors in different ranges of θ .

The positive nonlinear effect on the rate of change of VG magnitude grows rapidly as the VG magnitude increases. On the other hand, the viscous action becomes increasingly negative with

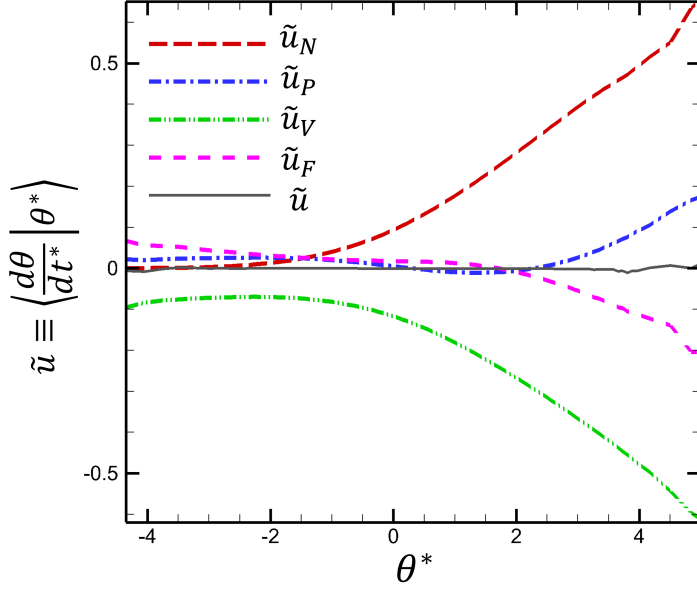


Figure 6.14: Conditional mean rate-of-change of θ ($\equiv \ln A$) conditioned on θ^* due to different processes, for FIT $Re_\lambda = 427$.

VG magnitude, balancing the nonlinear contribution. At extremely low VG magnitudes ($\theta \leq \langle \theta \rangle - 2\sigma_\theta$), the nonlinear effects are weak, while the positive pressure and forcing contributions are balanced by a negative viscous action. At moderately small VG magnitudes ($\langle \theta \rangle - 2\sigma_\theta \leq \theta \leq \langle \theta \rangle$), the nonlinear and viscous contributions begin to grow rapidly with θ^* . In this range, positive pressure and forcing contributions add to the increasingly positive nonlinear action, and their aggregate is balanced by a strongly negative viscous action. At intermediate VG magnitudes ($\langle \theta \rangle \leq \theta \leq \langle \theta \rangle + 2\sigma_\theta$), the pressure action becomes negative, while forcing contribution remains positive. The behavior of pressure and forcing switch as VG magnitude reaches a higher value ($\theta \geq \langle \theta \rangle + 2\sigma_\theta$). At high VG magnitudes, forcing action becomes increasingly negative to balance the equally positive pressure action. Thus, in regions of very high velocity gradient magnitudes, forcing makes a surprising negative contribution toward θ evolution.

The key findings are: (i) the total conditional mean rate of change of VG magnitude is nearly zero at all magnitudes; (ii) at high VG magnitudes, there is a clear balance between pressure and

forcing on one hand and viscous-inertial balance on the other; and (iii) at smaller VG magnitudes the viscous action balances all the other processes.

The insight and observations highlighted in this work provide important guidance for modeling velocity gradient dynamics. Numerous studies in literature have presented Langevin velocity gradient models to capture the Lagrangian evolution of VG tensor in turbulent flows (Girimaji and Pope, 1990a; Jeong and Girimaji, 2003; Chevillard and Meneveau, 2006; Johnson and Meneveau, 2016a). Most of these studies have focused on developing closure models to capture the non-local pressure and viscous effects on VG dynamics. We propose that inclusion of the "universal" forcing effects, presented in this work, will lead toward improved velocity gradient modeling in turbulent flows.

6.6 Conclusions

The profound role of large-scale forcing on the small-scale velocity-gradient (VG) dynamics is examined using direct numerical simulation (DNS) data. The evolution equations of normalized VG invariants (q,r) and VG magnitude $A (\equiv \sqrt{A_{ij}A_{ij}})$ are derived, along with their PDF equations. DNS data sets of forced isotropic turbulence (FIT) and turbulent channel flow are used to investigate the q - r joint PDF and the underlying probability currents due to various turbulence processes. It is first shown that the characteristic tear-drop shaped q - r joint PDF asymptotes toward a self-similar form at high enough Reynolds numbers. The q - r joint PDFs for isotropic turbulence and turbulent channel flow are shown to be nearly identical. The probability currents due to inertial, pressure and viscous effects are also very similar in both the flows.

The combined probability currents of inertial, pressure and viscous effects is not closed loop and cannot sustain the stationary tear-drop PDF shape. This clearly indicates that forcing plays a pivotal role in forming and sustaining the teardrop q - r joint PDF shape. Next, the flow-independent effect of large-scale forcing on q - r evolution is examined using FIT data. The effect of forcing is shown to be strongly dependent on the local topology. Forcing effects are much stronger in locally nodal/hyperbolic streamlines than in focal/spiraling streamlines. The forcing action strongly opposes the inertial and viscous action in these nodal streamlines, whereas it counters the anisotropic

pressure action in the unstable focal streamlines. It is further shown that the dilatational part of the forcing probability current balances the dilatational part of the inertial-pressure-viscous contribution at all topologies. The solenoidal part of forcing current is relatively smaller than that of the inertial-pressure-viscous effects. To a leading order, the solenoidal part of inertial-pressure-viscous action dictates the overall evolution of trajectories in the q - r phase-space.

The effect of large-scale forcing along with the inertial, pressure and viscous processes on the evolution of VG magnitude is examined by conditioning these processes on the invariants phase-space and on the VG magnitude itself. At smaller magnitudes, forcing along with inertia and pressure opposes the strongly negative viscous action. At larger magnitudes, forcing balances the increasingly positive pressure action, while viscosity counteracts the inertial action. The forcing contribution to the mean rate of change of VG magnitude is nearly independent of topology (q, r). The nonlinear-pressure-viscous action drives the overall conditional mean evolution of VG magnitude in the q - r plane, with a weaker but discernible influence of forcing. Altogether, the rotation-dominated unstable focal topology and the stable nodal topology exhibit overall diminishing VG magnitude, while all the other topologies demonstrate overall growing VG magnitude. These findings further our understanding of velocity gradient dynamics and suggest important simplifications that can be used for the development of improved velocity-gradient models.

7. DATA-DRIVEN MODEL FOR LAGRANGIAN VELOCITY GRADIENT DYNAMICS IN TURBULENCE

7.1 Introduction

Velocity gradient (VG) dynamics hold the key to understanding important turbulence features such as small-scale universality, intermittency, multifractal nature and local streamline geometry of turbulence (Yakhot and Donzis, 2017; Sreenivasan and Antonia, 1997; Meneveau and Sreenivasan, 1991; Soria et al., 1994; Chong et al., 1998). Velocity gradient dynamics influence material element deformation and mixing of passive scalars in turbulent flows (Girimaji and Pope, 1990b; Dresselhaus and Tabor, 1992; Sreenivasan, 2019; Fischer, 1973). It further governs the deformation and orientation dynamics of small-scale entities immersed in turbulent flows such as red-blood-cells in a turbulent blood stream (Arora et al., 2004; De Tullio et al., 2012), microorganisms swimming in water (Luchsinger et al., 1999), polymer molecules in wall-bounded flows (Balkovsky et al., 2000) and bubbles in a liquid flow stream (Biferale et al., 2014). Therefore, modeling the Lagrangian evolution of the velocity gradient tensor in a turbulent flow enhances our understanding of several important small-scale turbulence phenomena and our ability to model them. A velocity gradient model is further useful in reproducing the small-scale dynamics (Johnson and Meneveau, 2018) in scale-resolving simulations of complex turbulent flows.

The dynamics of velocity gradients broadly depend upon four turbulence processes - inertial, pressure, viscous and large-scale forcing contributions. The inertial and isotropic pressure contributions are closed and constitute the so-called restricted Euler (RE) dynamics (Vieillefosse, 1982; Cantwell, 1992). In the absence of the unclosed non-local processes, the earliest analyses of velocity gradient dynamics were developed based on the RE equations (Cantwell, 1992; Girimaji and Speziale, 1995; Martín et al., 1998a). However, purely inviscid equations can lead to finite-time singularity as the solution diverges to infinity. Girimaji and Pope (1990a) developed the first complete stochastic model that accounts for nonlocal processes. The addition of the nonlocal

terms help counteract the nonlinear growth of the RE terms, thus leading to a statistically stationary state that avoids finite-time singularity. This was followed by a series of stochastic models for velocity gradient dynamics (Chertkov et al., 1999; Jeong and Girimaji, 2003; Chevillard and Meneveau, 2006; Chevillard et al., 2008; Wilczek and Meneveau, 2014) using different analytical approaches to model the nonlocal pressure and viscous terms. The recent deformation of Gaussian field (RDGF) model proposed by Johnson and Meneveau (2016a) has showed significant improvements over the previous models, but is still unable to accurately capture the heavy-tailed PDFs and higher-order moments of velocity gradients at high Reynolds numbers. Pereira et al. (2018) presented a stochastic model based on multifractal process that emulates the Reynolds number scaling of VG moments with reasonable accuracy, but fails to capture the geometric features of the velocity gradient tensor with similar accuracy. Recently, a data-driven velocity gradient model has been developed employing tensor-basis neural network for the closure of the nonlocal pressure term (Tian et al., 2021), which show some improvements over previous models in reproducing certain small-scale statistics of turbulence. While much progress has been made in modeling velocity gradient dynamics, the closure models for the non-local processes in turbulence continue to require further improvement. A robust and complete velocity gradient model that is generalizable to different types of turbulent flows at different Reynolds number is still lacking.

The goal of this work is to develop a data-driven Lagrangian model that accurately reproduces the velocity gradient dynamics in turbulent flows for a broad range of Reynolds numbers with minimal computational effort. Modeling the nonlinear dynamics of the velocity gradient tensor ($A_{ij} \equiv \partial u_i / \partial x_j$) is difficult due to its intermittent nature. To overcome the complexity introduced by VG intermittency, we adapt the approach of Girimaji and Speziale (1995) to segregate the VG magnitude (A) and the bounded normalized VG tensor (b_{ij}), where:

$$b_{ij} \equiv \frac{A_{ij}}{A} \quad \text{and} \quad A \equiv \|\mathbf{A}\|_F = \sqrt{A_{mn}A_{mn}} \quad (7.1)$$

Such a factorization is consistent with the work of Kolmogorov (1962), which proposes that small-

scale turbulence is self-similar when consistent in terms of local rather than global dissipation. Thus, we develop separate stochastic models for b_{ij} and A , tailored for capturing the dynamical behavior of each uniquely and resulting in an overall improvement in prediction of A_{ij} dynamics.

The b_{ij} statistics are nearly universal in different types of turbulent flows of different Reynolds numbers, as demonstrated in chapters 2 and 3. In addition, chapters 5 and 6 exhibit that the b_{ij} -dynamics due to different turbulence processes such as inertial, pressure, viscous and forcing effects, are also nearly independent of Reynolds number. Additionally, modeling b_{ij} requires the closure of the normalized contributions of non-local pressure and viscosity, and these normalized processes are well-behaved and more amenable to modeling than the unnormalized pressure and viscous terms modeled in previous studies. In this work, we model the mean non-local effects in velocity gradient dynamics using a simple data-driven closure within the bounded b_{ij} state-space.

The Reynolds number dependence arises primarily through the velocity gradient magnitude. The velocity gradient magnitude or pseudodissipation has a nearly lognormal probability distribution and shows an exponential decay of autocorrelation in time (Kolmogorov, 1962; Oboukhov, 1962; Yeung and Pope, 1989). The exponentiated Ornstein-Uhlenbeck (OU) process is a statistically stationary process that satisfies both these properties (Uhlenbeck and Ornstein, 1930; Pope and Chen, 1990). While it has been pointed out that pseudodissipation cannot be precisely lognormal in the context of multifractal formalism (Mandelbrot, 1974; Meneveau and Sreenivasan, 1991), the OU process models the overall dynamics of pseudodissipation quite accurately (Pope and Chen, 1990; Girimaji and Pope, 1990a). In fact, a recent analysis of Lagrangian trajectories in high Reynolds number turbulence (Huang and Schmitt, 2014) has shown evidence that the autocorrelation function of pseudodissipation is consistent with both the exponential decay prescribed by the OU process as well as the logarithmic decay suggested by the multifractal framework, and the two are nearly indistinguishable at such high Reynolds numbers (Pereira et al., 2018). Since the focus of this work is to accurately reproduce the overall Lagrangian dynamics of the velocity gradients in turbulence, we model the velocity gradient magnitude as a modified lognormal process, without explicitly accounting for multifractal behavior. It is, however, expected that incorporating

DNS data based modifications within the OU process will help capture the intermittent nature of small-scale turbulence more accurately than a simple lognormal process.

In section 7.2 we discuss the properties and the governing differential equations for the normalized VG tensor and VG magnitude in an incompressible turbulent flow. The entire modeling methodology is described in section 7.3, including the philosophy of the modeling approach and its generalizability, formulation of the model equations and closures, and a complete model summary. The numerical procedure of the simulations performed using the model is outlined in section 7.4. Finally the results of the model are compared with that of DNS and previous models in section 7.5 and the conclusions are presented in section 7.6.

7.2 Properties and governing equations

Starting from the Navier-Stokes equations for velocity fluctuations, u_i , in an incompressible turbulent flow:

$$\frac{\partial u_i}{\partial t} + u_k \frac{\partial u_i}{\partial x_k} = -\frac{\partial p}{\partial x_i} + \nu \nabla^2 u_i + f_i \quad (7.2a)$$

$$\frac{\partial u_i}{\partial x_i} = 0 \quad (7.2b)$$

where, p is the pressure fluctuation, ν is the kinematic viscosity, and f_i represents large-scale forcing, one can derive the following governing equation for the velocity gradient tensor (section 6.2):

$$\frac{dA_{ij}}{dt} = -A_{ik}A_{kj} + \frac{1}{3}A_{mk}A_{km}\delta_{ij} + H_{ij} + T_{ij} + G_{ij} \quad (7.3)$$

The first term is the inertial term and the second term is the isotropic pressure effect. These two terms represent the nonlinear effect and are closed since they are explicit functions of A_{ij} itself. The tensor H_{ij} is the anisotropic pressure Hessian tensor, T_{ij} is the viscous Laplacian tensor, and G_{ij} is the anisotropic forcing tensor, defined as follows:

$$H_{ij} = -\frac{\partial^2 p}{\partial x_i \partial x_j} + \frac{\partial^2 p}{\partial x_k \partial x_k} \frac{\delta_{ij}}{3}; \quad T_{ij} = \nu \nabla^2 A_{ij}; \quad G_{ij} = \frac{\partial f_i}{\partial x_j} - \frac{\partial f_k}{\partial x_k} \frac{\delta_{ij}}{3}. \quad (7.4)$$

These three tensors represent the non-local effects in velocity gradient dynamics and require closure when modeling A_{ij} .

7.2.1 Normalized VG tensor

The normalized velocity gradient tensor (b_{ij}) is mathematically bounded, as shown in equations (2.13) and (2.14). As shown in section 3.2.4, without any loss of generality we can express b_{ij} in the principal (eigen) reference frame of normalized strain-rate tensor, s_{ij} , as

$$\tilde{\mathbf{b}} = \begin{bmatrix} a_1 & 0 & 0 \\ 0 & a_2 & 0 \\ 0 & 0 & a_3 \end{bmatrix} + \begin{bmatrix} 0 & -\omega_3 & \omega_2 \\ \omega_3 & 0 & -\omega_1 \\ -\omega_2 & \omega_1 & 0 \end{bmatrix} \quad \text{where } a_1 \geq a_2 \geq a_3 \quad (7.5)$$

Here, a_i are the eigenvalues of s_{ij} . The notation $\tilde{}$ is used to represent tensors in the principal reference frame. For incompressible flows, $a_1 (> 0)$ is the most expansive strain-rate, $a_3 (< 0)$ is the most compressive strain-rate and the intermediate strain-rate a_2 can be positive, negative or zero. The corresponding eigenvectors - \vec{E}_{a_1} , \vec{E}_{a_2} and \vec{E}_{a_3} - are mutually orthogonal and constitute the principal axes of the symmetric tensor s_{ij} . Further, ω_i are the components of the normalized vorticity vector ($\vec{\omega}$) along the strain-rate eigendirections. Although the eigen-decomposition is unique, the signs of the eigenvectors are not. Therefore, the directions of the eigenvectors are uniquely determined by the vorticity vector having all components of the same sign (all positive or all negative).

Applying the constraints of incompressibility ($\tilde{b}_{ii} = 0$) and normalization ($\tilde{b}_{ij}\tilde{b}_{ij} = 1$), the \tilde{b}_{ij} state-space can be reduced to a four-dimensional space of only four independent variables (shape-parameters) - q, r, a_2, ω_2 . Here, q and r are the second and third invariants of the tensor, respectively. All the remaining components of the tensor can be determined uniquely once these four variables are known, as shown in appendix C. Therefore, (q, r, a_2, ω_2) completely define \tilde{b}_{ij} and thence the geometric-shape of the local flow streamlines.

The evolution equation for b_{ij} in the laboratory frame of reference, derived from equation (7.3),

is

$$\begin{aligned} \frac{db_{ij}}{dt'} = & - b_{ik}b_{kj} + \frac{1}{3}b_{km}b_{mk}\delta_{ij} + b_{ij}b_{mk}b_{kn}b_{mn} + (h_{ij} - b_{ij}b_{kl}h_{kl}) \\ & + (\tau_{ij} - b_{ij}b_{kl}\tau_{kl}) + (g_{ij} - b_{ij}b_{kl}g_{kl}) \end{aligned} \quad (7.6)$$

where $dt' = A dt$ is time increment normalized by local VG magnitude and the timescale t' is referred to as the local timescale. Here,

$$\begin{aligned} h_{ij} = \frac{H_{ij}}{A^2} = \frac{1}{A^2} \left(- \frac{\partial^2 p}{\partial x_i \partial x_j} + \frac{\partial^2 p}{\partial x_k \partial x_k} \frac{\delta_{ij}}{3} \right), \quad \tau_{ij} = \frac{T_{ij}}{A^2} = \frac{\nu}{A^2} \nabla^2 A_{ij}, \\ g_{ij} = \frac{G_{ij}}{A^2} = \frac{1}{A^2} \left(\frac{\partial f_i}{\partial x_j} - \frac{\partial f_k}{\partial x_k} \frac{\delta_{ij}}{3} \right). \end{aligned} \quad (7.7)$$

are the normalized anisotropic pressure Hessian, viscous Laplacian and anisotropic forcing tensors, respectively. In the b_{ij} equation (7.6), the first three terms on the RHS are closed and represent the nonlinear (N) - inertial and isotropic pressure - effects. The next three terms constitute the non-local pressure (P), viscous (V), and forcing (F) effects on b_{ij} evolution that require closure. The advantage of using the local timescale is that the RHS of the b_{ij} evolution equation is a function of only b_{ij} and other normalized tensors. These normalized pressure Hessian and viscous Laplacian tensors are not necessarily bounded, but are well-characterized in the phase plane of b_{ij} invariants and are definitely more amenable to modeling than the unnormalized tensors in the A_{ij} equation (chapters 5 and 6). They further exhibit a nearly universal behavior across turbulent flows of different Reynolds numbers, at least from a modeling stand point. Therefore, the Lagrangian evolution of b_{ij} can be modeled in the local timescale t' without any explicit dependence on θ^* . The θ^* dependence comes in only when determining the b_{ij} evolution in real time.

7.2.2 VG magnitude

The velocity gradient magnitude or pseudodissipation has been shown to have a nearly lognormal distribution via theoretical arguments and numerical/experimental results (Kolmogorov, 1962; Oboukhov, 1962; Yeung and Pope, 1989; Monin and Yaglom, 2013). Therefore, we examine the

dynamics of VG magnitude (A) in terms of

$$\theta \equiv \ln A, \quad (7.8)$$

which is expected to exhibit a near-normal distribution in a turbulent flow field. In fact, for the ease of modeling, we introduce the variable – standardized VG magnitude:

$$\theta^* \equiv \frac{\theta - \langle \theta \rangle}{\sigma_\theta} \quad \text{where} \quad \sigma_\theta = \sqrt{\langle (\theta - \langle \theta \rangle)^2 \rangle} \quad (7.9)$$

which has a nearly standard normal distribution, $\mathcal{N}(0, 1)$, in turbulence as illustrated in figure 6.12 for isotropic turbulent flows at different Reynolds numbers. The evolution equation for θ^* , derived from equation (7.3) for statistically stationary turbulent flows is given by:

$$\frac{d\theta^*}{dt^*} = \frac{1}{\sigma_\theta \langle A \rangle} (-b_{ik} b_{kj} A_{ij} + h_{ij} A_{ij} + \tau_{ij} A_{ij} + g_{ij} A_{ij}) \quad (7.10)$$

where $t^* = \langle A \rangle t$ is referred to as global timescale and it represents time normalized by global mean VG magnitude. This normalization is in essence similar to normalization by the Kolmogorov timescale (τ_η) and is found to be more appropriate for examining VG magnitude than the local timescale used for b_{ij} . Here, the four terms on the RHS of the above equation represent the nonlinear (N), pressure (P), viscous (V), and forcing (F) effects on the VG magnitude evolution. The θ^* equation suggests that the θ^* dynamics in global timescale t^* , explicitly depends on b_{ij} . Therefore, accurate modeling of the θ^* dynamics likely requires a dependence on b_{ij} .

7.3 Model Formulation

A Lagrangian model is developed for the velocity gradient tensor, A_{ij} , by formulating separate models for the normalized velocity gradient tensor, b_{ij} , and the velocity gradient magnitude, A . In this section, the main strategies of the modeling approach are first described, followed by a discussion on the generalizability of the model. Then the detailed formulation of the individual models are presented and finally all the model equations and parameters are summarized.

7.3.1 Modeling strategy

The b_{ij} dynamics in the local timescale is a function of b_{ij} itself and other normalized non-local tensors (equation 7.6). As inferred from our analysis of DNS data in chapters 5 and 6, the conditional mean effects of these normalized non-local tensors can be considered as functions of b_{ij} itself. Therefore, a stochastic model is formulated for the Lagrangian evolution of b_{ij} in the local timescale (t') without any explicit dependence on θ^* . DNS data-driven closure models are developed for capturing the conditional mean nonlocal effects of normalized pressure and viscous processes in the strain-rate eigen reference frame within the four-dimensional bounded state-space of \tilde{b}_{ij} . The fluctuations of these nonlocal effects as well as the effect of large-scale forcing is modeled in the stochastic diffusion term using moment constraints.

Due to the near-normal distribution of θ^* (figure 6.12), the framework of Ornstein-Uhlenbeck (OU) process (Pope and Chen, 1990) is used to model θ^* . Three different stochastic models are developed for the Lagrangian evolution of θ^* in global timescale (t^*). The first model is the original OU model completely decoupled from the b_{ij} dynamics. In the second and third models, additional flow physics is incorporated into the θ^* dynamics of the model, using a DNS data based diffusion term that depends on the b_{ij} invariants. Thus, these two θ^* models include explicit dependence on b_{ij} .

An additional ordinary differential equation provides the relation between the local and the global timescales. Finally, the b_{ij} and θ^* models are combined to form an integrated system of model equations representing the Lagrangian evolution of A_{ij} in global time.

7.3.2 Generalizability

In a turbulent flow, the large scales of motion depend upon the flow geometry and driving mechanism of the flow. It is therefore difficult to develop generalizable models for the large scales that will apply to different turbulent flows. Modeling small scale dynamics is more generalizable in comparison, since the small scales in turbulent flows (with a large enough scale-separation) tend to be isotropic and universal. The notion of small-scale universality, which began with the emi-

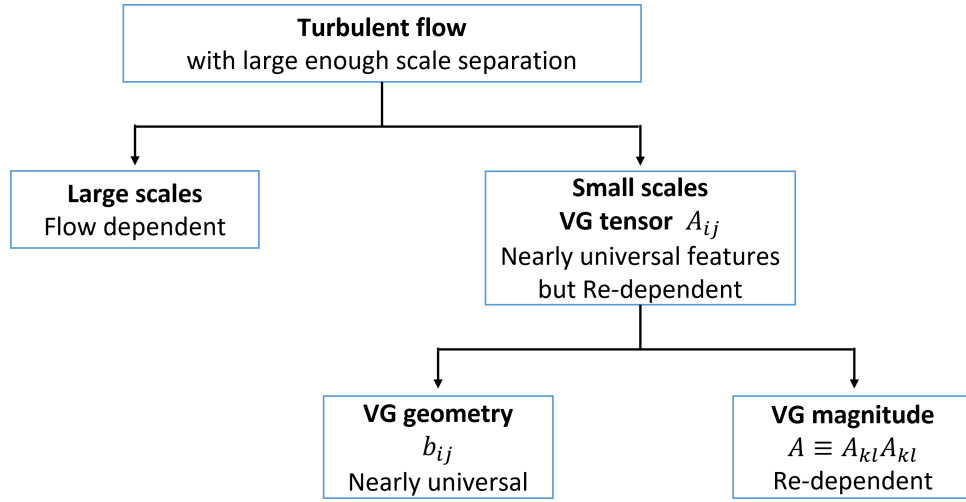


Figure 7.1: Flowchart to explain the behavior of velocity gradient tensor and its constituents in turbulence.

ment work of Kolmogorov (1941), has been refined significantly over the years to account for the intermittent nature of small-scale turbulence (Kolmogorov, 1962; Oboukhov, 1962; Sreenivasan and Antonia, 1997; Schumacher et al., 2014). The velocity gradient tensor, A_{ij} , governs these small-scale motions and exhibits certain universal features across different types of turbulent flows (Sreenivasan, 1998; Schumacher et al., 2014). However, it also shows a strong dependence on Reynolds number (Donzis et al., 2005; Yeung et al., 2018). Its multifractal and intermittent nature causes the higher order moments to grow with increasing Reynolds number, deviating far away from Gaussian behavior (Yakhot and Donzis, 2017).

In this model, we separate A_{ij} into normalized velocity gradient tensor (b_{ij}) and velocity gradient magnitude (A), such that the tensorial variable b_{ij} is nearly universal across different turbulent flows while the scalar variable A reflects all the Reynolds number dependence. The PDFs and higher order moments of b_{ij} are nearly invariant with Taylor Reynolds number (Re_λ) and across different turbulent flows as shown in chapters 2 and 3. Further, the b_{ij} dynamics due to turbulence processes such as inertial, pressure, viscous, and forcing are also shown to be nearly universal in chapters 5 and 6. Therefore, the b_{ij} model developed here using the DNS data of only one turbulent

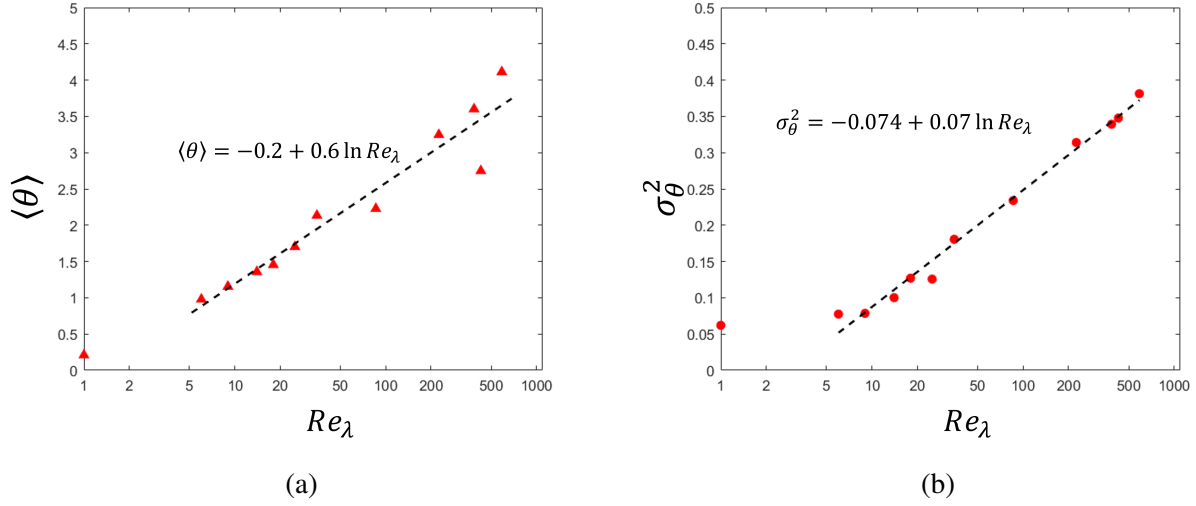


Figure 7.2: Statistics of θ from DNS datasets of forced isotropic turbulent flows at different Re_λ : (a) global mean $\langle \theta \rangle$ as a function of Re_λ (in natural log scale); dashed line represents a linear least-squares fit of the data ($\langle \theta \rangle = -0.2 + 0.6 \ln Re_\lambda$); and (b) variance $\sigma_\theta^2 = \langle \theta^2 - \langle \theta \rangle^2 \rangle$ as a function of Re_λ (in natural log scale); dashed line represents a linear least-squares fit of the data ($\sigma_\theta^2 = -0.074 + 0.07 \ln Re_\lambda$).

flow can be treated as universal up to a modeling approximation. It can be applied to reproduce the small-scale dynamics of different turbulent flows for a broad range of Reynolds numbers.

The magnitude A , on the other hand, exhibits strong dependence on the Reynolds number of the flow. The mean and variance of its logarithm ($\theta = \ln A$), plotted in figure 7.2, clearly increase with increasing Re_λ . The preliminary findings suggest that $\langle \theta \rangle$ and σ_θ follow approximate scaling laws with Re_λ , as mentioned in the figures. The scaling law for σ_θ^2 closely resembles the Re_λ -scaling of natural logarithm of pseudodissipation reported by Yeung and Pope (1989). But further simulations and analysis are required to develop universal scaling laws for $\langle \theta \rangle$ and σ_θ^2 . In fact, these two quantities are input parameters of our model for VG magnitude (section 7.3.4). This embodies the characteristic Reynolds number dependence of velocity gradients in this model.

As summarized in figure 7.1, the advantage of this modeling framework is that the nine components tensorial variable b_{ij} is nearly universal. Therefore, b_{ij} is modeled based on the DNS data of only one flow and the b_{ij} -model is potentially generalizable to all turbulent flows at different Reynolds numbers. Only the scalar θ -model is Reynolds number dependent, which can likely be

represented by universal scaling laws applicable to different types of turbulent flows.

7.3.3 Stochastic model for normalized VG tensor

The Lagrangian dynamics of normalized velocity gradient tensor, b_{ij} , is modeled here as a diffusion process (Karlin and Taylor, 1981). A diffusion process is a continuous-time Markov process and is generally modeled by using a stochastic differential equation (SDE) or a Langevin equation. The stochastic differential equation for A_{ij} commonly used in previously developed models (Girimaji and Pope, 1990a; Chevillard and Meneveau, 2006; Chevillard et al., 2008; Johnson and Meneveau, 2016a) is of the form

$$dA_{ij} = M_{ij}dt + K_{ijkl} dW_{kl} \quad (7.11)$$

where W_{ij} is a tensor-valued isotropic Wiener process such that

$$\langle dW_{ij} \rangle = 0 \quad \text{and} \quad \langle dW_{ij}dW_{kl} \rangle = \delta_{ik}\delta_{jl}dt. \quad (7.12)$$

M_{ij} represent the drift coefficients and K_{ijkl} constitute the diffusion coefficients of the model. Taking the trace of equation (7.11), one can show that $M_{ii} = K_{iikl} = 0$ satisfies the incompressibility condition $A_{ii} = 0$. Starting from the above equation and using the properties of an Itô process (Kloeden and Platen, 1992), one can derive the following SDE for b_{ij} in local timescale t' (see appendix D for derivation):

$$db_{ij} = (\mu_{ij} + \gamma_{ij})dt' + D_{ijkl} dW'_{kl} \quad (7.13)$$

where,

$$\begin{aligned} \mu_{ij} &= \frac{M_{ij}}{A^2} - b_{ij}b_{kl}\frac{M_{kl}}{A^2}, \quad D_{ijkl} = \frac{K_{ijkl}}{A^{3/2}} - b_{ij}b_{pq}\frac{K_{pqkl}}{A^{3/2}}, \\ \gamma_{ij} &= -\frac{1}{2}b_{ij}\frac{K_{pqkl}}{A^{3/2}}\frac{K_{pqkl}}{A^{3/2}} - b_{pq}\frac{K_{pqkl}}{A^{3/2}}\frac{K_{ijkl}}{A^{3/2}} + \frac{3}{2}b_{ij}b_{pq}\frac{K_{pqkl}}{A^{3/2}}b_{mn}\frac{K_{mnkl}}{A^{3/2}} \\ dt' &= A dt, \quad dW'_{ij} = A^{1/2}dW_{ij} \end{aligned} \quad (7.14)$$

and the Wiener process satisfies

$$\langle dW'_{ij} \rangle = 0 \quad \text{and} \quad \langle dW'_{ij} dW'_{kl} \rangle = \delta_{ik} \delta_{jl} dt'. \quad (7.15)$$

It is important to note that all the drift and diffusion coefficients of this system of SDEs are non-dimensional, unlike the A_{ij} -SDE. The drift coefficients of the b_{ij} equation have two parts: (i) μ_{ij} is obtained from the drift coefficient of the A_{ij} equation, M_{ij} , and (ii) γ_{ij} is obtained from the diffusion coefficient of the A_{ij} equation, K_{ijkl} . The diffusion coefficient of the b_{ij} equation, D_{ijkl} , is also obtained from K_{ijkl} . The coefficient γ_{ij} relates the drift and diffusion terms such that despite the random stochastic forcing term, b_{ij} remains mathematically bounded. All the coefficients are modeled in the specific functional forms given above. It can be proved that any system of SDEs for b_{ij} , that complies with the above forms of drift and diffusion terms, clearly satisfies the incompressibility constraint:

$$db_{ii} = 0. \quad (7.16)$$

It further satisfies the mathematical constraint of normalization:

$$d(b_{ij}b_{ij}) = 0 \quad (7.17)$$

which ensures that the Frobenius norm of the tensor \mathbf{b} is equal to unity at all times. The proofs are presented in appendix D.

The diffusion model for b_{ij} given by equation (7.13) results in an evolution of the modeled one-time joint PDF of b_{ij} , $\hat{\mathbb{F}}(\mathbf{b})$, given by the Fokker Planck equation (Pope, 1985):

$$\frac{d\hat{\mathbb{F}}}{dt'} = -\frac{\partial}{\partial b_{ij}} \left[\hat{\mathbb{F}}(\mu_{ij} + \gamma_{ij}) \right] + \frac{1}{2} \frac{\partial^2}{\partial b_{ij} \partial b_{pq}} (\hat{\mathbb{F}} D_{ijkl} D_{pqkl}) \quad (7.18)$$

Now, the exact differential equation for the joint PDF of b_{ij} , $\mathbb{F}(\mathbf{b})$, in a turbulent flow can be derived

from the Navier-Stokes equation or the b_{ij} governing equation (7.6) as

$$\begin{aligned} \frac{d\mathbb{F}}{dt'} = -\frac{\partial}{\partial b_{ij}} \left[\mathbb{F} \left(-b_{ik}b_{kj} + \frac{1}{3}b_{km}b_{mk}\delta_{ij} + b_{ij}b_{mk}b_{kn}b_{mn} + \langle h_{ij} - b_{ij}b_{kl}h_{kl} | \mathbf{b} \rangle \right. \right. \\ \left. \left. + \langle \tau_{ij} - b_{ij}b_{kl}\tau_{kl} | \mathbf{b} \rangle + \langle g_{ij} - b_{ij}b_{kl}g_{kl} | \mathbf{b} \rangle \right) \right] \end{aligned} \quad (7.19)$$

The drift and diffusion coefficients need to be modeled in a way that $\hat{\mathbb{F}}(\mathbf{b}) \approx \mathbb{F}(\mathbf{b})$. However, completely specifying the entire joint PDF of the nine components of b_{ij} is extremely difficult. Hence, in this work we constrain the equations of b_{ij} -moments up to third order to obtain the parameters of diffusion coefficients. This modeled diffusion process is, therefore, consistent up to order three, although the numerical results of the model show reasonable agreement of much higher order moments.

7.3.3.1 Drift coefficients

For statistical modeling, the key is to ensure that the modeled PDF ($\hat{\mathbb{F}}(\mathbf{b})$) closely resembles the exact PDF ($\mathbb{F}(\mathbf{b})$) obtained by DNS. Comparing the terms of equations (7.18) and (7.19), and considering that the role of D_{ijkl} is to model the large-scale forcing effect and the role of γ_{ij} is to maintain the unit Frobenius norm of b_{ij} , the drift coefficient μ_{ij} is modeled as:

$$\mu_{ij} = -b_{ik}b_{kj} + \frac{1}{3}b_{km}b_{mk}\delta_{ij} + b_{ij}b_{mk}b_{kn}b_{mn} + \langle h_{ij} - b_{ij}b_{kl}h_{kl} | \mathbf{b} \rangle + \langle \tau_{ij} - b_{ij}b_{kl}\tau_{kl} | \mathbf{b} \rangle \quad (7.20)$$

This ensures that the modeled PDF follows the dynamics of the exact PDF equation. Thus, μ_{ij} represents the dynamics of the inertial and isotropic pressure contributions and the conditional mean of the anisotropic pressure and viscous contributions.

The conditional mean normalized anisotropic pressure Hessian and viscous Laplacian tensors, $\langle h_{ij} | \mathbf{b} \rangle$ and $\langle \tau_{ij} | \mathbf{b} \rangle$, require closure modeling. As discussed in section 7.2.1, the tensor $\tilde{\mathbf{b}}$ in the principal reference frame of the strain-rate tensor can be expressed as a function of only four bounded variables. Therefore, in order to take advantage of this four-dimensional bounded state-space of $\tilde{\mathbf{b}}$, the conditional averaging of the normalized pressure Hessian and viscous Laplacian

tensors is performed in the principal reference frame. For a rotation tensor, \mathbf{Q} , with columns constituted by the right eigenvectors of \mathbf{s} , the required tensors in the principal reference frame are

$$\tilde{b}_{ij} = Q_{ki}b_{kl}Q_{lj} \quad , \quad \tilde{h}_{ij} = Q_{ki}h_{kl}Q_{lj} \quad , \quad \tilde{\tau}_{ij} = Q_{ki}\tau_{kl}Q_{lj}. \quad (7.21)$$

Then, the conditional mean pressure Hessian and viscous Laplacian tensors in the laboratory reference frame are given by

$$\begin{aligned} \langle h_{ij} | \mathbf{b} \rangle &= \langle Q_{ik}\tilde{h}_{kl}Q_{jl} | \mathbf{b} \rangle = Q_{ik}\langle \tilde{h}_{kl} | \tilde{\mathbf{b}} \rangle Q_{jl} \quad , \\ \langle \tau_{ij} | \mathbf{b} \rangle &= \langle Q_{ik}\tilde{\tau}_{kl}Q_{jl} | \mathbf{b} \rangle = Q_{ik}\langle \tilde{\tau}_{kl} | \tilde{\mathbf{b}} \rangle Q_{jl} \end{aligned} \quad (7.22)$$

since \mathbf{Q} is a function of \mathbf{b} . Therefore, the conditional mean pressure Hessian and viscous Laplacian tensors in the laboratory reference frame can be obtained if the conditional mean pressure Hessian and viscous Laplacian tensors in the principal frame are known and the local strain-rate eigenvectors are known.

In the principal reference frame, the tensor \tilde{b}_{ij} can be uniquely defined by a set of only four bounded variables – q, r, a_2 and ω_2 (appendix C). Therefore, the conditional mean pressure Hessian and viscous Laplacian tensors in the principal frame can be modeled as a function of only four bounded variables, as follows:

$$\langle \tilde{h}_{ij} | \tilde{\mathbf{b}} \rangle = \langle \tilde{h}_{ij} | q, r, a_2, \omega_2 \rangle \quad , \quad \langle \tilde{\tau}_{ij} | \tilde{\mathbf{b}} \rangle = \langle \tilde{\tau}_{ij} | q, r, a_2, \omega_2 \rangle \quad (7.23)$$

The goal is to develop a data-driven model for the above tensors in terms of a four-dimensional input. Recently, studies (Parashar et al., 2020; Tian et al., 2021) have used tensor-basis neural network to model the unnormalized pressure Hessian (H_{ij}) and viscous Laplacian (T_{ij}) tensors in the A_{ij} -equation as a function of A_{ij} . Since A_{ij} constitutes an unbounded space and the behavior of the tensors H_{ij} and T_{ij} is not necessarily invariant across turbulent flows of different Reynolds numbers, network-based modeling becomes essential. However, in our case (q, r, a_2, ω_2) form a

bounded state-space and the conditional mean dynamics of \tilde{h}_{ij} and $\tilde{\tau}_{ij}$ in the bounded \tilde{b}_{ij} space is nearly unaltered with Reynolds number variation for a broad range of Re_λ (chapters 5 and 6). Therefore, the simpler and more accurate data-driven approach of direct tabulation based on DNS data is used in this work. The data-driven approach is outlined below:

1. The (q, r, a_2, ω_2) is discretized into $(60, 60, 30, 30)$ uniform bins. This discretization strikes the appropriate balance between sampling accuracy in the bins and the desired details of nonlocal flow physics to be captured. Other discretizations are tested to show convergence to this combination for the most accurate results.
2. The conditional expectations of the tensors, $\langle \tilde{h}_{ij} | q, r, a_2, \omega_2 \rangle$ and $\langle \tilde{\tau}_{ij} | q, r, a_2, \omega_2 \rangle$, are computed in this discrete phase-space, using DNS data set of forced isotropic turbulence of $Re_\lambda = 427$ (see appendix A for details of the dataset). Note that only one lookup table is required to model the mean nonlocal dynamics for turbulent flows of different Re_λ .
3. This lookup table can then be accessed by an inexpensive array-indexing operation, to determine the conditional mean pressure and viscous dynamics in the principal frame for a given (q, r, a_2, ω_2) at any point in the flow field or following a fluid particle. This is then transformed to the laboratory reference frame (equation 7.22) based on the local eigendirections of strain-rate tensor, to be used in μ_{ij} for computations.

This completes the modeling of the drift coefficient μ_{ij} as a function of the local b_{ij} . The flow physics captured by this data-driven model does not depend on the orientation of the coordinate frame of the observer. Neither the four input variables nor the output tensors depend on the observer's frame of reference. Therefore, this data-driven closure naturally accounts for rotational invariance.

For use in the b_{ij} -SDE, the conditional mean \mathbf{h} and $\boldsymbol{\tau}$ tensors in the laboratory reference frame are obtained by using the local eigenvectors of the strain-rate tensor in equations (7.22). If we change the observer's coordinate frame, although the output of the data-driven closure model does not change, these final \mathbf{h} and $\boldsymbol{\tau}$ tensors used in the b_{ij} model will change. It is straightforward

to show that under a Galilean transformation such as rotation of the coordinate frame by certain angles, the \mathbf{h} and $\boldsymbol{\tau}$ tensors and by extension the $\boldsymbol{\mu}$ tensor also rotate by the same angles. This proves that our data-driven model for the mean drift term of the stochastic differential equation is Galilean invariant. The proof for the same is presented in appendix D. Next, we present the formulation for the diffusion coefficients of the model. As will be shown, these terms are explicit functions of \mathbf{b} itself, and are therefore Galilean invariant by construction.

7.3.3.2 Diffusion coefficients

As discussed at the beginning of this section, the interrelationship between the diffusion coefficient D_{ijkl} and the drift coefficient γ_{ij} is important in guaranteeing that the mathematical and physical constraints of b_{ij} are satisfied. This relationship holds if we use their functional forms as given in equation (7.14), in terms of K_{ijkl} from the A_{ij} SDE. For this, we assume a general isotropic form of the four dimensional tensor, K_{ijkl} , following previous models (Girimaji and Pope, 1990a; Chevillard et al., 2008; Johnson and Meneveau, 2016a):

$$K_{ijkl} = A^{3/2}(c_1\delta_{ij}\delta_{kl} + c_2\delta_{ik}\delta_{jl} + c_3\delta_{il}\delta_{jk}) \quad (7.24)$$

where c_1, c_2, c_3 are constant non-dimensional parameters of the model. Only two of these three parameters are independent if we impose the incompressibility condition:

$$\begin{aligned} K_{iikl} &= A^{3/2}(c_1\delta_{ii}\delta_{kl} + c_2\delta_{ik}\delta_{il} + c_3\delta_{il}\delta_{ik}) = (3c_1 + c_2 + c_3)\delta_{kl} = 0 \\ \implies c_1 &= -\frac{c_2+c_3}{3} \end{aligned} \quad (7.25)$$

From equations (7.14), (7.24) and (7.25), the diffusion coefficient of the b_{ij} equation is

$$D_{ijkl} = c_2 \left(-\frac{1}{3}\delta_{ij}\delta_{kl} + \delta_{ik}\delta_{jl} - b_{ij}b_{kl} \right) + c_3 \left(-\frac{1}{3}\delta_{ij}\delta_{kl} + \delta_{il}\delta_{jk} - b_{ij}b_{lk} \right) \quad (7.26)$$

and part of the drift coefficient is

$$\gamma_{ij} = -\left(\frac{7}{2}(c_2^2 + c_3^2) + (2 + 6q)c_2c_3\right)b_{ij} - 2c_2c_3b_{ji} \quad (7.27)$$

To determine the constant parameters, c_2 and c_3 , we use a moments constraint method similar to Girimaji and Pope (1990a). In this method, the equations of second and third order moments of b_{ij} are constrained to follow the dynamics of a statistically stationary turbulent flow, while driving the values of these moments toward the desired values obtained from DNS data. First, the SDEs for the second (q) and third (r) invariants are derived from the b_{ij} -SDE (7.13) using Itô's lemma (appendix D):

$$\begin{aligned} dq &= -\left(b_{ij}\mu_{ji} + b_{ij}\gamma_{ji} + \frac{1}{2}D_{ijkl}D_{jikl}\right)dt' - b_{ij}D_{jimn}dW'_{mn} \\ dr &= -\left(b_{ik}b_{kj}\mu_{ji} + b_{ik}b_{kj}\gamma_{ji} + b_{ij}D_{jkmn}D_{kimn}\right)dt' - b_{ij}b_{jk}D_{kimn}dW'_{mn} \end{aligned} \quad (7.28)$$

Taking mean of the above equations and substituting the expressions for D_{ijkl} and γ_{ij} from equations (7.26) and (7.27), yields the following differential equations of the moments – $\langle q \rangle$ and $\langle r \rangle$:

$$\begin{aligned} \frac{d\langle q \rangle}{dt'} &= -\langle b_{ij}\mu_{ji} \rangle - \langle b_{ij}\gamma_{ji} \rangle - \frac{1}{2}\langle D_{ijkl}D_{jikl} \rangle \\ &= -\langle b_{ij}\mu_{ji} \rangle - (c_2^2 + c_3^2)(8\langle q \rangle + 1) - c_2c_3(16\langle q^2 \rangle + 4\langle q \rangle + 4) \quad (7.29) \\ \frac{d\langle r \rangle}{dt'} &= -\langle b_{ik}b_{kj}\mu_{ji} \rangle - \langle b_{ik}b_{kj}\gamma_{ji} \rangle - \langle b_{ij}D_{jkmn}D_{kimn} \rangle \\ &= -\langle b_{ik}b_{kj}\mu_{ji} \rangle - (c_2^2 + c_3^2)\left(\frac{27}{2}\langle r \rangle\right) - c_2c_3(6\langle r \rangle + 30\langle qr \rangle - 6\langle b_{ij}b_{jk}b_{ik} \rangle) \end{aligned} \quad (7.30)$$

To model a statistically stationary solution of turbulence, the rate-of-change of moments must be driven to zero while ensuring that the moment values converge to that of DNS data. For this, we

equate the RHS to negative of the error term:

$$\begin{aligned}
\frac{d\langle q \rangle}{dt'} &= -\langle b_{ij}\mu_{ji} \rangle - (c_2^2 + c_3^2)(8\langle q \rangle + 1) - c_2c_3(16\langle q^2 \rangle + 4\langle q \rangle + 4) = -R(\langle q \rangle - \bar{q}) \\
\frac{d\langle r \rangle}{dt'} &= -\langle b_{ik}b_{kj}\mu_{ji} \rangle - (c_2^2 + c_3^2)\left(\frac{27}{2}\langle r \rangle\right) - c_2c_3(6\langle r \rangle + 30\langle qr \rangle - 6\langle b_{ij}b_{jk}b_{ik} \rangle) \\
&= -R(\langle r \rangle - \bar{r})
\end{aligned} \tag{7.31}$$

where \bar{q}, \bar{r} are the global mean of q, r obtained from DNS data. Here, R represents the rate of convergence of these moments and is set to unity. An *a priori* simulation of the b_{ij} model equations is run in the normalized timescale t' , with an ensemble of 40000 particles. At each time step, the above system of nonlinear equations is solved using Newton's method to determine the values of the parameters c_2, c_3 . In this *a priori* run, the parameters converge to the following values:

$$c_2 = 0.009877 \quad , \quad c_3 = -0.06402 \tag{7.32}$$

as the model's moments, $\langle q \rangle$ and $\langle r \rangle$, converge very close to the DNS values of \bar{q} and \bar{r} . These optimized diffusion parameter values are used in the stochastic model for b_{ij} and are independent of the Reynolds number.

7.3.4 Stochastic model for VG magnitude

The Lagrangian evolution of the standardized VG magnitude θ^* (equation 7.9) is modeled using a modified lognormal approach. Due to the resemblance of its statistical properties with the Ornstein-Uhlenbeck (OU) process (Uhlenbeck and Ornstein, 1930), such as its near normal probability distribution and exponential decay of the auto-correlation function, the stochastic differential equation of θ^* is formulated within the framework of the OU process. The OU process is a stationary continuous Gaussian Markov process that is often used in modeling systems of finance, mathematics and physical and biological sciences (Pope and Chen, 1990; Girimaji and Pope, 1990a; Klebaner, 2012). It further shows the property of mean-reversion. The SDE for a

general OU process θ^* evolving in time t^* is given by

$$d\theta^* = -\alpha(\theta^* - \langle\theta^*\rangle)dt^* + \beta dW^* \quad (7.33)$$

where, $\alpha, \beta > 0$ are parameters of the model, $t^* = \langle A \rangle t$ is the non-dimensional global time scale and dW^* is the increment of a Wiener process or a Gaussian random variable with zero mean and variance dt^* . The parameter α represents the rate of mean-reversion, and without loss of generality it is set to unity since the model propagates in timescale t^* which is already normalized. The expected value $\langle\theta^*\rangle = 0$, by construction, in DNS data. Therefore, the general form of θ^* -SDE used in this work is

$$d\theta^* = -\theta^* dt^* + \beta dW^*. \quad (7.34)$$

The diffusion coefficient, β , is modeled in three different ways as described below.

7.3.4.1 Model 1 - original OU process

In the first model, we consider the simple OU dynamics that satisfies the global mean and global variance of θ^* . In this case, the diffusion coefficient β is taken to be a constant value, which is calculated as follows. The equation for the global mean is obtained from equation (7.34),

$$\frac{d\langle\theta^*\rangle}{dt^*} = -\langle\theta^*\rangle = 0 \quad \text{since } \langle\theta^*\rangle = 0. \quad (7.35)$$

Thus, the model maintains a stationary mean value of θ^* once the solution is driven to the zero mean value by the mean-reversion property. Next, the equation for the global variance is obtained from equation (7.34) using Itô's product rule,

$$\frac{d\langle\theta^{*2}\rangle}{dt^*} = -2\langle\theta^{*2}\rangle + \beta^2 \quad (7.36)$$

For a statistically stationary solution, we must have

$$\frac{d\langle\theta^{*2}\rangle}{dt^*} = 0 \quad \implies \quad \beta = \sqrt{2\langle\theta^{*2}\rangle} \quad (7.37)$$

Therefore, the final form of the θ^* -SDE for Model 1 is given by

$$d\theta^* = -\theta^* dt^* + \sqrt{2\langle\theta^{*2}\rangle} dW^*. \quad (7.38)$$

Here, the value of the variance $\langle\theta^{*2}\rangle$ is obtained from DNS data. It is evident that this model for θ^* is completely decoupled from b_{ij} and can be solved numerically without any information of b_{ij} .

7.3.4.2 Model 2 - modified OU process

Next, we want to ensure that the conditional variance of θ^* conditioned on the local streamline geometry (q, r) is satisfied. This conditional variance is plotted in figure 7.3 for DNS data of forced isotropic turbulence at different Reynolds numbers. It is evident that θ^* shows a unique distribution of conditional variance in different regions of the q - r plane. Further, the conditional variance is nearly invariant with the Re_λ . Thus, in order to incorporate further flow physics into the model, we modify the diffusion coefficient such that it satisfies this unique conditional variance of θ^* in the q - r plane. For this, we consider the diffusion coefficient β to be a function of the VG invariants, i.e. $\beta = \beta(q, r)$. The equation for the conditional variance, $\langle(\theta^* - \langle\theta^*|q, r\rangle)^2|q, r\rangle$, can be derived from equation (7.34) as

$$\frac{d}{dt^*}\langle(\theta^* - \langle\theta^*|q, r\rangle)^2|q, r\rangle = -2\langle\theta^{*2}|q, r\rangle + \langle\theta^*|q, r\rangle^2 + (\beta(q, r))^2 \quad (7.39)$$

The conditional variance remains statistically stationary only if

$$\frac{d}{dt^*}\langle(\theta^* - \langle\theta^*|q, r\rangle)^2|q, r\rangle = 0 \quad \implies \quad \beta(q, r) = \sqrt{2(\langle\theta^{*2}|q, r\rangle - \langle\theta^*|q, r\rangle^2)} \quad (7.40)$$

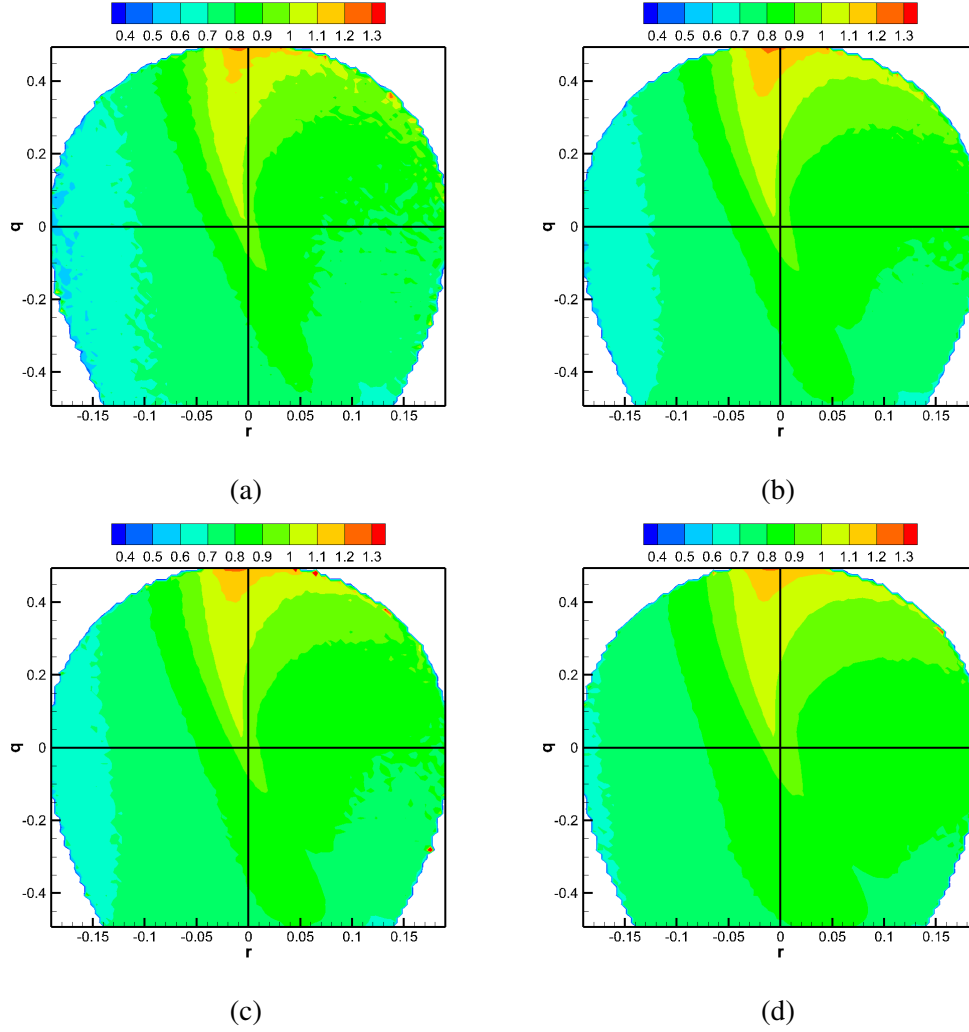


Figure 7.3: Conditional variance of θ^* conditioned on $q-r$, i.e. $\langle (\theta^* - \langle \theta^* | q, r \rangle)^2 | q, r \rangle$, for isotropic turbulent flows of Taylor Reynolds numbers: (a) $Re_\lambda = 225$, (b) $Re_\lambda = 385$, (c) $Re_\lambda = 427$, (d) $Re_\lambda = 588$.

Therefore, the final SDE of θ^* for Model 2 is given by

$$d\theta^* = -\theta^* dt^* + \sqrt{2(\langle \theta^{*2} | q, r \rangle - \langle \theta^* | q, r \rangle^2)} dW^*. \quad (7.41)$$

Here, the conditional variance values are obtained from DNS data of one Re_λ by discretizing the q, r space into 30×30 bins. The same conditional variance table is applicable when modeling turbulent flows of different Reynolds numbers, as evident from figure 7.3. This θ^* -model is weakly coupled with the b_{ij} dynamics since it depends on q, r .

7.3.4.3 Model 3 - consistent modified OU process

Model 1 ensures that the constant diffusion coefficient captures the accurate global variance of θ^* , while model 2 enforces the accurate modeling of conditional variance of θ^* for a given q, r . Finally, in Model 3 we propose an adjustment to model 2 such that both the conditional and global variances are satisfied. For this, we propose to shift the conditional variance based diffusion coefficient of model 2 by a constant value, β_0 , as follows:

$$d\theta^* = -\theta^* dt^* + (\sqrt{2(\langle \theta^{*2} | q, r \rangle - \langle \theta^* | q, r \rangle^2)} + \beta_0) dW^*. \quad (7.42)$$

Here, the value of β_0 is calculated based on the solutions of models 1 and 2. Model 3 also depends upon b_{ij} through its invariants (q, r) .

7.3.5 Model summary

The resulting model for the Lagrangian evolution of the complete velocity gradient tensor in a turbulent flow is constituted by a system of stochastic differential equations for the normalized velocity gradient tensor, b_{ij} , and a separate stochastic differential equation for the standardized VG magnitude, θ^* .

The final system of equations for b_{ij} in local timescale (t'):

$$db_{ij} = (\mu_{ij} + \gamma_{ij}) dt' + D_{ijkl} dW'_{kl} \quad (7.43)$$

$$\begin{aligned}
\mu_{ij} &= - b_{ik}b_{kj} + \frac{1}{3}b_{km}b_{mk}\delta_{ij} + b_{ij}b_{mk}b_{kn}b_{mn} + \langle h_{ij}|\mathbf{b} \rangle - b_{ij}b_{kl}\langle h_{kl}|\mathbf{b} \rangle \\
&\quad + \langle \tau_{ij}|\mathbf{b} \rangle - b_{ij}b_{kl}\langle \tau_{kl}|\mathbf{b} \rangle , \\
\gamma_{ij} &= - \left(\frac{7}{2}(c_2^2 + c_3^2) + (2 + 6q)c_2c_3 \right) b_{ij} - 2c_2c_3b_{ji} , \\
D_{ijkl} &= c_2 \left(-\frac{1}{3}\delta_{ij}\delta_{kl} + \delta_{ik}\delta_{jl} - b_{ij}b_{kl} \right) + c_3 \left(-\frac{1}{3}\delta_{ij}\delta_{kl} + \delta_{il}\delta_{jk} - b_{ij}b_{lk} \right) \quad (7.44)
\end{aligned}$$

Here, the parameter values are

$$c_2 = 0.009877 \quad , \quad c_3 = -0.06402. \quad (7.45)$$

The conditional mean normalized pressure Hessian and viscous Laplacian tensors are obtained from the data-driven closure in the strain-rate (s) eigen reference frame as a function of the current (q, r, a_2, ω_2), followed by a rotation to the laboratory reference frame using the local eigenvectors of s :

$$\langle h_{ij}|\mathbf{b} \rangle = Q_{ik}\langle \tilde{h}_{kl}|q, r, a_2, \omega_2 \rangle Q_{jl} \quad \text{and} \quad \langle \tau_{ij}|\mathbf{b} \rangle = Q_{ik}\langle \tilde{\tau}_{kl}|q, r, a_2, \omega_2 \rangle Q_{jl}. \quad (7.46)$$

The above parameter values and the data-driven closure can be applied to model velocity gradient dynamics of incompressible turbulent flows irrespective of the Taylor Reynolds number.

The final stochastic differential equation for θ^* in global timescale ($t^* = \langle A \rangle t$):

- Model 1 -

$$d\theta^* = -\theta^* dt^* + \sqrt{2\langle \theta^{*2} \rangle} dW^* , \quad (7.47)$$

- Model 2 -

$$d\theta^* = -\theta^* dt^* + \sqrt{2(\langle \theta^{*2}|q, r \rangle - \langle \theta^*|q, r \rangle^2)} dW^* , \quad (7.48)$$

- Model 3 -

$$d\theta^* = -\theta^* dt^* + \left(\sqrt{2(\langle \theta^{*2}|q, r \rangle - \langle \theta^*|q, r \rangle^2)} + \beta_0 \right) dW^* . \quad (7.49)$$

where, $\beta_0 = 0.103$. The diffusion coefficients of models 2 and 3 are obtained from the tabulated

Data-based component	Discretization of state-space	Re_λ dependence
$\langle \tilde{\mathbf{h}} q, r, a_2, \omega_2 \rangle$	(60,60,30,30)	Re_λ -independent
$\langle \tilde{\boldsymbol{\tau}} q, r, a_2, \omega_2 \rangle$	(60,60,30,30)	Re_λ -independent
$\langle (\theta^* - \langle \theta^* q, r \rangle)^2 q, r \rangle$	(30,30)	Re_λ -independent
$\langle \theta \rangle, \sigma_\theta, \langle A \rangle$	1	Re_λ -dependent

Table 7.1: Components of model based on DNS data.

conditional variance of θ^* invariant with Re_λ (figure 7.3). The VG magnitude and the VG tensor are then given by

$$A = e^{\theta^* \sigma_\theta + \langle \theta \rangle}, \quad A_{ij} = A b_{ij} \quad (7.50)$$

The Reynolds number dependent parameters of the model:

$$\langle \theta \rangle = 2.7493, \quad \sigma_\theta = 0.589655, \quad \langle A \rangle = 18.64173 \quad (7.51)$$

are calculated for the DNS dataset of $Re_\lambda = 427$. The above θ^* models can be used to reproduce the dynamics of VG magnitude for any Reynolds number, provided the corresponding parameter values are known. These parameters exhibit an approximate scaling-law in terms of Re_λ (figure 7.2). Further analysis and DNS data are required to establish universal scaling laws and thus present a robust and generalizable model for VG magnitude with an explicit dependence on Re_λ .

To reconcile between the two different timescales - t' used for b_{ij} evolution and t^* used for θ^* evolution - a third ordinary differential equation,

$$\frac{dt^*}{dt'} = \frac{\langle A \rangle}{A} \quad (7.52)$$

is solved to determine t^* for a given t' . Finally, the Lagrangian evolution of the velocity gradient tensor, A_{ij} , is obtained by multiplying A and b_{ij} at different global time t^* . Overall, the velocity

gradient model presented here consists of three types of data-based components that are listed in table 7.1. The four-dimensional lookup tables for normalized pressure Hessian and viscous Laplacian tensors and the two-dimensional table for conditional variance of θ^* can be used in modeling velocity gradient dynamics independent of Reynolds numbers; only the three scalar parameters of the model which are statistics of the VG magnitude are Reynolds number dependent and potentially generalizable in the future with universal scaling laws.

7.4 Numerical procedure

The numerical solution of the model equations involves numerically propagating the velocity gradient tensor, in terms of the variables b_{ij} and θ^* , of an ensemble of 40000 particles. As the initial conditions for the simulations, the particles are picked at random from a randomly generated incompressible isotropic velocity field. The trajectories are advanced for a total time period of approximately $1200\tau_\eta$ following these steps at each update:

1. The b_{ij} SDEs (equation 7.43) are numerically propagated in the normalized local timescale t' , using a second-order weak predictor-corrector scheme (see appendix D) with a constant time increment dt' . At each step, the conditional mean nonlocal pressure and viscous contributions are calculated based on the current (q, r, a_2, ω_2) values, using the (60, 60, 30, 30) sized lookup-table.
2. The θ^* SDE (equation 7.47, 7.48 or 7.49) is advanced using the second-order weak predictor-corrector numerical scheme (appendix D) in the global timescale t^* , using a first order approximation of the increment $dt^* = (\langle A \rangle / A) dt'$ for a fixed value of dt' .
3. The global timescale, t^* , is obtained for every particle at each t' by numerically solving the ordinary differential equation,

$$\frac{dt^*}{dt'} = \frac{\langle A \rangle}{A} \tag{7.53}$$

using the implicit second-order Trapezium rule method.

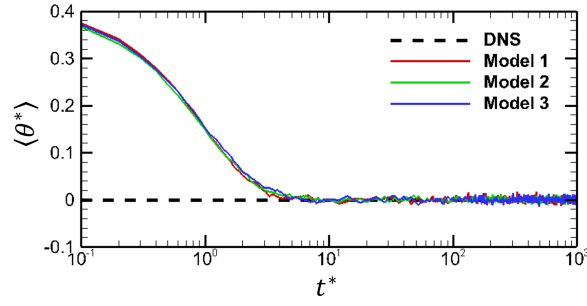
The model solution propagates all particles at a uniform local time increment of $dt' = 0.01$, but

the global timescale t^* varies from one particle to the other depending upon its current velocity gradient magnitude. A particle with a smaller magnitude requires fewer steps in t' to reach a certain t^* , than a particle with a larger magnitude. The VG magnitude θ^* evolves in global time t^* , which approximately scales with Kolmogorov timescale. On the other hand, b_{ij} evolves in local timescale t' which varies depending on the local value of A . Issues may arise when $A < \langle A \rangle$, i.e. when b_{ij} evolves faster than θ^* , and appropriate measures should be taken to ensure that the dt' is suitable to propagate the b_{ij} equations. However, particles with such low A values do not contribute significantly toward the overall velocity gradient statistics and convergence of the model's results for $dt' = 0.05, 0.01$ and 0.002 reveal that $dt' = 0.01$ is sufficient here for accurate statistical modeling.

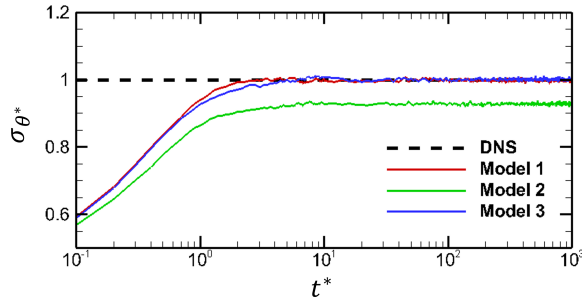
The incompressibility and normalization constraints are automatically upheld by the model, but are only valid up to the order of numerical error. Therefore, to avoid the accretion of numerical errors over large periods of time, hard constraints of $b_{ii} = 0$ and $\|\mathbf{b}\|_F = 1$ are enforced after every update. The computation time is approximately 1.5-2 hours on a single processor for the model's simulations to achieve statistically stationary solutions. The results of model simulations illustrated in the next section are marked as model 1 if equation (7.47) is used for θ^* , model 2 if equation (7.48) is used for θ^* , and model 3 if equation (7.49) is used for θ^* , each along with the b_{ij} equation (7.43). The convergence of all the major results have been tested for these models by performing the simulations with 40000 and 100000 particles.

7.5 Results and comparison with DNS data

This section presents a statistical analysis of the solutions of the three models and a comparison with the statistics of the corresponding DNS data and some of the previous models. First, the statistics of θ^* are illustrated, followed by the statistics of b_{ij} . Finally the complete velocity gradient tensor A_{ij} -statistics are shown. The time evolution of model's statistics are illustrated as a function of the global normalized time t^* . The converged stationary statistics are obtained by averaging over multiple time realizations of the model's solution, separated by at least $5\tau_\eta$, well after it has achieved statistical stationarity.



(a)



(b)

Figure 7.4: Evolution of θ^* statistics: (a) mean, $\langle \theta^* \rangle$ and (b) standard deviation, σ_{θ^*} , for the three models with different θ^* equations. The DNS statistics are marked by the dashed lines. The time axis is in logscale.

7.5.1 VG magnitude

First, the evolution of the mean and standard deviation of θ^* over global normalized time t^* are plotted for all the three θ^* -model equations in figure 7.4. Note that the time axes are plotted in logscale to display the transients clearly. The numerical simulation starts from an initially random field, which is inconsistent with the DNS parameter values of $\langle \theta \rangle$ and σ_{θ} , and therefore the initial values of $\langle \theta^* \rangle$ and σ_{θ^*} are different from zero and unity, respectively. Over time, the model's solution evolves toward the correct values achieving statistically stationary state at $t^* \approx 6 \implies t \approx 7\tau_{\eta}$, where t is the real time. As expected, the global mean of θ^* is captured equally well by all three models due to the mean-reverting property of the OU process. The global standard deviation of θ^* is reproduced accurately by both the models 1 and 3. However, it worsens in

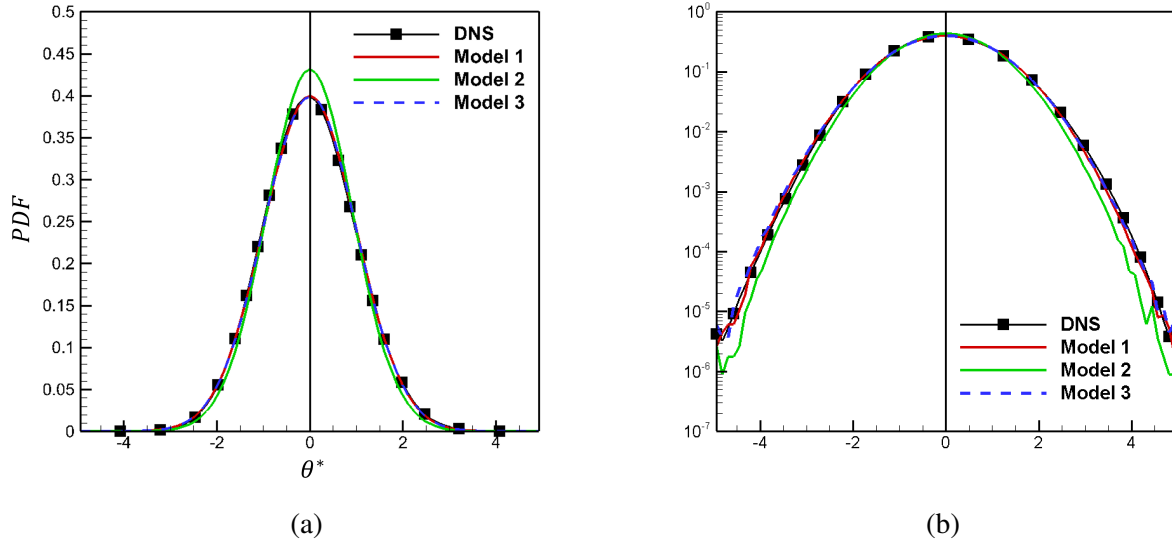


Figure 7.5: PDF of standardized VG magnitude θ^* in: (a) linear-linear scale and (b) linear-log scale, for the three models. The black solid line with symbols represent the θ^* -PDF from DNS data.

model 2 compared to the original OU model (model 1). This reflects the fact that imposing θ^* to satisfy the conditional variance conditioned on local streamline geometry (q, r) in model 2 does not necessarily guarantee that the global variance is also satisfied. This justifies the need for the third model that guarantees both the features and thus provides the correct global standard deviation value.

The probability density function (PDF) of the VG magnitudes are now investigated. The converged PDF of the standardized VG magnitude, θ^* , for all the models and DNS data are plotted in figure 7.5. It is clearly visible that models 1 and 3 are able to reproduce the θ^* PDF very well, while the model 2 shows deviation from the desired DNS result. The plot in the log-linear scale confirms that the converged PDFs of models 1 and 3 agree well with that of DNS even near the extreme tails of the PDFs. Next, the converged PDFs of the VG magnitude ($A/\langle A \rangle$) in each of the three models and DNS are plotted in figure 7.6. All three models capture the peak of the PDF reasonably well but model 2 deviates at higher values of the magnitude. Model 3 is able to reproduce the tails of the PDF near the moderate to extreme A values slightly better than the model 1.

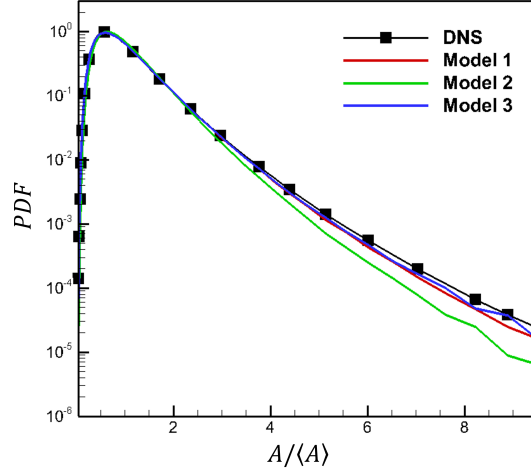


Figure 7.6: PDF of VG magnitude $A/\langle A \rangle$.

7.5.2 Normalized VG tensor

The conditional mean trajectories (CMTs) in the phase plane of normalized velocity gradient invariants (q, r) are examined as an *a priori* test of the data-driven model used to capture the conditional mean nonlocal effects of pressure and viscosity (section 7.3.3) on the b_{ij} -dynamics. The q - r CMTs are obtained by integrating the vector field of conditional mean velocity ($\tilde{\mathbf{v}}$) in the q - r plane:

$$\begin{aligned} \tilde{\mathbf{v}} &= \begin{pmatrix} \tilde{v}_q \\ \tilde{v}_r \end{pmatrix} = \left\langle \begin{pmatrix} dq/dt' \\ dr/dt' \end{pmatrix} \middle| q, r \right\rangle \\ &= \left\langle \begin{pmatrix} -3r + 2qb_{ij}b_{ik}b_{kj} - h_{ij}(b_{ji} + 2qb_{ij}) - \tau_{ij}(b_{ji} + 2qb_{ij}) \\ \frac{2}{3}q^2 + 3rb_{ij}b_{ik}b_{kj} - h_{ij}(b_{jk}b_{ki} + 3rb_{ij}) - \tau_{ij}(b_{jk}b_{ki} + 3rb_{ij}) \end{pmatrix} \middle| q, r \right\rangle. \end{aligned} \quad (7.54)$$

due to the inertial, pressure and viscous processes in the turbulent flow. Note that the effect of the large-scale forcing is not included in the CMTs shown here because it is not accounted for by the data-driven closure but rather by the stochastic forcing term in the b_{ij} -SDE, which can not be tested *a priori*. The q - r CMTs obtained using DNS data directly are plotted in figure 7.7(a).

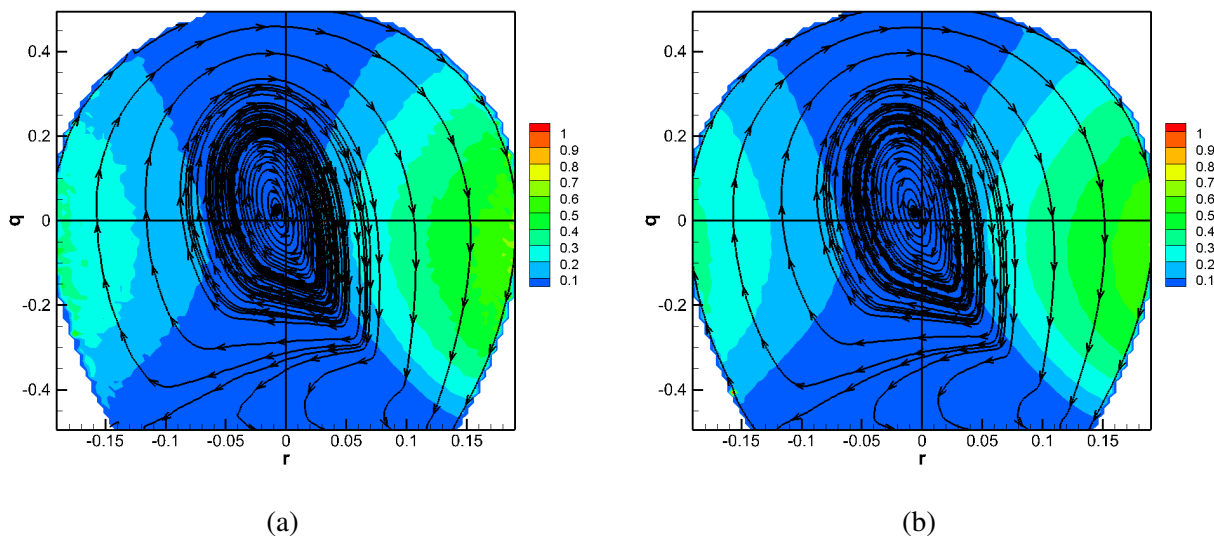


Figure 7.7: Conditional mean trajectories in the q - r plane due to the inertial, pressure and viscous effects obtained using (a) DNS data and (b) b_{ij} data-driven model. Background contours represent the speed of the trajectory at each point, given by the magnitude of the conditional mean velocity vector, $|\tilde{\mathbf{v}}|$.

As discussed in chapter 5, trajectories closer to the origin converge toward the attractor near the origin (represents pure-shear streamlines) while trajectories that are outside the separatrix loop are attracted toward the bottom line attractor (represents pure-strain streamlines). This behavior is almost exactly replicated by the q - r CMTs of the model, computed using the data-driven closure for the conditional mean pressure Hessian and viscous Laplacian tensors in the above equation and illustrated in figure 7.7(b). The close resemblance between the two is somewhat expected given the very nature of the lookup table approach for closure.

Now, we compare the *a posteriori* results of the normalized VG tensor of the model with that of the DNS. The second (q) and third (r) invariants of the tensor are important quantities as they determine the geometry of the local flow streamlines. The evolution of up to fourth order moments of q and r in global normalized time t^* are plotted for each of the three models in figure 7.8. It is first evident that all the three models with the same b_{ij} -SDE but different θ^* -SDEs produce nearly identical q, r moment values. Thus, it appears that the variation in θ^* model does not have

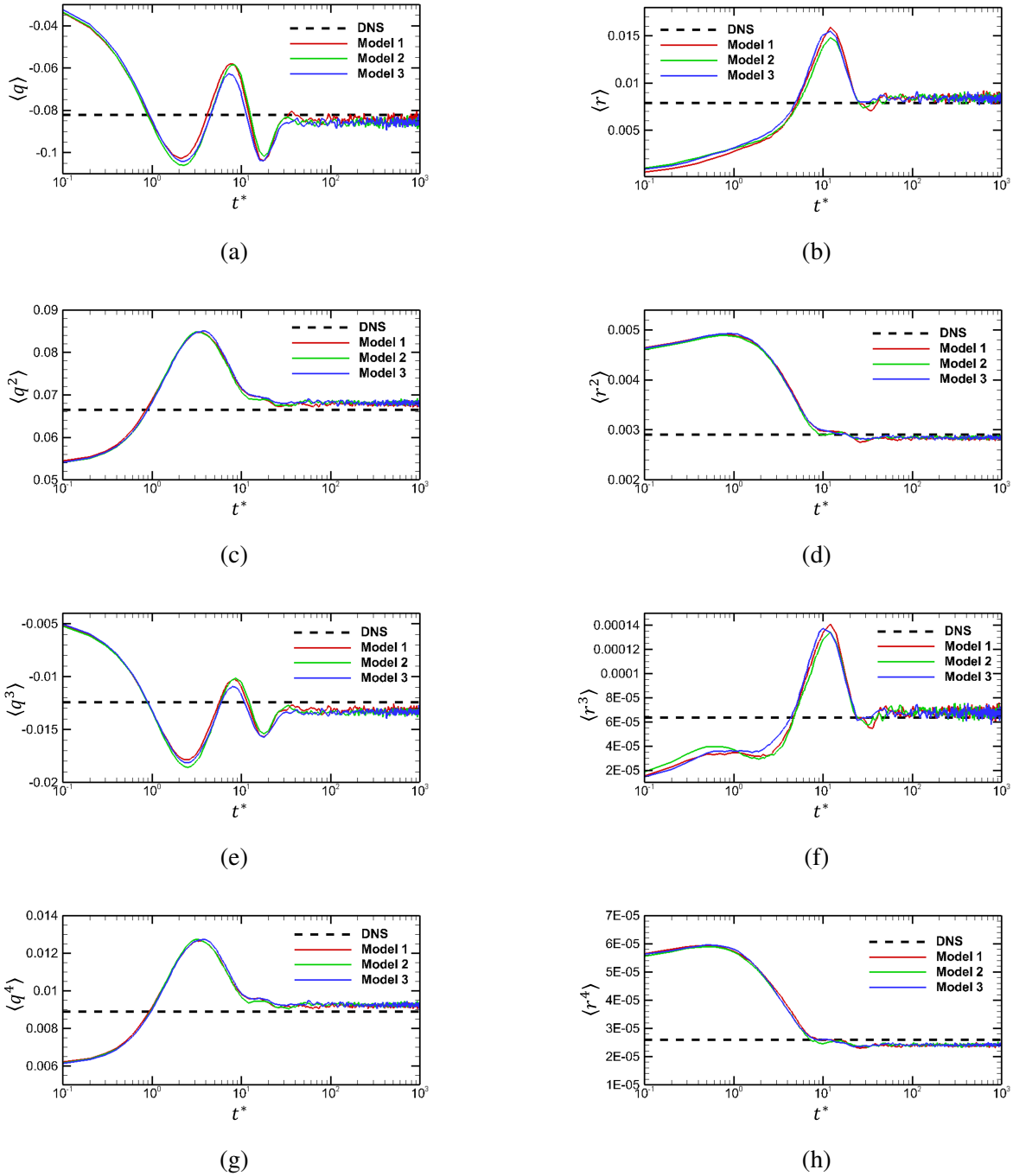


Figure 7.8: Evolution of q and r statistics in global normalized time t^* . Means: (a) $\langle q \rangle$ and (b) $\langle r \rangle$; second order moments: (c) $\langle q^2 \rangle$ and (d) $\langle r^2 \rangle$; third order moments: (e) $\langle q^3 \rangle$ and (f) $\langle r^3 \rangle$; fourth order moments: (g) $\langle q^4 \rangle$ and (h) $\langle r^4 \rangle$ for the three models with different θ^* equations. The dashed lines represent the DNS statistics. The time axis is in log-scale.

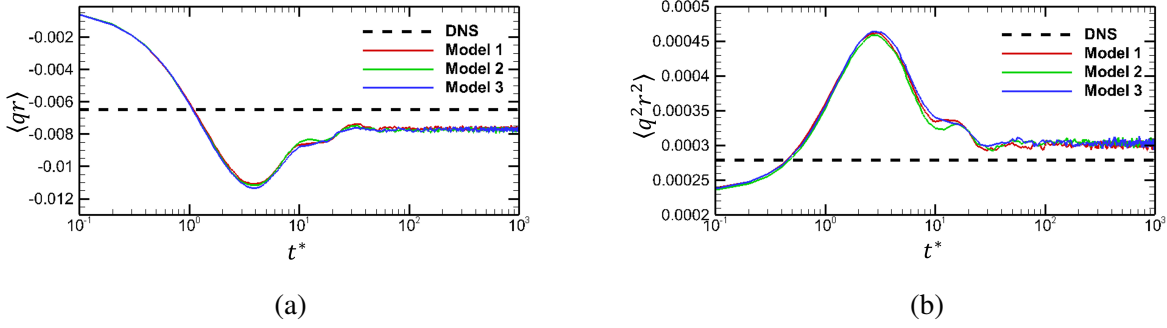


Figure 7.9: Evolution of the q and r moments: (a) $\langle qr \rangle$, and (b) $\langle q^2 r^2 \rangle$, in global normalized time t^* . The dashed lines represent the DNS statistics. The time axis is in log-scale.

a discernible impact on the b_{ij} statistics of the models. Starting from a randomly generated set of initial conditions, the b_{ij} model drives the solution toward convergence to a statistically stationary state at $t \approx 72\tau_\eta$ ($t^* \approx 60$). Therefore, the b_{ij} model takes approximately 10 times as long as the θ^* model to reach stationarity. The converged moment values of both q and r up to at least fourth order are reasonably close to the DNS values. Further, the time evolution of two of the moments of correlation between q and r , i.e. $\langle qr \rangle$, and $\langle q^2 r^2 \rangle$, are plotted in figure 7.9. The $\langle qr \rangle$ moment shows a slightly larger deviation ($\approx 18\%$) from the DNS moments as compared to all the other moments. The model's $\langle q^2 r^2 \rangle$ moment displays a closer approximation of the DNS value.

The evolution of q - r joint PDF is now investigated for the propagation of model 3. The solutions of the other two models show similar trends and are, therefore, not presented separately. The q - r joint PDF is plotted with ensembles of only 40000 particles at different t^* times in figure 7.10. The joint PDF for the initial field ($t^* = 0$) is symmetric in r , as expected from a joint Gaussian distribution. As time evolves, the modeled dynamics cause the joint PDF to skew towards the right zero-discriminant line. Overall, the joint PDF shrinks as the particles on both sides of the q -axis move closer and this leads to a higher density of particles accumulating along the right zero discriminant line. This finally results in the characteristic teardrop-like shape, which becomes nearly invariant beyond $t^* \approx 60$. Therefore, the solution of the model SDEs reproduces the teardrop shaped q - r joint PDF, one of the most important signatures of small-scale turbulence.

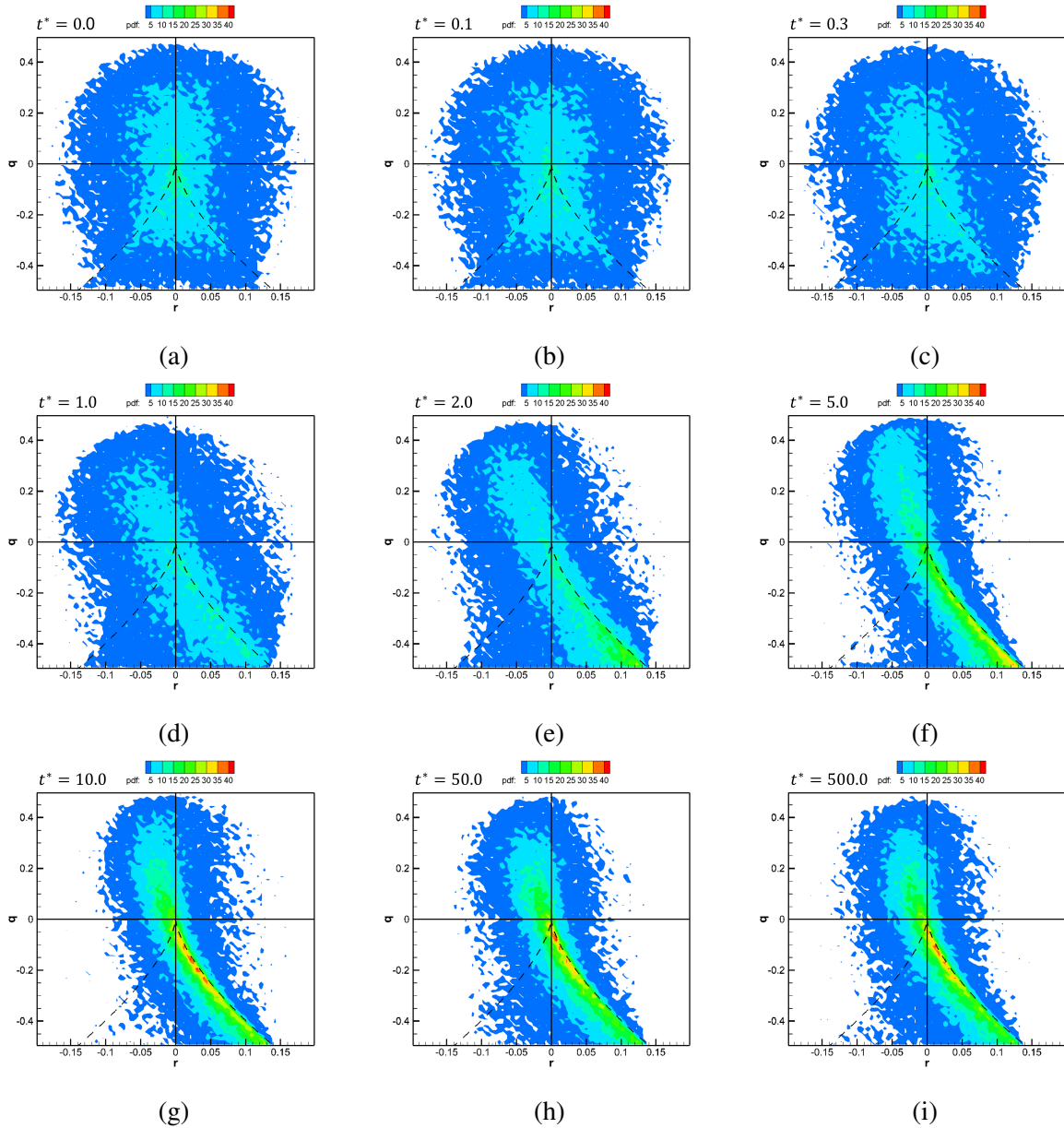


Figure 7.10: The evolution of the q - r joint PDF during numerical propagation of model 3 at different global normalized time: (a) $t^* = 0.0$, (b) $t^* = 0.1$, (c) $t^* = 0.3$, (d) $t^* = 1.0$, (e) $t^* = 2.0$, (f) $t^* = 5.0$, (g) $t^* = 10.0$, (h) $t^* = 50.0$, (i) $t^* = 500.0$. The dashed lines represent the lines of zero-discriminant ($d = q^3 + (27/4)r^2 = 0$).

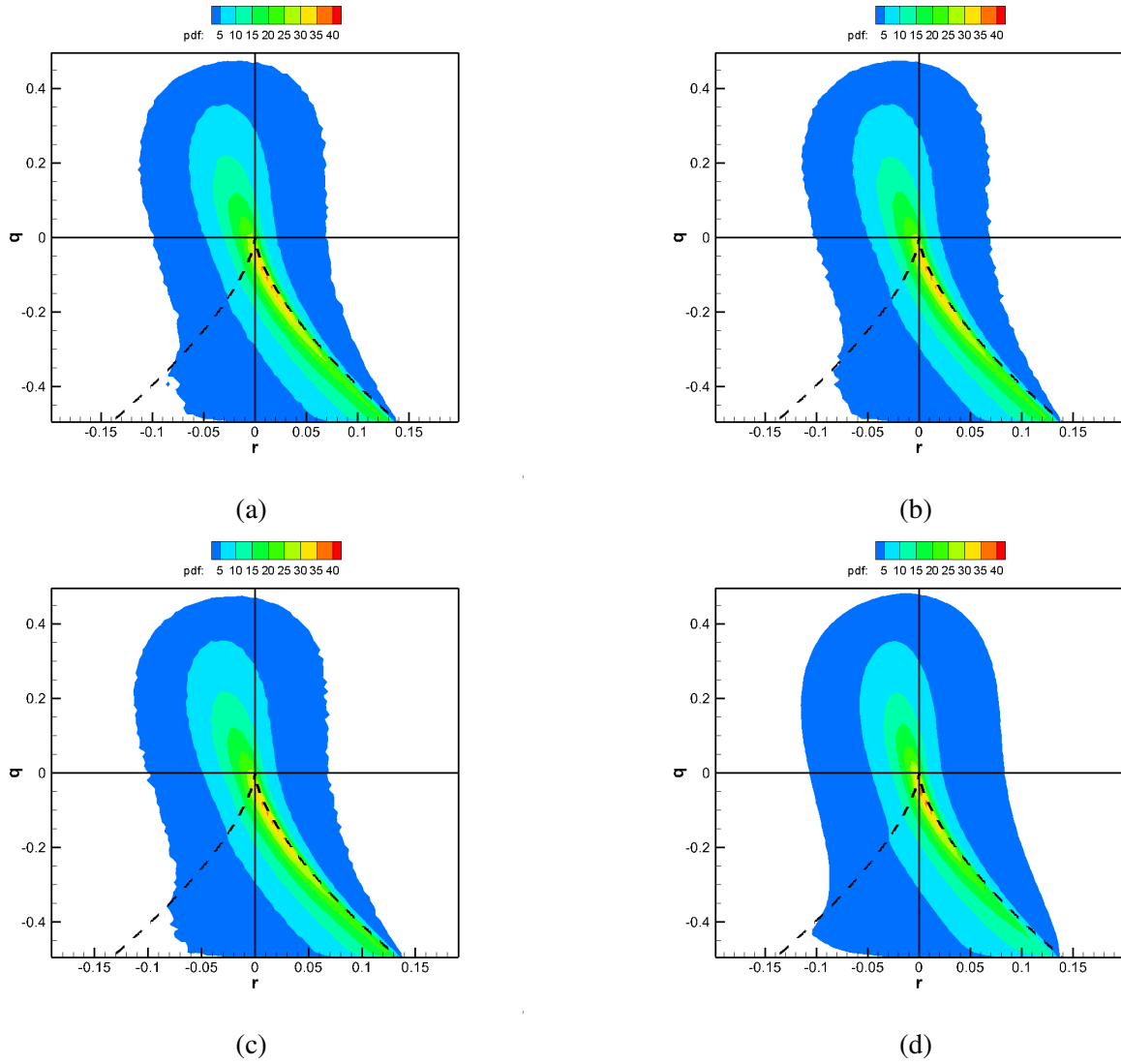


Figure 7.11: Joint PDFs of $q-r$ obtained from the: solutions of (a) model 1, (b) model 2, and (c) model 3, and (d) DNS data. The dashed lines represent the zero-discriminant lines.

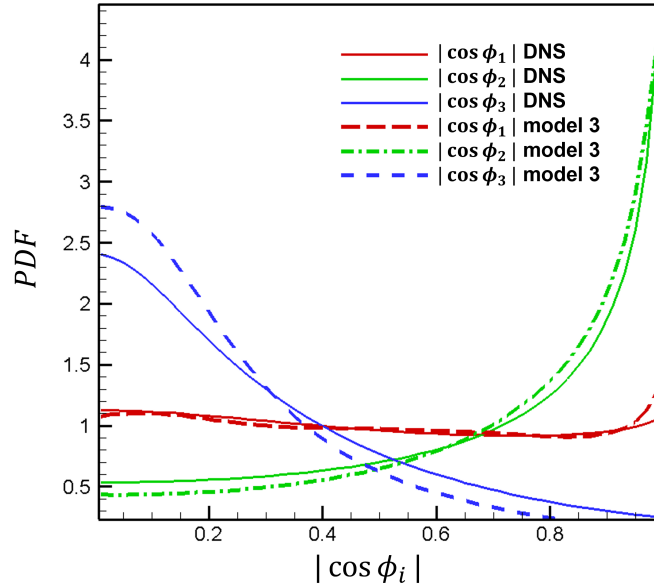


Figure 7.12: PDFs of absolute values of cosine of angles between vorticity vector and strain-rate eigenvectors (1 - most expansive, 2 - intermediate, 3 - most compressive). The solid lines are the PDFs obtained from DNS data.

The converged q - r joint PDFs, averaged over multiple time realizations in the stationary state of the models' solutions, are plotted in figure 7.11(a-c) for the three models. It is clear that all three models produce nearly identical q - r joint PDFs. Further, these joint PDFs show excellent resemblance to the q - r joint PDF obtained from DNS data (figure 7.11d). A closer comparison with the DNS joint PDF shows that the model's joint PDF contours have a slightly thinner tail in the strain-dominated bottom half of the teardrop while it is slightly wider in the rotation-dominated top half. Overall, the model is able to reproduce the joint PDF of q - r , one of the key features of velocity gradient geometry in turbulence with reasonable accuracy and without any distortion which is commonly observed in previous velocity gradient models (Johnson and Meneveau, 2016a; Pereira et al., 2016).

The alignment of vorticity with strain-rate eigendirections is another important attribute of small-scale turbulence. From equation (7.5) in the eigen reference frame of the strain-rate tensor, the cosine of the angles of alignment between the vorticity vector and the three strain-rate

eigenvectors are given by,

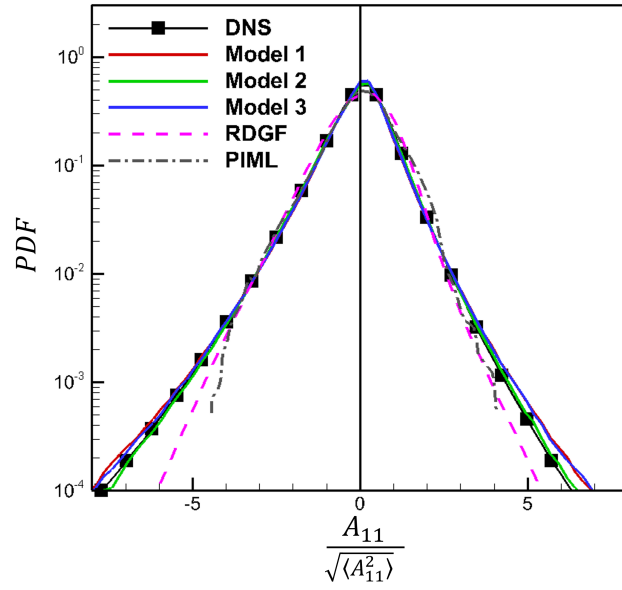
$$\cos \phi_i = \frac{\omega_i}{|\boldsymbol{\omega}|} \quad \forall i = 1, 2, 3 \quad (7.55)$$

The angles ϕ_1, ϕ_2, ϕ_3 represent the angles of alignment of vorticity with the most expansive, intermediate, and most compressive strain-rate eigenvectors, respectively. In figure 7.12, the converged PDFs of the absolute values of the cosine of alignment angles are plotted for model 3 in comparison with that of DNS. Similar to other b_{ij} statistics, the alignment PDFs produced by the other two models are nearly identical to that of model 3 and are therefore not displayed separately. It is evident that the model is able to capture these PDFs with reasonable accuracy. It reproduces the preferential alignment of vorticity with the intermediate strainrate eigendirections fairly well, but slightly overpredicts the tendency of the vorticity vector to be perpendicular to the compressive strain-rate eigenvector. The alignment with the most expansive strain-rate eigenvector is also captured reasonably well by the model.

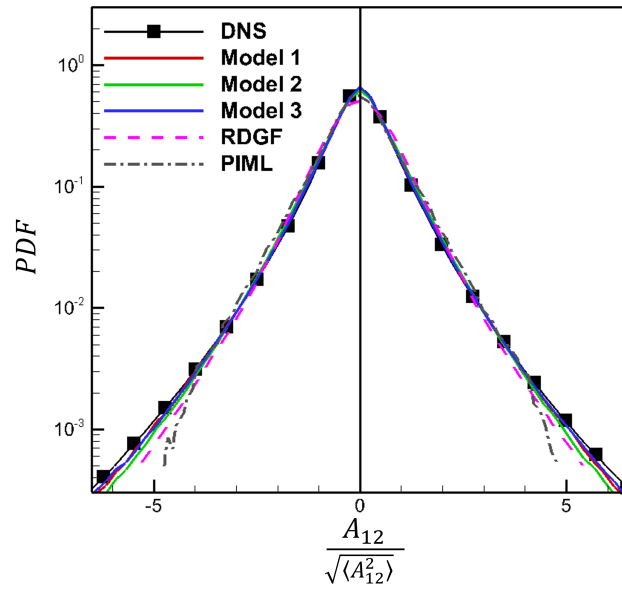
So far, we have established that in terms of the θ^* statistics, model 3 shows a slight advantage over model 1, while model 2 shows the highest deviation from the DNS. Further, the b_{ij} model performs remarkably well in reproducing the b_{ij} statistics accurately, which does not vary with the θ^* model. While the SDE for b_{ij} in local time t' does not have an explicit dependence on θ^* , the real time evolution of b_{ij} indirectly depends on the local VG magnitude value A ($\sim e^{\theta^*}$). Yet, the b_{ij} statistics of the model appear to be unaffected by the change in θ^* model equation. In the next section, model's capacity to capture the statistics of the velocity gradient tensor, $A_{ij} = A b_{ij}$, is investigated.

7.5.3 VG tensor

First, the PDFs of the longitudinal (A_{11}) and transverse (A_{12}) velocity gradients, normalized by its global RMS, are examined for all the three models in figure 7.13. The corresponding PDFs of the DNS data and of the most recent velocity gradient models in literature that have shown improved results compared to the past models - (i) recent deformation of Gaussian field (RDGF) model by Johnson and Meneveau (2016a) and (ii) physics-informed machine learning (PIML)



(a)



(b)

Figure 7.13: PDFs of: (a) longitudinal component of velocity gradient tensor, $A_{11}/\sqrt{\langle A_{11}^2 \rangle}$, and (b) transverse component of velocity gradient tensor, $A_{12}/\sqrt{\langle A_{12}^2 \rangle}$, in log-linear scale obtained from the solutions of the three models. The solid line marked with symbols represent the PDFs obtained from DNS data. The dashed and dash-dotted lines represent the PDFs obtained from previous models - RDGF (Johnson and Meneveau, 2016a) and PIML (Tian et al., 2021), respectively.

	A			A_{11}			A_{12}		
	$\frac{\langle A^3 \rangle}{\langle A^2 \rangle^{3/2}}$	$\frac{\langle A^4 \rangle}{\langle A^2 \rangle^2}$	$\frac{\langle A^6 \rangle}{\langle A^2 \rangle^3}$	$\frac{\langle A_{11}^3 \rangle}{\langle A_{11}^2 \rangle^{3/2}}$	$\frac{\langle A_{11}^4 \rangle}{\langle A_{11}^2 \rangle^2}$	$\frac{\langle A_{11}^6 \rangle}{\langle A_{11}^2 \rangle^3}$	$\frac{\langle A_{12}^3 \rangle}{\langle A_{12}^2 \rangle^{3/2}}$	$\frac{\langle A_{12}^4 \rangle}{\langle A_{12}^2 \rangle^2}$	$\frac{\langle A_{12}^6 \rangle}{\langle A_{12}^2 \rangle^3}$
DNS	1.73	4.30	71.0	- 0.59	7.90	259	0.0	12.14	760
Model 1	1.68	4.00	60.5	- 0.58	10.2	607	0.0	10.3	511
Model 2	1.58	3.38	39.7	- 0.53	8.06	298	0.0	8.89	342
Model 3	1.70	4.14	78.0	- 0.55	9.65	507	0.0	11.04	707
RDGF	-	-	-	- 0.45	4.7	-	0.0	6.8	-

Table 7.2: Third, fourth and sixth order moments of VG magnitude ($A = \sqrt{A_{ij}A_{ij}}$), longitudinal VG component (A_{11}), transverse VG component (A_{12}) from DNS data, model 1, model 2, model 3 and RDGF model of Johnson and Meneveau (2016a). For each moment, the DNS value and the model’s value closest to DNS are written in bold type font.

model by Tian et al. (2021), are also plotted for comparison. Our models are able to reproduce the skewed A_{11} -PDF and the symmetric A_{12} -PDF, as observed in DNS, quite accurately. All the three models of this work show significant improvement in capturing the PDFs of both A_{11} and A_{12} compared to both the previous models - RDGF and PIML. On a closer observation, it is evident that while the PDFs are captured nearly perfectly in the densely populated part by all three models, there are smaller differences near the tails of the PDFs. Models 1 and 3 predict a slightly heavier-tailed distribution of A_{11} than DNS, while model 2 produces a more accurate A_{11} -PDF. On the other hand, model 3 appears to capture the A_{12} -PDF tails slightly more accurately than the other two.

In order to determine the finer differences in the PDFs, we examine the higher order moments of the velocity gradient magnitude, A , as well as the velocity gradient components, A_{11} and A_{12} . These moment values for all three models of this work, DNS data and the RDGF model of Johnson and Meneveau (2016a) are presented in table 7.2. The moment values closest to the DNS value are marked in bold type font. It is clearly visible that the moments of A are best captured by model 3. The skewness, kurtosis and 6th order moment of A_{11} are reproduced best in model 2, although model 3 is not far behind and is slightly better than model 1. The skewness of the transverse

component A_{12} is nearly zero in all the models as nearly all of them maintain the symmetry of its probability distribution. The kurtosis and 6^{th} order moment of A_{12} are also captured best by model 3. Overall, it can be inferred that model 3 provides the best representation of the probability distributions of velocity gradient tensor and its magnitude.

Finally, the PDFs of the dissipation rate ($\nu S_{ij}S_{ij}$), enstrophy ($\nu W_{ij}W_{ij}$), and pseudodissipation rate ($\nu A_{ij}A_{ij}$), normalized by their global means, are computed from the converged stationary state solution of all the three models and plotted in figure 7.14. The PDFs obtained from the DNS data and that available from the RDGF model (Johnson and Meneveau, 2016a) are also illustrated for comparison. The PDFs of the initial field used in our model's simulations, also plotted in the figures, are close to Gaussian and do not show extended tails reaching high values. The model is able to start from this initial field and develop a statistically stationary field with the characteristic PDF-tails at extreme values, closely resembling DNS. It is clear that all three models reproduce the heavy-tailed probability distributions of both dissipation and enstrophy more accurately than the RDGF model. Model 2 provides the most accurate representation of the dissipation PDF while models 1 and 3 overpredict the probability of occurrence of large dissipation rates near the tails of the PDF. Enstrophy, which is more intermittent in nature than dissipation rate, is captured best by model 3. Models 1 and 2 underpredict the probability density of enstrophy near the extreme tails. Taking the sum of the dissipation rate and enstrophy results in the pseudodissipation rate, which is reproduced quite accurately by model 3, even near the extreme tails. The overall results of this subsection suggest that model 3 provides the closest representation of the velocity gradient statistics in turbulent flows.

7.6 Conclusion

A stochastic model for the Lagrangian evolution of velocity gradient (VG) tensor in an incompressible turbulent flow is presented. The bounded and well-behaved dynamics of the normalized velocity gradient tensor (b_{ij}) is modeled separately from the intermittent velocity gradient magnitude (A). The main nonlocal flow physics of pressure and viscous processes are modeled within the bounded framework of b_{ij} using a simple but effective lookup table approach in the eigen ref-

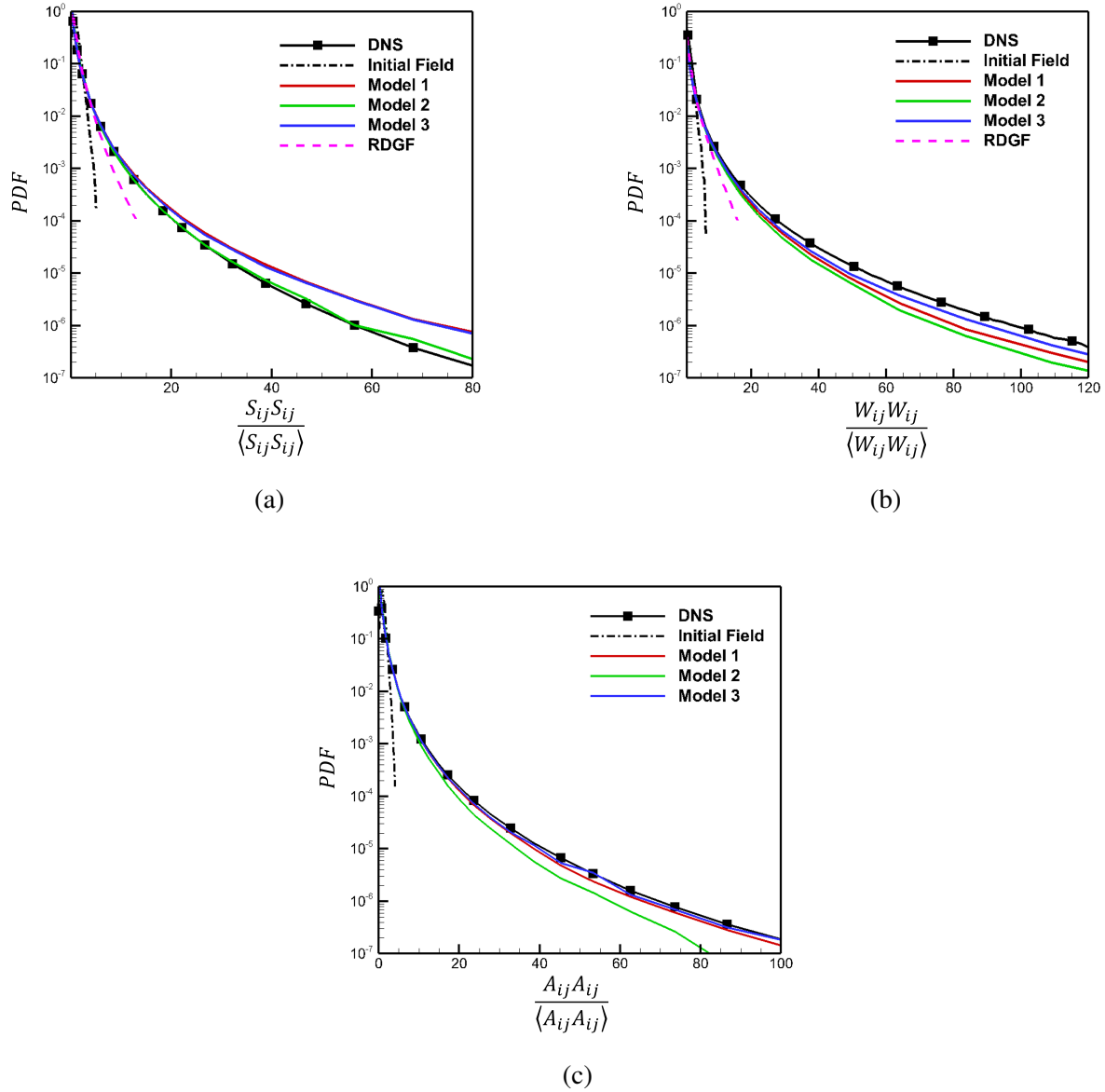


Figure 7.14: PDFs of: (a) dissipation rate, $S_{ij}S_{ij}/\sqrt{\langle S_{ij}S_{ij} \rangle}$, (b) entropy, $W_{ij}W_{ij}/\sqrt{\langle W_{ij}W_{ij} \rangle}$, and (c) pseudodissipation rate, $A_{ij}A_{ij}/\sqrt{\langle A_{ij}A_{ij} \rangle}$, in log-linear scale obtained from the solutions of the three models. The black solid line marked with symbols represent the PDFs obtained from DNS data; black dash-dotted line marks the PDFs for the initial field used in the model's simulations; dashed line represent the PDFs from the RDGF model of Johnson and Meneveau (2016a).

erence frame of the local strain-rate tensor. The intermittent magnitude of the velocity gradient tensor is modeled as a modified lognormal process, in which DNS-data based conditional variance is incorporated to better capture the intermittency. The b_{ij} model is generalizable to turbulent flows at different Reynolds numbers, while only the model for the scalar magnitude requires Reynolds number dependent parameters.

Numerical simulation of the model equations take an initially random system and drive it toward a statistically stationary solution closely resembling DNS small-scale behavior. The model performs remarkably well in capturing the Eulerian PDFs and higher order moments of b_{ij} . Further, it is able to reproduce the characteristic teardrop shape of the joint probability distribution of the b_{ij} invariants (q, r) without any discernible distortion, commonly observed in previous models. The vorticity-strainrate alignment angles are also captured with reasonable accuracy. The model reproduces the heavy-tailed PDFs of velocity gradient magnitude or pseudodissipation quite accurately. It slightly over predicts the probability density of dissipation and under predicts that of enstrophy near the extreme tails of the PDF. However, the heavy-tailed PDFs and up to sixth order moments of velocity gradients produced by the model show significant improvement over the previous models in literature. This suggests that the present model is able to capture the intermittent nature of velocity gradients better than the previous velocity-gradient models.

The main nonlinearities and nonlocal flow physics involved in the velocity-gradient dynamics is reproduced quite accurately by the b_{ij} stochastic model based on tabulated data, without using machine learning. The intermittent behavior of the velocity gradients observed in DNS is also reproduced to a reasonable extent by the modified lognormal model of VG magnitude. In future work, the magnitude will be modeled as a multifractal process to fully capture the extreme tails of the PDFs and the higher order moments with a greater accuracy.

8. SUMMARY AND CONCLUSIONS

This dissertation presents a new framework to study the highly nonlinear and complex turbulence velocity gradient dynamics, analyzes large DNS datasets to gain novel insights into the nature of small-scale dynamics and turbulence processes, and develops a highly accurate model for the Lagrangian evolution of velocity gradients in a turbulent flow. The primary conclusions of this work and the relevant future research directions are summarized below.

8.1 Velocity gradient framework of geometry and magnitude

A new framework to study velocity gradients in turbulence is formulated in chapters 2 and 3. This framework segregates a normalized velocity gradient (VG) tensor from a scalar velocity gradient magnitude (Frobenius norm). Using DNS data of forced isotropic turbulence, it is demonstrated that the bounded normalized velocity gradient tensor reflects the self-similar and universal aspects of the small-scales in turbulence while the VG magnitude constitutes the intermittent nature of the velocity gradients. Unlike the velocity gradient tensor which exhibits increasingly intermittent and non-Gaussian behavior with increasing Reynolds number, the normalized velocity gradient tensor remains bounded and sub-Gaussian at all Reynolds numbers. In fact, the probability distributions of the normalized velocity gradient quantities are shown to be nearly universal in turbulent flows above a certain Taylor Reynolds number (Re_λ). Within this normalized framework, the behavior of important turbulence processes such as the non-local pressure and viscous effects is characterized as a function of Reynolds number. The distinct advantage of modeling the velocity gradient dynamics based on this well-behaved normalized velocity gradient tensor is thus apparent.

The geometric shape of the local flow streamlines in a turbulent flow field is demonstrated to be completely determined by the normalized VG tensor, while the scale-factor of the streamline is inversely dependent on the VG magnitude. The geometric shape is defined in terms of only four bounded shape-parameters. Analysis of DNS datasets reveals that the probability distribution of the local streamline shape in this four-dimensional shape-parameter space is invariant with Reynolds

number above a certain Re_λ . These distributions indicate important features of local streamline geometry in turbulence, such as the preferential alignment of vorticity with intermediate strain-rate eigenvector. Out of the four shape-parameters, the two frame-independent parameters are the second (q) and third (r) invariants of the normalized velocity gradient tensor. Using critical point analysis, the exact geometric shapes of local flow streamlines are uniquely characterized in the bounded and compact q - r phase plane. DNS data of isotropic turbulence as well as turbulent channel flow reveal a nearly universal joint probability distribution of geometric shape in the q - r plane.

8.2 Velocity gradient decomposition into shear, rotation and normal-strain

A procedure for triple decomposition of the velocity gradient tensor into tensors representing three elementary deformations of the local fluid element – shear, rigid-body-rotation and normal-strain, is proposed in chapter 4. This decomposition procedure is able to separate shear from strain-rate and vorticity at any point of the entire turbulent flow field at an affordable computational cost. Based on DNS data of isotropic turbulent flows, the study reveals the important result that shear is the most dominating constituent of velocity gradients in turbulent flows at all Reynolds numbers, while rigid-body-rotation contributes the least on average. In fact, shear is the most responsible for the heavy-tailed probability distribution of velocity gradients and its intermittent nature. It is the absence of shear in the expression for Laplacian of pressure that renders it far less intermittent than velocity gradient magnitude. This work highlights the important role of shear in maintaining the statistical nature of small-scale turbulence as we know it and paves the way for further investigation into understanding its dynamical consequences.

8.3 Velocity gradient dynamics

The dynamics of velocity gradient structure (geometry) and velocity gradient magnitude (scale) as well as the interrelation between the two are studied in chapters 5 and 6 of this dissertation. The mean evolution of the geometric shape is studied in isotropic turbulence and turbulent channel flow by examining conditional mean trajectories in the q - r phase plane. This work resolves sev-

eral ambiguities encountered in the previously studied trajectories of the unnormalized velocity gradient invariants Q - R , and develops a new understanding of the effect of the different turbulence processes on velocity gradient dynamics. The inertial effect tries to make stable geometries unstable. Pressure reacts to inertial action such that together they drive all flow geometries toward pure-shear. The viscous effect drives trajectories toward pure-strain geometries. Together, inertial-pressure-viscous effects drive small-scale geometries either toward pure-shear or toward pure-strain depending upon its current geometric shape. It is further shown in this study that large-scale forcing plays a pivotal role in the evolution of small-scale geometry. It strongly opposes inertial and viscous action in strain-dominated geometries, while it counters pressure action in unstable spiraling geometries. This effect of large-scale forcing is essential in guaranteeing that the aggregate of all four processes results in closed loop trajectories in the q - r plane, thus, maintaining the characteristic probability distribution of q - r in statistically steady turbulent flows. The dilatational (curl-free) part of large-scale forcing contribution balances the dilatational part of the other processes, while its solenoidal (divergence-free) component has a relatively smaller effect than that of the other three processes. As a result, the solenoidal part of inertial-pressure-viscous action dictates the overall evolution of small-scale geometry in turbulent flows.

The study of the mean rate of change of velocity gradient magnitude in a statistically steady turbulence reveals the existence of a balance between the four processes at different magnitude levels. At the strongest VG magnitudes, viscosity cancels out strongly positive inertial rate of change while forcing balances the weaker positive pressure action. At smaller magnitudes, inertial, pressure and forcing effects together oppose a strongly negative viscous action.

8.4 Velocity gradient modeling

A data-driven model is presented for the Lagrangian dynamics of velocity gradient tensor in incompressible turbulence within the framework proposed in chapter 2. Separate stochastic diffusion models are developed for the bounded normalized velocity gradient tensor and the intermittent velocity gradient magnitude. The mean nonlocal pressure and viscous effects on VG dynamics are modeled using a Re_λ -independent data-driven closure in the bounded phase-space of the normal-

ized VG tensor, without using machine learning. The VG magnitude is modeled as a modified Ornstein-Uhlenbeck process, with a data-driven diffusion coefficient to ensure accurate conditional variance in different local geometries. Numerical propagation of the two models together constitutes the Lagrangian evolution of the complete velocity gradient tensor in time. The velocity gradient model is fairly generalizable as most of the data-driven components of the model are nearly independent of Reynolds number and only the three scalar parameters are Reynolds number dependent. Starting from randomly generated initial field of particles, the model's solution converges to a statistically stationary state that closely resembles the small-scale statistics of DNS. It reproduces the key features of small-scale turbulence such as the characteristic teardrop shaped joint probability density function of velocity gradient invariants and the preferential alignment of vorticity with the intermediate strain-rate eigenvector, with much improved accuracy. The heavy-tailed probability distributions of dissipation, enstrophy and pseudodissipation, as well as the moments of the velocity gradients are captured by the model with reasonable accuracy, showing definite improvement over previous models. These results reflect the model's enhanced capacity to represent the intermittency of velocity gradients, while there is still some scope for improvement specifically in capturing the extreme events more accurately.

8.5 Future directions

As shown in chapter 3, the local streamline geometry is completely defined by four shape-parameters. The dynamics of velocity gradient geometry is studied in terms of the two frame-invariant parameters, q and r . While this has improved our understanding of the turbulence processes affecting small-scale geometry, the next step toward a more complete understanding is examining the dynamics of all four shape-parameters in turbulence.

The triple decomposition of velocity gradient tensor revealed that shear is the most dominant component contributing towards turbulence intermittency in isotropic flows. Using this procedure in inhomogeneous anisotropic turbulent flows such as channel flow or turbulent boundary layers will help identify the effect of large-scale anisotropy on local fluid-element deformations and intermittency in turbulence. This method will be particularly useful to examine the impact of local

shear, normal-strain and rigid-body-rotation on the deformation and orientation of small-scale entities, such as bubbles, polymer molecules, and red-blood-cells, immersed in turbulent flows. Aside from turbulent flows, this procedure can be applied in transition flows to understand the role of local shear in triggering shear-driven instabilities.

The new intuition developed in this dissertation on the role of different turbulence processes in the velocity gradient dynamics of turbulence opens up new avenues of research. It paves the way toward a deeper understanding of the formation of specific small-scale flow geometries, the occurrence of extreme velocity gradient magnitudes, and potential control over such events in turbulent flows of practical significance.

The data-driven model for Lagrangian velocity gradient dynamics developed in this work reproduces the self-similar turbulence statistics of the small-scale geometry quite accurately. While it also captures the statistical features indicating intermittency of velocity gradient magnitude with a reasonable accuracy and shows significant improvement over previous models, there is still scope for more advanced modeling. As a first step, the magnitude is modeled as a near-lognormal process with a data-driven diffusion term. In future, additional data-driven physics will be incorporated within a multifractal framework to replicate the desired intermittent behavior and prediction of rare events with improved accuracy. One of the advantages of our framework is that the modeling of geometric features of velocity gradients are segregated from the modeling of intermittent ones. As a result, it is expected that a multifractal model can be developed for the VG magnitude while preserving all the nonlocal flow physics and the geometric characteristics of the velocity gradient model.

REFERENCES

- Arora, D., Behr, M., and Pasquali, M. (2004). A tensor-based measure for estimating blood damage. *Artificial organs*, 28(11):1002–1015.
- Arun, S., Sameen, A., Srinivasan, B., and Girimaji, S. (2019). Topology-based characterization of compressibility effects in mixing layers. *Journal of Fluid Mechanics*, 874:38–75.
- Ashurst, W. T., Kerstein, A., Kerr, R., and Gibson, C. (1987). Alignment of vorticity and scalar gradient with strain rate in simulated Navier–Stokes turbulence. *The Physics of fluids*, 30(8):2343–2353.
- Atkinson, C., Chumakov, S., Bermejo-Moreno, I., and Soria, J. (2012). Lagrangian evolution of the invariants of the velocity gradient tensor in a turbulent boundary layer. *Physics of Fluids*, 24(10):871–884.
- Balkovsky, E., Fouxon, A., and Lebedev, V. (2000). Turbulent dynamics of polymer solutions. *Physical review letters*, 84(20):4765.
- Barton, G. and Barton, G. (1989). *Elements of Green’s functions and propagation: potentials, diffusion, and waves*. Oxford University Press.
- Bechlers, P. and Sandberg, R. (2017a). Evolution of the velocity gradient tensor invariant dynamics in a turbulent boundary layer. *Journal of Fluid Mechanics*, 815:223–242.
- Bechlers, P. and Sandberg, R. (2017b). Variation of enstrophy production and strain rotation relation in a turbulent boundary layer. *Journal of Fluid Mechanics*, 812:321–348.
- Biferale, L., Meneveau, C., and Verzicco, R. (2014). Deformation statistics of sub-Kolmogorov-scale ellipsoidal neutrally buoyant drops in isotropic turbulence. *Journal of fluid mechanics*, 754:184–207.
- Biferale, L. and Vergassola, M. (2001). Isotropy vs anisotropy in small-scale turbulence. *Physics of Fluids*, 13(8):2139–2141.
- Bikkani, R. K. and Girimaji, S. S. (2007). Role of pressure in nonlinear velocity gradient dynamics in turbulence. *Physical Review E*, 75(3):036307.

- Blackburn, H. M., Mansour, N. N., and Cantwell, B. J. (1996). Topology of fine-scale motions in turbulent channel flow. *Journal of Fluid Mechanics*, 310:269–292.
- Blackett, D. (2014). *Elementary Topology: A Combinatorial and Algebraic Approach*. Elsevier Science.
- Blaisdell, G. and Shari, K. (1996). Simulation and modeling of the elliptic streamline flow. In *Proceedings of the Summer Program*, page 1. Citeseer.
- Buaria, D., Pumir, A., Bodenschatz, E., and Yeung, P.-K. (2019). Extreme velocity gradients in turbulent flows. *New Journal of Physics*, 21(4):043004.
- Cantwell, B. J. (1992). Exact solution of a restricted euler equation for the velocity gradient tensor. *Physics of Fluids A: Fluid Dynamics*, 4(4):782–793.
- Cantwell, B. J. (1993). On the behavior of velocity gradient tensor invariants in direct numerical simulations of turbulence. *Physics of Fluids A: Fluid Dynamics*, 5(8):2008–2013.
- Chacin, J. M. and Cantwell, B. J. (2000). Dynamics of a low reynolds number turbulent boundary layer. *Journal of Fluid Mechanics*, 404:87–115.
- Chacín, J. M., Cantwell, B. J., and Kline, S. J. (1996). Study of turbulent boundary layer structure using the invariants of the velocity gradient tensor. *Experimental thermal and fluid science*, 13(4):308–317.
- Chakraborty, P., Balachandar, S., and Adrian, R. J. (2005). On the relationships between local vortex identification schemes. *Journal of fluid mechanics*, 535:189–214.
- Chertkov, M., Pumir, A., and Shraiman, B. I. (1999). Lagrangian tetrad dynamics and the phenomenology of turbulence. *Physics of fluids*, 11(8):2394–2410.
- Chevillard, L. and Meneveau, C. (2006). Lagrangian dynamics and statistical geometric structure of turbulence. *Physical review letters*, 97(17):174501.
- Chevillard, L., Meneveau, C., Biferale, L., and Toschi, F. (2008). Modeling the pressure Hessian and viscous Laplacian in turbulence: comparisons with direct numerical simulation and implications on velocity gradient dynamics. *Physics of Fluids*, 20(10):101504.
- Chong, M. S., Perry, A. E., and Cantwell, B. J. (1990). A general classification of three-

- dimensional flow fields. *Physics of Fluids A: Fluid Dynamics*, 2(5):765–777.
- Chong, M. S., Soria, J., Perry, A., Chacin, J., Cantwell, B., and Na, Y. (1998). Turbulence structures of wall-bounded shear flows found using dns data. *Journal of Fluid Mechanics*, 357:225–247.
- Chorin, A. and Marsden, J. (2012). *A Mathematical Introduction to Fluid Mechanics*. Texts in Applied Mathematics. Springer New York.
- Danaila, L., Anselmet, F., and Antonia, R. (2002). An overview of the effect of large-scale inhomogeneities on small-scale turbulence. *Physics of Fluids*, 14(7):2475–2484.
- Danish, M. and Meneveau, C. (2018). Multiscale analysis of the invariants of the velocity gradient tensor in isotropic turbulence. *Physical Review Fluids*, 3(4):044604.
- Danish, M., Suman, S., and Girimaji, S. S. (2016). Influence of flow topology and dilatation on scalar mixing in compressible turbulence. *Journal of Fluid Mechanics*, 793:633–655.
- Das, R. and Girimaji, S. S. (2019). On the Reynolds number dependence of velocity-gradient structure and dynamics. *Journal of Fluid Mechanics*, 861:163–179.
- Das, R. and Girimaji, S. S. (2020a). Characterization of velocity-gradient dynamics in incompressible turbulence using local streamline geometry. *Journal of Fluid Mechanics*, 895.
- Das, R. and Girimaji, S. S. (2020b). Revisiting turbulence small-scale behavior using velocity gradient triple decomposition. *New Journal of Physics*, 22(6):063015.
- De Tullio, M., Nam, J., Pascazio, G., Balaras, E., and Verzicco, R. (2012). Computational prediction of mechanical hemolysis in aortic valved prostheses. *European Journal of Mechanics-B/Fluids*, 35:47–53.
- Dodd, M. S. and Jofre, L. (2019). Small-scale flow topologies in decaying isotropic turbulence laden with finite-size droplets. *Physical Review Fluids*, 4(6):064303.
- Dong, X., Gao, Y., and Liu, C. (2019). New normalized vortex/vortex identification method. *Physics of Fluids*, 31(1):011701.
- Donzis, D., Sreenivasan, K., and Yeung, P. (2005). Scalar dissipation rate and dissipative anomaly in isotropic turbulence. *Journal of Fluid Mechanics*, 532:199–216.
- Donzis, D., Sreenivasan, K., and Yeung, P. (2012). Some results on the Reynolds number scaling of

- pressure statistics in isotropic turbulence. *Physica D: Nonlinear Phenomena*, 241(3):164–168.
- Donzis, D. and Yeung, P. (2010). Resolution effects and scaling in numerical simulations of passive scalar mixing in turbulence. *Physica D: Nonlinear Phenomena*, 239(14):1278–1287.
- Donzis, D., Yeung, P., and Sreenivasan, K. (2008). Dissipation and enstrophy in isotropic turbulence: Resolution effects and scaling in direct numerical simulations. *Physics of Fluids*, 20(4):045108.
- Donzis, D. A. and Sreenivasan, K. (2010). Short-term forecasts and scaling of intense events in turbulence. *Journal of Fluid Mechanics*, 647:13–26.
- Dresselhaus, E. and Tabor, M. (1992). The kinematics of stretching and alignment of material elements in general flow fields. *Journal of Fluid Mechanics*, 236:415–444.
- Eisma, J., Westerweel, J., Ooms, G., and Elsinga, G. E. (2015). Interfaces and internal layers in a turbulent boundary layer. *Physics of Fluids*, 27(5):055103.
- Elsinga, G., Ishihara, T., Goudar, M., Da Silva, C., and Hunt, J. (2017). The scaling of straining motions in homogeneous isotropic turbulence. *Journal of Fluid Mechanics*, 829:31–64.
- Elsinga, G. and Marusic, I. (2010a). Evolution and lifetimes of flow topology in a turbulent boundary layer. *Physics of Fluids*, 22(1):015102.
- Elsinga, G. and Marusic, I. (2010b). Universal aspects of small-scale motions in turbulence. *Journal of Fluid Mechanics*, 662:514–539.
- Eswaran, V. and Pope, S. B. (1988). An examination of forcing in direct numerical simulations of turbulence. *Computers & Fluids*, 16(3):257–278.
- Fischer, H. B. (1973). Longitudinal dispersion and turbulent mixing in open-channel flow. *Annual Review of Fluid Mechanics*, 5(1):59–78.
- Frisch, U. (1985). On the singularity structure of fully developed turbulence. *Turbulence and predictability in geophysical fluid dynamics and climate dynamics*.
- Frisch, U., Sulem, P.-L., and Nelkin, M. (1978). A simple dynamical model of intermittent fully developed turbulence. *Journal of Fluid Mechanics*, 87(4):719–736.
- Gao, Y. and Liu, C. (2019). Rortex based velocity gradient tensor decomposition. *Physics of*

Fluids, 31(1):011704.

- Gibbon, J. D., Donzis, D. A., Gupta, A., Kerr, R. M., Pandit, R., and Vincenzi, D. (2014). Regimes of nonlinear depletion and regularity in the 3d Navier–Stokes equations. *Nonlinearity*, 27(10):2605.
- Girimaji, S. and Pope, S. (1990a). A diffusion model for velocity gradients in turbulence. *Physics of Fluids A: Fluid Dynamics*, 2(2):242–256.
- Girimaji, S. S. (1994). Modeling turbulent scalar mixing as enhanced diffusion. *Combustion science and technology*, 97(1-3):85–98.
- Girimaji, S. S. and Pope, S. B. (1990b). Material-element deformation in isotropic turbulence. *Journal of fluid mechanics*, 220:427–458.
- Girimaji, S. S. and Speziale, C. G. (1995). A modified restricted Euler equation for turbulent flows with mean velocity gradients. *Physics of Fluids*, 7(6):1438–1446.
- Gui, N., Qi, H.-b., Ge, L., Cheng, P.-x., Wu, H., Yang, X.-t., Tu, J.-y., and Jiang, S.-y. (2019). Analysis and correlation of fluid acceleration with vorticity and liutex (rortex) in swirling jets. *Journal of Hydrodynamics*, pages 1–9.
- Hamlington, P. E., Schumacher, J., and Dahm, W. J. (2008). Direct assessment of vorticity alignment with local and nonlocal strain rates in turbulent flows. *Physics of Fluids*, 20(11):111703.
- Hosokawa, I., Oide, S.-i., and Yamamoto, K. (1997). Existence and significance of ‘soft worms’ in isotropic turbulence. *Journal of the Physical Society of Japan*, 66(10):2961–2964.
- Huang, Y. and Schmitt, F. G. (2014). Lagrangian cascade in three-dimensional homogeneous and isotropic turbulence. *Journal of Fluid Mechanics*, 741.
- Ishihara, T., Gotoh, T., and Kaneda, Y. (2009). Study of high–reynolds number isotropic turbulence by direct numerical simulation. *Annual Review of Fluid Mechanics*, 41:165–180.
- Iyer, K. P., Schumacher, J., Sreenivasan, K. R., and Yeung, P. (2019). Scaling of locally averaged energy dissipation and enstrophy density in isotropic turbulence. *New Journal of Physics*, 21(3):033016.
- Jeong, E. and Girimaji, S. S. (2003). Velocity-gradient dynamics in turbulence: effect of viscosity

- and forcing. *Theoretical and computational fluid dynamics*, 16(6):421–432.
- Jimenez, J. and Wray, A. A. (1998). On the characteristics of vortex filaments in isotropic turbulence. *Journal of Fluid Mechanics*, 373:255–285.
- Johnson, P. L. and Meneveau, C. (2016a). A closure for Lagrangian velocity gradient evolution in turbulence using recent-deformation mapping of initially Gaussian fields. *Journal of Fluid Mechanics*, 804:387–419.
- Johnson, P. L. and Meneveau, C. (2016b). Large-deviation statistics of vorticity stretching in isotropic turbulence. *Physical Review E*, 93(3):033118.
- Johnson, P. L. and Meneveau, C. (2018). Predicting viscous-range velocity gradient dynamics in large-eddy simulations of turbulence. *Journal of Fluid Mechanics*, 837:80–114.
- Kailasnath, P., Sreenivasan, K., and Stolovitzky, G. (1992). Probability density of velocity increments in turbulent flows. *Physical review letters*, 68(18):2766.
- Kalelkar, C. (2006). Statistics of pressure fluctuations in decaying isotropic turbulence. *Physical Review E*, 73(4):046301.
- Kaneda, Y., Ishihara, T., Yokokawa, M., Itakura, K., and Uno, A. (2003). Energy dissipation rate and energy spectrum in high resolution direct numerical simulations of turbulence in a periodic box. *Physics of Fluids*, 15(2):L21–L24.
- Kaplan, W. (1958). *Ordinary Differential Equations*. Addison-Wesley series in the engineering sciences. Electrical and control systems. Addison-Wesley.
- Karlin, S. and Taylor, H. (1981). *A Second Course in Stochastic Processes*. Elsevier Science.
- Kerr, R. M. (1987). Histograms of helicity and strain in numerical turbulence. *Physical review letters*, 59(7):783.
- Keylock, C. J. (2017). A Schur decomposition reveals the richness of structure in homogeneous, isotropic turbulence as a consequence of localised shear. *arXiv:1701.02541*.
- Keylock, C. J. (2018). The Schur decomposition of the velocity gradient tensor for turbulent flows. *Journal of Fluid Mechanics*, 848:876–905.
- Kinsey, L. (1993). *Topology of Surfaces*. Undergraduate Texts in Mathematics. Springer-Verlag.

- Klebaner, F. (2012). *Introduction To Stochastic Calculus With Applications (3rd Edition)*. World Scientific Publishing Company.
- Kloeden, P. E. and Platen, E. (1992). Stochastic differential equations. In *Numerical Solution of Stochastic Differential Equations*, pages 103–160. Springer.
- Kolář, V. (2007). Vortex identification: New requirements and limitations. *International journal of heat and fluid flow*, 28(4):638–652.
- Kolmogorov, A. N. (1941). The local structure of turbulence in incompressible viscous fluid for very large reynolds numbers. *Cr Acad. Sci. URSS*, 30:301–305.
- Kolmogorov, A. N. (1962). A refinement of previous hypotheses concerning the local structure of turbulence in a viscous incompressible fluid at high reynolds number. *Journal of Fluid Mechanics*, 13(1):82–85.
- Lawson, J. and Dawson, J. (2015). On velocity gradient dynamics and turbulent structure. *Journal of Fluid Mechanics*, 780:60–98.
- Lee, M. and Moser, R. D. (2015). Direct numerical simulation of turbulent channel flow up to. *Journal of Fluid Mechanics*, 774:395–415.
- Li, H., Yu, T., Wang, D., and Xu, H. (2019). Heat-transfer enhancing mechanisms induced by the coherent structures of wall-bounded turbulence in channel with rib. *International Journal of Heat and Mass Transfer*, 137:446–460.
- Li, Y., Perlman, E., Wan, M., Yang, Y., Meneveau, C., Burns, R., Chen, S., Szalay, A., and Eyink, G. (2008). A public turbulence database cluster and applications to study lagrangian evolution of velocity increments in turbulence. *Journal of Turbulence*, (9):N31.
- Liu, C., Gao, Y., Tian, S., and Dong, X. (2018). Rortex—a new vortex vector definition and vorticity tensor and vector decompositions. *Physics of Fluids*, 30(3):035103.
- Lozano-Durán, A., Holzner, M., and Jiménez, J. (2015). Numerically accurate computation of the conditional trajectories of the topological invariants in turbulent flows. *Journal of Computational Physics*, 295:805–814.
- Luchsinger, R. H., Bergersen, B., and Mitchell, J. G. (1999). Bacterial swimming strategies and

- turbulence. *Biophysical journal*, 77(5):2377–2386.
- Lüthi, B., Holzner, M., and Tsinober, A. (2009). Expanding the Q–R space to three dimensions. *Journal of Fluid Mechanics*, 641:497–507.
- Lüthi, B., Tsinober, A., and Kinzelbach, W. (2005). Lagrangian measurement of vorticity dynamics in turbulent flow. *Journal of Fluid mechanics*, 528:87–118.
- Machiels, L. (1997). Predictability of small-scale motion in isotropic fluid turbulence. *Physical review letters*, 79(18):3411.
- Maciel, Y., Robitaille, M., and Rahgozar, S. (2012). A method for characterizing cross-sections of vortices in turbulent flows. *International Journal of Heat and Fluid Flow*, 37:177–188.
- Mandelbrot, B. B. (1974). Intermittent turbulence in self-similar cascades: divergence of high moments and dimension of the carrier. *Journal of fluid Mechanics*, 62(2):331–358.
- Mandelbrot, B. B. (1999). Lognormal hypothesis and distribution of energy dissipation in intermittent turbulence. In *Multifractals and 1/f Noise*, pages 294–316. Springer.
- Martín, J., Dopazo, C., and Valiño, L. (1998a). Dynamics of velocity gradient invariants in turbulence: Restricted Euler and linear diffusion models. *Physics of Fluids*, 10(8):2012–2025.
- Martín, J., Ooi, A., Chong, M., and Soria, J. (1998b). Dynamics of the velocity gradient tensor invariants in isotropic turbulence. *Physics of Fluids*, 10(9):2336–2346.
- Meneveau, C. (2011). Lagrangian dynamics and models of the velocity gradient tensor in turbulent flows. *Annual Review of Fluid Mechanics*, 43:219–245.
- Meneveau, C. and Sreenivasan, K. (1987a). Simple multifractal cascade model for fully developed turbulence. *Physical review letters*, 59(13):1424.
- Meneveau, C. and Sreenivasan, K. (1991). The multifractal nature of turbulent energy dissipation. *Journal of Fluid Mechanics*, 224:429–484.
- Meneveau, C. and Sreenivasan, K. R. (1987b). The multifractal spectrum of the dissipation field in turbulent flows. *Nuclear Physics B-Proceedings Supplements*, 2:49–76.
- Moisy, F. and Jiménez, J. (2004). Geometry and clustering of intense structures in isotropic turbulence. *Journal of fluid mechanics*, 513:111–133.

- Monin, A. S. and Yaglom, A. M. (2013). *Statistical fluid mechanics, volume II: mechanics of turbulence*, volume 2. Courier Corporation.
- Nagata, R., Watanabe, T., Nagata, K., and da Silva, C. B. (2019). Triple decomposition of velocity gradient tensor in homogeneous isotropic turbulence. *Computers & Fluids*, page 104389.
- Naso, A. and Pumir, A. (2005). Scale dependence of the coarse-grained velocity derivative tensor structure in turbulence. *Physical Review E*, 72(5):056318.
- Naso, A., Pumir, A., and Chertkov, M. (2006). Scale dependence of the coarse-grained velocity derivative tensor: influence of large-scale shear on small-scale turbulence. *Journal of Turbulence*, (7):N41.
- Nomura, K. K. and Post, G. K. (1998). The structure and dynamics of vorticity and rate of strain in incompressible homogeneous turbulence. *Journal of Fluid Mechanics*, 377:65–97.
- Novikov, E. (1971). Intermittency and scale similarity in the structure of a turbulent flow: Pmm vol. 35, n2, 1971, pp. 266–277. *Journal of Applied Mathematics and Mechanics*, 35(2):231–241.
- Oboukhov, A. M. (1962). Some specific features of atmospheric turbulence. *Journal of Fluid Mechanics*, 13(1):77–81.
- Ohkitani, K. (2002). Numerical study of comparison of vorticity and passive vectors in turbulence and inviscid flows. *Physical Review E*, 65(4):046304.
- Ooi, A., Martín, J., Soria, J., and Chong, M. (1999). A study of the evolution and characteristics of the invariants of the velocity-gradient tensor in isotropic turbulence. *Journal of Fluid Mechanics*, 381:141–174.
- Orszag, S. A. (1970a). Comments on “Turbulent hydrodynamic line stretching: consequences of isotropy”. *The Physics of Fluids*, 13(8):2203–2204.
- Orszag, S. A. (1970b). Indeterminacy of the moment problem for intermittent turbulence. *The Physics of Fluids*, 13(9):2211–2212.
- Ottino, J., M. O., Crighton, D., Ablowitz, M., Davis, S., Hinch, E., Iserles, A., Ockendon, J., and Olver, P. (1989). *The Kinematics of Mixing: Stretching, Chaos, and Transport*. Cambridge Texts in Applied Mathematics. Cambridge University Press.

- Ottino, J. M. (1990). Mixing, chaotic advection, and turbulence. *Annual Review of Fluid Mechanics*, 22(1):207–254.
- Overholt, M. R. and Pope, S. B. (1998). A deterministic forcing scheme for direct numerical simulations of turbulence. *Computers & Fluids*, 27(1):11–28.
- O’Neill, P. and Soria, J. (2005). The relationship between the topological structures in turbulent flow and the distribution of a passive scalar with an imposed mean gradient. *Fluid dynamics research*, 36(3):107.
- Parashar, N., Sinha, S. S., and Srinivasan, B. (2019). Lagrangian investigations of velocity gradients in compressible turbulence: lifetime of flow-field topologies. *Journal of Fluid Mechanics*, 872:492–514.
- Parashar, N., Srinivasan, B., and Sinha, S. S. (2020). Modeling the pressure-hessian tensor using deep neural networks. *Physical Review Fluids*, 5(11):114604.
- Pereira, R. M., Garban, C., and Chevillard, L. (2016). A dissipative random velocity field for fully developed fluid turbulence. *Journal of Fluid Mechanics*, 794:369–408.
- Pereira, R. M., Moriconi, L., and Chevillard, L. (2018). A multifractal model for the velocity gradient dynamics in turbulent flows. *Journal of Fluid Mechanics*, 839:430–467.
- Perlman, E., Burns, R., Li, Y., and Meneveau, C. (2007). Data exploration of turbulence simulations using a database cluster. In *Proceedings of the 2007 ACM/IEEE Conference on Supercomputing*, pages 1–11.
- Perry, A. and Chong, M. (1994). Topology of flow patterns in vortex motions and turbulence. *Applied Scientific Research*, 53(3-4):357–374.
- Perry, A. and Fairlie, B. (1975). Critical points in flow patterns. In *Advances in geophysics*, volume 18, pages 299–315. Elsevier.
- Perry, A. E. and Chong, M. S. (1987). A description of eddying motions and flow patterns using critical-point concepts. *Annual Review of Fluid Mechanics*, 19(1):125–155.
- Petronetto, F., Paiva, A., Lage, M., Tavares, G., Lopes, H., and Lewiner, T. (2009). Meshless helmholtz-hodge decomposition. *IEEE transactions on visualization and computer graphics*,

16(2):338–349.

- Pope, S. and Chen, Y. (1990). The velocity-dissipation probability density function model for turbulent flows. *Physics of Fluids A: Fluid Dynamics*, 2(8):1437–1449.
- Pope, S. B. (1985). Pdf methods for turbulent reactive flows. *Progress in energy and combustion science*, 11(2):119–192.
- Pope, S. B. (2000). *Turbulent Flows*. Cambridge University Press.
- Pujara, N., Koehl, M., and Variano, E. (2018). Rotations and accumulation of ellipsoidal microswimmers in isotropic turbulence. *Journal of Fluid Mechanics*, 838:356–368.
- Quadrio, M., Frohnapfel, B., and Hasegawa, Y. (2016). Does the choice of the forcing term affect flow statistics in dns of turbulent channel flow? *European Journal of Mechanics-B/Fluids*, 55:286–293.
- Rogallo, R. S. (1981). *Numerical experiments in homogeneous turbulence*, volume 81315. National Aeronautics and Space Administration.
- Rogers, M. M. and Moin, P. (1987). The structure of the vorticity field in homogeneous turbulent flows. *Journal of Fluid Mechanics*, 176:33–66.
- Rosales, R. R., Seibold, B., Shirokoff, D., and Zhou, D. (2020). High-order methods for a pressure poisson equation reformulation of the navier-stokes equations with electric boundary conditions. *arXiv preprint arXiv:2002.09801*.
- Sanada, T., Ishii, K., and Kuwahara, K. (1991). Statistics of energy-dissipation clusters in three-dimensional homogeneous turbulence. *Progress of Theoretical Physics*, 85(3):527–539.
- Schumacher, J., Scheel, J. D., Krasnov, D., Donzis, D. A., Yakhot, V., and Sreenivasan, K. R. (2014). Small-scale universality in fluid turbulence. *Proceedings of the National Academy of Sciences*, 111(30):10961–10965.
- Šístek, J., Kolář, V., Cirak, F., and Moses, P. (2012). Fluid-structure interaction and vortex identification. In *Proceedings of the 18th Australasian Fluid Mechanics Conference*. Australasian Fluid Mechanics Society Australia.
- Smart, J. (1998). *Modern Geometries*. Number 9780534351885 in A Gary W. Ostedt book.

Brooks/Cole.

- Soria, J., Sondergaard, R., Cantwell, B., Chong, M., and Perry, A. (1994). A study of the fine-scale motions of incompressible time-developing mixing layers. *Physics of Fluids*, 6(2):871–884.
- Sreenivasan, K., Antonia, R., and Danh, H. (1977). Temperature dissipation fluctuations in a turbulent boundary layer. *The Physics of Fluids*, 20(8):1238–1249.
- Sreenivasan, K. R. (1998). An update on the energy dissipation rate in isotropic turbulence. *Physics of Fluids*, 10(2):528–529.
- Sreenivasan, K. R. (2019). Turbulent mixing: A perspective. *Proceedings of the National Academy of Sciences*, 116(37):18175–18183.
- Sreenivasan, K. R. and Antonia, R. (1997). The phenomenology of small-scale turbulence. *Annual review of fluid mechanics*, 29(1):435–472.
- Suman, S. and Girimaji, S. S. (2010). Velocity gradient invariants and local flow-field topology in compressible turbulence. *Journal of Turbulence*, 11(2):N2.
- Taylor, G. I. (1938). Production and dissipation of vorticity in a turbulent fluid. *Proceedings of the Royal Society of London. Series A-Mathematical and Physical Sciences*, 164(916):15–23.
- Tennekes, H. and Lumley, J. L. (2018). *A first course in turbulence*. MIT press.
- Tian, S., Gao, Y., Dong, X., and Liu, C. (2018). Definitions of vortex vector and vortex. *Journal of Fluid Mechanics*, 849:312–339.
- Tian, Y., Livescu, D., and Chertkov, M. (2021). Physics-informed machine learning of the lagrangian dynamics of velocity gradient tensor. *Physical Review Fluids*, 6(9):094607.
- Tsinober, A., Kit, E., and Dracos, T. (1992). Experimental investigation of the field of velocity gradients in turbulent flows. *Journal of Fluid Mechanics*, 242:169–192.
- Tsinober, A., Shtilman, L., Sinyavskii, A., and Vaisburd, H. (1995). Vortex stretching and enstrophy generation in numerical and laboratory turbulence. In *Small-Scale Structures in Three-Dimensional Hydrodynamic and Magnetohydrodynamic Turbulence*, pages 9–16. Springer.
- Uhlenbeck, G. and Ornstein, L. (1930). On the theory of the brownian motion. *Phys. Rev*, 36:823–841.

- van der Bos, F., Tao, B., Meneveau, C., and Katz, J. (2002). Effects of small-scale turbulent motions on the filtered velocity gradient tensor as deduced from holographic particle image velocimetry measurements. *Physics of Fluids*, 14(7):2456–2474.
- Vieillefosse, P. (1982). Local interaction between vorticity and shear in a perfect incompressible fluid. *Journal de Physique*, 43(6):837–842.
- Vieillefosse, P. (1984). Internal motion of a small element of fluid in an inviscid flow. *Physica A: Statistical Mechanics and its Applications*, 125(1):150–162.
- Wang, X., Szalay, A., Aragón-Calvo, M. A., Neyrinck, M. C., and Eyink, G. L. (2014). Kinematic morphology of large-scale structure: evolution from potential to rotational flow. *The Astrophysical Journal*, 793(1):58.
- Wilczek, M. and Meneveau, C. (2014). Pressure Hessian and viscous contributions to velocity gradient statistics based on gaussian random fields. *Journal of Fluid Mechanics*, 756:191–225.
- Wu, H., Moreau, S., and Sandberg, R. (2019). Effects of pressure gradient on the evolution of velocity-gradient tensor invariant dynamics on a controlled-diffusion aerofoil at. *Journal of Fluid Mechanics*, 868:584–610.
- Yakhot, V. (2006). Probability densities in strong turbulence. *Physica D: Nonlinear Phenomena*, 215(2):166–174.
- Yakhot, V. and Donzis, D. (2017). Emergence of multiscaling in a random-force stirred fluid. *Physical review letters*, 119(4):044501.
- Yakhot, V. and Donzis, D. A. (2018). Anomalous exponents in strong turbulence. *Physica D: Nonlinear Phenomena*, 384:12–17.
- Yakhot, V. and Sreenivasan, K. R. (2005). Anomalous scaling of structure functions and dynamic constraints on turbulence simulations. *Journal of statistical physics*, 121(5-6):823–841.
- Yale, P. (1968). *Geometry and Symmetry*. Number 9780486657790 in Dover Books on Mathematics Series. Dover Publications.
- Yeung, P. and Brasseur, J. G. (1991). The response of isotropic turbulence to isotropic and anisotropic forcing at the large scales. *Physics of Fluids A: Fluid Dynamics*, 3(5):884–897.

- Yeung, P., Donzis, D., and Sreenivasan, K. (2012). Dissipation, enstrophy and pressure statistics in turbulence simulations at high Reynolds numbers. *Journal of Fluid Mechanics*, 700:5–15.
- Yeung, P., Pope, S., Lamorgese, A., and Donzis, D. (2006). Acceleration and dissipation statistics of numerically simulated isotropic turbulence. *Physics of fluids*, 18(6):065103.
- Yeung, P., Sreenivasan, K., and Pope, S. (2018). Effects of finite spatial and temporal resolution in direct numerical simulations of incompressible isotropic turbulence. *Physical Review Fluids*, 3(6):064603.
- Yeung, P., Zhai, X., and Sreenivasan, K. R. (2015). Extreme events in computational turbulence. *Proceedings of the National Academy of Sciences*, 112(41):12633–12638.
- Yeung, P.-K. and Pope, S. B. (1989). Lagrangian statistics from direct numerical simulations of isotropic turbulence. *Journal of Fluid Mechanics*, 207:531–586.
- Yu, H. and Meneveau, C. (2010a). Lagrangian refined kolmogorov similarity hypothesis for gradient time evolution and correlation in turbulent flows. *Physical review letters*, 104(8):084502.
- Yu, H. and Meneveau, C. (2010b). Scaling of conditional lagrangian time correlation functions of velocity and pressure gradient magnitudes in isotropic turbulence. *Flow, turbulence and combustion*, 85(3-4):457–472.
- Zheng, T., You, J., and Yang, Y. (2017). Principal curvatures and area ratio of propagating surfaces in isotropic turbulence. *Physical Review Fluids*, 2(10):103201.

APPENDIX A

DIRECT NUMERICAL SIMULATION DATASETS

Several direct numerical simulation (DNS) datasets of incompressible forced homogeneous isotropic turbulence (FIT) and turbulent channel flow are used in this dissertation to investigate velocity gradient statistics and dynamics in turbulence. The details are presented below.

Twelve incompressible forced isotropic turbulence datasets have been obtained from the Turbulent and Advanced Computations Laboratory (TACL) of Dr. Diego Donzis at Texas A&M University (TAMU). These datasets have been used previously to study intermittency, anomalous exponents, Reynolds number scaling and non-linear depletion (Donzis et al., 2008; Donzis and Sreenivasan, 2010; Donzis et al., 2012; Gibbon et al., 2014). The simulations employ stochastic forcing at large scales to maintain statistical-stationarity in a periodic box of dimensions $2\pi \times 2\pi \times 2\pi$. The Taylor Reynolds number (Re_λ) of these datasets ranges from 1 to 588. The details of these simulations are shown in table A.1. Here,

$$Re_\lambda \equiv \frac{u' \lambda}{\nu} \quad (\text{A.1})$$

where u' is root-mean-square (rms) velocity and ν is the kinematic viscosity. λ (Taylor Microscale) and ϵ (mean dissipation rate) are given by

$$\lambda = \left(\frac{15\nu(u')^2}{\epsilon} \right)^{1/2}, \quad \epsilon = 2\nu \langle S_{ij} S_{ij} \rangle \quad (\text{A.2})$$

where S_{ij} is the strain-rate tensor (symmetric part of VG tensor). Here, $k_{max}\eta$ is the highest resolved wave number (k_{max}) normalized by the Kolmogorov length scale (η). All the derivatives used in this study are calculated using spectral method.

The forced isotropic turbulence data from the Johns Hopkins Turbulence Database (Perlman et al., 2007; Li et al., 2008) has been widely used for investigating velocity gradient statistics

Re_λ	Grid points	$k_{max}\eta$	Source
1	256^3	105.6	TACL, TAMU: Yakhot and Donzis (2017)
6	256^3	34.8	TACL, TAMU: Yakhot and Donzis (2017)
9	256^3	26.6	TACL, TAMU: Yakhot and Donzis (2017)
14	256^3	19.87	TACL, TAMU: Yakhot and Donzis (2017)
18	256^3	15.59	TACL, TAMU: Yakhot and Donzis (2017)
25	256^3	11.51	TACL, TAMU: Yakhot and Donzis (2017)
35	64^3	1.45	TACL, TAMU: Yakhot and Donzis (2017)
86	256^3	2.83	TACL, TAMU: Donzis et al. (2008)
225	512^3	1.34	TACL, TAMU: Donzis et al. (2008)
385	1024^3	1.41	TACL, TAMU: Donzis et al. (2008)
414	1024^3	1.32	JHTDB: Li et al. (2008)
427	1024^3	1.39	JHTDB: Li et al. (2008)
588	2048^3	1.39	TACL, TAMU: Donzis et al. (2008)

Table A.1: Details of forced isotropic incompressible turbulence datasets used in this study. Here, JHTDB represents Johns Hopkins Turbulence Data Base, TACL represents Turbulent and Advanced Computations Laboratory, and TAMU represents Texas A&M University.

(Johnson and Meneveau, 2016b; Elsinga et al., 2017; Danish and Meneveau, 2018) as well as its Lagrangian dynamics (Yu and Meneveau, 2010a,b) in turbulence. The data used in the present study is obtained from computations performed on a 1024^3 grid using a pseudo-spectral solver. Datasets at Taylor Reynolds numbers: $Re_\lambda = 414$ and 427 are used in the chapters of this dissertation. The simulation is well resolved with $k_{max}\eta > 1.3$. In this study, we have used field velocity data at multiple consecutive time steps, separated by $\Delta t = 0.0002$, to compute the temporal derivatives for the $Re_\lambda = 427$ dataset.

Incompressible turbulent channel flow data from the Johns Hopkins Turbulence Database (Li et al., 2008; Lee and Moser, 2015) is also used in this dissertation. The turbulent flow inside the channel is simulated on a $10240 \times 1536 \times 7680$ grid with a spatially uniform pressure gradient

varying in time to ensure a constant mass flux through the channel. The data set used in the computations here is obtained after statistical stationarity is achieved. The friction velocity Reynolds number of the channel flow is

$$Re_\tau \equiv \frac{u_\tau h}{\nu} = 5186 \quad (\text{A.3})$$

where u_τ is the friction velocity and h is the channel half-height. The velocity field is homogeneous in the stream-wise (x) and span-wise (z) directions and inhomogeneous in the wall-normal (y) direction. As suggested in the work of Lozano-Durán et al. (2015), integrating over a statistically inhomogeneous region can considerably bias the Lagrangian statistics. Therefore, to circumvent averaging over statistically inhomogeneous wall-normal (y) direction, we use data at specific y^+ planes, each with a different Taylor Reynolds number: $y^+ = 100$ ($Re_\lambda = 81$), $y^+ = 203$ ($Re_\lambda = 110$), $y^+ = 302$ ($Re_\lambda = 132$), and $y^+ = 852$ ($Re_\lambda = 183$). Data from multiple time instants are considered to achieve adequate sampling. In this work, all spatial derivatives in homogeneous directions are computed using spectral methods, while the spatial derivatives in inhomogeneous directions (y direction in channel flow) are computed using the 4th-order central difference scheme.

APPENDIX B

UPPER BOUND OF NORMALIZED SHEAR-ROTATION CORRELATION TERM

The VG magnitude can be expressed as follows in terms of the elements of normal-strain-rate, shear and rigid-body-rotation-rate tensors when the flow is locally rotational (from equations (4.6,4.18)),

$$A^2 = 6\lambda_{cr}^2 + 2\phi^2 + s_1^2 + s_2^2 + s_3^2 + 2\phi s_3 \quad (\text{B.1})$$

Here, $2\phi s_3$ is the shear-rotation correlation term which is positive by definition for rotational flow.

This term is first normalized by A^2 such that

$$2rh = \frac{2\phi s_3}{6\lambda_{cr}^2 + 2\phi^2 + s_1^2 + s_2^2 + s_3^2 + 2\phi s_3} \quad (\text{B.2})$$

The next step is to obtain the maximum value that $2rh$ can attain. Since the five variables in the above expression are independent and the denominator is a sum of non-negative terms, we can assume that $2rh$ is maximum when $\lambda_{cr}^2 = s_1^2 = s_2^2 = 0$. Note that this represents planar flow with only pure-rotation and in-plane shear. Then, the normalized correlation term has the following upper bound

$$2rh \leq \frac{2\phi s_3}{2\phi^2 + s_3^2 + 2\phi s_3} \quad (\text{B.3})$$

Dividing the numerator and denominator by $4\phi^2$, we obtain

$$2rh \leq \frac{s_3/2\phi}{1/2 + (s_3/2\phi)^2 + s_3/2\phi} = \frac{x}{1/2 + x^2 + x} \equiv f(x) \quad \text{where } x = s_3/2\phi \quad (\text{B.4})$$

The maximum of function $f(x)$ occurs when

$$x = \frac{1}{\sqrt{2}} \quad (\text{B.5})$$

Therefore, the maximum value of $2rh$ is given by

$$2rh \leq f\left(x = \frac{1}{\sqrt{2}}\right) \implies 2rh \leq \frac{1}{\sqrt{2} + 1} \quad (\text{B.6})$$

APPENDIX C

FOUR-VARIABLE REPRESENTATION OF NORMALIZED VG TENSOR

The normalized velocity gradient tensor in the principal reference frame of the strain-rate tensor is given by

$$\tilde{\mathbf{b}} = \begin{bmatrix} a_1 & -\omega_3 & \omega_2 \\ \omega_3 & a_2 & -\omega_1 \\ -\omega_2 & \omega_1 & a_3 \end{bmatrix} \quad \text{where } a_1 \geq a_2 \geq a_3 \quad (\text{C.1})$$

The four variables chosen to represent \tilde{b}_{ij} are q, r, a_2 and ω_2 . The remaining components of the tensor can be expressed in terms of these four variables as follows (see section 3.2.4 for derivation):

$$a_1 = \frac{1}{2}(-a_2 + \sqrt{1 - 3a_2^2 - 2q}) \quad (\text{C.2})$$

$$a_3 = \frac{1}{2}(-a_2 - \sqrt{1 - 3a_2^2 - 2q}) \quad (\text{C.3})$$

$$\omega_1 = \pm \frac{1}{2\sqrt{2}} \sqrt{(1 + 2q - 4\omega_2^2) - \frac{8a_2^3 + 8r - a_2(3 - 2q - 12\omega_2^2)}{\sqrt{1 - 3a_2^2 - 2q}}} \quad (\text{C.4})$$

$$\omega_3 = \pm \frac{1}{2\sqrt{2}} \sqrt{(1 + 2q - 4\omega_2^2) + \frac{8a_2^3 + 8r - a_2(3 - 2q - 12\omega_2^2)}{\sqrt{1 - 3a_2^2 - 2q}}} \quad (\text{C.5})$$

The kinematic bounds of all these variables are given below:

$$-\frac{1}{2} \leq q \leq \frac{1}{2} \quad (\text{C.6})$$

$$-\frac{1+q}{3} \left(\frac{1-2q}{3} \right)^{1/2} \leq r \leq \frac{1+q}{3} \left(\frac{1-2q}{3} \right)^{1/2} \quad (\text{C.7})$$

$$-\sqrt{\frac{1-2q}{12}} \leq a_2 \leq \sqrt{\frac{1-2q}{12}} \quad (\text{C.8})$$

$$0 \leq a_1 \leq \sqrt{\frac{1-2q}{3}} \quad (\text{C.9})$$

$$-\sqrt{\frac{1-2q}{3}} \leq a_3 \leq 0 \quad (\text{C.10})$$

$$-\sqrt{\frac{q}{2} + \frac{1}{4}} \leq \omega_i \leq \sqrt{\frac{q}{2} + \frac{1}{4}} \quad \forall \quad i = 1, 2, 3 \quad (\text{C.11})$$

APPENDIX D

VELOCITY GRADIENT MODEL: DERIVATIONS AND NUMERICAL METHODS

D.1 Relevant properties of Itô process

Itô's lemma for scalar variables: For a stochastic differential equation (SDE) of a scalar (x) of the form

$$dx = f(x)dt + g(x) dW, \quad (\text{D.1})$$

the SDE for a function of the variable, $\varphi = \varphi(x)$, is given by

$$d(\varphi(x)) = \left(\frac{\partial \varphi}{\partial t} + f(x) \frac{\partial \varphi}{\partial x} + \frac{1}{2} g^2(x) \frac{\partial^2 \varphi}{\partial x^2} \right) dt + g(x) \frac{\partial \varphi}{\partial x} dW \quad (\text{D.2})$$

Itô's lemma for tensorial variables: For a system of SDEs of a tensor, X_{ij} , of the form

$$dX_{ij} = F_{ij}(\mathbf{X})dt + G_{ijkl}(\mathbf{X}) dW_{kl}, \quad (\text{D.3})$$

the SDE for a function of the tensor, $\phi = \phi(\mathbf{X})$, is given by

$$d\phi = \left(\frac{\partial \phi}{\partial t} + F_{ij} \frac{\partial \phi}{\partial X_{ij}} + \frac{1}{2} G_{ijkl} G_{pqkl} \frac{\partial^2 \phi}{\partial X_{ij} \partial X_{pq}} \right) dt + G_{ijkl} \frac{\partial \phi}{\partial X_{ij}} dW_{kl} \quad (\text{D.4})$$

Itô's product rule: For SDEs of two scalar variables, x_1 and x_2 , given by

$$dx_1 = f_1(x_1)dt + g_1(x_1) dW, \quad (\text{D.5})$$

$$dx_2 = f_2(x_2)dt + g_2(x_2) dW \quad (\text{D.6})$$

the SDE of the product of the two variables is

$$d(x_1 x_2) = x_1 d(x_2) + d(x_1) x_2 + d(x_1) d(x_2) \quad (\text{D.7})$$

D.2 Derivation of b_{ij} SDE from A_{ij} SDE

The system of SDEs for the velocity gradient tensor A_{ij} is given by

$$dA_{ij} = M_{ij}dt + K_{ijkl} dW_{kl}$$

$$\text{where, } \langle dW_{ij} \rangle = 0 \quad \text{and} \quad \langle dW_{ij} dW_{kl} \rangle = \delta_{ik} \delta_{jl} dt \quad (\text{D.8})$$

Applying Itô's lemma we can obtain the SDE of the Frobenius norm of the tensor, $\phi = A^2 = A_{ij}A_{ij}$, as

$$d(\phi) = (2A_{ij}M_{ij} + K_{ijkl}K_{ijkl})dt + 2A_{ij}K_{ijkl} dW_{kl} \quad (\text{D.9})$$

neglecting terms of the order of $\mathcal{O}(dt^n) \forall n > 1$. Then, the SDE of the VG magnitude, $A = \sqrt{A^2} = \sqrt{\phi}$, is obtained using Itô's lemma:

$$d(A) = \left(\frac{A_{ij}M_{ij}}{A} + \frac{K_{ijkl}K_{ijkl}}{2A} - \frac{A_{ij}K_{ijkl}A_{mn}K_{mnkl}}{2A^3} \right) dt + \frac{A_{ij}K_{ijkl}}{A} dW_{kl} \quad (\text{D.10})$$

Next, the SDE of its reciprocal is obtained using Itô's lemma

$$d\left(\frac{1}{A}\right) = -\frac{1}{A^2} \left[\left(\frac{A_{ij}M_{ij}}{A} + \frac{K_{ijkl}K_{ijkl}}{2A} - \frac{3}{2} \frac{A_{ij}K_{ijkl}A_{mn}K_{mnkl}}{A^3} \right) dt + \frac{A_{ij}K_{ijkl}}{A} dW_{kl} \right] \quad (\text{D.11})$$

Finally, applying Itô's product rule to determine the SDE for the normalized VG tensor, $b_{ij} \equiv \frac{A_{ij}}{A}$,

$$db_{ij} = d\left(\frac{1}{A} \cdot A_{ij}\right) = \frac{1}{A} dA_{ij} + A_{ij} d\left(\frac{1}{A}\right) + dA_{ij} d\left(\frac{1}{A}\right) \quad (\text{D.12})$$

and using equations (D.8) and (D.11), we obtain

$$\begin{aligned} db_{ij} = & \left(\frac{M_{ij}}{A} - \frac{b_{ij}b_{kl}M_{kl}}{A} - \frac{b_{ij}K_{pqkl}K_{pqkl}}{2A^2} - \frac{b_{pq}K_{pqkl}K_{ijkl}}{A^2} \right. \\ & \left. + \frac{3}{2} \frac{b_{ij}b_{pq}K_{pqkl}b_{mn}K_{mnkl}}{A^2} \right) dt + \left(\frac{K_{ijkl}}{A} - \frac{b_{ij}b_{pq}K_{pqkl}}{A} \right) dW_{kl}. \end{aligned} \quad (\text{D.13})$$

Rearranging, we can write the final form of the b_{ij} -SDE as follows

$$db_{ij} = \left(\frac{M_{ij}}{A^2} - b_{ij}b_{kl} \frac{M_{kl}}{A^2} - \frac{1}{2}b_{ij} \frac{K_{pqkl}}{A^{3/2}} \frac{K_{pqkl}}{A^{3/2}} - b_{pq} \frac{K_{pqkl}}{A^{3/2}} \frac{K_{ijkl}}{A^{3/2}} + \frac{3}{2}b_{ij}b_{pq} \frac{K_{pqkl}}{A^{3/2}} b_{mn} \frac{K_{mnkl}}{A^{3/2}} \right) dt' + \left(\frac{K_{ijkl}}{A^{3/2}} - b_{ij}b_{pq} \frac{K_{pqkl}}{A^{3/2}} \right) dW'_{kl} \quad (\text{D.14})$$

where, $dt' = A dt$ and $dW'_{ij} = A^{1/2} dW_{ij}$. Note that all the terms on the RHS of the b_{ij} SDE are non-dimensional, including dt' , dW'_{kl} , M_{ij}/A^2 and $K_{ijkl}/A^{3/2}$. This equation can also be written as

$$db_{ij} = (\mu_{ij} + \gamma_{ij})dt' + D_{ijkl} dW'_{kl} \quad \text{where}$$

$$\mu_{ij} = \frac{M_{ij}}{A^2} - b_{ij}b_{kl} \frac{M_{kl}}{A^2}, \quad D_{ijkl} = \frac{K_{ijkl}}{A^{3/2}} - b_{ij}b_{pq} \frac{K_{pqkl}}{A^{3/2}},$$

$$\gamma_{ij} = -\frac{1}{2}b_{ij} \frac{K_{pqkl}}{A^{3/2}} \frac{K_{pqkl}}{A^{3/2}} - b_{pq} \frac{K_{pqkl}}{A^{3/2}} \frac{K_{ijkl}}{A^{3/2}} + \frac{3}{2}b_{ij}b_{pq} \frac{K_{pqkl}}{A^{3/2}} b_{mn} \frac{K_{mnkl}}{A^{3/2}} \quad (\text{D.15})$$

where μ_{ij} is the mean drift coefficient, γ_{ij} is the additional drift coefficient and D_{ijkl} is the diffusion coefficient.

D.3 Incompressibility constraint

To prove that the system of SDEs of b_{ij} in equation (7.14) satisfies the incompressibility constraint, we take the trace on both sides of the b_{ij} -SDE:

$$db_{ii} = (\mu_{ii} + \gamma_{ii})dt' + D_{iikl} dW'_{kl} \quad (\text{D.16})$$

Now, since $b_{ii} = 0$, we have

$$\mu_{ii} = \frac{M_{ii}}{A^2} - b_{ii}b_{kl} \frac{M_{kl}}{A^2} = 0. \quad (\text{D.17})$$

Further, since $K_{iikl} = 0$ by construction, it can be easily showed that

$$\gamma_{ii} = -\frac{1}{2}b_{ii} \frac{K_{pqkl}}{A^{3/2}} \frac{K_{pqkl}}{A^{3/2}} - b_{pq} \frac{K_{pqkl}}{A^{3/2}} \frac{K_{iikl}}{A^{3/2}} + \frac{3}{2}b_{ii}b_{pq} \frac{K_{pqkl}}{A^{3/2}} b_{mn} \frac{K_{mnkl}}{A^{3/2}} = 0$$

$$D_{iikl} = \frac{K_{iikl}}{A^{3/2}} - b_{ii}b_{pq} \frac{K_{pqkl}}{A^{3/2}} = 0 \quad (\text{D.18})$$

Therefore, from equations (D.16-D.18), we have

$$db_{ii} = 0 \quad (\text{D.19})$$

D.4 Normalization constraint

Next, we prove that the b_{ij} SDE maintains the Frobenius norm of unity. For this, we first derive the SDE for the Frobenius norm of b_{ij} , using Itô's product rule:

$$d(b_{ij}b_{ij}) = (2b_{ij}\mu_{ij} + 2b_{ij}\gamma_{ij} + D_{ijkl}D_{ijkl})dt' + 2b_{ij}D_{ijkl}dW'_{kl} \quad (\text{D.20})$$

Now, the first term is zero by construction since

$$2b_{ij}\mu_{ij} = 2b_{ij}\left(\frac{M_{ij}}{A^2} - b_{ij}b_{kl}\frac{M_{kl}}{A^2}\right) = 2\frac{b_{kl}M_{kl}}{A^2} - 2b_{ij}b_{ij}\frac{b_{kl}M_{kl}}{A^2} = 0 \quad (\text{D.21})$$

provided $b_{ij}b_{ij} = 1$. The second term can be expanded as follows:

$$\begin{aligned} 2b_{ij}\gamma_{ij} &= 2b_{ij}\left(-\frac{1}{2}b_{ij}\frac{K_{pqkl}}{A^{3/2}}\frac{K_{pqkl}}{A^{3/2}} - b_{pq}\frac{K_{pqkl}}{A^{3/2}}\frac{K_{ijkl}}{A^{3/2}} + \frac{3}{2}b_{ij}b_{pq}\frac{K_{pqkl}}{A^{3/2}}b_{mn}\frac{K_{mnkl}}{A^{3/2}}\right) \\ &= -b_{ij}b_{ij}\frac{K_{pqkl}}{A^{3/2}}\frac{K_{pqkl}}{A^{3/2}} - 2b_{ij}\frac{K_{ijkl}}{A^{3/2}}b_{pq}\frac{K_{pqkl}}{A^{3/2}} + 3b_{ij}b_{ij}b_{pq}\frac{K_{pqkl}}{A^{3/2}}b_{mn}\frac{K_{mnkl}}{A^{3/2}} \\ &= -\left(\frac{K_{pqkl}}{A^{3/2}}\frac{K_{pqkl}}{A^{3/2}} - b_{ij}\frac{K_{ijkl}}{A^{3/2}}b_{pq}\frac{K_{pqkl}}{A^{3/2}}\right) \end{aligned} \quad (\text{D.22})$$

since $b_{ij}b_{ij} = 1$. And the third term can be expanded as

$$\begin{aligned} D_{ijkl}D_{ijkl} &= \left(\frac{K_{ijkl}}{A^{3/2}} - b_{ij}b_{pq}\frac{K_{pqkl}}{A^{3/2}}\right)\left(\frac{K_{ijkl}}{A^{3/2}} - b_{ij}b_{pq}\frac{K_{pqkl}}{A^{3/2}}\right) \\ &= \frac{K_{ijkl}}{A^{3/2}}\frac{K_{ijkl}}{A^{3/2}} - b_{ij}\frac{K_{ijkl}}{A^{3/2}}b_{pq}\frac{K_{pqkl}}{A^{3/2}} \end{aligned} \quad (\text{D.23})$$

Therefore, the second and third terms cancel each other out. Finally the diffusion term is also zero due to the form of the diffusion coefficient as:

$$2b_{ij}D_{ijkl} = 2b_{ij}\left(\frac{K_{ijkl}}{A^{3/2}} - b_{ij}b_{pq}\frac{K_{pqkl}}{A^{3/2}}\right) = 2b_{ij}\frac{K_{ijkl}}{A^{3/2}} - 2b_{ij}b_{ij}b_{pq}\frac{K_{pqkl}}{A^{3/2}} = 0 \quad (\text{D.24})$$

Thus, it is proved that for the given form of μ_{ij} , γ_{ij} and D_{ijkl} , the equation (D.20) simplifies to

$$d(b_{ij}b_{ij}) = 0. \quad (\text{D.25})$$

In other words, the form of the b_{ij} -SDE (equation D.15) automatically ensures that $b_{ij}b_{ij}$ remains unity at all times provided it is initially unity.

D.5 Galilean invariance

Now we demonstrate that the approach of closure modeling of the normalized anisotropic pressure Hessian (\mathbf{h}) and viscous Laplacian ($\boldsymbol{\tau}$) tensors satisfies Galilean invariance. The tensor \mathbf{h} is modeled as

$$\mathbf{h} = \mathbf{Q} \tilde{\mathbf{h}} \mathbf{Q}^T \quad (\text{D.26})$$

where $\tilde{\mathbf{h}}$ is the pressure Hessian tensor in the principal frame of strain-rate tensor (\mathbf{s}). This $\tilde{\mathbf{h}}$ is obtained from data-driven closure as a function of $\tilde{\mathbf{b}}$, also in principal reference frame. Thus,

$$\mathbf{Q} = [\mathbf{E}_1 \ \mathbf{E}_2 \ \mathbf{E}_3] \quad (\text{D.27})$$

where \mathbf{E}_i are the right eigenvectors of \mathbf{s} corresponding to its eigenvalues a_i and \mathbf{E}_i constitute the columns of the rotation matrix \mathbf{Q} . Let us rotate the coordinate frame of the observer by certain angles, using a rotation matrix \mathbf{R} . Let the tensors and vectors in new reference frame be marked by $'$. Then the tensor \mathbf{s} becomes

$$\mathbf{s}' = \mathbf{R} \mathbf{s} \mathbf{R}^T \quad (\text{D.28})$$

and its eigenvectors also rotate by the same angles since

$$\begin{aligned} s\mathbf{E}_i = a_i\mathbf{E}_i &\implies \mathbf{R}^T s' \mathbf{R} \mathbf{E}_i = a_i \mathbf{E}_i \\ \implies s' \mathbf{R} \mathbf{E}_i = a_i \mathbf{R} \mathbf{E}_i &\implies s' \mathbf{E}'_i = a_i \mathbf{E}'_i \text{ where } \mathbf{E}'_i = \mathbf{R} \mathbf{E}_i \end{aligned} \quad (\text{D.29})$$

Since \mathbf{E}'_i constitute the columns of the rotated tensor \mathbf{Q}' , we can say

$$\mathbf{Q}' = \mathbf{R} \mathbf{Q} \quad (\text{D.30})$$

Therefore, using equations (D.26) and (D.30), the pressure Hessian tensor in the new reference frame becomes,

$$\mathbf{h}' = \mathbf{Q}' \tilde{\mathbf{h}} \mathbf{Q}'^T = \mathbf{R} \mathbf{Q} \tilde{\mathbf{h}} \mathbf{Q}^T \mathbf{R}^T = \mathbf{R} \mathbf{h} \mathbf{R}^T \quad (\text{D.31})$$

Note that $\tilde{\mathbf{h}} = \tilde{\mathbf{h}}(q, r, a_2, \omega_2)$, all four of which are either frame invariant or specifically defined in the principal reference frame and therefore $\tilde{\mathbf{h}}$ is unaltered by frame rotation. It is evident from equation (D.31) that the new tensor \mathbf{h}' also rotates by the same angles with respect to the old \mathbf{h} as the new frame rotates with respect to the old frame. This proves that the model for pressure Hessian tensor \mathbf{h} is Galilean invariant. The same proof applies to the viscous Laplacian tensor $\boldsymbol{\tau}$.

Aside from the mean pressure and viscous terms discussed above, all the other terms in the b_{ij} stochastic differential equation are functions of b_{ij} itself and it can be shown that they are also Galilean invariant by construction.

D.6 Numerical schemes for stochastic differential equations

In this work, the numerical scheme used to propagate the b_{ij} -SDE in computational time t' is a second order weak predictor-corrector scheme given by:

$$b'_{ij} = b_{ij}^{(n)} + \mu_{ij}(\mathbf{b}^{(n)})\Delta t' + \gamma_{ij}(\mathbf{b}^{(n)})\Delta t' + D_{ijkl}(\mathbf{b}^{(n)}) \xi_{kl}\sqrt{\Delta t'} \quad (\text{D.32})$$

$$\begin{aligned} b_{ij}^{(n+1)} &= b_{ij}^{(n)} + \frac{1}{2}[\mu_{ij}(\mathbf{b}^{(n)}) + \mu_{ij}(\mathbf{b}')] \Delta t' + \frac{1}{2}[\gamma_{ij}(\mathbf{b}^{(n)}) + \gamma_{ij}(\mathbf{b}')] \Delta t' \\ &\quad + \frac{1}{2}[D_{ijkl}(\mathbf{b}^{(n)}) + D_{ijkl}(\mathbf{b}')] \xi_{kl}\sqrt{\Delta t'} \end{aligned} \quad (\text{D.33})$$

where each component of ξ_{ij} is an independent standardized Gaussian random variable. The θ^* -SDE can be written in the computational timescale t' as follows:

$$\begin{aligned} d\theta^* &= -\theta^* dt^* + \beta(q, r) dW^* \\ &= -\theta^* \frac{\langle A \rangle}{A} dt' + \beta(q, r) \sqrt{\frac{\langle A \rangle}{A}} dW' \end{aligned} \quad (\text{D.34})$$

where, $\beta(q, r)$ represents the different diffusion coefficients discussed in section 7.3.4. The θ^* -SDE is also propagated using the second order weak predictor-corrector scheme:

$$\theta^{*'} = \theta^{*(n)} - \theta^{*(n)} \frac{\langle A \rangle}{A} \Delta t' + \beta(q^{(n)}, r^{(n)}) \xi \sqrt{\frac{\langle A \rangle}{A}} \sqrt{\Delta t'} \quad (\text{D.35})$$

$$\theta^{*(n+1)} = \theta^{*(n)} - \frac{1}{2}[\theta^{*(n)} + \theta^{*'}] \frac{\langle A \rangle}{A} \Delta t' + \frac{1}{2}[\beta(q^{(n)}, r^{(n)}) + \beta(q', r')] \xi \sqrt{\frac{\langle A \rangle}{A}} \sqrt{\Delta t'} \quad (\text{D.36})$$

where $q^{(n)}, r^{(n)}$ represent the second and third invariants of the $\mathbf{b}^{(n)}$ tensor and q', r' represent the second and third invariants of the \mathbf{b}' tensor. Here, the VG magnitude $A = e^{(\sigma_\theta \theta^* + \langle \theta \rangle)}$, for constant values of $\langle \theta \rangle, \sigma_\theta$ from DNS.